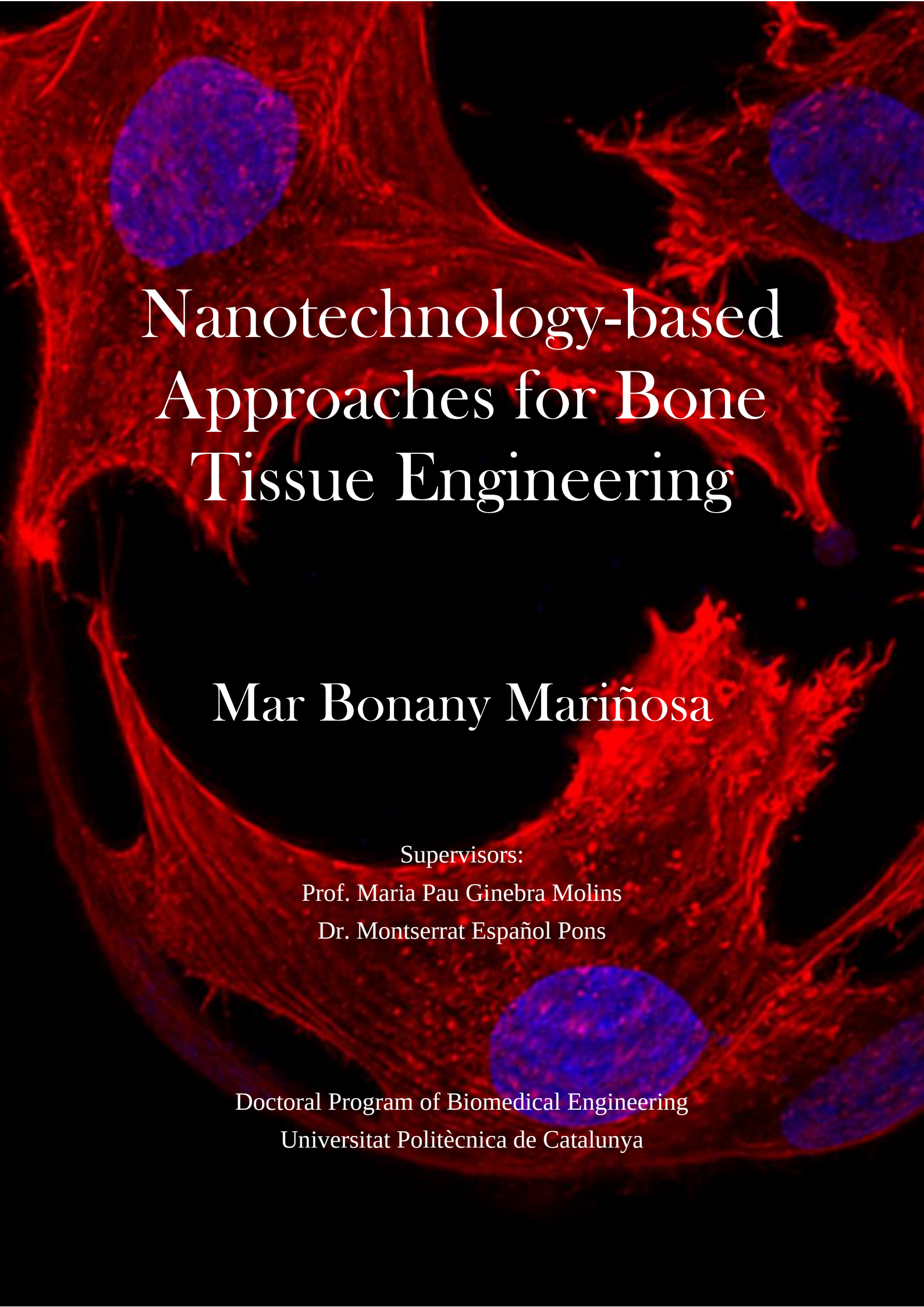

Nanotechnology-based Approaches for Bone Tissue Engineering

Mar Bonany Mariñosa

Supervisors:

Prof. Maria Pau Ginebra Molins

Dr. Montserrat Español Pons

Doctoral Program of Biomedical Engineering

Universitat Politècnica de Catalunya

UNIVERSITAT POLITÈCNICA DE CATALUNYA BARCELONATECH

Nanotechnology-based Approaches for Bone Tissue Engineering

Mar Bonany Mariñosa

PhD Thesis

NANOTECHNOLOGY-BASED APPROACHES FOR BONE TISSUE ENGINEERING

Doctoral Program of Biomedical Engineering

Mar Bonany Mariñosa

Supervisors:
Prof. Maria Pau Ginebra Molins
Dr. Montserrat Español Pons

Biomaterials, Biomechanics and Tissue Engineering Group
Department of Materials Science and Engineering
Universitat Politècnica de Catalunya

Barcelona, 2021

Als meus pares, que s'ho mereixen tot.
I a la meva àvia, que és bona, forta i entregada.

Au milieu de l'hiver,
j'apprenais enfin qu'il y avait en moi un été invincible.

Albert Camus

Table of Contents

ABSTRACT ..... **VIII**

RESUM ..... **IX**

ACKNOWLEDGEMENTS ..... **X**

OBJECTIVES OF THE THESIS ..... **XIII**

ABBREVIATIONS ..... **XIV**

CHAPTER 1: INTRODUCTION **1**

1.1. Bone Tissue **2**

1.1.1. Function 2
1.1.2. Bone Structure 2
1.1.3. Bone Composition 3
1.1.4. Bone Cells 5
1.1.5. Bone Remodelling Process 5

1.2. Bone Affections **6**

1.2.1. Bone Cancer 6
1.2.2. Bone Defects 7

1.3. Bone Cancer Therapy **7**

1.3.1. Hydroxyapatite Nanoparticles in Cancer Treatment 7
1.3.2. Cytotoxicity Mechanisms of Hydroxyapatite Nanoparticles 8

1.4. Bone Grafting Strategies **9**

1.4.1. Bone Grafts of Natural Origin 9
1.4.2. Synthetic Bone Grafts 10
1.4.3. Three-Dimensional Printing of Bone Grafts 10

1.5. Bioinks for Bone Regeneration **12**

1.5.1. Bioink Formulations 12
1.5.2. Strategies to Tune the Mechanical Properties and Degradability of Alginate Bioinks 12
1.5.3. Strategies to Confer Bioactivity to Alginate Bioinks 14

1.6. References **16**

CHAPTER 2: HYDROXYAPATITE NANOPARTICLES-CELL INTERACTION: THE FATE OF MEMBRANE-BOUND AND INTERNALISED NANOPARTICLES **30**

Scope **31**
2.1. Introduction **32**
2.2. Experimental Section **33**

2.2.1. Synthesis and Characterisation of Non-doped and Magnesium-doped Hydroxyapatite Nanoparticles 33
2.2.2. Fluorescent Functionalisation of the Nanoparticles 34
2.2.3. Cell Culture 34
2.2.4. Nanoparticles – Cell Membrane Interaction 35
2.2.5. Flow Cytometry Assay 35
2.2.6. Intracellular Calcium Evaluation 36
2.2.7. Transmission Electron Microscopy 36
2.2.8. Cryo-Soft X-ray Tomography 36
2.2.9. Statistical Analysis 37

2.3. Results and Discussion 37

2.3.1. Characterisation of the Nanoparticles 37
2.3.2. Functionalisation of the Nanoparticles 39
2.3.3. Study of the Nanoparticles – Cell Membrane Interaction 40
2.3.4. Flow Cytometry Assay 43
2.3.5. Intracellular Calcium Evaluation 46
2.3.6. Transmission Electron Microscopy and Cryo-Soft X-ray Tomography 49

2.4. Conclusions 54
2.5. References 54

CHAPTER 3: MICROSPHERES WITH ION-DOPED HYDROXYAPATITE NANOPARTICLES FOR ENHANCED BONE REGENERATION **....60**

Scope 61
3.1. Introduction 62
3.2. Experimental Section 63

3.2.1. Synthesis of Mg-, Zn- and Sr-Doped Hydroxyapatite Nanoparticles 63
3.2.2. Synthesis of Nanoparticle-Charged Gelatine Microspheres 64
3.2.3. Physicochemical Characterisation of the Nanoparticles 64
3.2.4. Physicochemical Characterisation of the Microspheres 64
3.2.5. Study of the Ion Release in Cell Culture Media 65
3.2.6. Statistical Analysis 65

3.3. Results and Discussion 65

3.3.1. Physicochemical Characterisation of the Doped HA Nanoparticles 65
3.3.2. Physicochemical Characterisation of the Microspheres 67
3.3.3. Ion Release in Cell Culture Media 70

3.4. Conclusion 76
3.5. References 77

CHAPTER 4: MICROSPHERE INCORPORATION AS A STRATEGY TO TUNE THE BIOLOGICAL PERFORMANCE OF BIOINKS **....84**

Scope 85
4.1. Introduction 86
4.2. Experimental Section 87

4.2.1. Synthesis of Gelatine Microspheres 87
4.2.2. Synthesis of Hydroxyapatite-Containing Gelatine Microspheres 87

4.2.3. Synthesis of Calcium-Deficient Hydroxyapatite Microspheres 88
4.2.4. Physicochemical Characterisation of the Microspheres 88
4.2.5. Preparation of the Bioinks 89
4.2.6. Rheological Study 90
4.2.7. Direct Cell Culture on the Microspheres 90
4.2.8. Cell Viability Analysis 90
4.2.9. Cell Proliferation and Cell Morphology Evaluation 91
4.2.10. Gene Expression Assessment 91
4.2.11. Statistical Analysis 92

4.3. Results 92

4.3.1. Physicochemical Characterisation of the Microspheres 92
4.3.2. Rheology and Shape Fidelity of the Bioinks 95
4.3.3. Cell Cultures on the Microspheres 96
4.3.4. Cell Viability and Cell Migration in the Bioinks 98
4.3.5. Cell Proliferation and Cell Morphology in the Bioinks 101
4.3.6. Gene Expression of the Cells in the Bioinks 102

4.4. Discussion 103
4.5. Conclusions 107
4.6. References 107

CHAPTER 5: BIOINK FUNCTIONALISATION WITH INTEGRIN-SELECTIVE PEPTIDOMIMETICS **..... 113**

Scope 114
5.1. Introduction 115
5.2. Experimental Section 116

5.2.1. Alginate Functionalisation and Characterisation 116
5.2.2. Cell Culture 116
5.2.3. Bioink Synthesis 117
5.2.4. Cell Viability and Proliferation 117
5.2.5. Osteogenic Differentiation 117
5.2.6. Statistical Analysis 118

5.3. Results and Discussion 119

5.3.1. Alginate Bioink Characterisation 119
5.3.2. Cell Viability and Morphology 120
5.3.3. Cell Proliferation 123
5.3.4. Osteogenic Differentiation 123

5.4. Conclusions 126
5.5. References 126

GENERAL CONCLUSIONS 133

PUBLICATIONS AND CONFERENCES 136

Publications 137
Conference Participation 138

Abstract

Substantial research efforts in the field of tissue engineering have been done in recent years to overcome the bone regeneration limitations of the human body and to treat bone-related pathologies like osteosarcoma. Nanotechnology offers limitless ways to improve bone regeneration and to fight bone cancer by means of hydroxyapatite (HA) nanoparticles (NPs) and through the design of small organic molecules with the capacity to trigger specific biological reactions. In the present thesis, the implementation of these molecules in cancer therapy and in the bone regeneration field is studied, and their interaction with biological systems is investigated.

Chapter 1 offers a general perspective of the topic and introduces the state of the art with the main strategies for bone cancer therapy and bone regeneration reported in the literature. **Chapter 2** explores the use of hydroxyapatite nanoparticles for bone cancer therapies, with a view to elucidate their underlying cytotoxic mechanism. Moreover, the techniques commonly used to study the cellular uptake of these materials are compared with more novel characterisation alternatives. Indeed, the implementation of cryo-soft X-ray tomography is presented as a key tool for tracking and monitoring the fate of internalised HA NPs, as it allows visualising both solid and liquid calcium deposits resulting from the dissolution of the nanomaterials. **Chapter 3** investigates the use of gelatine microspheres (MS) as carriers of HA NPs for bone regeneration. Additionally, the ionic doping of these NPs with Mg^{2+}, Zn^{2+} and Sr^{2+}, with recognised benefits in the bone remodelling process, is studied and their release kinetics in cell culture medium is further quantified. Although dissolution and precipitation events take place simultaneously, MS demonstrate to be an effective method to deliver the therapeutical loaded ions. **Chapter 4** and **Chapter 5** focus on the design of bioinks as a strategy for bone tissue engineering. Alginate is chosen as the bioink binder due to its mild and straightforward cross-linking process, as well as for its high tuneability and adequate rheological properties. Two different strategies are proposed to solve the poor bioactivity of this polymer by conferring biological functionality to the cells embedded in the inks. **Chapter 4** studies the incorporation of different types of MS (gelatine, gelatine containing HA NPs and calcium-deficient HA) to the formulation of these cell-laden inks. Furthermore, two cross-linking procedures are compared. Both, the addition of MS and the cross-linking using Ca^{2+}-supplemented cell culture medium, resulted in increased stiffness of the bioinks. Importantly, the capacity of cells to migrate to the MS in the bioink formulation affected the cellular performance. In the case of inks loaded with gelatine-containing MS, promotion of cell migration, attachment and proliferation inside the bioink was observed. In addition, despite the superior osteogenic differentiation potential of the fully mineral MS when cells were cultured directly onto them, this behaviour was not evidenced when these particles were added in the bioink formulation. Finally, **Chapter 5** explores the use of two peptidomimetics with selective activity towards $\alpha_5\beta_1$ and $\alpha_v\beta_3$ integrins, which play a crucial role in the osteogenic pathway. Alginate polymer is functionalised with either molecule prior to the preparation of the cell-laden inks. The use of both non-peptidic ligands results in enhanced osteogenic differentiation of the mesenchymal stem cells embedded in the bioinks. Besides, the boost of osteodifferentiation is higher than in the traditional RGD-coupled alginate hydrogels.

Resum

En els últims anys s'ha fet un gran esforç de recerca en el camp de l'enginyeria de teixits per tal de superar les limitacions de regeneració òssia del cos humà, així com per tractar patologies relacionades amb l'os com ara l'osteosarcoma. La nanotecnologia ofereix múltiples maneres de millorar la regeneració òssia i de lluitar contra el càncer d'os, gràcies a l'ús de nanopartícules d'hidroxiapatita (NPs HA) i a través del disseny de molècules orgàniques molt petites amb capacitat per desencadenar reaccions biològiques específiques. En aquesta tesi, s'estudia la implementació d'aquestes molècules en la teràpia anticàncer i en el camp de la regeneració òssia, així com la seva interacció amb els sistemes biològics.

El **capítol 1** ofereix una perspectiva general del tema i introdueix l'estat de l'art amb les estratègies per al tractament del càncer d'os i la regeneració òssia més comunes reportades en la literatura. En el **capítol 2** s'explora l'ús de les nanopartícules d'hidroxiapatita com a teràpia per al càncer d'os amb la intenció d'investigar-ne el mecanisme de citotoxicitat subjacent. A més, les tècniques més utilitzades per a l'estudi de la internalització cel·lular d'aquests materials es comparen amb alternatives de caracterització més innovadores. D'aquesta manera, la implementació de la crio-tomografia de raigs X tous es presenta com una eina clau per al seguiment i la monitorització del destí d'aquestes NPs internalitzades, ja que permet la visualització de dipòsits de calci en estat sòlid i líquid, que deriven de la dissolució del nanomaterial. En el **capítol 3** s'investiga l'ús de microesferes (MS) de gelatina com a portadores de NPs HA per a la regeneració òssia. S'estudia el dopatge iònic de les NPs amb Mg^{2+}, Zn^{2+} i Sr^{2+}, que són ions molt implicats en el procés de remodelació òssia, i es quantifica la seva cinètica d'alliberació en medi de cultiu cel·lular. Tot i que hi ha processos de dissolució i precipitació simultanis, es demostra que les MS són un mètode efectiu per alliberar els ions terapèutics carregats. El **capítol 4** i el **capítol 5** se centren en el disseny de biotintes en el camp de l'enginyeria de teixits ossis. S'escull l'alginat com a matriu, donat el seu procés d'entrecreuament simple i suau per a les cèl·lules, així com per la seva alta capacitat de modificació i les seves propietats reològiques. Es proposen dues estratègies diferents per solucionar la falta de bioactivitat d'aquest polímer, i donar així funcionalitats biològiques a les cèl·lules incorporades a les biotintes. En el **capítol 4** s'estudia la incorporació de diferents tipus de MS (gelatina, gelatina amb NPs HA, i HA deficient en calci) per a la formulació d'aquestes biotintes. També es comparen dos protocols d'entrecreuament. Tant la incorporació de MS com l'entrecreuament usant medi de cultiu suplementat amb Ca^{2+} incrementen la rigidesa de les biotintes. També s'aprecia com la capacitat de migració de les cèl·lules cap a les MS en la formulació de les biotintes afecta el comportament cel·lular. En el cas de les tintes carregades amb MS que contenen gelatina, s'observa una promoció de la migració, adhesió i proliferació cel·lular dins les biotintes. D'altra banda, tot i la major capacitat de diferenciació osteogènica de les MS minerals quan les cèl·lules s'hi sembren a sobre, no s'aprecien aquests altres fenòmens. Finalment, en el **capítol 5** s'explora l'ús de dos peptidomimètics amb activitat selectiva per a les integrines $\alpha_5\beta_1$ i $\alpha_v\beta_3$, que s'han vist molt implicades en la ruta osteogènica. El polímer d'alginat es funcionalitza amb aquestes molècules abans de preparar-ne biotintes. L'aplicació d'aquests dos lligands no peptídics té com a resultat una millor diferenciació osteogènica de les cèl·lules mare mesenquimals incorporades en les biotintes. A part, aquest estímul de l'osteodiferenciació és més important que en els hidrogels d'alginat funcionalitzats amb RGD, que és la solució tradicional.

Acknowledgements

Hi ha una cita de Pere Casaldàliga que diu: “Al final del camí em diran: «Has viscut? Has estimat?» I jo, sense dir res, obriré el cor ple de noms.” I sento que em trobo una mica en aquest punt. En el final d’un camí, on toca fer un repàs de tot el que han significat aquests quatre anys i mig llargs. És el moment d’obrir el cor i trobar-hi noms.

Els primers que em venen al cap són la Pau i la Montse, les meves directores de tesi. És evident que sense vosaltres aquesta tesi no hauria existit, però m’enduc moltes altres coses a part de la culminació de tanta feina feta: un aprenentatge immens i també una mica de l’esperit crític i la recerca de la perfecció que us caracteritzen. Pau, gràcies per confiar en mi des del principi i donar-me aquesta oportunitat. Gràcies per ser guia durant tots aquests anys, per tot el suport rebut, la disponibilitat i el temps que m’has dedicat a mi i a aquesta tesi. Sempre recordaré amb un afecte especial els dos congressos que vam poder compartir, on la teva presència em feia estar tranquil·la i segura. Montse, gràcies per la confiança a nivell professional i personal. Ets tot cor i això ho ha fet tot molt més fàcil. Et vull donar les gràcies per confiar en mi a l’hora d’explorar camins nous que ens eren totalment desconeguts. Gràcies per fer-me sentir capaç d’acabar el que havia començat. Gràcies per no haver-me fallat.

Gràcies a la Txell, la Meri i la Noelia, sense les quals aquest vaixell s’enfonsaria. Gràcies per la vostra feina incansable, per fer que tot això funcioni, per tenir-nos en compte i per estar sempre obertes a millores i noves propostes. Vull agrair-vos sincerament el temps (i la paciència) que m’heu dedicat al llarg d’aquests anys. Gràcies a en Carles, amb qui he compartit la passió viatgera sempre que hem tingut dos minuts. Gràcies per la confiança que has dipositat en mi i per donar-me l’oportunitat de treballar a prop teu. Ets un dels meus grans referents al grup, l’exemple que ser un científic brillant no és incompatible amb viure la vida. Gràcies a l’Osnat, que als doctorands ens ha tingut molt en compte. *Your support in Dresden ESB was deeply appreciated, as well as every international dinner we did there together. Thank you for your trust in me and for the valuable knowledge you were always willing to share with us. You’re impressive, and it has been a pleasure learning from you.* Vull fer extensiu el meu agraïment a la resta d’integrants del BBT, perquè m’heu acompanyat, aconsellat i guiat durant aquest temps. L’ambient als laboratoris és de les coses que estic segura que trobaré a faltar.

Pel que fa al mateix BBT, vull dedicar unes paraules especials a la Joanna gran i l’Anna, que són la definició de dedicació i feina ben feta. Valoro molt que m’acollíssiu des del primer moment i em féssiu sentir tan acompanyada al principi d’aquest camí. Gràcies per ensenyar-m’ho tot al *lab* i, sobretot, per alegrar-me els dies amb la vostra manera de ser. Joanna, *gracias también por ese viaje a Cracovia donde tú y tu familia me tratasteis tan bien. Gracias por seguir estando a mi lado en la distancia. Te quiero, golda.* Gràcies a en Cédric, que és el millor veí que algú podria tenir *(en esto también has ganado). Gracias por cada visita, cada conversación y por nuestras cenas románticas improvisadas. Gracias por preocuparte tanto por mí y por convertirte en un amigo.* La Linh, que desborda empatia i sensibilitat. *Gracias por tu alegría y los momentos vividos juntas.* A en Diego, que m’acompanya des del TFM. *Gracias por tu sentido del humor y tu generosidad, y por quererme a tu manera. Parece increíble, pero tus abrazos siguen siendo especiales después de tanto tiempo.*

Gràcies a la Marta, en Dani, l'Elisabetta i en Rolando, que van ser els meus estudiants. Gràcies per la vostra implicació en el projecte i la feina feta. Per confiar en mi com a científica – quin remei...! – i pel bon rotllo que he tingut amb tots quatre. Sou especials, ha sigut un plaer haver pogut treballar junts i estic molt orgullosa de cadascun de vosaltres. També vull donar les gràcies a en Trifon i en Lucho, que sempre m'han cuidat molt, i a en Kim i l'Isaac per la seva ajuda. A la gent amb qui he tingut el plaer de compartir despatx: l'Erica, en Miquel, en Hossein, l'Ana, la Violeta, la Inès, la Laura, en Sergio, la Mona, la Junhui i en Marc. Gràcies per crear un ambient de treball distès i agradable. Per la paciència que heu tingut. Hossein, *thank you for every anecdote you talk me about, for all the times you made me laugh*. I al Sergio, *por ser tan, tan cuqui!*

Una gran part del meu cor l'ocupa la Panxa, que són uns magnífics científics, però sobretot unes grans persones. Quina delícia les cerveses als diferents asiàtics després de llargues jornades de feina! I aquell *anti-uolesbí* que el Covid va aixafar, però per totes les festes del canvi d'hora que encara queden! Tinc tantes coses a agrair-vos que vull anar un per un. A la que va arribar primer, la Joanna. *Por esos meses que compartimos mano a mano, en los que te enfadabas conmigo en inglés. Gracias por tu locura, por ser tan femenina y por estar siempre reinventando el idioma y revolucionando el* lab *con tus algoritmos. Me haces mucho de reír.* A en Miguel, que és un esperit lliure. Gràcies per les abraçades on no calien paraules, i per ser l'exemple de com gestionar la vida, així en general. A en Lluís, que és constància i voluntat. Tot bondat, sempre atent i disposat a ajudar. Gràcies per obrir-me les portes de casa teva i deixar que m'hi quedi sempre que t'ho demano. Gràcies per cada cançó que ens has regalat, amb tot el que comporta. Suposo que ja ho saps, però si hi hagués més persones com tu, el món seria un lloc molt més bonic. T'estime molt. A la Claudia, que és tan de veritat, un referent en molts aspectes. *Muchas gracias por tus palabras, por tus abrazos y por estar. Siempre. Gracias por tanta confianza y comprensión. Eres preciosa por fuera, pero aún más por dentro.* Gràcies a en Víctor per la serenor i la ironia. Per aportar la calma que tots hem necessitat en algun moment. I també per aquelles (vergonyoses, per què no dir-ho) primeres vegades junts, que espero que no s'acabin mai. Per deixar-nos fer broma dels teus excels, i per la Maria, que no va fugir corrent quan ens va conèixer. A en Xavi, que des del principi va omplir-ho tot de bon rotllo. Gràcies per les trucades quan més calien. Pel teatre, el *nanotwerk* i Sant Llorenç, per fer pinya des del primer moment. A en David, que porta un somriure gravat a la cara. *Gracias por recordarme que el doctorado también ha sido ilusión.* A vosaltres, infinites gràcies, perquè molts cops heu sigut l'únic motiu per venir al *lab*. El comboi que tant m'ha salvat. Sou els millors companys de viatge que podria haver tingut, i estic segura que us tindré a prop molt de temps.

Vaig tenir la sort de poder marxar uns mesos a fer ciència fora, i de la meva estada a Maastricht vull recordar algunes persones. Perquè ara sí, ara és quan la nostàlgia pesa més que la maleta. Sabine, *thank you for receiving me at the moment when I needed it the most. I want to acknowledge you for giving me the opportunity to enjoy Maastricht and the MERLN, which is full of wonderful professionals. Thank you for your time, availability and for all the knowledge you shared with me*. Gràcies a en Víctor, que em va acollir des del primer moment. *Gracias por tu compañía y tu apoyo. Por nuestros largos paseos, los* shortcakes *que echo tanto de menos, y por descubrirme cada rincón de esta pequeña ciudad.* A en Pere, que va ser la meva millor casualitat en terres neerlandeses. Gràcies pels sopars de pizza, les tardes de diumenge al Koffie, els partits de futbol i, sobretot, per les converses que acompanyaven tots aquells moments. Saps que no tinc prou paraules. Gràcies, simplement, per ser casa meva quan la sentia tan lluny. A la Lea, la meva amiga suïssa. Lea, *thank you very much for every single gift, for being*

real and unique. For your last-minute presence in all the plans and for our true friendship. Thank you for visiting me in Barcelona, my door is always open for you. I wish you the best and I hope to see you soon. No vull oblidar-me de la Pichaporn, que recordar-me'n sempre em treu un somriure. Per últim, vull fer extensiu l'agraïment a tots els qui em van ajudar d'alguna manera o altra durant aquells mesos: en Francis, en Nello, la María, en Tristan, la Giotta, la Chloe, la Yousra, l'Aygül, i tants d'altres que em deixo.

I dels que hi van ser uns mesos, als que hi són des de fa tants anys. Per començar, les meves amigues, el meu tresor: la Sara, la Marta, la Núria, la Marina i l'Ari, que han aguantat estoicament els efectes col·laterals d'aquesta tesi. Gràcies per ser-hi sempre, per ajudar-me en tot el que heu pogut. Per fer-me sentir tan estimada i recolzada. Per ser pilars que no s'enfonsen mai, per més que passin els anys i les coses. I a en Dani, el meu oasi. Gràcies també a la Mari, que té una personalitat que t'atrapa.

No puc deixar-me les persones més importants de la meva vida, que m'omplen el cor des que soc petita i a qui ho dec tot, els meus pares. Gràcies per donar-me ales, pentinar-me les plomes i acompanyar-me en el vol. Gràcies per ser paraigua quan a la meva vida hi plovia tant. Gràcies, perquè sempre sou niu i refugi. Vull agrair-vos el tros de vida que m'heu donat, i prometre-us que jo també hi seré sempre que ho necessiteu. Gràcies també al meu germà, en Pol, que m'ha fet sensible, empàtica i tolerant. T'estimo molt, sé que pots amb tot i estic molt orgullosa de tu.

Gràcies a la iaia i les meves tietes. Sé que he tingut molta sort i em sento molt afortunada de tenir-vos. Gràcies, perquè tinc la certesa que sempre us tindré a prop. I als meus cosins, la Berta, en Biel, en Pau i en Dídac, que m'alegren l'existència i estic segura que faran amb la vida tot allò que vulguin.

I per últim, a en Yago, a qui admiro moltíssim. Vull donar-te les gràcies per aparèixer i revolucionar-me la vida. Per ensenyar-me a mirar el món des d'altres perspectives. Per ajudar-me a créixer mentre intentem ser cada dia una mica millors. Gràcies per tanta màgia i llibertat. Per creure en mi quan jo mateixa vaig deixar de fer-ho. Gràcies per seguir al meu costat després de tot, perquè soc conscient que ha sigut difícil, però també preciós. Ets el més bonic que m'enduc d'aquesta tesi.

A tots, gràcies per acompanyar-me. Gràcies per donar tanta llum a la meva vida i fer-ho tot més fàcil.

Objectives of the Thesis

The aim of the present Philosophy Doctor (PhD) thesis was to apply different nanotechnology-based approaches to bone tissue engineering. On the one hand, this thesis focuses on investigating the cytotoxic mechanism of hydroxyapatite nanoparticles in bone cancer treatments. On the other hand, it is devoted to developing new strategies to improve bone regeneration in critical-sized defects.

Specifically, the following objectives were established and addressed in this thesis:

- Understand the cellular toxicity of hydroxyapatite nanoparticles in bone cancer therapies. Investigate the commonly used techniques to study the behaviour of these materials once internalised in the cells, and compare with to more novel characterisation alternatives (**Chapter 2**).
- Develop composite microspheres made of gelatine and ion-doped hydroxyapatite nanoparticles for the delivery of therapeutic ions in bone regeneration applications. Study the physicochemical implications of magnesium, zinc and strontium incorporation into hydroxyapatite nanoparticles, as well as the addition of the doped-hydroxyapatite nanoparticles into the final microspheres. Evaluate the ion release kinetics of the synthesised microspheres (**Chapter 3**).
- Study the incorporation of microspheres of different natures to improve alginate/gelatine bioinks for bone tissue engineering. Evaluate the rheological properties of the developed formulations. Investigate the performance of the cells seeded either directly on top of the microspheres or embedded in microsphere-containing bioinks, in terms of cell viability, proliferation, morphology and osteogenic differentiation (**Chapter 4**).
- Functionalise alginate with peptidomimetics designed to have selective activity for two bone-related integrins: $\alpha_5\beta_1$ and $\alpha_v\beta_3$. Use the functionalised alginates to synthesise cell-laden inks. Study the cell behaviour in the constructs and compare it to the more common RGD-coupled alginate bioinks (**Chapter 5**).

Abbreviations

^{1}H NMR	Proton nuclear magnetic resonance
2D / 3D	Two-dimensional / Three-dimensional
3-ITT	Three interval thixotropy test
α-TCP	Alpha-tricalcium phosphate
Adv. DMEM	Advanced Dulbecco's modified eagle medium
ALP	Alkaline phosphatase
ANOVA	Analysis of variance
AO	Acridine orange staining
ART	Algebraic reconstruction techniques
ATR	Attenuated total reflectance mode
BG	Bioactive glass / Bioglass
BMP-2	Bone morphogenetic protein 2
BMU	Basic multicellular unit
BSP	Bone sialoprotein
CAD	Computer-aided design
CaP	Calcium phosphate
CDHA	Calcium-deficient hydroxyapatite
cDNA	Complementary deoxyribonucleic acid
CF	Carboxyfluorescein
CL	Cross-linking
Col. I	Collagen type I
Cryo-SXT	Cryo-soft X-ray tomography
CT	Computed tomography
DAPI	4′,6-diamidino-2-phenylindole
DMEM	Dulbecco's modified eagle medium
DOPA	L-3,4-dihydroxyphenylalanine
ECM	Extracellular matrix
EDC	N-(3-dimethylaminopropyl)-N′-ethylcarbodiimide hydrochloride
EDTA	Ethylenediaminetetraacetic acid
EPR	Enhanced retention and permeability effect
ER	Endoplasmic reticulum
FBS	Foetal bovine serum
FC	Flow cytometry
FESEM	Field emission scanning electron microscopy
FTIR	Fourier-transform infrared spectroscopy
Fw	Forward primer
G	α-L-guluronate subunit
G'	Storage modulus
G'_{eq}	Storage modulus at rest conditions
G"	Loss modulus
GAPDH	Glyceraldehyde 3-phosphate dehydrogenase
GelMA	Methacrylated gelatine
HA	Hydroxyapatite
hMSC	Human mesenchymal stem cells
hBM-MSC	Human bone marrow-derived mesenchymal stem cells
HEPES	4-(2-hydroxyethyl)-1-piperazineethanesulfonic acid buffer
ICP	Inductively coupled plasma
ICP-MS	ICP mass spectrometry
ICP-OES	ICP optical emission spectrometry
L/D	Live/dead staining
LAB	Laser-assisted bioprinting
LAC	Linear absorption coefficient
LD	Lipid droplet
LDH	Lactate dehydrogenase
LSM	Laser scanning microscopy
LVR	Linear viscoelastic region
M	β-D-mannuronate subunit
MES	2-(N-morpholino)ethanesulfonic acid
M-PER	Mammalian protein extraction reagent
MS	Microspheres
MSC	Mesenchymal stem cell
MVB	Multivesicular body
MW	Molecular weight
NHS	N-hydroxysuccinimide
NP	Nanoparticle
OA	Oscillatory amplitude
OA	Oxidised alginate
OCN	Osteocalcin
OPN	Osteopontin
OS	Osteosarcoma / Osteogenic sarcoma
OSX	Osterix / Transcription factor Sp7
PB / PBS	Phosphate-buffered saline
PEG	Polyethylene glycol
PFA	Paraformaldehyde
PhD	Philosophy doctor
PI	Propidium iodide
PLA	Polylactic acid
PLGA	Poly(lactic-co-glycolic acid)
PMMA	Poly(methyl methacrylate)
RGD	Arg-Gly-Asp (Arginine, Glycine, Aspartic acid)
RNA	Ribonucleic acid

RP-HPLC	Reversed-phase analytical high-performance liquid chromatography
RT-qPCR	Reverse transcription quantitative polymerase chain reaction
RUNX2	Runt-related transcription factor 2
Rv	Reverse primer
SEM	Scanning electron microscopy
SIBLING	Small integrin-binding ligand N-linked glycoprotein
SLA	Stereolithography
SPPS	Solid-phase peptide synthesis
TEM	Transmission electron microscopy
TRPM7	Transient receptor potential; subfamily: melastatin; member: 7
UV	Ultraviolet
XRD	X-ray diffraction

Chapter 1

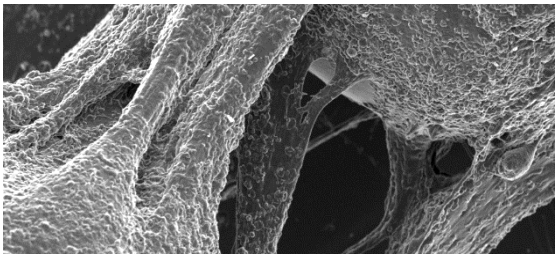

Introduction

Bone is reported to be the second most transplanted tissue after blood [1], and bone injuries account for more than 500000 grafting procedures per year only in the United States [2]. Moreover, age-associated musculoskeletal diseases are the 4th main cause of disability worldwide, and their incidence is expected to increase due to the global ageing of the population. Indeed, it is predicted that the proportion of the world's population over 60 years will duplicate by the end of 2050 [3].

In addition, bone cancer is another major problem of this tissue, being osteosarcoma (OS) the most common type of primary solid tumour originated in bone. This disease mainly affects children and young adults, as well as adults with previous bone pathologies [4].

The following sections provide an overview of the main characteristics of bone tissue, describing its function, composition and structure, as well as its remodelling process. Afterwards, a brief description of the two major bone-related alterations is exposed. The main bone cancer treatments will be covered, as well as the use of hydroxyapatite nanoparticles in bone cancer therapy. Finally, an insight into bone grafts and bioinks will be given, together with different approaches to both tune the mechanical properties and the cell behaviour of alginate cell-laden inks.

1.1. Bone Tissue

1.1.1. Function

Bone is a complex organ that exerts important functions in the body. On the one hand, bone provides shape and support to the body through the skeletal system which, in turn, protects and supports other internal organs and soft tissues. In this sense, bone has a clear locomotive and biomechanical function as it acts as attachment points for the muscles [5]. On the other hand, at the metabolic level, bone tissue serves as a storage site for certain ions, especially calcium and phosphorus, regulating their levels throughout the body. Finally, bones harbour marrow which is divided into yellow and red marrow. Whilst yellow bone marrow serves as fat storage, the red marrow produces blood cells (*i.e.* red blood cells, white blood cells and platelets) through haematopoiesis [6,7].

1.1.2. Bone Structure

The human skeleton is composed of more than 200 different bones, which are usually classified by their shape. The four big families are: (1) long bones, presenting a central shaft called diaphysis and two edges (epiphyses) covered by cartilaginous tissue, such as tibia, femur, ulna and radius; (2) short or cuboidal bones, like carpals and tarsals; (3) flat bones, that usually protect organs or serve for muscle attachment, for example, parietal, scapulae, ribs or sternum; (4) irregular bones with complex shapes, such as vertebrae or maxilla [8].

There are two types of bone tissue, *i.e.* cortical or compact tissue and trabecular tissue, also known as spongy or cancellous bone. Although all the bones present a similar structure, the distribution and concentration of each type of tissue will depend on the bone's overall function. In an adult human, cortical bone accounts for approximately 80 wt% of the skeletal system. This tissue exhibits a high calcification and is responsible for providing mechanical strength to the system. It possesses high rigidity and resistance to bending and torsion. Differently, trabecular bone comprises the remaining 20 wt% of the

skeleton. This tissue presents an important porosity, that permits the accommodation of the bone marrow [9,10].

1.1.3. Bone Composition

Bone can be described as a composite material, formed by the combination of an extracellular matrix (ECM), different kinds of cells and water. The ECM is composed of a major inorganic phase (representing the 60 wt%) together with an organic phase (that accounts for the remaining 40 wt%) [11]. While the inorganic phase provides stiffness to the structure, the organic phase supplies toughness [12].

The main inorganic components of the bone ECM are calcium and phosphorus ions that precipitate to form non-stoichiometric hydroxyapatite (HA) crystals, with a length of 20 – 50 nm, a width of 15 nm and a thickness of 2 – 5 nm [13]. Moreover, hydroxyapatite has an open crystalline structure that allows several ionic substitutions in its crystal lattice, where different monovalent or divalent cations such as Na^+, K^+, Mg^{2+}, Zn^{2+} or Sr^{2+} can substitute Ca^{2+}, while PO_4^{3-} and OH^- sites can be substituted by other anions such as CO_3^{2-} (**Figure 1.1**). Indeed, the chemical formula for biological HA can be described as $Ca_{10-x}M_x(PO_4)_{6-y}(HPO_4, CO_3)_y(OH)_{2-z}N_z$, where M and N represent cationic and anionic ions, respectively, and x, y and z stand for the molar number of the incorporated ions [14]. **Table 1.1** summarises the composition of bone tissue in the human body. As can be observed, bone presents small amounts of certain foreign ions that cause the poorly crystalline structure of the biological apatites, presenting nanosized hexagonal plate-like crystals [15].

Table 1.1. Composition of the mineral phase of bone, adapted from [16].

Element (Symbol)		Quantity	
Calcium	(Ca)	36.60	wt%
Phosphorus	(P)	17.10	wt%
Carbonate	(CO_3)	4.80	wt%
Sodium	(Na)	1.00	wt%
Magnesium	(Mg)	0.60	wt%
Chlorine	(Cl)	0.10	wt%
Fluorine	(F)	0.10	wt%
Potassium	(K)	0.07	wt%
Strontium	(Sr)	0.05	wt%
Silicon	(Si)	500	ppm
Zinc	(Zn)	39	ppm

Aside from the crystalline HA structure, another ionic environment can be found in form of a hydrated layer on the surface of the apatite (**Figure 1.1**). This layer permits the rapid and reversible exchange of ions with the surrounding fluids. It has been observed that this

hydrated layer decreases with maturity and, thus, the amount of freely exchangeable ions to assure homeostasis drops [17–19].

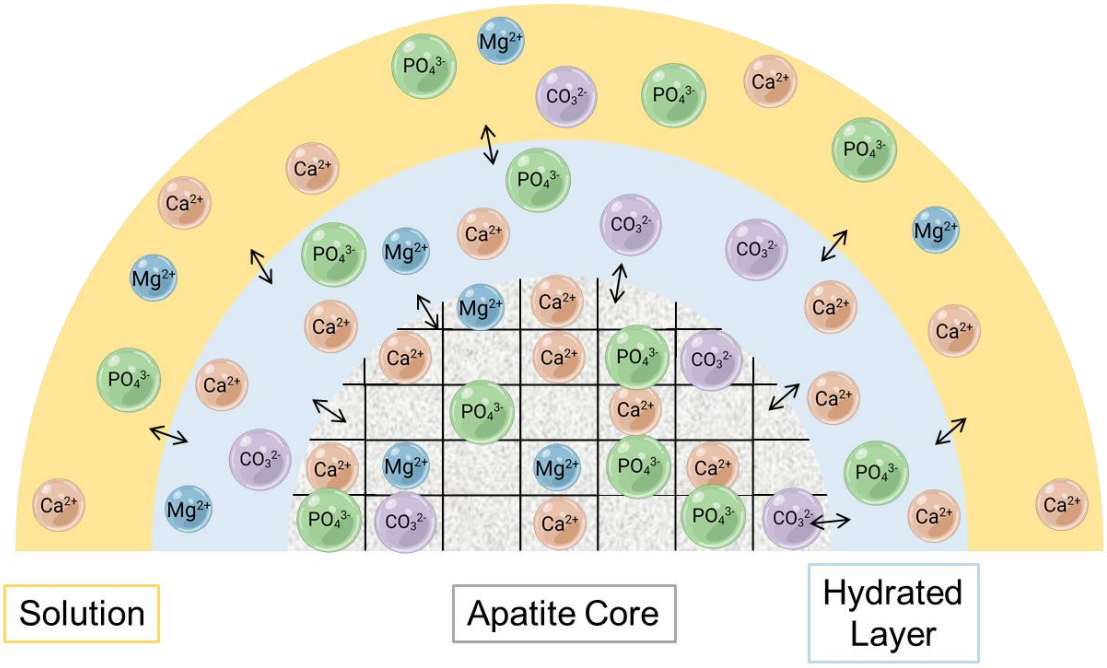

Figure 1.1. Scheme of the ionic substitutions in hydroxyapatite crystals, taking place either in the crystalline lattice or in the hydrated layer of the surface.

Although presented in small levels, all these ions play a major role in the bone properties and are crucial for the proper development of the tissue. For instance, magnesium is crucial in bone metabolism and is involved in the stimulation of osteoblast proliferation in the initial stages of osteogenesis [20,21]. On the other hand, zinc promotes bone growth and further mineralisation by stimulating osteoblasts and collagen secretion and inhibiting osteoclastic differentiation [22–24]. Finally, strontium inhibits bone resorption and boosts osteoblastic differentiation [25,26]. Since the presence of these ions in biological apatite play such important roles in bone formation, ionic substitutions into synthetic HA have been studied to improve the biological performance of these materials in bone tissue engineering [27].

On the other hand, the organic ECM is 90 wt% formed by type I collagen. This protein plays an important role in determining the architecture of bone by the creation of fibrils that interact with other proteins and generate lamellar arrangements. Non-collagenous proteins account for the remaining 10 wt% of the ECM organic phase. Among them, several proteoglycans, osteocalcin and osteonectin can be found, together with other small integrin-binding ligand N-linked glycoproteins (SIBLINGs) including bone sialoprotein (BSP) or osteopontin (OPN) [28].

In this PhD thesis, hydroxyapatite nanoparticles will be doped with bone-related therapeutic ions as a way to enhance the bone regeneration process.

1.1.4. Bone Cells

Bone tissue contains five main cell types: osteoprogenitor cells, osteoblasts, bone lining cells, osteocytes and osteoclasts. Each of them has individual functions, the combination of which makes the bone remodelling process possible.

Osteoprogenitor cells come from mesenchymal stem cells (MSCs) and are the precursors to more specialised bone cells such as osteoblasts and osteocytes. They are located in the red bone marrow from where they are released during the remodelling process [29]. With age, the body loses the ability to synthesise this kind of cell, contributing to the ageing of the bones.

Osteoblast, derived from osteoprogenitor cells, comprise around 5% of the total resident bone cells and are located in the surface of the bones. These cells are responsible for the ECM deposition and its subsequent mineralisation [30]. Bone lining cells are quiescent osteoblasts covering the bone surfaces. These cells present a thin and flat shape and their functions are not yet completely understood [31].

Osteocytes are the most abundant bone cells and comprise more than 90% of the total bone cells [32]. Osteocytes derive from MSCs through osteoblast differentiation, present a dendritic morphology, and are located within lacunae surrounded by mineralised ECM. Due to their location, osteocytes have a mechanosensitive function as they are able to convert mechanical stimuli to biochemical signals through mechanisms that are still unknown [33].

Osteoclasts are derived from the hematopoietic lineage. These multinucleated cells are responsible for the dissolution and absorption of the bone, either during the remodelling process or motivated by the need for ions in the body [6].

1.1.5. Bone Remodelling Process

During lifetime, healthy bone is under constant renewal. The old bone is progressively reabsorbed giving space for new bone formation. The replacement of old bone by new bone is called bone remodelling or bone turnover. This process permits the continuous adaptation of the bone [34]. Precisely, during childhood, the bone remodelling cycle allows the bone growth and, during adulthood, permits modifications in shape depending on the mechanical demands of the body [8]. Moreover, bone remodelling is of major importance during healing after a bone injury.

The remodelling process is complex and requires close interaction of the bone cells with each other and with the ECM. The turnover takes place in basic multicellular units (BMUs) located in the bone cavities [8]. These fundamental units are made of small groups of cells organised into a cutting cone with osteoclastic resorption at the apex and osteoblasts creating new osteoid at the base filling the cavity, together with endothelial cells from the blood vessels [35].

In the remodelling process, five phases can be distinguished: resting or quiescence, resorption, reversal, bone formation and mineralisation, as represented in **Figure 1.2**. The first step is the separation of lining cells to expose the bone surface, followed by the recruitment and guidance of hematopoietic stem cells by osteoclastogenic factors to the site of interest. During the resorption stage, these cells differentiate into mature osteoclasts that attach to the bone surface by polarising their membrane. Osteoclasts secrete acidic enzymes to locally dissolve both organic and inorganic bone phases, which results in small fragments that are digested within cytoplasmic vacuoles of the osteoclasts

[36]. The resulting products are calcium and phosphorus ions that are released into the bloodstream. Resorption lacunae are created as a consequence of this process (reversal stage). Afterwards, the bone formation stage takes place. The MSC-derived osteoblasts deposit the organic matrix (also named osteoid) in the lacunae by secreting collagen type I, as well as alkaline phosphatase (ALP), different growth factors and osteocalcin, among others. Finally, during the mineralisation step, osteoblasts calcify the osteoid. Subsequently, they undergo apoptosis or become trapped into the ECM and transform into osteocytes [37].

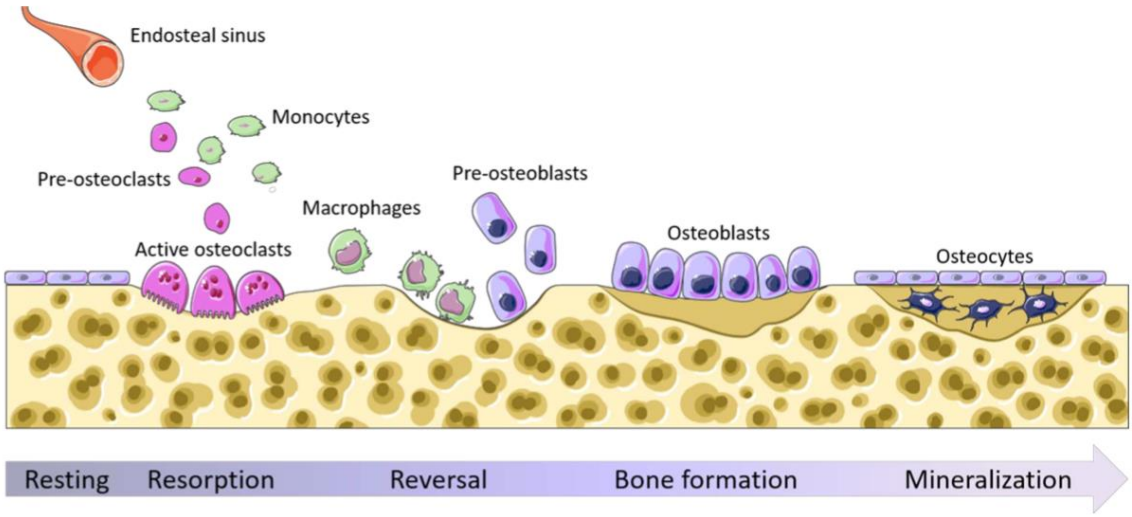

Figure 1.2. Schematic representation of bone remodelling process, from [38].

1.2. Bone Affections

The two main bone affections encountered in the clinics are bone cancer and bone defects and, therefore, they represent a field of interest in medical research. These affections have multiple origins and strategies to be treated. Down below these two aspects are developed.

1.2.1. Bone Cancer

Bone cancer is the presence of a malignant tumour in the bone tissue. Usually, cancer in the bone is caused by metastasis of other primary tumours, such as breast, prostate or lung cancer [39,40]. Among the primary bone cancers, osteosarcoma (also called osteogenic sarcoma) is the most common one. Although this type of cancer can develop in any bone, it is frequently found in quickly growing bones, like the distal femur (30%), proximal tibia (15%) or proximal humerus (15%) [41]. Therefore, it mostly affects children and young adults, whose bone cells experience rapid growth and a higher risk of mutations [4]. Moreover, OS is developed as an osteoid-producing solid tumour. Despite this type of cancer occurs with a low incidence compared to other solid tumours, it is ranked among the most usual cause of cancer-related child death [42,43].

Interestingly, it has been demonstrated that some cancer cells have ionic channels dysregulated in their membrane, compared to normal cells of the same tissue. For example, the TRPM7 magnesium-transporter is overexpressed on MG-63 osteosarcoma

cells [44,45], ZIP4 expression is increased in the membrane of pancreatic cancer cells and ZIP1 is downregulated in malignant prostate cells, both of them being zinc transporters [46].

1.2.2. Bone Defects

Bone defects can be originated by different causes, where the most common is trauma, followed by osteoporosis. Osteoporosis is a skeletal disorder characterised by a progressive reduction of the bone mineral density over time, leading to micro-fractures in the bone architecture and, ultimately, bone fragility. Bone mass loss may increase during menopause due to the reduction in estrogenic levels [47]. Moreover, surgical procedures can cause morphological alterations in bone such in the case of osteotomies to remove bone tumours [48], craniotomies performed to access the brain or harvesting of the patients' bone to use it as an autologous graft. Additionally, the deficiency in mechanical stimuli can lead to bone resorption, which is frequent in dental medicine [49]. Finally, bone defects can also be the consequence of certain congenital diseases like cleft lip and cleft palate [50].

Despite the remarkable self-regenerative capacity of bone, sometimes the help of a bone graft to regenerate is required. This is the case of critical-sized defects, where the bone is not able to completely heal [51].

1.3. Bone Cancer Therapy

Nowadays, surgical resection of the tumour combined with chemotherapy is the first-line treatment for bone cancer, and specifically, for OS [52]. Although this strategy has increased the cure rate of the patients, the survival rate is still insufficient, around 50% [53]. In addition, conventional chemotherapy lacks sensitivity and specificity, presents drug toxicity and severe side effects, as it affects both malignant and healthy cells [54]. Furthermore, the development of drug resistance is a major problem [55]. Although the advances done in cancer therapy are considerable, these are still far from being an optimum treatment. Therefore, new disruptive solutions based on completely different approaches need to be investigated.

1.3.1. Hydroxyapatite Nanoparticles in Cancer Treatment

Besides the well-established use of hydroxyapatite as bone graft, this biomaterial has also been explored in form of nanoparticles (NPs) in various new-emerging biomedical fields such as gene and drug delivery applications, bio-imaging and cancer therapy [56–59]. Regarding the latter approach, NPs are a promising solution due to their selective retention into the tumour mass caused by the enhanced retention and permeability (EPR) effect that characterise malignant cells [60,61]. In addition, the increased metabolic activity of cancer cells leads to a higher uptake of NPs on tumour cells than on healthy ones, requiring lower doses than other chemotherapeutic solutions [62].

Among the different methods to synthesise HA NPs, the wet methods are the most popular and, in particular, chemical precipitation by titration of calcium hydroxide slurry with phosphoric acid (**Equation 1.1**) at the body or room temperature, which usually results in poorly crystalline needle-like NPs [63].

$$10\ Ca(OH)_2 + 6\ H_3PO_4 \rightarrow Ca_{10}(PO_4)_6(OH)_2 + 18\ H_2O \qquad \textbf{Equation 1.1}$$

This process presents several advantages compared to other options, such as its simplicity, water being the only by-product and no need for special equipment or additional chemicals to control the reaction. Another additional asset is the facility in tuning several morphological and chemical properties of the final materials, such as the shape, the size and the specific surface area [64]. Furthermore, wet precipitation allows the ion doping of the HA structure by adding the salt of interest during the precipitation, which has been found to improve their bioactivity, as stated previously [65].

Currently, the use of HA NPs in cancer treatment is based on two different strategies: as chemotherapeutic drug carriers and as a drug by themselves. The application of HA NPs as transfection vehicles solves the degradation and poor solubility problems of some chemotherapeutic drugs, as well as their low internalisation rates into cancer cells. Indeed, this approach has been found to be helpful in the transport of cisplatin and doxorubicin [66–68]. On the other hand, it has been observed that HA NPs themselves were cytotoxic for several cancer cell types (*i.e.* colorectal cancer, hepatoma, osteosarcoma and glioma) whilst causing minimal side effects on healthy cells [69–72]. Moreover, ion-doped HA NPs have been investigated in cancer therapy. On the one hand, iron-doped HA NPs with magnetic properties have been used in hyperthermia therapy, both *in vitro* causing malignant liver cell death through elevated ROS levels [73], and *in vivo* showing an important reduction of the colorectal tumour volume after 14 days [74]. On the other hand, magnesium-doped HA NPs have been reported to present a remarkable killing potential in MG-63 osteosarcoma cells, being more selective than non-doped HA [75].

1.3.2. Cytotoxicity Mechanisms of Hydroxyapatite Nanoparticles

HA NPs are internalised into the cells by endocytosis and, subsequently, degraded under the acidic conditions of these vesicles. However, the interaction of HA NPs with cells and their cell death mechanisms are still under debate. First, while the reactivity of the bulk HA with cell culture media and its consequences in cells have been extensively studied, few works have focused on the effects of the same material in the form of NPs and their influence on cell behaviour [76,77]. Contrastingly, the internalisation of HA NPs is commonly believed to be the cause of cell toxicity. The most accepted hypothesis to explain the cytotoxic effects of HA NPs is that their degradation leads to an increase of intracellular calcium and phosphorus ions, inducing apoptosis [78], as schematised in **Figure 1.3**. These effects are usually demonstrated by techniques such as transmission electron microscopy, flow cytometry or fluorescent microscopy, all of them based on the visualisation of the uptaken NPs. However, as the degradation of HA NPs is needed to achieve a cytotoxic behaviour, these techniques are insufficient to predict and study their toxicity. Recent alternatives to investigate the HA NPs solubilisation are the use of intracellular calcium straining and the application of cryo-soft X-ray tomography [79–82].

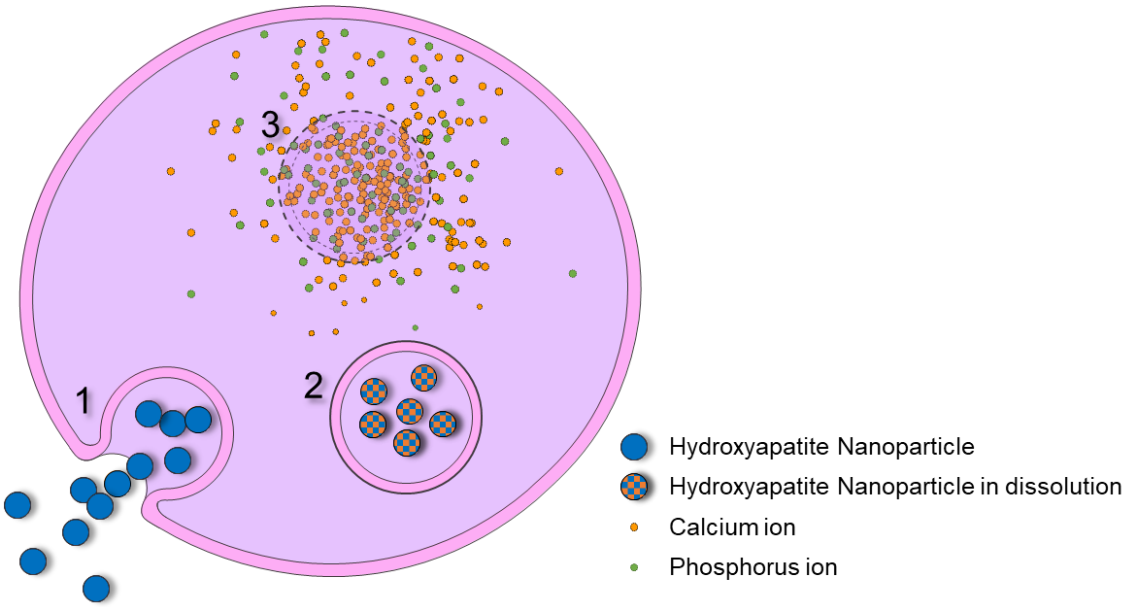

Figure 1.3. Cytotoxic mechanism of hydroxyapatite nanoparticles (HA NPs) in cancer therapy. (1) Internalisation of the HA NPs through endocytosis. (2) Dissolution of the HA NPs due to the acidic environment in the endocytic vesicle. (3) Massive release of calcium and phosphorus ions to the cytoplasm of the cell.

This PhD thesis aims to improve our understanding of the cytotoxicity mechanisms of hydroxyapatite nanoparticles for cancer treatment. To do so, conventional techniques to study their cell uptake will be compared to more advanced strategies.

1.4. Bone Grafting Strategies

In spite of the self-regeneration capacity of the bones, when a bone defect exceeds a critical size, the tissue is not able to heal spontaneously. In these cases, external help is needed to achieve the desired regeneration and bone grafts are crucial in this process [51].

Bone grafting is a surgical procedure to reconstruct bone in a defect by means of a bone substitute. The use of bone grafts accelerates the formation of new bone tissue by permitting the regeneration in volume instead of the layer-by-layer process that occurs in the natural bone remodelling. Bone grafts can be classified into four different groups depending on their origin: autografts, allografts, xenografts and synthetic bone grafts.

1.4.1. Bone Grafts of Natural Origin

Within this family of bone grafts, autografts stand out as the clinical gold standard. These grafts consist of bone tissue harvested from the patient's own body and retrieved from a second anatomical site [83]. Although their biocompatibility and bioactivity are unbeatable, they require additional surgery to extract the needed bone tissue which implies added morbidity, longer surgical times and aesthetic concerns. Moreover, there is a limitation on their availability [84,85].

Other natural options are allografts and xenografts, which derive from a donor of the same species as the patient or from a donor of a different species (usually bovine origin), respectively. Both of them provide a proper architecture for the bone to regenerate, however, due to the harsh sterilisation processes required, they are substantially less bioactive than autografts, leading to longer regeneration times and reduced performance. Additionally, these grafts may cause immune rejection or disease transmission [86,87].

1.4.2. Synthetic Bone Grafts

In order to overcome the limitations of the more traditional – and natural – bone grafts, synthetic bone substitutes emerged as an alternative solution [88]. This strategy consists of manufacturing bone substitutes using biocompatible materials. Indeed, numerous synthetic bone grafts with similar behaviour to the natural bone substitutes have been successfully developed [89]. Moreover, these grafts provide attractive features such as unlimited availability, avoidance of a second surgery, absence of disease transmission and, in some cases, control of the geometrical shape and internal architecture.

The following properties are sought in a synthetic bone graft: osteoconduction, osteogenicity, osteoinduction and structural integrity [90]. Osteoconduction is the capacity of the graft to guide the bone formation, supporting cell attachment and allowing the migration and ingrowth of these cells within its structure. Osteogenicity is the potential of the graft to regenerate bone inside the grafted volume. Osteoinduction is the ability of the bone substitute to induce the differentiation of MSCs to bone-lineage cells. Finally, structural integrity is related to the mechanical performance of the bone substitutes, which have to be stable but also biodegradable.

Multiple families can be distinguished depending on the composition of the bone substitutes: metallic, polymeric, ceramic, or composites made by the combination of them [91]. Among the metallic-based substitutes, titanium and its alloys, stainless steel and cobalt-chromium alloys are the most used materials. On the other hand, polylactic acid (PLA), poly(methyl methacrylate) (PMMA) and silicone are the usual components within the polymer-based grafts.

Regarding the ceramic-based substituted, although bioactive glass, calcium sulphates or magnesium phosphates have been used, calcium phosphates (CaPs) are the most studied compounds [89]. CaPs are of special interest due to their similarity to the mineral phase of the natural bone. Moreover, these materials exhibit appropriate biological performance, as they are found to be bioactive, osteoconductive, resorbable and, in some cases, also osteoinductive [91,92].

1.4.3. Three-Dimensional Printing of Bone Grafts

Bone graft substitutes can be fabricated by a wide variety of techniques achieving different final shapes (*e.g.* granules, putties, standard blocks, etc.). Among the different approaches, three-dimensional (3D) printing is gaining popularity in the last few years. This strategy permits the elaboration of personalised scaffolds with specific and complex shapes, controlled composition and interconnected porosity, which is a key factor in the tissue regeneration process [93].

In this way, 3D-printed scaffolds manufactured by different approaches have been developed, some of them with outstanding bone regeneration properties [94]. However, these solutions are still far from the gold standard and, therefore, in recent years,

important efforts have been done looking for a closer resemblance to the natural bone. In this sense, 3D bioprinting has emerged as a promising alternative. This technique is based on the application of common 3D printing technologies to cells or other biological entities. Hence, the presence of living cells in the system accelerates the regeneration process, as further cell colonisation is not necessary. However, 3D bioprinting presents an additional layer of complexity compared to traditional material-only printing techniques [95].

Complex 3D structures can be designed in computer-aided design (CAD) technologies from medical data obtained with imaging techniques like X-ray, magnetic resonance or computed tomography (CT) [96]. The further 3D biofabrication is carried out using different manufacturing methodologies, summarised in **Figure 1.4**: (1) Inkjet bioprinting, where small droplets of material are delivered on a substrate by piezoelectric or thermal means. (2) Extrusion-based or microextrusion bioprinting, which is the most widespread method for the development of 3D cell-laden scaffolds. In it, a bioink is extruded through a nozzle by either pneumatic or mechanical methods (piston- or screw-driven). (3) Laser-assisted bioprinting (LAB), where a pulsed laser beam is used to volatilise a sacrificial layer covering the substrate. (4) Other more recent techniques include the use of stereolithography (SLA) to print cells, which implies the use of a UV light beam on a photopolymer to cross-link it [97].

Inkjet bioprinting is a low-cost technique with precise deposition of cells and biomaterials. The fast speed is one of its main advantages, together with the achieved resolution (close to 50 µm) [98]. However, heat and mechanical stress can negatively influence cell viability [99]. Therefore, the bioinks used for inkjet printing must present low viscosity (<10 mPa s) and low cell density (<10^6 cells ml^{-1}) [100,101]. On the contrary, microextrusion permits printing high-viscosity bioinks with high cell densities, and even cell spheroids [96]. Per contra, the final resolution is lower (50 – 500 µm) [102] and shear stress may damage the printed cells [103]. LAB is a nozzle-free technique and, thus, is not affected by shear stress to the cells, nor clogging problems. It is possible to obtain high resolutions, but the process tends to be slow and with lower throughout capabilities than the others [97]. On the other hand, although SLA is characterised by its high accuracy, resolution and control of the scaffold architecture, its high cost and maintenance limit its use [104]. It is worth noting that in all of these bioprinting strategies, the bioink is a common and essential component.

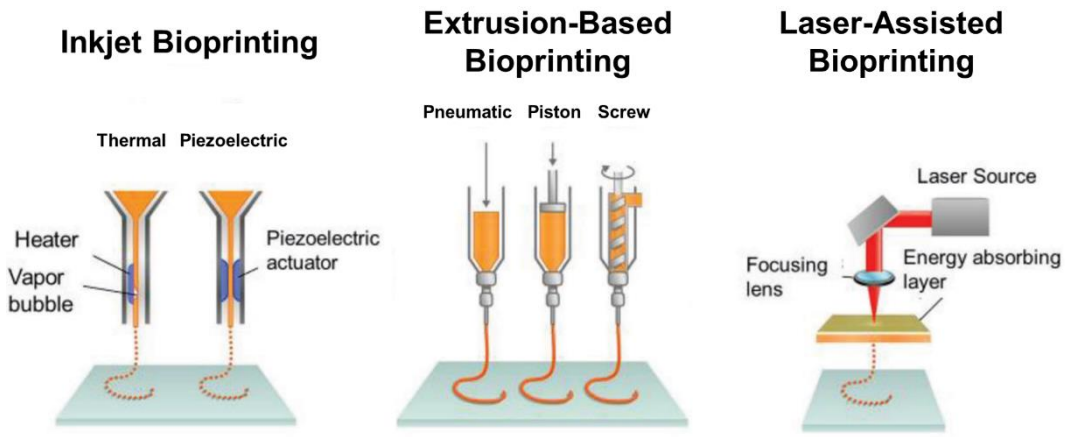

Figure 1.4. The three most common 3D bioprinting techniques: inkjet bioprinting or microextrusion, extrusion-based bioprinting and laser-assisted bioprinting (LAB), adapted from [105].

1.5. Bioinks for Bone Regeneration

1.5.1. Bioink Formulations

The term bioink is used to designate a formulation containing living cells suitable for 3D biofabrication, which is usually combined with one (or more) cell-encapsulation biomaterial [106]. It is expected that, after the implantation, the matrix of these scaffold-based bioinks degrades in a controlled manner and the embedded cells colonise the grafted region to regenerate the needed tissue.

Hydrogels are the most commonly used biomaterial for cell embedding due to their attractive chemical and physical characteristics. On the one hand, hydrogels are able to absorb and retain large quantities of water allowing the efficient diffusion of oxygen and nutrients supporting living cells [107,108]. On the other hand, they present highly tuneable mechanical properties, such as controlled biodegradability or rheological features.

A wide variety of polymeric hydrogels have been investigated for this purpose: some of them with natural origins like alginate, collagen, chitosan or hyaluronic acid, and some others with synthetic origin such as PLA and Pluronic® F-127 [109]. Amongst all of them, alginate is the most studied for bone tissue engineering and bioprinting applications [110].

Alginate is a linear polysaccharide made of 1,4-linked β-D-mannuronate (M) and α-L-guluronate (G) residues, where the ratio between them depends on its natural origin [111]. It is typically extracted from brown algae through aqueous alkali solutions. Apart from being biocompatible, non-toxic, non-immunogenic and biodegradable, alginate presents a wide availability and an affordable price [112]. Additionally, a critical feature that makes this polymer of special interest for the development of cell-laden inks is its gentle and easy gelation [113]. Notwithstanding, its main drawback is the lack of cell-adhesive moieties with limited bioactivity. Different strategies have been conducted to overcome this issue, which will be explained in the following sections.

In view of the promising performance of alginate hydrogels, the cell-laden inks developed in this work will be based on this polymer.

1.5.2. Strategies to Tune the Mechanical Properties and Degradability of Alginate Bioinks

The mechanical properties of alginate hydrogels can be either tuned by physical factors such as controlling the molecular weight (MW), the type of cross-linker and the cross-linking concentration, or by chemical modification of the polymer [114].

a. Chain Architecture and Mechanical Properties of Alginate

Alginates with different features have been described in the literature, with various ratios of M and G subunits and presenting MW ranging from 30 to 400 kDa [115]. In addition to this diversity of options, the polymer concentration and the cross-linking conditions

used can highly influence the features of the final bioinks, including their mechanical properties, printability and degradability [116], which also affect cell behaviour.

On the one hand, the MW and the final concentration of the polymer affect the viscosity of the resulting cell-laden ink, achieving more viscous bioinks with alginates of high MW [117] and with higher polymer concentrations. Indeed, it is reported that with alginate concentrations lower than 3% the post-printing stability of bioinks is compromised [118]. Contrastingly, high-viscosity hydrogels (> 5%) may be unfavourable due to an increase in shear forces that can damage the cells embedded within [119].

On the other hand, the gelling conditions and the type of cross-linker used are of major interest to tailor the mechanical properties of the bioinks. Although the covalent cross-linking of alginate is explored in the literature, this technique requires chemical modifications of the polymer. Therefore, the majority of alginate hydrogels are obtained by ionic cross-linking [116]. As alginate has a high affinity for divalent cations, calcium salts are commonly used to gellify it. Two main strategies are employed: diffusion gelation and internal gelation. For diffusion gelation, $CaCl_2$ is usually applied. This technique is of special interest in the generation of alginate beads or in extrusion-based 3D printing techniques, as alginate is dripped into a $CaCl_2$ solution and immediately cross-links [120]. However, this process sometimes results in inhomogeneities. However, by lowering the temperature the diffusion of Ca^{2+} ions is reduced and the cross-linking slowed down, leading to a more homogeneous network [121]. Another way to delay alginate cross-linking is by internal gelation. In this case, $CaCO_3$ or $CaSO_4$ are typically dispersed in the initial alginate solution and calcium ions are released under acidic environments [122]. As the process is slow, the resulting bioinks are more homogeneous.

Furthermore, other ways to control the physical stability of 3D-printed bioinks lay in modifying the concentration or ratio of the cross-linking salt in the solution, as well as changing the gelation treatment time. Moreover, some studies supplemented the media with small amounts of $CaCl_2$ to achieve better maintenance of the structural integrity of the cell-laden inks over time [123].

Different cross-linking conditions will be assessed to optimise the performance of the cells embedded in the developed alginate-based bioinks.

---

b. Degradability of Alginate

All the above-mentioned parameters not only determine the physical features of the bioinks but also their degradability, which is vital in bone tissue engineering. However, several strategies have been developed to specifically modify the degradability of alginate-based bioinks, as their *in vivo* degradation is compromised due to the lack of special enzymes to lyse in human bodies [115].

The most common chemical modifications are the adjustment of the polymer MW by gamma radiation [119,124], or by its oxidation [125,126]. In this latter, sodium periodate is commonly used as an oxidising agent, as it can oxidise both M and G subunits. Oxidised alginate (OA) is sometimes preferable as it degrades faster than alginate due to the presence of more reactive groups [127], which are susceptible to hydrolytic degradation [128]. In contrast, OAs present lower mechanical properties than non-oxidised ones, mainly because there are fewer GG blocks in the polymeric chain, which reduces the interaction between cross-linker ions and alginate [129]. In this manner, the oxidation

degree directly alters the network cross-linking level, as well as its mechanical behaviour [130,131].

Other approaches to tune the degradability of alginate are the use of methacrylated alginates that are covalently cross-linked but sensitive to hydrolytic degradability [132,133], the addition of linkages that can be cleavable by metalloproteinases to the polymer [134], or the inclusion of enzymatically-degradable peptides [135]. Other options explored in the literature to increase alginate biodegradability are hydrogen bond cleavage, reversible chemical bonds [136] or the coupling of polyethylene glycol (PEG) spacers that hinder the cross-linking by steric interactions [137].

1.5.3. Strategies to Confer Bioactivity to Alginate Bioinks

Although the *in vivo* degradation of alginate is an important factor to tailor, the cell interactions within the bioinks are the most crucial properties to control [122]. Three main strategies have been explored in the literature to provide bioactivity to alginate bioinks: the addition of particles in the micro- and nanometric size range; the combination with other hydrogels; and the functionalisation of alginate to incorporate different bioactive molecules.

a. Combination with Micro- and Nanoparticles

Composite materials present the advantages of multiple materials in one [138,139]. A bio-inspired approach is the combination of organic and inorganic compounds to develop new biomaterials. In this sense, bioactive glasses (BGs) and calcium phosphates have been explored to create inorganic particles for their further incorporation in alginate hydrogels.

Under the appropriate environment, BGs are able to enhance the nucleation and growth of HA crystals thanks to their high surface reactivity [140,141]. The addition of BGs in the form of nanoparticles to alginate bioinks has been found to enhance the proliferation, mineralisation and osteogenic differentiation of both SaOS-2 cells and MSC [142–144].

On the other hand, hydroxyapatite has also been widely investigated due to its intrinsic osteoconductive and biodegradable properties. Indeed, the release of calcium and phosphorus ions caused by the dissolution of HA promotes new bone formation [145]. Some authors have reported that the incorporation of HA nanoparticles in alginate bioinks significantly improves the mechanical properties of the ink and the osteogenic differentiation of MSC embedded within [123]. Moreover, other studies adding HA NPs to alginate gels reported an enhancement of the mechanical properties of the scaffolds [146,147] as well as an increased cell performance in terms of attachment, proliferation and osteogenic differentiation [146,148,149]. In addition, earlier bone formation in critical-sized bone defects in rabbits was observed [150].

As an alternative to nano-sized materials, the incorporation of microparticles – mainly microspheres (MS) – in alginate bioinks may improve the aforementioned results by providing additional adhesion sites for the cells, which is crucial in the bone regeneration field. In spite of the development of CaP MS, both alone or in combination with different polymers [151,152], these particles have not been added in the formulation of bioinks. Actually, the incorporation of ceramic-based particles (either with nanometric or micrometric sizes) presents some challenges that need to be overcome. On the one hand, it may require the use of nozzles with larger orifices, which results in lower resolution of

the final scaffolds. Moreover, embedding living cells in these matrixes is a difficult task. Another option is the use of cell-laden inks with low ceramic loading obtaining reduced mechanical properties [110].

Furthermore, some works explored the addition of polymeric MS to cell-laden inks which are not based on alginate. Specifically, PLA MS were studied in the composition of bioinks, showing to improve their rheological properties together with their cellular behaviour [153–155].

The incorporation of calcium phosphate-based microspheres into the cell-laden inks will be studied as a strategy to improve attachment and osteogenic differentiation of the embedded cells.

---

b. Combination with Other Hydrogels

In the field of bone tissue engineering, the use of ECM proteins that target bone-related integrins is the most straightforward approach to control cell behaviour. The ECM possess the capacity to activate certain cell signalling pathways by means of a bidirectional communication through transmembrane receptors of the cells, mainly integrins.

Since collagen is the major component of the bone tissue ECM, a popular strategy has consisted in using composite bioinks made of alginate and collagen (or its hydrolysed form, gelatine) [157,158]. However, this modification affects the rheological and mechanical properties of the resulting cell-laden inks. Furthermore, due to the complexity of the added proteins, it becomes difficult to control the specific biochemical signals presented to the cells.

c. Biochemical Functionalisation of Alginate

Polymer functionalisation is another of the strategies investigated to tune the cell behaviour within alginate hydrogels. This approach commonly consists in the use of small peptidic sequences containing only a very specific cue of the full-length protein of interest, achieving a higher level of control. Indeed, these bioactive peptides are able to mimic the adhesive properties of several ECM proteins, as well as to stimulate cellular proliferation and differentiation. Although REDV (from fibronectin), YIGSR (from laminin) and VAPG (found in elastin) peptides have been studied [159,160], the most investigated peptidic sequence remains to be RGD (*i.e.* arginine, glycine, aspartic acid), which has been found in different ECM proteins like fibronectin, vitronectin, laminin or fibrinogen. RGD sequence has been described as the minimal adhesive binding motif, recognised by different integrin subtypes. By addressing such integrins other important biological processes like cell differentiation, immune response or wound healing can also be tackled [161,162].

Alginate hydrogels can be functionalised by covalently grafting RGD peptides through carbodiimide chemistry [163]. Enhanced cell proliferation and osteogenic differentiation of committed cells (*i.e.* preosteoblasts) have been reported in RGD-coupled alginates in a density-depending manner [164,165]. Despite this strategy has started to draw attention for the development of bioinks, few studies have reported its application in alginate-based cell-laden inks [166,167]. RGD sequences are easy to synthesise in large amounts and at

a low cost and are stable under pH and temperature changes. However, the use of such short molecules entails several constraints related to their stability against enzymatic degradation *in vivo* and their lack of specificity for particular integrins. Moreover, their cellular stimulation is limited compared to full-length proteins [168].

To overcome these drawbacks, synthetic non-peptidic ligands (also known as peptidomimetics) have raised interest. These artificial molecules are designed to present a high affinity for a specific integrin subtype mimicking the pharmacophore of their natural ligands and improving their biological performance. In general, peptidomimetics present high stability in serum and almost no immune reaction [169,170]. $\alpha_v\beta_3$ and $\alpha_5\beta_1$ integrin subtypes are found to be essential in the osteogenesis process [171–173] and, thus, artificial ligands selective for these two types of integrins have been developed for bone tissue applications. Both peptidomimetics exhibited selective cell adhesion and high specificity when applied as surface coatings [174–177]. Furthermore, other studies reported enhanced osteogenic differentiation and cell proliferation [178,179]. However, integrin-selective peptidomimetics have only been applied in 2D systems and no data on bioinks or other 3D strategies can be found in the literature.

In the present PhD thesis, the use of $\alpha_5\beta_1$- and $\alpha_v\beta_3$-selective peptidomimetics will be studied as a novel strategy to enhance the bioactivity and osteogenic differentiation capabilities of alginate bioinks.

1.6. References

[1] H. Shegarfi, O. Reikeras, Review Article: Bone Transplantation and Immune Response, J. Orthop. Surg. 17 (2009) 206–211. doi:10.1177/230949900901700218.

[2] Healthcare Cost and Utilization Project (HCUP) | Agency for Healthcare Research and Quality, (n.d.). https://www.ahrq.gov/data/hcup/index.html (accessed July 6, 2021).

[3] Ageing and health, World Heal. Organ. (2018). https://www.who.int/news-room/fact-sheets/detail/ageing-and-health (accessed June 25, 2021).

[4] J. Gill, M.K. Ahluwalia, D. Geller, R. Gorlick, New targets and approaches in osteosarcoma, Pharmacol. Ther. 137 (2013) 89–99. doi:10.1016/j.pharmthera.2012.09.003.

[5] A.G. Robling, A.B. Castillo, C.H. Turner, Biomechanical and molecular regulation of bone remodeling, Annu. Rev. Biomed. Eng. 8 (2006) 455–498. doi:10.1146/annurev.bioeng.8.061505.095721.

[6] R. Florencio-Silva, G.R.D.S. Sasso, E. Sasso-Cerri, M.J. Simões, P.S. Cerri, Biology of Bone Tissue: Structure, Function, and Factors That Influence Bone Cells, Biomed Res. Int. 2015 (2015) 1–17. doi:10.1155/2015/421746.

[7] J.G. Betts, K.A. Young, J.A. Wise, E. Johnson, B. Poe, D.H. Kruse, O. Korol, J.E. Johnson, M. Womble, P. DeSaix, The Functions of the Skeletal System, in: O.S. University (Ed.), Anat. Physiol., OpenStax, 2013.

[8] B. Clarke, Normal Bone Anatomy and Physiology, Clin. J. Am. Soc. Nephrol. 3

(2008) S131–S139. doi:10.2215/CJN.04151206.

[9] J.S. Khurana, E.F. McCarthy, P.J. Zhang, Essentials in Bone and Soft-Tissue Pathology, Springer US, Boston, MA, 2010. doi:10.1007/978-0-387-89845-2.

[10] P.H. Schlesinger, H.C. Blair, D.B. Stolz, V. Riazanski, E.C. Ray, I.L. Tourkova, D.J. Nelson, Cellular and extracellular matrix of bone, with principles of synthesis and dependency of mineral deposition on cell membrane transport, Am J Physiol Cell Physiol. 318 (2020) 111–124. doi:10.1152/ajpcell.00120.2019.-Bone.

[11] X. Lin, S. Patil, Y.-G. Gao, A. Qian, The Bone Extracellular Matrix in Bone Formation and Regeneration, Front. Pharmacol. 11 (2020) 1–15. doi:10.3389/fphar.2020.00757.

[12] J. Sun, B. Bhushan, Hierarchical structure and mechanical properties of nacre: a review, RSC Adv. 2 (2012) 7617. doi:10.1039/c2ra20218b.

[13] J.D. Pasteris, B. Wopenka, E. Valsami-Jones, Bone and Tooth Mineralization: Why Apatite?, Elements. 4 (2008) 97–104. doi:10.2113/GSELEMENTS.4.2.97.

[14] R. Zapanta LeGeros, Apatites in biological systems, Prog. Cryst. Growth Charact. 4 (1981) 1–45. doi:10.1016/0146-3535(81)90046-0.

[15] J.A. Buckwalter, M.J. Glimcher, R.R. Cooper, R. Recker, Bone Biology, This Is an Enhanc. PDF from J. Bone Jt. Surg. 77 (1995) 1256–1275. www.jbjs.org (accessed July 6, 2021).

[16] E. Boanini, M. Gazzano, A. Bigi, Ionic substitutions in calcium phosphates synthesized at low temperature, Acta Biomater. 6 (2010) 1882–1894. doi:10.1016/j.actbio.2009.12.041.

[17] D. Eichert, C. Combes, C. Drouet, C. Rey, Formation and Evolution of Hydrated Surface Layers of Apatites, Key Eng. Mater. 284–286 (2005) 3–6. doi:10.4028/www.scientific.net/KEM.284-286.3.

[18] C. Rey, C. Combes, C. Drouet, H. Sfihi, Chemical Diversity of Apatites, Adv. Sci. Technol. 49 (2006) 27–36. doi:10.4028/www.scientific.net/AST.49.27.

[19] C. Drouet, M. Aufray, S. Rollin-Martinet, N. Vandecandelaère, D. Grossin, F. Rossignol, E. Champion, A. Navrotsky, C. Rey, Nanocrystalline apatites: The fundamental role of water, Am. Mineral. 103 (2018) 550–564. doi:10.2138/am-2018-6415.

[20] F. Witte, The history of biodegradable magnesium implants: A review☆, Acta Biomater. 6 (2010) 1680–1692. doi:10.1016/j.actbio.2010.02.028.

[21] A. Bigi, E. Foresti, R. Gregorini, A. Ripamonti, N. Roveri, J.S. Shah, The role of magnesium on the structure of biological apatites, Calcif. Tissue Int. 1992 505. 50 (1992) 439–444. doi:10.1007/BF00296775.

[22] E.S. Thian, T. Konishi, Y. Kawanobe, P.N. Lim, C. Choong, B. Ho, M. Aizawa, Zinc-substituted hydroxyapatite: a biomaterial with enhanced bioactivity and antibacterial properties, J. Mater. Sci. Mater. Med. 24 (2013) 437–445. doi:10.1007/s10856-012-4817-x.

[23] T. Huang, G. Yan, M. Guan, Zinc Homeostasis in Bone: Zinc Transporters and Bone Diseases, Int. J. Mol. Sci. 21 (2020) 1236. doi:10.3390/ijms21041236.

[24] C.O. Molokwu, Y. V Li, Zinc Homeostasis and Bone Mineral Density, Ohio Res. Clin. Rev. 15 (2006).

[25] S. Pors Nielsen, The biological role of strontium, Bone. 35 (2004) 583–588. doi:10.1016/j.bone.2004.04.026.

[26] E. Boanini, P. Torricelli, M. Fini, A. Bigi, Osteopenic bone cell response to strontium-substituted hydroxyapatite, J. Mater. Sci. Mater. Med. 22 (2011) 2079–2088. doi:10.1007/s10856-011-4379-3.

[27] T. Tite, A.-C. Popa, L.M. Balescu, I.M. Bogdan, I. Pasuk, J.M.F. Ferreira, G.E. Stan, Cationic Substitutions in Hydroxyapatite: Current Status of the Derived Biofunctional Effects and Their In Vitro Interrogation Methods, Materials (Basel). 11 (2018) 2081. doi:10.3390/ma11112081.

[28] A. Aszódi, J.F. Bateman, E. Gustafsson, R. Boot-Handford, R. Fässler, Mammalian Skeletogenesis and Extracellular Matrix: What can We Learn from Knockout Mice?, CELL Struct. Funct. 25 (2000) 73–84. doi:10.1247/csf.25.73.

[29] J.E. Aubin, J.T. Triffitt, Mesenchymal Stem Cells and Osteoblast Differentiation, in: Princ. Bone Biol. Second Ed., 2002: pp. 59–81.

[30] M. Capulli, R. Paone, N. Rucci, Osteoblast and osteocyte: Games without frontiers, Arch. Biochem. Biophys. 561 (2014) 3–12. doi:10.1016/j.abb.2014.05.003.

[31] S. Miller, L. de Saint-Georges, B. Bowman, W. Jee, Bone Lining Cells: Structure and Function, Scanning Microsc. 3 (1989).

[32] T.A. Franz-Odendaal, B.K. Hall, P.E. Witten, Buried alive: How osteoblasts become osteocytes, Dev. Dyn. 235 (2006) 176–190. doi:10.1002/dvdy.20603.

[33] M.L. Knothe Tate, "Whither flows the fluid in bone?" An osteocyte's perspective, J. Biomech. 36 (2003) 1409–1424. doi:10.1016/S0021-9290(03)00123-4.

[34] N.A. Sims, J.H. Gooi, Bone remodeling: Multiple cellular interactions required for coupling of bone formation and resorption, Semin. Cell Dev. Biol. 19 (2008) 444–451. doi:10.1016/j.semcdb.2008.07.016.

[35] L.J. Raggatt, N.C. Partridge, Cellular and Molecular Mechanisms of Bone Remodeling, J. Biol. Chem. 285 (2010) 25103–25108. doi:10.1074/jbc.R109.041087.

[36] N. Takahashi, U. Nobuyuki, T. Masamichi, S. Tatsuo, Cells of Bone: Osteoclast Generation, in: Princ. Bone Biol. Second Ed., 2002: pp. 109–126.

[37] Parfitt M., Bone-forming cells in clinical condictions, The Osteoblast and Osteocyte. (1990). https://ci.nii.ac.jp/naid/10020547637 (accessed July 6, 2021).

[38] J.M. Sadowska, Effect of microstructural and chemical cues on the in vitro cell response to calcium phosphates, Universitat Politècnica de Catalunya (UPC), 2018.

[39] Understanding Bone Cancer | American Cancer Society, (n.d.). https://www.cancer.org/cancer/bone-cancer/about/what-is-bone-cancer.html (accessed July 8, 2021).

[40] J.T. Buijs, G. van der Pluijm, Osteotropic cancers: From primary tumor to bone,

Cancer Lett. 273 (2009) 177–193. doi:10.1016/j.canlet.2008.05.044.

[41] M.C. Parry, M. Laitinen, J. Albergo, L. Jeys, S. Carter, C.L. Gaston, V. Sumathi, R.J. Grimer, Osteosarcoma of the pelvis, Bone Joint J. 98-B (2016) 555–563. doi:10.1302/0301-620X.98B4.36583.

[42] G. Ottaviani, N. Jaffe, The Epidemiology of Osteosarcoma, in: Cancer Treat. Res., Kluwer Academic Publishers, 2009: pp. 3–13. doi:10.1007/978-1-4419-0284-9_1.

[43] S.M. Botter, D. Neri, B. Fuchs, Recent advances in osteosarcoma, Curr. Opin. Pharmacol. 16 (2014) 15–23. doi:10.1016/j.coph.2014.02.002.

[44] E. Abed, R. Moreau, Importance of melastatin-like transient receptor potential 7 and cations (magnesium, calcium) in human osteoblast-like cell proliferation, Cell Prolif. 40 (2007) 849–865. doi:10.1111/j.1365-2184.2007.00476.x.

[45] L.Y. He, X.M. Zhang, B. Liu, Y. Tian, W.H. Ma, Effect of magnesium ion on human osteoblast activity, Brazilian J. Med. Biol. Res. 49 (2016) 1–6. doi:10.1590/1414-431X20165257.

[46] R.B. Franklin, L.C. Costello, The Important Role of the Apoptotic Effects of Zinc in the Development of Cancers, J Cell Biochem. 106 (2009) 750–757. doi:10.1002/jcb.22049.The.

[47] Osteoporosis, Natl. Inst. Arthritis Musculoskelet. Ski. Dis. (2020). https://www.niams.nih.gov/health-topics/osteoporosis/advanced (accessed June 29, 2021).

[48] D.S. Geller, R. Gorlick, Osteosarcoma: A review of diagnosis, management, and treatment strategies , Clin. Adv. Hematol. Oncol. 8 (2010) 705–718.

[49] J. Pietrokovski, M. Massler, Alveolar ridge resorption following tooth extraction, J. Prosthet. Dent. 17 (1967) 21–27. doi:10.1016/0022-3913(67)90046-7.

[50] P.A. Mossey, J. Little, R.G. Munger, M.J. Dixon, W.C. Shaw, Cleft lip and palate, Lancet. 374 (2009) 1773–1785. doi:10.1016/S0140-6736(09)60695-4.

[51] H. Petite, V. Viateau, W. Bensaïd, A. Meunier, C. de Pollak, M. Bourguignon, K. Oudina, L. Sedel, G. Guillemin, Tissue-engineered bone regeneration, Nat. Biotechnol. 18 (2000) 959–963. doi:10.1038/79449.

[52] Z. Yao, L. Han, Y. Chen, F. He, B. Sun, S. Kamar, Y. Zhang, Y. Yang, C. Wang, Z. Yang, Hedgehog signalling in the tumourigenesis and metastasis of osteosarcoma, and its potential value in the clinical therapy of osteosarcoma, Cell Death Dis. 9 (2018) 701. doi:10.1038/s41419-018-0647-1.

[53] A. Longhi, C. Errani, M. De Paolis, M. Mercuri, G. Bacci, Primary bone osteosarcoma in the pediatric age: State of the art, Cancer Treat. Rev. 32 (2006) 423–436. doi:10.1016/j.ctrv.2006.05.005.

[54] Y. Xin, M. Yin, L. Zhao, F. Meng, L. Luo, Recent progress on nanoparticle-based drug delivery systems for cancer therapy, Cancer Biol. Med. 14 (2017) 228. doi:10.20892/j.issn.2095-3941.2017.0052.

[55] M. van Driel, J.P.T.M. van Leeuwen, Cancer and bone: A complex complex, Arch. Biochem. Biophys. 561 (2014) 159–166. doi:10.1016/j.abb.2014.07.013.

[56] S. Dorozhkin, Nanodimensional and Nanocrystalline Apatites and Other Calcium

Orthophosphates in Biomedical Engineering, Biology and Medicine, Materials (Basel). 2 (2009) 1975–2045. doi:10.3390/ma2041975.

[57] S.C.J. Loo, T. Moore, B. Banik, F. Alexis, Biomedical applications of hydroxyapatite nanoparticles., Curr. Pharm. Biotechnol. 11 (2010) 333–42. doi: 10.2174/138920110791233343.

[58] T.N. Tram Do, W.-H. Lee, C.-Y. Loo, A. V Zavgorodniy, R. Rohanizadeh, Hydroxyapatite nanoparticles as vectors for gene delivery, Ther. Deliv. 3 (2012) 623–632. doi:10.4155/tde.12.39.

[59] V. Uskoković, D.P. Uskoković, Nanosized hydroxyapatite and other calcium phosphates: Chemistry of formation and application as drug and gene delivery agents, J. Biomed. Mater. Res. Part B Appl. Biomater. 96B (2011) 152–191. doi:10.1002/jbm.b.31746.

[60] Y. Matsumura, H. Maeda, A new concept for macromolecular therapeutics in cancer chemotherapy: mechanism of tumoritropic accumulation of proteins and the antitumor agent smancs., Cancer Res. 46 (1986) 6387–6392.

[61] H. Maeda, G.Y. Bharate, J. Daruwalla, Polymeric drugs for efficient tumor-targeted drug delivery based on EPR-effect, Eur. J. Pharm. Biopharm. 71 (2009) 409–419. doi:10.1016/J.EJPB.2008.11.010.

[62] A.J. Levine, A.M. Puzio-Kuter, The Control of the Metabolic Switch in Cancers by Oncogenes and Tumor Suppressor Genes, Science (80-.). 330 (2010) 1340–1344. doi:10.1126/science.1193494.

[63] M. Sadat-Shojai, M. Khorasani, E. Dinpanah-Khoshdargi, A. Jamshidi, Synthesis methods for nanosized hydroxyapatite with diverse structures, Acta Biomater. 9 (2013) 7591–7621. doi:10.1016/j.actbio.2013.04.012.

[64] A. Afshar, M. Ghorbani, N. Ehsani, M.R. Saeri, C.C. Sorrell, Some important factors in the wet precipitation process of hydroxyapatite, Mater. Des. 24 (2003) 197–202. doi: 10.1016/S0261-3069(03)00003-7.

[65] M.D. Sikirić, H. Füredi-Milhofer, The influence of surface active molecules on the crystallization of biominerals in solution, Adv. Colloid Interface Sci. 128–130 (2006) 135–158. doi:10.1016/j.cis.2006.11.022.

[66] B. Palazzo, M. Iafisco, M. Laforgia, N. Margiotta, G. Natile, C.L. Bianchi, D. Walsh, S. Mann, N. Roveri, Biomimetic Hydroxyapatite–Drug Nanocrystals as Potential Bone Substitutes with Antitumor Drug Delivery Properties, Adv. Funct. Mater. 17 (2007) 2180–2188. doi:10.1002/adfm.200600361.

[67] I. Rodríguez-Ruiz, J.M. Delgado-López, M.A. Durán-Olivencia, M. Iafisco, A. Tampieri, D. Colangelo, M. Prat, J. Gómez-Morales, pH-Responsive Delivery of Doxorubicin from Citrate–Apatite Nanocrystals with Tailored Carbonate Content, Langmuir. 29 (2013) 8213–8221. doi:10.1021/la4008334.

[68] Y.-H. Yang, C.-H. Liu, Y.-H. Liang, F.-H. Lin, K.C.-W. Wu, Hollow mesoporous hydroxyapatite nanoparticles (hmHANPs) with enhanced drug loading and pH-responsive release properties for intracellular drug delivery, J. Mater. Chem. B. 1 (2013) 2447. doi:10.1039/c3tb20365d.

[69] Z.-S. Liu, S.-L. Tang, Z.-L. Ai, Effects of hydroxyapatite nanoparticles on proliferation and apoptosis of human hepatoma BEL-7402 cells., World J. Gastroenterol. 9 (2003) 1968–71. doi:10.3748/wjg.v9.i9.1968.

[70] S.-H. Chu, D.-F. Feng, Y.-B. Ma, Z.-Q. Li, Hydroxyapatite nanoparticles inhibit the growth of human glioma cells in vitro and in vivo, Int. J. Nanomedicine. 7 (2012) 3659–3666. doi:10.2147/IJN.S33584.

[71] F. Qing, Z. Wang, Y. Hong, M. Liu, B. Guo, H. Luo, X. Zhang, Selective effects of hydroxyapatite nanoparticles on osteosarcoma cells and osteoblasts, J. Mater. Sci. Mater. Med. 23 (2012) 2245–2251. doi:10.1007/s10856-012-4703-6.

[72] S. Dey, M. Das, V.K. Balla, Effect of hydroxyapatite particle size, morphology and crystallinity on proliferation of colon cancer HCT116 cells, Mater. Sci. Eng. C. 39 (2014) 336–339. doi:10.1016/j.msec.2014.03.022.

[73] C.-T. Yang, K.-Y. Li, F.-Q. Meng, J.-F. Lin, I.-C. Young, R. Ivkov, F.-H. Lin, ROS-induced HepG2 cell death from hyperthermia using magnetic hydroxyapatite nanoparticles, Nanotechnology. 29 (2018) 375101. doi:10.1088/1361-6528/aacda1.

[74] C.-H. Hou, S.-M. Hou, Y.-S. Hsueh, J. Lin, H.-C. Wu, F.-H. Lin, The in vivo performance of biomagnetic hydroxyapatite nanoparticles in cancer hyperthermia therapy, Biomaterials. 30 (2009) 3956–3960. doi:10.1016/j.biomaterials.2009.04.020.

[75] Z. Zhao, M. Espanol, J. Guillem-Marti, D. Kempf, A. Diez-Escudero, M.-P. Ginebra, Ion-doping as a strategy to modulate hydroxyapatite nanoparticle internalization, Nanoscale. 8 (2015) 1595–1607. doi:10.1039/C5NR05262A.

[76] M. Epple, Review of potential health risks associated with nanoscopic calcium phosphate, Acta Biomater. 77 (2018) 1–14. doi:10.1016/j.actbio.2018.07.036.

[77] M. Šupová, T. Suchý, Z. Sucharda, E. Filová, J.N.L.M. Kinderen, M. Steinerová, L. Bačáková, G.S. Martynková, The comprehensive in vitro evaluation of eight different calcium phosphates: Significant parameters for cell behavior, J. Am. Ceram. Soc. 102 (2019) 2882–2904. doi:10.1111/jace.16110.

[78] Y. Wang, J. Wang, H. Hao, M. Cai, S. Wang, J. Ma, Y. Li, C. Mao, S. Zhang, In Vitro and in Vivo Mechanism of Bone Tumor Inhibition by Selenium-Doped Bone Mineral Nanoparticles, ACS Nano. 10 (2016) 9927–9937. doi:10.1021/acsnano.6b03835.

[79] Z. Liu, Y. Xiao, W. Chen, Y. Wang, B. Wang, G. Wang, X. Xu, R. Tang, Calcium phosphate nanoparticles primarily induce cell necrosis through lysosomal rupture: the origination of material cytotoxicity, J. Mater. Chem. B. 2 (2014) 3480. doi:10.1039/c4tb00056k.

[80] S. Neumann, A. Kovtun, I.D. Dietzel, M. Epple, R. Heumann, The use of size-defined DNA-functionalized calcium phosphate nanoparticles to minimise intracellular calcium disturbance during transfection, Biomaterials. 30 (2009) 6794–6802. doi:10.1016/j.biomaterials.2009.08.043.

[81] W. Tang, Y. Yuan, C. Liu, Y. Wu, X. Lu, J. Qian, Differential cytotoxicity and particle action of hydroxyapatite nanoparticles in human cancer cells, Nanomedicine. 9 (2014) 397–412. doi:10.2217/nnm.12.217.

[82] J. Groen, J.J. Conesa, R. Valcárcel, E. Pereiro, The cellular landscape by cryo soft X-ray tomography, Biophys. Rev. 11 (2019) 611–619. doi:10.1007/s12551-019-00567-6.

[83] C. Myeroff, M. Archdeacon, Autogenous Bone Graft: Donor Sites and

Techniques, J. Bone Jt. Surg. 93 (2011) 2227–2236. doi:10.2106/JBJS.J.01513.

[84] G.M. Calori, M. Colombo, E.L. Mazza, S. Mazzola, E. Malagoli, G.V. Mineo, Incidence of donor site morbidity following harvesting from iliac crest or RIA graft, Injury. 45 (2014) S116–S120. doi:10.1016/j.injury.2014.10.034.

[85] R.M. Klar, The Induction of Bone Formation: The Translation Enigma, Front. Bioeng. Biotechnol. 6 (2018) 74. doi:10.3389/fbioe.2018.00074.

[86] R. Dimitriou, E. Jones, D. McGonagle, P. V Giannoudis, Bone regeneration: current concepts and future directions, BMC Med. 9 (2011) 66. doi:10.1186/1741-7015-9-66.

[87] G. Fernandez de Grado, L. Keller, Y. Idoux-Gillet, Q. Wagner, A.-M. Musset, N. Benkirane-Jessel, F. Bornert, D. Offner, Bone substitutes: a review of their characteristics, clinical use, and perspectives for large bone defects management, J. Tissue Eng. 9 (2018). doi:10.1177/2041731418776819.

[88] S.J. Hollister, Scaffold Design and Manufacturing: From Concept to Clinic, Adv. Mater. 21 (2009) 3330–3342. doi:10.1002/adma.200802977.

[89] W.R. Moore, S.E. Graves, G.I. Bain, Synthetic bone graft substitutes, ANZ J. Surg. 71 (2001) 354–361. doi:10.1046/j.1440-1622.2001.02128.x.

[90] J.A. McAuliffe, Bone graft substitutes, J. Hand Ther. 16 (2003) 180–187. doi:10.1016/S0894-1130(03)80013-3.

[91] P. Habibovic, K. de Groot, Osteoinductive biomaterials—properties and relevance in bone repair, J. Tissue Eng. Regen. Med. 1 (2007) 25–32. doi:10.1002/term.5.

[92] H. Yuan, H. Fernandes, P. Habibovic, J. de Boer, A.M.C. Barradas, A. de Ruiter, W.R. Walsh, C.A. van Blitterswijk, J.D. de Bruijn, Osteoinductive ceramics as a synthetic alternative to autologous bone grafting, Proc. Natl. Acad. Sci. 107 (2010) 13614–13619. doi:10.1073/pnas.1003600107.

[93] S. Bose, S. Vahabzadeh, A. Bandyopadhyay, Bone tissue engineering using 3D printing, Mater. Today. 16 (2013) 496–504. doi:10.1016/j.mattod.2013.11.017.

[94] S.-W. Mok, R. Nizak, S.-C. Fu, K.-W.K. Ho, L. Qin, D.B.F. Saris, K.-M. Chan, J. Malda, From the printer: Potential of three-dimensional printing for orthopaedic applications, J. Orthop. Transl. 6 (2016) 42–49. doi:10.1016/j.jot.2016.04.003.

[95] A. Schwab, R. Levato, M. D'Este, S. Piluso, D. Eglin, J. Malda, Printability and Shape Fidelity of Bioinks in 3D Bioprinting, Chem. Rev. 120 (2020) 11028–11055. doi:10.1021/acs.chemrev.0c00084.

[96] S. V. Murphy, A. Atala, 3D bioprinting of tissues and organs, Nat. Biotechnol. 32 (2014) 773–785. doi:10.1038/nbt.2958.

[97] N. Ashammakhi, S. Ahadian, C. Xu, H. Montazerian, H. Ko, R. Nasiri, N. Barros, A. Khademhosseini, Bioinks and bioprinting technologies to make heterogeneous and biomimetic tissue constructs, Mater. Today Bio. 1 (2019). doi:10.1016/J.MTBIO.2019.100008.

[98] N.A. Sears, D.R. Seshadri, P.S. Dhavalikar, E. Cosgriff-Hernandez, A Review of Three-Dimensional Printing in Tissue Engineering, Tissue Eng. Part B Rev. 22 (2016) 298–310. doi:10.1089/ten.teb.2015.0464.

[99] X. Cui, D. Dean, Z.M. Ruggeri, T. Boland, Cell damage evaluation of thermal inkjet printed Chinese hamster ovary cells, Biotechnol. Bioeng. 106 (2010) 963–969. doi:10.1002/bit.22762.

[100] T. Xu, J. Jin, C. Gregory, J.J. Hickman, T. Boland, Inkjet printing of viable mammalian cells, Biomaterials. 26 (2005) 93–99. doi:10.1016/j.biomaterials.2004.04.011.

[101] J.D. Kim, J.S. Choi, B.S. Kim, Y. Chan Choi, Y.W. Cho, Piezoelectric inkjet printing of polymers: Stem cell patterning on polymer substrates, Polymer (Guildf). 51 (2010) 2147–2154. doi:10.1016/j.polymer.2010.03.038.

[102] I.T. Ozbolat, M. Hospodiuk, Current advances and future perspectives in extrusion-based bioprinting, Biomaterials. 76 (2016) 321–343. doi:10.1016/j.biomaterials.2015.10.076.

[103] R. Chang, J. Nam, W. Sun, Effects of Dispensing Pressure and Nozzle Diameter on Cell Survival from Solid Freeform Fabrication–Based Direct Cell Writing, Tissue Eng. Part A. 14 (2008) 41–48. doi:10.1089/ten.a.2007.0004.

[104] N.J. Castro, J. O'Brien, L.G. Zhang, Integrating biologically inspired nanomaterials and table-top stereolithography for 3D printed biomimetic osteochondral scaffolds, Nanoscale. 7 (2015) 14010–14022. doi:10.1039/C5NR03425F.

[105] N. Ashammakhi, A. Hasan, O. Kaarela, B. Byambaa, A. Sheikhi, A.K. Gaharwar, A. Khademhosseini, Advancing Frontiers in Bone Bioprinting, Adv. Healthc. Mater. 8 (2019) 1–24. doi:10.1002/adhm.201801048.

[106] J. Groll, J.A. Burdick, D.-W. Cho, B. Derby, M. Gelinsky, S.C. Heilshorn, T. Jüngst, J. Malda, V.A. Mironov, K. Nakayama, A. Ovsianikov, W. Sun, S. Takeuchi, J.J. Yoo, T.B.F. Woodfield, A definition of bioinks and their distinction from biomaterial inks, Biofabrication. 11 (2018) 013001. doi:10.1088/1758-5090/aaec52.

[107] S.J. Buwalda, K.W.M. Boere, P.J. Dijkstra, J. Feijen, T. Vermonden, W.E. Hennink, Hydrogels in a historical perspective: From simple networks to smart materials, J. Control. Release. 190 (2014) 254–273. doi:10.1016/j.jconrel.2014.03.052.

[108] E.S. Dragan, Design and applications of interpenetrating polymer network hydrogels. A review, Chem. Eng. J. 243 (2014) 572–590. doi:10.1016/j.cej.2014.01.065.

[109] M. Hospodiuk, M. Dey, D. Sosnoski, I.T. Ozbolat, The bioink: A comprehensive review on bioprintable materials, Biotechnol. Adv. 35 (2017) 217–239. doi:10.1016/j.biotechadv.2016.12.006.

[110] A.C. Hernández-González, L. Téllez-Jurado, L.M. Rodríguez-Lorenzo, Alginate hydrogels for bone tissue engineering, from injectables to bioprinting: A Review, Carbohydr. Polym. (2019) 115514. doi:10.1016/j.carbpol.2019.115514.

[111] A. Haug, K. Claeson, S.E. Hansen, R. Sömme, E. Stenhagen, H. Palmstierna, Fractionation of Alginic Acid., Acta Chem. Scand. 13 (1959) 601–603. doi:10.3891/acta.chem.scand.13-0601.

[112] J. Venkatesan, I. Bhatnagar, P. Manivasagan, K.H. Kang, S.K. Kim, Alginate composites for bone tissue engineering: A review, Int. J. Biol. Macromol. 72

(2015) 269–281. doi:10.1016/j.ijbiomac.2014.07.008.

[113] G. Klöck, A. Pfeffermann, C. Ryser, P. Gröhn, B. Kuttler, H.-J. Hahn, U. Zimmermann, Biocompatibility of mannuronic acid-rich alginates, Biomaterials. 18 (1997) 707–713. doi:10.1016/S0142-9612(96)00204-9.

[114] N.A. Peppas, J.Z. Hilt, A. Khademhosseini, R. Langer, Hydrogels in Biology and Medicine: From Molecular Principles to Bionanotechnology, Adv. Mater. 18 (2006) 1345–1360. doi:10.1002/adma.200501612.

[115] K.Y. Lee, D.J. Mooney, Alginate: Properties and biomedical applications, Prog. Polym. Sci. 37 (2012) 106–126. doi:10.1016/j.progpolymsci.2011.06.003.

[116] C.C. Piras, D.K. Smith, Multicomponent polysaccharide alginate-based bioinks, J. Mater. Chem. B. 8 (2020) 8171–8188. doi:10.1039/D0TB01005G.

[117] F.E. Freeman, D.J. Kelly, Tuning Alginate Bioink Stiffness and Composition for Controlled Growth Factor Delivery and to Spatially Direct MSC Fate within Bioprinted Tissues, Sci. Rep. 7 (2017) 1–12. doi:10.1038/s41598-017-17286-1.

[118] L.D. Loozen, F. Wegman, F.C. Öner, W.J.A. Dhert, J. Alblas, Porous bioprinted constructs in BMP-2 non-viral gene therapy for bone tissue engineering, J. Mater. Chem. B. 1 (2013) 6619. doi:10.1039/c3tb21093f.

[119] H. Kong, M.K. Smith, D.J. Mooney, Designing alginate hydrogels to maintain viability of immobilized cells, Biomaterials. 24 (2003) 4023–4029. doi:10.1016/S0142-9612(03)00295-3.

[120] G. Kaklamani, D. Cheneler, L.M. Grover, M.J. Adams, J. Bowen, Mechanical properties of alginate hydrogels manufactured using external gelation, J. Mech. Behav. Biomed. Mater. 36 (2014) 135–142. doi:10.1016/j.jmbbm.2014.04.013.

[121] J.L. Drury, R.G. Dennis, D.J. Mooney, The tensile properties of alginate hydrogels, Biomaterials. 25 (2004) 3187–3199. doi:10.1016/j.biomaterials.2003.10.002.

[122] T. Andersen, P. Auk-Emblem, M. Dornish, 3D Cell Culture in Alginate Hydrogels, Microarrays. 4 (2015) 133–161. doi:10.3390/microarrays4020133.

[123] T.T. Demirtaş, G. Irmak, M. Gümüşderelioğlu, A bioprintable form of chitosan hydrogel for bone tissue engineering, Biofabrication. 9 (2017) 035003. doi:10.1088/1758-5090/aa7b1d.

[124] H.J. Kong, D. Kaigler, K. Kim, D.J. Mooney, Controlling Rigidity and Degradation of Alginate Hydrogels via Molecular Weight Distribution, Biomacromolecules. 5 (2004) 1720–1727. doi:10.1021/bm049879r.

[125] J.-S. Yang, Y.-J. Xie, W. He, Research progress on chemical modification of alginate: A review, Carbohydr. Polym. 84 (2011) 33–39. doi:10.1016/j.carbpol.2010.11.048.

[126] S. Reakasame, A.R. Boccaccini, Oxidized Alginate-Based Hydrogels for Tissue Engineering Applications: A Review, Biomacromolecules. 19 (2018) 3–21. doi:10.1021/acs.biomac.7b01331.

[127] C.G. Gomez, M. Rinaudo, M.A. Villar, Oxidation of sodium alginate and characterization of the oxidized derivatives, Carbohydr. Polym. 67 (2007) 296–304. doi:10.1016/j.carbpol.2006.05.025.

[128] A. Lueckgen, D.S. Garske, A. Ellinghaus, R.M. Desai, A.G. Stafford, D.J. Mooney, G.N. Duda, A. Cipitria, Hydrolytically-degradable click-crosslinked alginate hydrogels, Biomaterials. 181 (2018) 189–198. doi:10.1016/j.biomaterials.2018.07.031.

[129] A. Jejurikar, X.T. Seow, G. Lawrie, D. Martin, A. Jayakrishnan, L. Grøndahl, Degradable alginate hydrogels crosslinked by the macromolecular crosslinker alginate dialdehyde, J. Mater. Chem. 22 (2012) 9751. doi:10.1039/c2jm30564j.

[130] B. Wright, P.A. De Bank, K.A. Luetchford, F.R. Acosta, C.J. Connon, Oxidized alginate hydrogels as niche environments for corneal epithelial cells, J. Biomed. Mater. Res. Part A. 102 (2014) 3393–3400. doi:10.1002/jbm.a.35011.

[131] T. Zehnder, B. Sarker, A.R. Boccaccini, R. Detsch, Evaluation of an alginate–gelatine crosslinked hydrogel for bioplotting, Biofabrication. 7 (2015) 025001. doi:10.1088/1758-5090/7/2/025001.

[132] O. Jeon, K.H. Bouhadir, J.M. Mansour, E. Alsberg, Photocrosslinked alginate hydrogels with tunable biodegradation rates and mechanical properties, Biomaterials. 30 (2009) 2724–2734. doi:10.1016/j.biomaterials.2009.01.034.

[133] O. Jeon, C. Powell, S.M. Ahmed, E. Alsberg, Biodegradable, Photocrosslinked Alginate Hydrogels with Independently Tailorable Physical Properties and Cell Adhesivity, Tissue Eng. Part A. 16 (2010) 2915–2925. doi:10.1089/ten.tea.2010.0096.

[134] K.B. Fonseca, S.J. Bidarra, M.J. Oliveira, P.L. Granja, C.C. Barrias, Molecularly designed alginate hydrogels susceptible to local proteolysis as three-dimensional cellular microenvironments, Acta Biomater. 7 (2011) 1674–1682. doi:10.1016/j.actbio.2010.12.029.

[135] A. Lueckgen, D.S. Garske, A. Ellinghaus, D.J. Mooney, G.N. Duda, A. Cipitria, Enzymatically-degradable alginate hydrogels promote cell spreading and in vivo tissue infiltration, Biomaterials. 217 (2019) 1–11. doi:10.1016/j.biomaterials.2019.119294.

[136] P.M. Kharkar, K.L. Kiick, A.M. Kloxin, Designing degradable hydrogels for orthogonal control of cell microenvironments, Chem. Soc. Rev. 42 (2013) 7335–7372. doi:10.1039/C3CS60040H.

[137] O. Chaudhuri, L. Gu, D. Klumpers, M. Darnell, S.A. Bencherif, J.C. Weaver, N. Huebsch, H.-P. Lee, E. Lippens, G.N. Duda, D.J. Mooney, Hydrogels with tunable stress relaxation regulate stem cell fate and activity, Nat. Mater. 15 (2016) 326–334. doi:10.1038/nmat4489.

[138] L.M. Rodríguez-Lorenzo, R. García-Carrodeguas, M.A. Rodríguez, S. De Aza, J. Jiménez, A. López-Bravo, M. Fernandez, J.S. Román, Synthesis, characterization, bioactivity and biocompatibility of nanostructured materials based on the wollastonite-poly(ethylmethacrylate- co -vinylpyrrolidone) system, J. Biomed. Mater. Res. Part A. 88A (2009) 53–64. doi:10.1002/jbm.a.31867.

[139] D.A. Sánchez-Téllez, L. Téllez-Jurado, J.F. Chávez-Alcalá, Bioactivity and degradability of hybrids nano-composites materials with great application as bone tissue substitutes, J. Alloys Compd. 615 (2014) S670–S675. doi:10.1016/j.jallcom.2014.04.078.

[140] B. Sarker, W. Li, K. Zheng, R. Detsch, A.R. Boccaccini, Designing Porous Bone

Tissue Engineering Scaffolds with Enhanced Mechanical Properties from Composite Hydrogels Composed of Modified Alginate, Gelatin, and Bioactive Glass, ACS Biomater. Sci. Eng. 2 (2016) 2240–2254. doi:10.1021/acsbiomaterials.6b00470.

[141] A.A. El-Rashidy, J.A. Roether, L. Harhaus, U. Kneser, A.R. Boccaccini, Regenerating bone with bioactive glass scaffolds: A review of in vivo studies in bone defect models, Acta Biomater. 62 (2017) 1–28. doi:10.1016/j.actbio.2017.08.030.

[142] X. Wang, E. Tolba, H.C. Schröder, M. Neufurth, Q. Feng, B. Diehl-Seifert, W.E.G. Müller, Effect of Bioglass on Growth and Biomineralization of SaOS-2 Cells in Hydrogel after 3D Cell Bioprinting, PLoS One. 9 (2014) e112497. doi:10.1371/journal.pone.0112497.

[143] J. Olmos Buitrago, R.A. Perez, A. El-Fiqi, R.K. Singh, J.-H. Kim, H.-W. Kim, Core–shell fibrous stem cell carriers incorporating osteogenic nanoparticulate cues for bone tissue engineering, Acta Biomater. 28 (2015) 183–192. doi:10.1016/j.actbio.2015.09.021.

[144] M. Ojansivu, A. Rashad, A. Ahlinder, J. Massera, A. Mishra, K. Syverud, A. Finne-Wistrand, S. Miettinen, K. Mustafa, Wood-based nanocellulose and bioactive glass modified gelatin–alginate bioinks for 3D bioprinting of bone cells, Biofabrication. 11 (2019) 035010. doi:10.1088/1758-5090/ab0692.

[145] N.E. Fedorovich, H.M. Wijnberg, W.J.A. Dhert, J. Alblas, Distinct Tissue Formation by Heterogeneous Printing of Osteo- and Endothelial Progenitor Cells, Tissue Eng. Part A. 17 (2011) 2113–2121. doi:10.1089/ten.tea.2011.0019.

[146] Y. Luo, A. Lode, C. Wu, J. Chang, M. Gelinsky, Alginate/Nanohydroxyapatite Scaffolds with Designed Core/Shell Structures Fabricated by 3D Plotting and in Situ Mineralization for Bone Tissue Engineering, ACS Appl. Mater. Interfaces. 7 (2015) 6541–6549. doi:10.1021/am508469h.

[147] G. Turco, E. Marsich, F. Bellomo, S. Semeraro, I. Donati, F. Brun, M. Grandolfo, A. Accardo, S. Paoletti, Alginate/Hydroxyapatite Biocomposite For Bone Ingrowth: A Trabecular Structure With High And Isotropic Connectivity, Biomacromolecules. 10 (2009) 1575–1583. doi:10.1021/BM900154B.

[148] H.-R. Lin, Y.-J. Yeh, Porous alginate/hydroxyapatite composite scaffolds for bone tissue engineering: Preparation, characterization, and in vitro studies, J. Biomed. Mater. Res. 71B (2004) 52–65. doi:10.1002/jbm.b.30065.

[149] X.-F. Wang, P.-J. Lu, Y. Song, Y.-C. Sun, Y.-G. Wang, Y. Wang, Nano hydroxyapatite particles promote osteogenesis in a three-dimensional bio-printing construct consisting of alginate/gelatin/hASCs, RSC Adv. 6 (2016) 6832–6842. doi:10.1039/C5RA21527G.

[150] A. Sarker, J. Amirian, Y.K. Min, B.T. Lee, HAp granules encapsulated oxidized alginate–gelatin–biphasic calcium phosphate hydrogel for bone regeneration, Int. J. Biol. Macromol. 81 (2015) 898–911. doi:10.1016/j.ijbiomac.2015.09.029.

[151] R.A. Perez, G. Altankov, E. Jorge-Herrero, M.P. Ginebra, Micro- and nanostructured hydroxyapatite-collagen microcarriers for bone tissue-engineering applications, J. Tissue Eng. Regen. Med. 7 (2013) 353–361. doi:10.1002/term.530.

[152] R.A. Perez, S. Del Valle, G. Altankov, M.-P. Ginebra, Porous hydroxyapatite and gelatin/hydroxyapatite microspheres obtained by calcium phosphate cement emulsion, J. Biomed. Mater. Res. B Appl. Biomater. 97B (2011) 156–166. doi: 10.1002/jbm.b.31798.

[153] R. Levato, J. Visser, J.A. Planell, E. Engel, J. Malda, M.A. Mateos-Timoneda, Biofabrication of tissue constructs by 3D bioprinting of cell-laden microcarriers, Biofabrication. 6 (2014) 035020. doi:10.1088/1758-5082/6/3/035020.

[154] Y.J. Tan, X. Tan, W.Y. Yeong, S.B. Tor, Hybrid microscaffold-based 3D bioprinting of multi-cellular constructs with high compressive strength: A new biofabrication strategy, Sci. Rep. 6 (2016) 39140. doi:10.1038/srep39140.

[155] H.A.-D.M. Abu Awwad, L. Thiagarajan, J.M. Kanczler, M.H. Amer, G. Bruce, S. Lanham, R.M.H. Rumney, R.O.C. Oreffo, J.E. Dixon, Genetically-programmed, mesenchymal stromal cell-laden & mechanically strong 3D bioprinted scaffolds for bone repair, J. Control. Release. 325 (2020) 335–346. doi:10.1016/j.jconrel.2020.06.035.

[156] J.J. Rice, M.M. Martino, L. De Laporte, F. Tortelli, P.S. Briquez, J.A. Hubbell, Engineering the Regenerative Microenvironment with Biomaterials, Adv. Healthc. Mater. 2 (2013) 57–71. doi:10.1002/adhm.201200197.

[157] R.A. Perez, M. Kim, T.-H. Kim, J.-H. Kim, J.H. Lee, J.-H. Park, J.C. Knowles, H.-W. Kim, Utilizing Core–Shell Fibrous Collagen-Alginate Hydrogel Cell Delivery System for Bone Tissue Engineering, Tissue Eng. Part A. 20 (2014) 103–114. doi:10.1089/ten.tea.2013.0198.

[158] C. Liu, D. Lewin Mejia, B. Chiang, K.E. Luker, G.D. Luker, Hybrid collagen alginate hydrogel as a platform for 3D tumor spheroid invasion, Acta Biomater. 75 (2018) 213–225. doi:10.1016/j.actbio.2018.06.003.

[159] J.L. West, Biofunctional polymers, in: Encycl. Biomater. Biomed. Eng., 2004: pp. 89–95.

[160] N.O. Dhoot, C.A. Tobias, I. Fischer, M.A. Wheatley, Peptide-modified alginate surfaces as a growth permissive substrate for neurite outgrowth, J. Biomed. Mater. Res. 71A (2004) 191–200. doi:10.1002/jbm.a.30103.

[161] E. Ruoslahti, M. Pierschbacher, New perspectives in cell adhesion: RGD and integrins, Science. 238 (1987) 491–497. doi:10.1126/science.2821619.

[162] J. Travis, Biotech Gets a Grip on Cell Adhesion, Science. 260 (1993) 906–908. doi:10.1126/science.8493523.

[163] J.A. Rowley, G. Madlambayan, D.J. Mooney, Alginate hydrogels as synthetic extracellular matrix materials, Biomaterials. 20 (1999) 45–53. doi:10.1016/S0142-9612(98)00107-0.

[164] J.A. Rowley, D.J. Mooney, Alginate type and RGD density control myoblast phenotype, J. Biomed. Mater. Res. 60 (2002) 217–223. doi:10.1002/jbm.1287.

[165] K.Y. Lee, E. Alsberg, S. Hsiong, W. Comisar, J. Linderman, R. Ziff, D. Mooney, Nanoscale Adhesion Ligand Organization Regulates Osteoblast Proliferation and Differentiation, Nano Lett. 4 (2004) 1501–1506. doi:10.1021/nl0493592.

[166] M.D. Sarker, S. Naghieh, A.D. McInnes, L. Ning, D.J. Schreyer, X. Chen, Bio-fabrication of peptide-modified alginate scaffolds: Printability, mechanical

stability and neurite outgrowth assessments, Bioprinting. 14 (2019) e00045. doi:10.1016/j.bprint.2019.e00045.

[167] J. Jia, D.J. Richards, S. Pollard, Y. Tan, J. Rodriguez, R.P. Visconti, T.C. Trusk, M.J. Yost, H. Yao, R.R. Markwald, Y. Mei, Engineering alginate as bioink for bioprinting, Acta Biomater. 10 (2014) 4323–4331. doi:10.1016/j.actbio.2014.06.034.

[168] J.H. Collier, T. Segura, Evolving the use of peptides as components of biomaterials, Biomaterials. 32 (2011) 4198–4204. doi:10.1016/j.biomaterials.2011.02.030.

[169] J. Marchand-Brynaert, E. Detrait, O. Noiset, T. Boxus, Y.-J. Schneider, C. Remacle, Biological evaluation of RGD peptidomimetics, designed for the covalent derivatization of cell culture substrata, as potential promotors of cellular adhesion, Biomaterials. 20 (1999) 1773–1782. doi:10.1016/S0142-9612(99)00072-1.

[170] L. Pollaro, C. Heinis, Strategies to prolong the plasma residence time of peptidedrugs, Medchemcomm. 1 (2010) 319–324. doi:10.1039/C0MD00111B.

[171] C. Mas-Moruno, R. Fraioli, F. Rechenmacher, S. Neubauer, T.G. Kapp, H. Kessler, αvβ3- or α5β1-Integrin-Selective Peptidomimetics for Surface Coating, Angew. Chemie Int. Ed. 55 (2016) 7048–7067. doi:10.1002/anie.201509782.

[172] O. Fromigué, J. Brun, C. Marty, S. Da Nascimento, P. Sonnet, P.J. Marie, Peptide-based activation of alpha5 integrin for promoting osteogenesis, J. Cell. Biochem. 113 (2012) 3029–3038. doi:10.1002/jcb.24181.

[173] Z. Hamidouche, O. Fromigue, J. Ringe, T. Haupl, P. Vaudin, J.-C. Pages, S. Srouji, E. Livne, P.J. Marie, Priming integrin 5 promotes human mesenchymal stromal cell osteoblast differentiation and osteogenesis, Proc. Natl. Acad. Sci. 106 (2009) 18587–18591. doi:10.1073/pnas.0812334106.

[174] C. Dahmen, J. Auernheimer, A. Meyer, A. Enderle, S.L. Goodman, H. Kessler, Improving Implant Materials by Coating with Nonpeptidic, Highly Specific Integrin Ligands, Angew. Chemie Int. Ed. 43 (2004) 6649–6652. doi:10.1002/anie.200460770.

[175] F. Rechenmacher, S. Neubauer, J. Polleux, C. Mas-Moruno, M. De Simone, E.A. Cavalcanti-Adam, J.P. Spatz, R. Fässler, H. Kessler, Functionalizing αvβ3- or α5β1-Selective Integrin Antagonists for Surface Coating: A Method To Discriminate Integrin Subtypes In Vitro, Angew. Chemie Int. Ed. 52 (2013) 1572–1575. doi:10.1002/anie.201206370.

[176] F. Rechenmacher, S. Neubauer, C. Mas-Moruno, P.M. Dorfner, J. Polleux, J. Guasch, B. Conings, H.-G. Boyen, A. Bochen, T.R. Sobahi, R. Burgkart, J.P. Spatz, R. Fässler, H. Kessler, A Molecular Toolkit for the Functionalization of Titanium-Based Biomaterials That Selectively Control Integrin-Mediated Cell Adhesion, Chem. - A Eur. J. 19 (2013) 9218–9223. doi:10.1002/chem.201301478.

[177] R. Fraioli, F. Rechenmacher, S. Neubauer, J.M. Manero, J. Gil, H. Kessler, C. Mas-Moruno, Mimicking bone extracellular matrix: Integrin-binding peptidomimetics enhance osteoblast-like cells adhesion, proliferation, and differentiation on titanium, Colloids Surfaces B Biointerfaces. 128 (2015) 191–

200. doi:10.1016/j.colsurfb.2014.12.057.

[178] R. Fraioli, P.M. Tsimbouri, L.E. Fisher, A.H. Nobbs, B. Su, S. Neubauer, F. Rechenmacher, H. Kessler, M.-P. Ginebra, M.J. Dalby, J.M. Manero, C. Mas-Moruno, Towards the cell-instructive bactericidal substrate: exploring the combination of nanotopographical features and integrin selective synthetic ligands, Sci. Rep. 7 (2017) 16363. doi:10.1038/s41598-017-16385-3.

[179] R. Fraioli, S. Neubauer, F. Rechenmacher, B.M. Bosch, K. Dashnyam, J.-H. Kim, R.A. Perez, H.-W. Kim, F.J. Gil, M.P. Ginebra, J.M. Manero, H. Kessler, C. Mas-Moruno, Control of stem cell response and bone growth on biomaterials by fully non-peptidic integrin selective ligands, Biomater. Sci. 7 (2019) 1281–1285. doi:10.1039/C8BM01466C.

Chapter 2

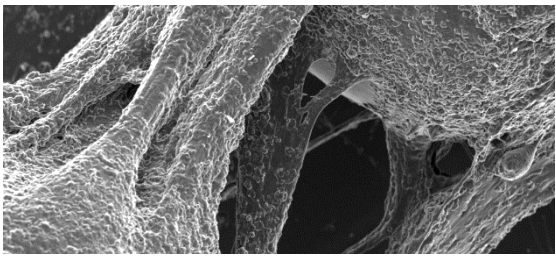

Hydroxyapatite Nanoparticles-Cell Interaction: the Fate of Membrane-Bound and Internalised Nanoparticles

HYDROXYAPATITE NANOPARTICLES-CELL INTERACTION: THE FATE OF MEMBRANE-BOUND AND INTERNALISED NANOPARTICLES

Scope

Hydroxyapatite (HA) nanoparticles (NPs) are employed to selectively kill cancer cells. But, how do they do it? Which is their mechanism of action? As there is no universal technique that can help answer this question, **Chapter 2** aims to compare traditional methods used to study the fate of the HA NPs once internalised in the cells (*i.e.* flow cytometry, transmission electron microscopy and intracellular calcium fluorescent visualisation) with more novel techniques. In this sense, cryo-soft X-ray tomography will be investigated as a potential screening tool to have a wide overview of the cytotoxicity of this type of nanomaterials, as well as its consequences. The main advantages and drawbacks of each technology will be further explored and discussed.

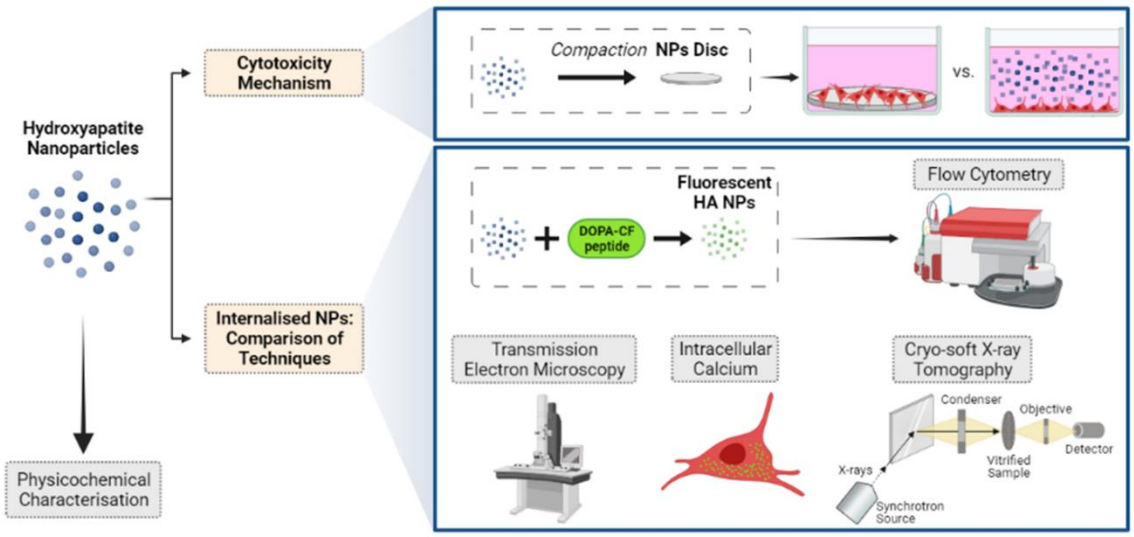

2.1. Introduction

Over the past few years, the application of hydroxyapatite (HA) in the form of nanoparticles (NPs) has received considerable attention as a transfection vehicle for the transport of genetic material into cells [1]. HA NPs have also been proposed as a useful tool in cancer therapy. It has been observed that they were able to cause cell death of several cancer cell types whilst having minimal side effects on healthy cells [2–6]. Moreover, ion-doped HA NPs have been investigated for cancer treatment showing improved cytotoxic potential towards cancer cells and being more selective than non-doped HA [7]. Actually, ions are particularly interesting in cancer treatment, as it has been demonstrated that some specific cancer cells have ionic channel dysregulations in their membrane, *e.g.* TRPM7 magnesium transporter is upregulated in breast and pancreatic cancer, as well as in osteosarcoma MG-63 cell line [8–12]. However, the exact mechanisms of cell death are still under debate.

Three different scenarios which can potentially drive towards cytotoxicity can be anticipated: (1) reactivity of the NPs with the surrounding fluids, causing the release or depletion of ions and proteins crucial for cells; (2) interaction of NPs with cell membrane receptors that may induce apoptotic signalling cascades; and (3) NP internalisation and subsequent effects inside the cell.

The most accepted hypothesis is based on the third assumption and relies on the degradability of the NPs upon internalisation. Indeed, after HA NPs uptake by endocytosis, they degrade under the acidic conditions in the lysosome, yielding an increase of calcium and phosphorus ions. Whereas a slow and sustained dissolution of HA in the lysosomes would be innocuous to cells and would benefit transfection [13], a more efficient and fast internalisation would release a high concentration of calcium ions that would lead to cell death [14]. This has been hypothesised to be caused either by apoptosis triggered by a disruption of cell homeostasis [15] or by necrosis when the rapid dissolution of the NPs causes an imbalance of the osmotic pressure in the lysosomes that results in their massive breaking [16,17].

In order to describe in detail the HA NPs mode of action, it is necessary to have reliable methods to assess not only their internalisation but also their dissolution once inside the cells. Internalised NPs can be detected either by transmission electron microscopy or by tracking fluorescently labelled NPs with different techniques (*e.g.* flow cytometry, fluorescent microscopy, etc.). However, with some of these techniques, it is not possible to differentiate the cell surface-associated particles from the ones internalised into the cells [18,19]. Moreover, techniques based on the visualisation of pristine NPs are insufficient to correlate the amount of internalised particles to their toxicity, as they cannot determine their solubilisation [20]. Thereby, various studies have used calcium probes to measure intracellular calcium levels, to check HA NPs dissolution [14,16,17,20]. In addition, in this study, we propose the use of cryo-soft X-ray tomography as a novel approach to analyse the ultrastructure of intact and unstained cells, as well as to obtain quantitative data on the Ca elemental composition of each organelle. Compared to calcium imaging, this technique offers the advantage of visualising soluble calcium-rich vesicles without losing the information of solid calcium material.

Beyond the effects associated with NP internalisation, little attention has been paid in the literature to the influence of ionic exchanges between HA NPs and the surrounding fluids on cell viability [7,21,22]. This may be relevant, as drastic ionic fluctuations, especially of calcium, phosphorus and magnesium, elicited by nanostructured hydroxyapatite

materials, have been reported to result in cytotoxicity [23–25]. On the other hand, to the best of our knowledge, there is no literature studying the interaction of HA NPs with receptors in the membrane that may be crucial for cell viability.

In this context, the objectives of the present work are: (1) to unravel the influence of nanoparticle-cell membrane interaction on cell cytotoxicity, leading to a better understanding of the mechanisms behind the use of HA NPs in cancer treatment applications; and (2) to investigate fundamental aspects of HA NPs internalisation and fate within the cells. The conventional techniques will be compared to calcium fluorescence probes and cryo-soft X-ray tomography as alternatives to track calcium-rich vesicles and the degradation state of internalised HA NPs.

2.2. Experimental Section

2.2.1. Synthesis and Characterisation of Non-doped and Magnesium-doped Hydroxyapatite Nanoparticles

Non-doped and magnesium-doped hydroxyapatite nanoparticles (HA NPs and MgHA NPs, respectively) were obtained by the neutralisation of calcium hydroxide with ortho-phosphoric acid, as described elsewhere [7]. Briefly, 200 mM H_3PO_4 (85 wt% pure, Panreac) was added dropwise into a solution of 333 mM $Ca(OH)_2$ (96 wt% pure, Fluka) at a rate of 1 ml min^{-1}. The reaction, described in **Equation 2.1**, was performed under constant stirring at 40 ^oC in thermojacketed vessels and the pH was continuously monitored.

$$10\ Ca(OH)_2 + 6\ H_3PO_4 \rightarrow Ca_{10}(PO_4)_6(OH)_2 + 18\ H_2O \qquad \textbf{Equation 2.1}$$

At pH 8, the reaction was stopped and the solution was stirred for 30 min at 40 ^oC. Afterwards, it was left to mature overnight at room temperature. The suspension was then rinsed three times with bi-distilled water, performing centrifugation cycles of 5 min at 800 g (5430 R, Eppendorf). Finally, the product was freeze-dried (Cryodos, Telstar).

The synthesis of MgHA NPs was done similarly, with the incorporation of magnesium chloride ($MgCl_2 \cdot 6\ H_2O$, 99 wt% pure, PanReac) into the calcium hydroxide solution prior to H_3PO_4 addition. The final Mg^{2+} content in these NPs was ≈2.3 wt% [7].

The NPs were suspended in bi-distilled water to a final concentration of 10 mg ml^{-1} and sonicated with a high-frequency ultrasound probe sonicator (450D, Branson Digital) to improve their deagglomeration. A 3 mm diameter tip was used with 40% amplitude for 2 min in an ice bath. In addition, specular discs were prepared by compacting 200 mg of NPs into 10 mm diameter moulds and applying a uniaxial pressure of 3 tons for 2 min.

Characterisation of the NPs comprised analysis of the phase composition by X-ray diffraction (XRD, D8 Advance, Bruker) using Cu Kα radiation at 40 kV and 40 mA. Data were collected with a step size of 0.02^o over the 2θ range from 20 to 40^o with a counting time of 2 s per step. Phase identification was accomplished by comparing the results with the standard patterns of HA (ICDD PDF 09-0432). In addition, morphological evaluation of the NPs was assessed by transmission electron microscopy (TEM, JEM-1010, JEOL) after soaking a 300-mesh carbon-coated copper grid into the NPs suspensions. Finally, the surface morphology of the discs was studied by scanning electron microscopy (SEM, JSM-7001F, JEOL). Prior to the observation, the samples were coated with a thin gold-palladium layer using vapour deposition (SCD 004, Balzers).

2.2.2. Fluorescent Functionalisation of the Nanoparticles

In order to track the NPs, a fluorescent biomolecule was attached to HA by means of strong hydrogen bonds via catechol groups [26]. To this end, a custom-made linear peptide containing DOPA and carboxyfluorescein (CF) (**Table 2.1**) was synthesised by solid-phase peptide synthesis (SPPS) following the Fmoc/tBu strategy and using Rink Amide MBHA resin (243 mg, 0.45 mmol g^{-1}) as a solid support, according to the protocols optimised in our group [27]. The peptide was used with a purity of ≥ 90%, as determined by reversed-phase analytical high-performance liquid chromatography (RP-HPLC, Prominence UFLC XR, Shimadzu).

Table 2.1. Chemical sequence of the fluorescent peptide and properties

Sequence[a]	**Purity (%)**[b]	**t_R (min)**[b]	**Molecular weight (g mol^{-1})**
CF-$(Ahx)_2$-βAla-$DOPA_2$-NH_2	90.3	6.127	1031.07

[a] CF: (5)6-carboxyfluorescein; Ahx: 6-aminohexanoic acid; βAla: beta-alanine; DOPA: L-3,4-dihydroxyphenylalanine

[b] Characterised by HPLC using a reversed-phase XBridge (Waters) C18 column (4.6 mm x 100 mm, 3.5 µm) and a linear gradient from 20:100 (0.036% TFA in ACN/0.045% TFA in H_2O) in 8 min at 25 ºC.

The lyophilised peptide was dissolved in distilled water to a series of concentrations from 500 µM down to 1 µM, adjusting the pH to 7. Carboxyfluorescein (CF) alone was also studied at the same concentrations and pH. The functionalisation of the HA NPs was accomplished by mixing under constant stirring 200 µl of 1 wt% NPs suspension and 100 µl of either peptide or CF solutions for 2 h. The resulting suspension was centrifuged and rinsed three times with bi-distilled water and re-suspended to a final concentration of 1 wt%. After functionalisation, supernatants and washing residues were collected and their fluorescent intensity was measured by means of a microplate reader (Synergy HTX, BioTek Instruments). Knowing the difference between the initial amount of peptide added and the quantity that remained in the supernatants, data were correlated to a calibration curve to determine the final concentration of peptide adsorbed on the NPs.

The fluorescent NPs (*i.e.* HA-F and MgHA-F) functionalised using a concentration of 500 µM of the fluorescent peptide were selected for the cell culture studies. In addition, direct fluorescence intensity was measured in 100 µg ml^{-1} NP suspension by means of a fluorescence spectrophotometer (Cary Eclipse, Agilent). Finally, the zeta potential of the different NPs (*i.e.* HA and MgHA, before and after functionalisation) was measured in 300 µg ml^{-1} NPs suspensions using a Zetasizer Nano (Malvern Panalytical).

2.2.3. Cell Culture

Human osteosarcoma MG-63 cells (ATCC) were cultured in Dulbecco's Modified Eagle medium (DMEM) supplemented with 10% foetal bovine serum (FBS), 20 mM 4-(2-hydroxyethyl)-1-piperazineethanesulfonic acid buffer (HEPES), 2 mM L-glutamine, 50

U ml^{-1} penicillin and 50 µg ml^{-1} streptomycin (all from Gibco), in a 95% humidified atmosphere containing 5% CO_2 at 37 ºC. Confluent cells were detached using TrypLE Express (Gibco).

For the cell culture studies, the NPs suspensions were sonicated in a bath sonicator (JP Selecta) for 5 min before their addition to the cell culture media, in order to avoid agglomerates. The experiments were carried out in serum-containing (*i.e.* NPs supplemented or cells seeded on discs in 10% FBS-containing media, FBS+) and in serum-free (FBS-) conditions to assess the influence of the protein corona. Moreover, different time points were studied, ranging from 3 to 24 h, depending on the study, and the supplemented dose of NPs was 100 µg ml^{-1} in all cases. Controls were prepared seeding the cells on sterile coverslips (Ø=10 mm).

2.2.4. Nanoparticles – Cell Membrane Interaction

MG-63 cells were seeded on sterile coverslips (Ø=10 mm) in a 48-well plate at a density of 25,000 cells per well and incubated overnight to allow cell adhesion. The following day, culture media containing 100 µg ml^{-1} of each NPs were prepared and supplemented to the cells. At the same time, previously compacted discs were sterilised with ethanol 70% for 30 min and rinsed with phosphate-buffered saline (PBS, Gibco). Afterwards, cells were seeded on top of them and left interaction for 4 h. The morphology of the cells was assessed by confocal microscopy (LSM 800, Zeiss) using acridine orange staining (AO, Sigma-Aldrich). Cell morphology was further analysed by scanning electron microscopy (SEM, JSM-7001F, JEOL). To do so, samples were fixed with 2.5% glutaraldehyde (Sigma-Aldrich) in PBS for 1 h at 4 ºC. Subsequently, fixed samples were rinsed with PBS and dehydrated in an increasing series of ethanol solutions. Dried discs and coverslips were covered with a thin gold-palladium layer using vapour deposition (SCD 004, Balzers). To quantify the results, a cytotoxicity assay was carried out using WST-1 reagent (Roche) and following the manufacturer's indications.

2.2.5. Flow Cytometry Assay

For the flow cytometry (FC) studies, MG-63 cells were seeded on 6-well plates at a density of 300,000 cells per well and incubated overnight. The following day, fresh culture media containing 100 µg ml^{-1} of functionalised NPs (*i.e.* HA-F and MgHA-F) were supplemented into the wells. After 4, 6 and 24 h of exposure, cells were detached from the wells using trypsin and the supernatant was removed after centrifugation. The pellet was rinsed and re-dispersed in PBS prior to analysis by flow cytometry (Accuri C6, BD Biosciences) at an emission wavelength of 488 nm. Controls were used to gate living cells and to determine the fluorescence threshold. A total of 10,000 events were evaluated for each condition, except for serum-free samples at 24 h, due to cell death. Data analysis was performed with FlowJo software (FlowJo LLC, version 10). In addition, cells supplemented with functionalised NPs were imaged in a confocal fluorescence microscope (LSM 800, Zeiss) to assess aggregation of NPs during cell culture. Before visualisation, cells were fixed and stained with Alexa Fluor 568-phalloidin (Thermo Fisher) and 4′,6-diamidino-2-phenylindole (DAPI, Sigma-Aldrich) after 4 h of interaction with the materials.

2.2.6. Intracellular Calcium Evaluation

For the quantification of intracellular calcium, MG-63 cells were seeded on a black 96-well plate at a density of 10000 cells per well and incubated overnight, whereas for the imaging 25000 cells were seeded on sterile coverslips in a 48-well plate. The following day, culture media containing either HA or MgHA NPs were supplemented to the cells. An apoptosis control was also tested by adding H_2O_2 in the medium at a final concentration of 200 µM, instead of NPs. After 3 h of incubation, cells were stained with Fluo-4 AM intracellular calcium indicator (Thermo Fisher) following the manufacturer's indications. The green intensity was quantified in a fluorescence microplate reader (Synergy HTX, BioTek Instruments) and the imaging was performed in a confocal microscope (LSM 800, Zeiss).

2.2.7. Transmission Electron Microscopy

For TEM imaging, 90-mm Petri dishes were coated with poly-L-lysine prior to MG-63 seeding. After overnight cell attachment, FBS-free culture media containing each type of NPs were supplemented to the cells. A control sample without NPs was also studied. The cells were exposed for 3 h and afterwards fixed with 2.5% glutaraldehyde (Sigma-Aldrich) in 0.1 M phosphate buffer (PB) for 1 h and detached to form a pellet. The pellet was rinsed and put in contact with a solution of 1 wt% OsO_4 and 0.8 wt% potassium ferricyanide for 2 h. Subsequently, it was dehydrated in an ascending series of acetone and infiltrated with EPON resin. Finally, blocks were sectioned with an ultramicrotome (Ultracut UCT, Leica) and the sections were stained with 2 wt% uranyl acetate and imaged with an optical microscope (DM2000 LED, Leica) and TEM (Tecnai Spirit Twin, FEI).

2.2.8. Cryo-Soft X-ray Tomography

For cryo-soft X-ray tomography (cryo-SXT), gold Quantifoil R2/2 G200F1 finder grids were coated with fibronectin (Sigma). Cells were seeded on the grids and incubated overnight. The following day, culture media without FBS containing NPs was supplemented to the cells. After 3 h of incubation, the grids were rinsed with PBS and immediately frozen in liquid ethane cooled with liquid nitrogen using an automatic plunge freezer for the bare grid technique (EM GP, Leica Microsystems). The samples were initially examined by means of a cryo-visible light microscope (Axioscope, Zeiss) provided with a cryo-stage (CMS196, Linkam Scientific). Samples were stored under liquid nitrogen and subsequently kept under cryogenic conditions at all times during the measurements by X-ray microscopy in the vitrified state. Cryo-SXT imaging was performed at the MISTRAL beamline of the ALBA Synchrotron light source. Tomographic data was collected at 520 eV, irradiating the samples for 2 – 10 s per projection. 520 eV is the energy range in which water is transparent for X-rays and there are mostly absorbed by carbon, allowing the visualisation of biological material. In tomographic setup, images obtained at different sample orientations are computationally combined to produce a three-dimensional (3D) image, permitting the 3D representation of the sub-cellular ultrastructure of whole intact cells. A tilt series was acquired for each cell using an angular step of 1^o on a 70^o angular range.

Each transmission projection image of the tilt series was normalised using flat-field. This process also considers the possibly different exposure time, as well as the slight decrease

of the electron beam current during the acquisition. In order to increase the image quality, wiener deconvolution taking into account the experimental impulse response of the optical system [28] was applied to the normalised data. Finally, the Naperian logarithm was used to reconstruct the linear absorption coefficient (LAC). The resulting stacks were then loaded into IMOD software [29] and the individual projections were aligned to the common tilt-axis using the internal cellular structures as markers. Afterwards, the aligned stacks were reconstructed with algebraic reconstruction techniques (ART) [30]. The visualisation, segmentation and quantification of the volumes were carried out using Amira 3D software (Thermo Fisher). Each voxel of the reconstructed tomogram represents the LAC (μ_l, in cm^{-1}) of the material contained in it, as it is related to the measured transmission signal I through the Beer-Lambert law (**Equation 2.2**):

$$\text{Voxel} = \mu_l = -\ln\left(\frac{I}{I_0}\right) = \int \mu_l\,(z)dz \qquad \textbf{Equation 2.2}$$

Where μ corresponds to the mass absorption coefficient of the cell structure ($cm^2\ g^{-1}$), I_0 to the incoming flux, and z to the thickness of the material.

2.2.9. Statistical Analysis

Data distribution was checked with Shapiro-Wilk test. Significant differences between samples were determined using non-parametric Kruskal-Wallis test followed by multiple pairwise comparisons. The significance level was set for $p<0.05$. Statistical analysis was performed using Minitab 19. All data are reported as mean ± standard error of the mean.

2.3. Results and Discussion

2.3.1. Characterisation of the Nanoparticles

Hydroxyapatite (HA) nanoparticles (NPs) were synthesised using a wet precipitation method, obtaining non-doped HA and magnesium-doped HA (MgHA) powders. **Figure 2.1A** shows the XRD results of the synthesised NPs. All peaks matched those corresponding to HA (ICDD PDF 09-0432) with no secondary crystalline phases detected, demonstrating the precipitation of phase pure HA. Moreover, the broad peaks indicated the poor crystallinity of the powders obtained. As expected, magnesium doping caused a slight shift of the (002) diffraction peak, which correlates with the lattice contraction caused by the incorporation of Mg into the HA structure substituting Ca ions, due to the smaller ionic radius of the Mg cation compared to Ca [31].

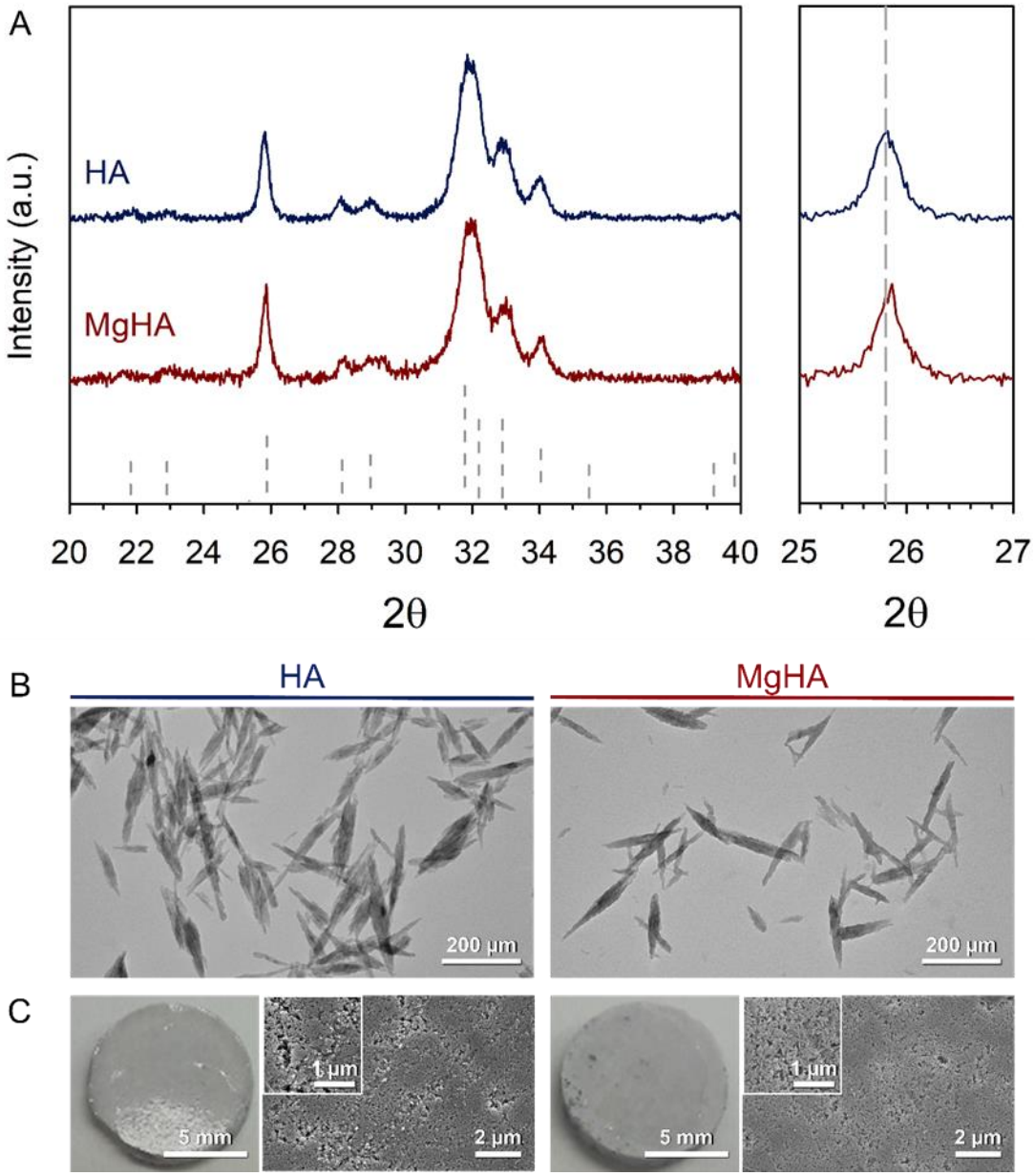

Figure 2.1. Physicochemical characterisation of the synthesised HA NPs. **A** X-ray diffraction for the non-doped (HA) and magnesium-doped (MgHA) NPs. **B** TEM micrographs for both types of nanoparticles. **C** Images of the discs made of compacted HA and MgHA NPs. Insets with higher magnification of the SEM pictures showing the nanoparticles of the discs.

No differences in the morphology of the two types of NPs were observed (**Figure 2.1B***)*, both consisting of needle-like crystals with sizes of around 150 nm in length and 20 nm in width. The discs obtained by NPs compaction showed a homogeneous surface microstructure, with specular faces (**Figure 2.1C**). A close-up view in the insets allowed to observed the individual nanoparticles in the discs by SEM. Immersion of the discs in the culture medium did not alter their surface and no particles were dislodged from the samples, indicating excellent compaction.

2.3.2. Functionalisation of the Nanoparticles

L-3,4-dihydroxyphenylalanine (DOPA) is a molecule that presents an excellent affinity for hydroxyapatite through the catechol groups [26,32]. Although the adsorption of DOPA to HA NPs has been explored to enhance the osteoconductive properties of scaffolds and to improve protein adhesion for drug delivery purposes [33,34], to the best of our knowledge this is the first time that it is used to fluorescently label HA NPs, by combining it with a fluorescent molecule such as carboxyfluorescein (CF).

The evaluation of the adsorption capacity of either CF or the DOPA-CF peptide on the nanoparticles was done by measuring the difference in the concentration of the staining solution before and after NPs incubation. The direct adsorption of CF on the NPs was almost non-existent, or binding was so weak that the fluorophore was lost during the subsequent rinsing steps (data not reported). **Figure 2.2A** illustrates the quantity of DOPA-CF peptide adsorbed on the surface of the NPs, for both non-doped (HA-F) and magnesium-doped (MgHA-F) after rinsing. It is observed that in the case of non-doped NPs, the adsorption of DOPA-CF was about half of the concentration added, whereas in the case of MgHA powders, this adsorption was slightly lower, around 40% of the initially added peptide. This reduction of adsorbed DOPA-CF was further confirmed by direct fluorescence intensity data, shown in **Figure 2.2B**, where the intensity of MgHA-F NPs was 80% with respect to the HA-F sample. This variation might be due to physicochemical differences between both types of nanoparticles. After functionalisation of the NPs, various rinsing steps with bi-distilled water were carried out to eliminate the non-adhered peptide and the fluorescence intensity of the supernatants was measured. It is worth mentioning that the intensity in the first rinse after vortexing of the fluorescently labelled NPs was about 5%, which explained the excellent binding between DOPA-CF and the NPs.

The zeta potential of the NPs measured in water is displayed in **Figure 2.2C**, revealing a slightly negative surface charge for the pristine nanoparticles. When functionalising the NPs with the fluorescent peptide, the surface charge decreased to -13 mV for both HA-F and MgHA-F, which confirmed the success in the functionalisation of the NPs.

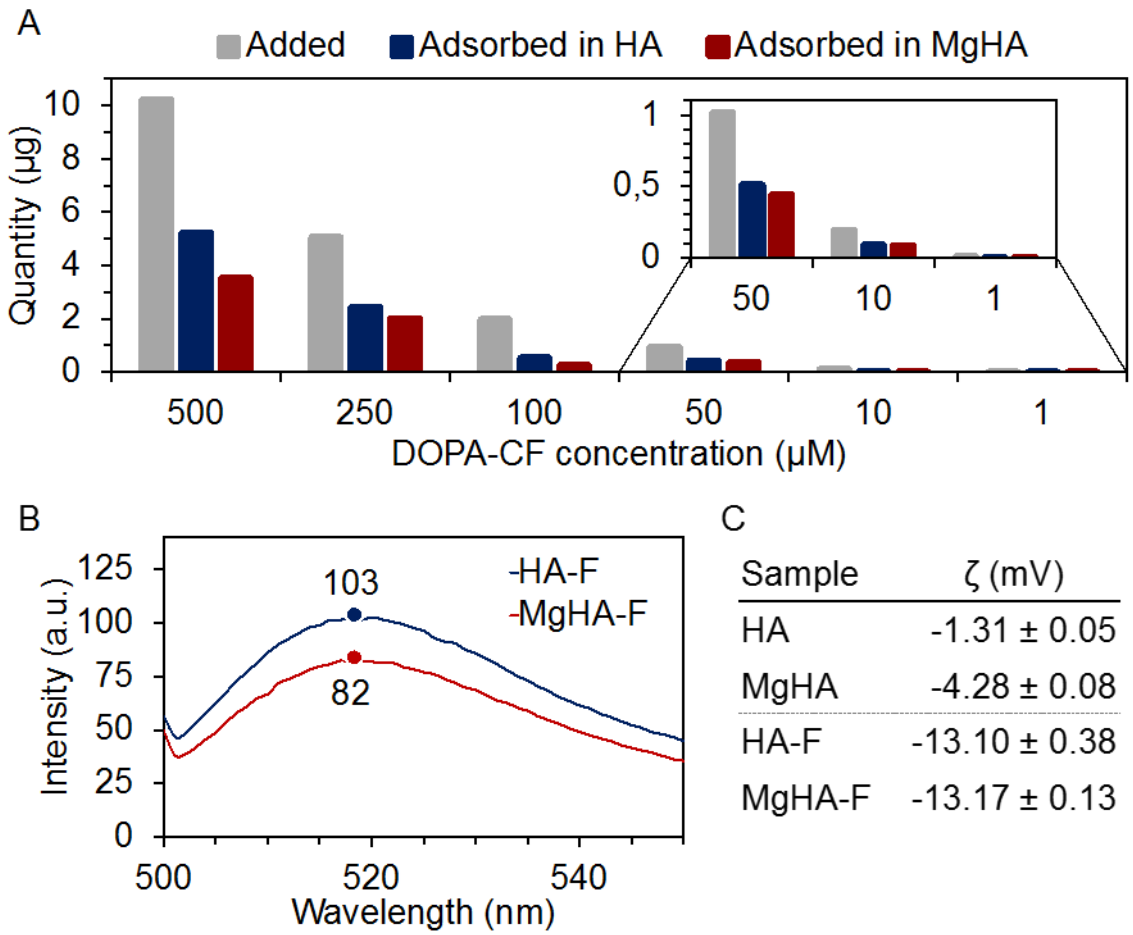

Figure 2.2. Characterisation of the fluorescently functionalised NPs. **A** Adsorption of DOPA-CF peptide to HA and MgHA NPs at different initial concentrations. **B** Direct fluorescence intensity of the HA-F and MgHA-F NPs. **C** Zeta potential of the different materials.

2.3.3. Study of the Nanoparticles – Cell Membrane Interaction

Any NPs internalisation process starts with the interaction of NPs on the cell membrane. Since the cell membrane is rich in receptors and some of them have a strong affinity for calcium, NPs could potentially induce changes in cells. From a fundamental point of view, it is essential to disclose if the cytotoxic effect of the HA NPs comes mainly from their interaction with the cell membrane or it is due to their internalisation inside the cells. Indeed, it has been reported that the toxicity of certain NPs (*e.g.* positively charged NPs) can derive from their reactivity when interfacing with the cellular membrane [35]. For this purpose, cell culture studies were done either by supplementing HA NPs on the cells or by seeding cells on NPs-compacted discs. In these homogeneous discs, uptake of the nanoparticles into the cells is prevented, and the interaction is limited to surface interaction with the cell membrane. In contrast, when the cells are exposed to the NPs suspended in the cell culture medium, both interactions are possible: not only the contact with the cell membrane but also their internalisation. In addition, the assay was done either with or without the supplementation of FBS in the cell culture medium to validate the direct interaction of the NPs with the cell membrane (FBS-) without the interference of adsorbed proteins, which are known to have a strong affinity for HA [36]. In general,

these adsorbed proteins block the interaction of cellular receptors with the nanomaterial surface [37] causing a reduction in the cytotoxic effect due to a lower cell uptake [38].

Figure 2.3A shows the morphology of the cells adhered to the samples imaged with acridine orange (AO) staining in the confocal microscope and by SEM. The well-spread morphology of the cells accounts for their viability when seeded on the discs – both in HA and MgHA –, similarly to the control condition (*i.e.* cells seeded on coverslips, without material), regardless of the removal of FBS. The cells on the discs of the serum-free samples presented minor differences in their morphology compared to the glass coverslip, exhibiting star-like shapes instead of elongated profiles, probably caused by the nature of the material. However, this difference was not relevant since the cells appeared perfectly attached to the discs' surfaces. The results of the samples with the NPs suspensions demonstrated that the cells supplemented with both types of NPs in serum-containing medium presented no cytotoxicity. In contrast, in the absence of FBS, cells in contact with the suspension of HA or MgHA mostly died after 4 h, as observed by the drastic drop in the cell population. **Figure 2.3B** quantifies these findings by WST-1. The data obtained are consistent with the images, as cell death of 70% for HA NPs suspension was revealed, whilst MgHA NPs presented a killing potential for 80% of the cells, with statistically significant differences between the two conditions. In contrast, although a slight decrease in cell number was observed in HA FBS+ and in both types of discs in the FBS- condition compared to the control, the differences were not statistically significant.

The higher cytotoxicity observed for MgHA NPs, although limited in the present work, aligns with other studies in the literature, where the authors reported that doping HA NPs with small amounts of magnesium was observed to improve cytotoxicity in MG-63, leaving mesenchymal stem cells alive [7]. The fact that here the effect was small could be related to differences in the aggregation state of the HA and MgHA NPs, as will be later discussed.

Regarding the differences observed in NPs suspension between FBS+ and FBS- conditions, several authors have demonstrated that the adsorption of proteins on the surface of HA NPs can strongly affect the adhesion properties to the cell membrane, reducing the uptake levels [37,38]. The reason for the reduced internalisation was explained by the electrostatic repulsion between the cell membrane and the negative charge that proteins confer to the HA NPs [7,39]. Overall, the results obtained suggest that the direct interaction of the cell surface with the material was not sufficient to cause cell death and it must be ruled out as the main mechanism of cytotoxicity, HA NPs internalisation being a requirement for cell toxicity.

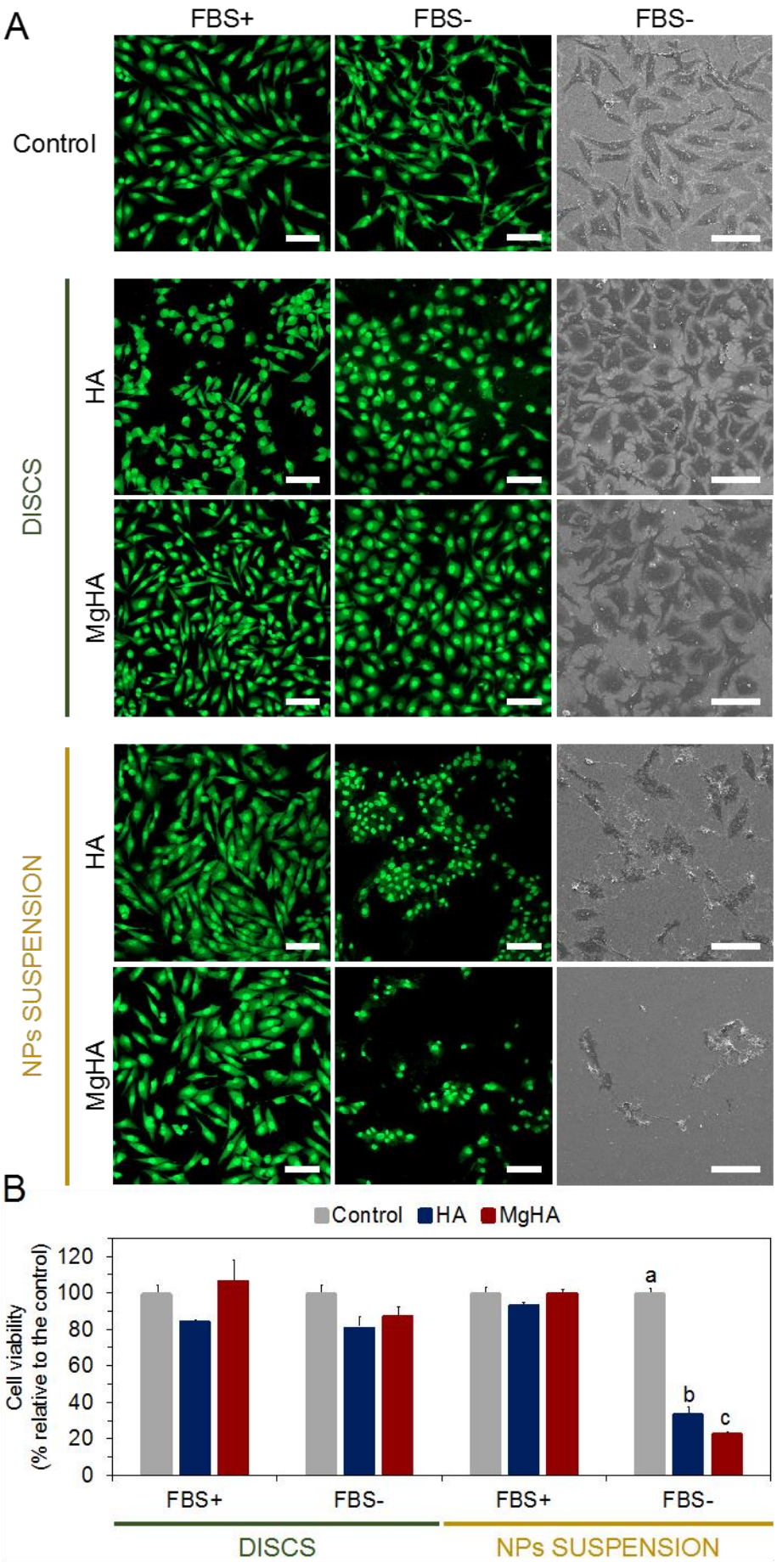
A
FBS+
FBS-
FBS-
Control
DISCS
HA
MgHA
NPs SUSPENSION
HA
MgHA
B
Control
HA
MgHA
Cell viability
(% relative to the control)
120
100
80
60
40
20
0
a
b
c
FBS+
FBS-
FBS+
FBS-
DISCS
NPs SUSPENSION

Figure 2.3. Cytotoxicity assay comparing NPs compacted into discs and free NPs in suspension after 4 h of interaction with MG-63 cells. **A** Confocal microscopy visualisation of AO staining (first two columns) and SEM images (third column). Scale bars denote 100 µm. **B** Cell viability quantified using WST-1 reagent. Different letters indicate statistically significant differences between samples.

2.3.4. Flow Cytometry Assay

Flow cytometry (FC) has become an indispensable technique in cellular studies with nanomaterials. This method is based on high-throughput single-cell analysis, offering data that allow understanding the traffic of NPs inside the cells [40]. In order to monitor the nanoparticles' interaction with cells, a FC assay was performed using fluorescently labelled NPs (*i.e.* HA-F, MgHA-F) to track them in the cells. The results of non-doped NPs (HA-F) and magnesium-doped NPs (MgHA-F) are displayed in **Figure 2.4A** and **B**, respectively. The threshold of the graphs was established from the analysis of negative controls (*i.e.* cells without the supplementation of fluorescent NPs). In addition, 10000 events (*i.e.* cells) were analysed for all conditions, except for FBS- samples after 24 h incubation, where less than 1000 events were evaluated due to cell death.

At a first glance, the results from FC and cytotoxicity seemed to correlate well for the serum-free conditions (FBS-), since the high cytotoxicity observed from WST-1 (**Figure 2.3**) paired with high percentages of cells associated with fluorescently labelled NPs, which is typically related to NPs internalisation. Indeed, 89.9% of the cells at 4 h and 81.4% at 6 h were fluorescently labelled with HA-F NPs in serum-free conditions. After 24 h the population of cells in the FC assay was too low, making the results less reliable. Although we did not use FC to evaluate cytotoxicity, the marked drop in the cell population at 24 h clearly differed from the WST-1 assay, where 80% of cell death was observed already at 4 h. We attribute this delay to the changes associated with the chemical binding of the DOPA-CF peptide on the surface of the NPs prior to the FC assay.

Analysing the behaviour of the HA-F NPs in serum-containing conditions (FBS+) it was observed a lower percentage of cells with labelled NPs at all the time points compared to the FBS- condition (**Figure 2.4A**). However, there was a rather high percentage of cells with labelled NPs already at 4 h (*i.e.* 68.4%) but no signs of cytotoxicity were detected by WST-1. This may indicate that the presence of serum proteins adsorbed on HA NPs modifies their uptake and degradation behaviour. However, one aspect that should not be overlooked to correctly interpret these results is that in all cell culture conditions except for MgHA NPs in FBS+, namely for HA-F FBS+/- and MgHA-F FBS-, the NPs tended to aggregate and sediment on top of the cells (**Figure 2.5**). Upon sedimentation, the NPs could not be easily detached, indicating adhesion to the cell surface membrane. These results revealed that the detection of fluorescently labelled NPs in the FC studies cannot be solely associated with internalisation. NPs can be present inside the cells (internalised), but they can also remain attached to the external cell membrane. Moreover, this may apply to FBS- and FBS+ conditions. Thus, by FC it is not possible to distinguish where the NPs are located, and additional complementary techniques would be required to answer this question.

The results for the MgHA-F NPs exhibited an interesting behaviour (**Figure 2.4B**). In serum-containing conditions (FBS+) a very low population of cells were stained by the NPs especially at 4 and 6 h, which aligned with the fact that in this condition NPs were well dispersed in the cell culture and NPs sedimentation did not occur. In serum-free

conditions, however, both NPs internalisation and NPs adhesion on the cell membrane simultaneously took place, which may complicate the interpretation of the results. However, it was clear that higher numbers of labelled cells were detected, especially at 6 h, which agreed with the high cytotoxicity observed by WST-1. The differences in terms of timing can be associated, as previously explained, with changes due to the fluorescent labelling of the NPs. As in the case of HA-F NPs, the reliability of the values at 24 h are compromised due to the low number of cells at that time point.

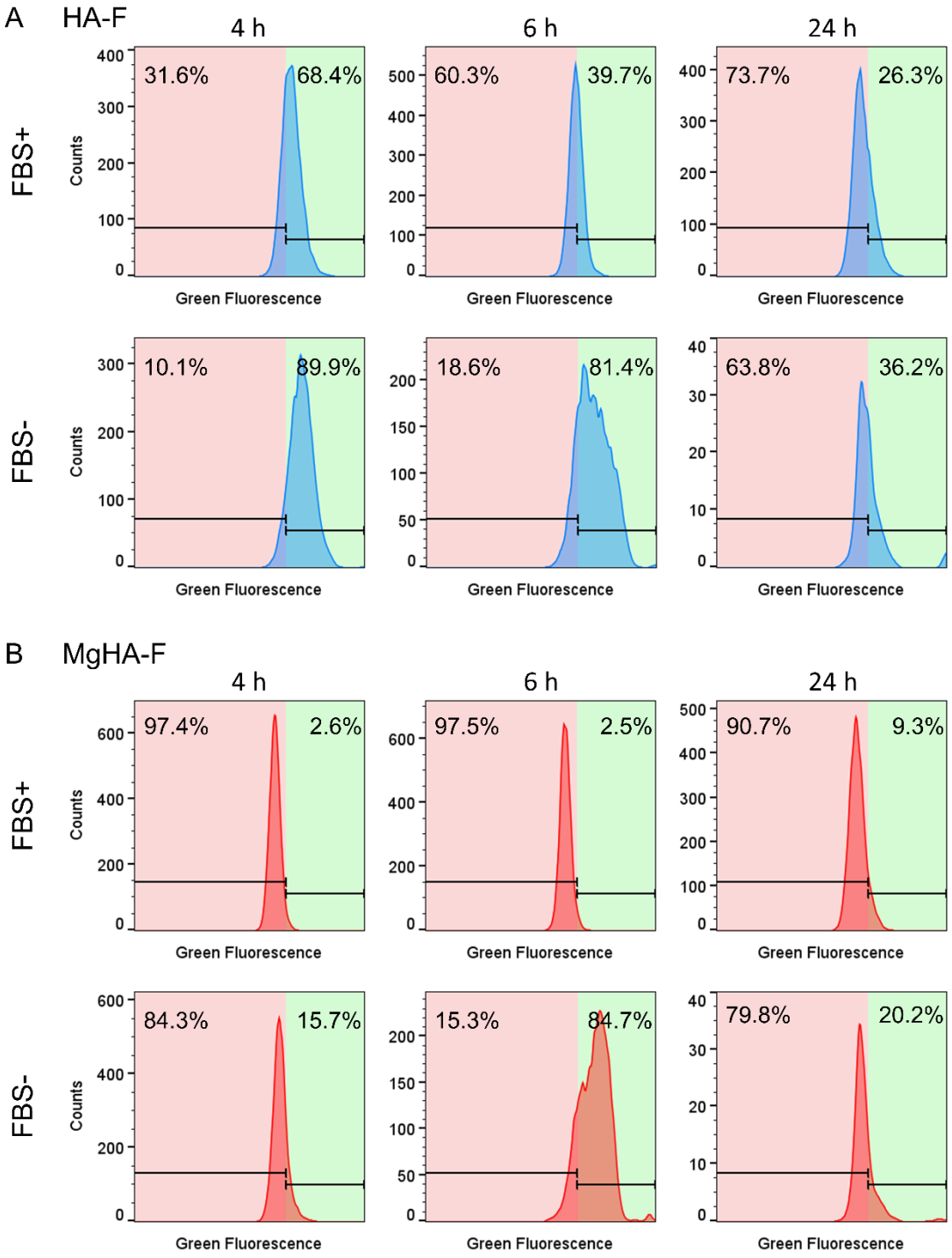

Figure 2.4. Flow cytometry results of cells exposed to HA-F (**A**) and MgHA-F (**B**) for 4, 6 and 24 h. Histograms showing cell counts negatives (left, red-shadowed area) and

positives (right, green-shadowed area) in green fluorescence. The threshold between positive and negative fluorescence was established from negative controls. In all cases, 10000 events were analysed, except for the 24 h FBS- samples, where less than 1000 events were evaluated due to cell death.

To further understand the different outcomes obtained for HA-F and MgHA-F in FBS+ and FBS- conditions, cells with fluorescent NPs were imaged in a confocal microscope after being fixed and stained. The results illustrated in **Figure 2.5** clearly proved the sedimentation of NPs in serum-free media for both types of NPs (the green NPs were observed on the outer surface of the cell membrane, which was stained in red). In addition, the same tendency although to a lesser extent was observed for HA-F NPs in the FBS+ condition. However, magnesium-doped nanoparticles presented a different behaviour, as they formed a stable colloidal suspension with the addition of FBS, avoiding their sedimentation on top of the cells. Although stability studies of the NPs in cell culture media were not performed, we consistently observed by optical microscopy the sedimentation of NPs on top of the cells in all conditions (FBS- and FBS+) except for MgHA in serum-containing samples. As already mentioned, these findings agree with the FC results of MgHA in FBS+, which barely showed any sign of fluorescent NPs. Interestingly, the comparison of both types of NPs puts also forward that doping HA NPs may result in substantial changes in their properties (*e.g.* colloidal stability), which can affect, in turn, their adsorption and uptake behaviour.

Overall, despite the robustness of the FC technique, it did not allow to differentiate internalised NPs from those attached to the surface of the cells. This calls for cautious analysis to avoid erroneous conclusions. Other authors have also highlighted the importance of differentiating membrane-bound NPs when using FC to quantify NPs internalisation and the danger when failing to do so [19].

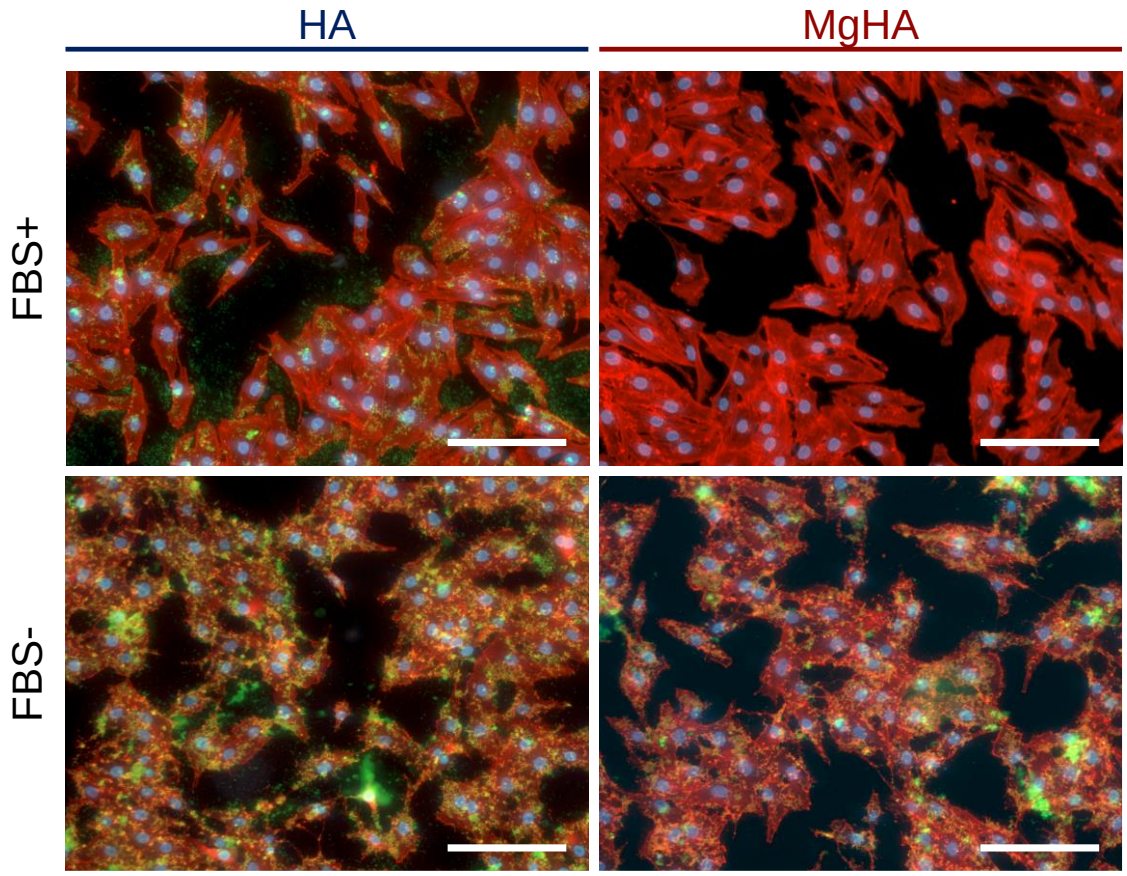

Figure 2.5. Fluorescence images of MG-63 cells supplemented with HA-F and MgHA-F NPs for 4 h both in FBS+ and FBS- conditions. Red staining indicates actin filaments, blue dots denote cell nuclei and green intensity marks fluorescent nanoparticles. Scale bars represent 200 µm.

Nonetheless, even being able to discriminate and quantify the real amount of NPs internalised, it would not be sufficient to predict their toxicity, as it has been previously demonstrated that the dissolution degree of the HA NPs is what eventually determines the toxicity. Therefore, the cytotoxicity does not only depend on the amount of NPs internalised but also on their crystallinity, specific surface area and composition, as well as on the cell type tested [41,42].

In light of this, the toxic effect of the HA NPs would be associated with the levels of calcium and phosphorus ions released in the cytosol after their dissolution: if the levels increase too much, it will induce cell death, whereas if the intracellular calcium levels remain low and sustained, cells will maintain their viability [14]. Therefore, a useful approach to predict cytotoxicity is to monitor intracellular calcium.

2.3.5. Intracellular Calcium Evaluation

As earlier mentioned, once the HA NPs enter in contact with the cellular membrane, the most common mechanism of internalisation is endocytosis, mostly by micropinocytosis [43]. Subsequently, the endosomes containing the NPs will fuse with lysosomes, which contain many acidic hydrolysing enzymes that decrease their pH to approximately 4.5.

The most accepted hypothesis to explain the cytotoxic effect of the HA NPs is that HA is dissolved in these organelles, causing a notorious increase of calcium and phosphorus ions. The local accumulation of these ions can cause an osmotic pressure imbalance which can induce disruption of the lysosomes unless ions are pumped out sufficiently rapid to the cytosol. The cytotoxicity of HA NPs will depend on the levels of Ca^{2+} and P_i ions reaching the cytoplasm of the cell, where they can trigger programmed cell death or even necrosis [16,17].

To check this hypothesis, intracellular calcium markers are fundamental to help to quantify changes in the Ca^{2+} levels. In the present work, Fluo-4 AM probe was used for quantification, together with the corresponding imaging of calcium ions. Additionally, a positive apoptosis control was employed to distinguish between the increase of Ca^{2+} produced as part of the programmed cell death mechanism and the contribution of released ions after the dissolution of the NPs. Indeed, calcium, as a secondary messenger molecule, is highly involved in the signalling pathway of apoptosis [44].

Figure 2.6A summarises the fluorescence intensity levels of Fluo-4 AM after 3 h of incubation with the NPs, relative to the controls. The intracellular Ca^{2+} levels of the samples FBS+ were similar for all the conditions, with slightly higher fluorescence in the case of HA NPs. On the contrary, the fluorescence intensity of the samples supplemented with HA and MgHA in serum-free media dramatically rose to 4 times the values of the controls (*i.e.* control without NPs and apoptosis control). The significant increase in the levels of intracellular Ca^{2+} may be attributed to the contribution of dissolved HA NPs inside the lysosomes, as hypothesised. Moreover, the values obtained for the samples with FBS confirm the difficulty of the cells to uptake NPs when they are coated with a protein corona.

Images illustrating the calcium distribution in MG-63 cells are presented in **Figure 2.6B**. Regardless of the addition of NPs, the cells exhibited a similar appearance in all FBS+ conditions, showing homogenous staining throughout the cytosol. Interestingly, the cells of the apoptosis control (**Figure 2.6B ii**) showed a singular morphology, exhibiting stressed fibres due to the nature of the sample (*i.e.* initial steps of the apoptotic process). In the serum-free condition, the control sample revealed homogeneous staining of cytosolic Ca^{2+}, similar to the serum-containing condition. In contrast, noticeable differences were observed for the other samples (*i.e.* HA, MgHA and apoptosis control, **Figure 2.6B vi-viii**), where Ca^{2+} was found concentrated in vesicles distributed all over the cytosol. Although several calcium-rich vesicles were observed in the control of apoptosis, the number of the vesicles was markedly higher for the nanoparticles-containing samples, indicating that the Ca^{2+} contribution mostly comes from the massive uptake of HA NPs. The presence of calcium-rich vesicles in the FBS- apoptosis sample may indicate the membrane break of important intracellular calcium stores and the subsequent Fluo-4 permeability to them, caused by the advanced stage of the cell death process.

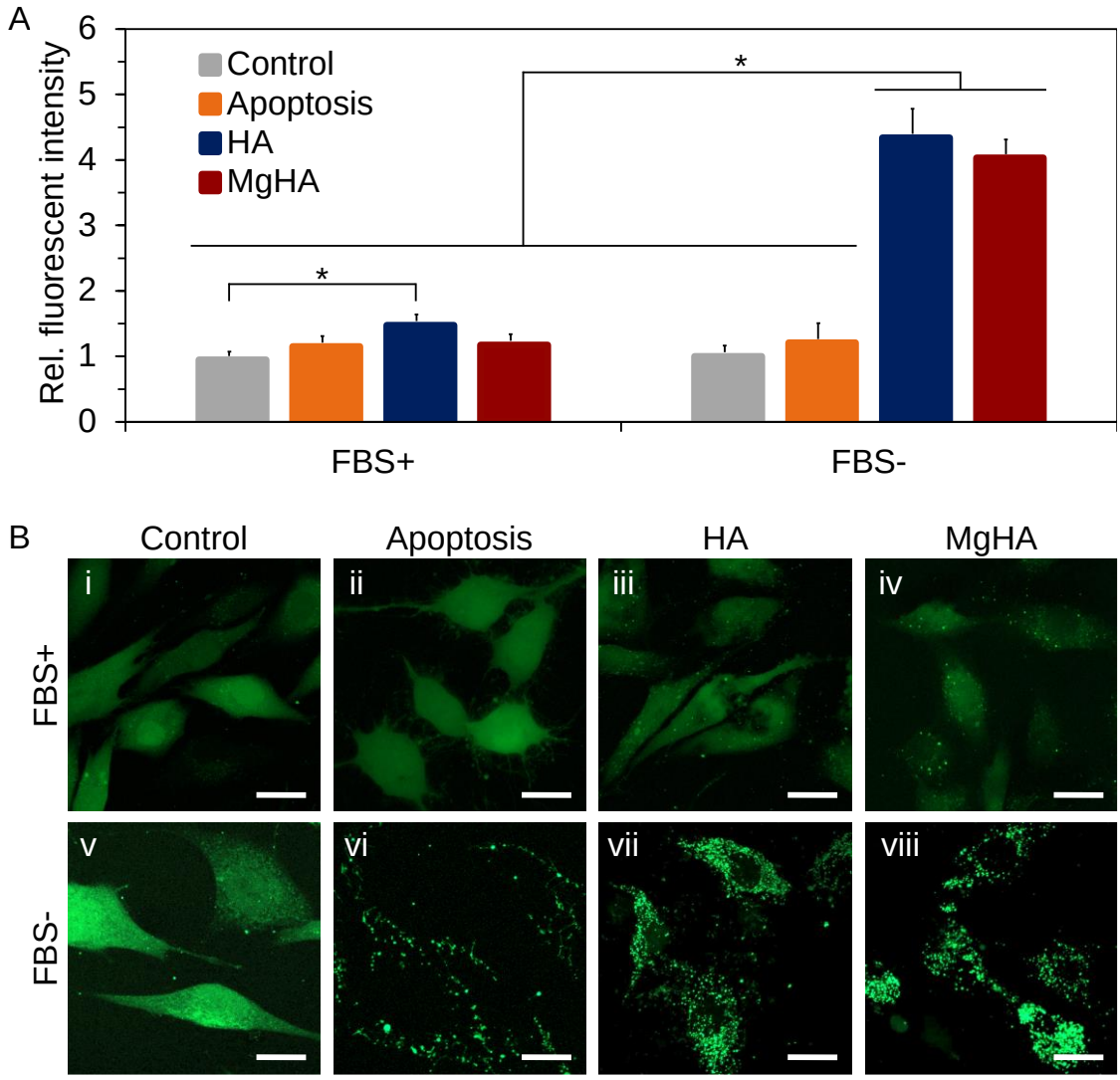

Figure 2.6. Intracellular calcium evaluation of cells exposed to the NPs for 3 h and stained with Fluo-4 AM. An apoptosis control was also studied. **A** Intracellular calcium quantified in a fluorescence microplate reader. **B** Intracellular calcium imaged by fluorescence confocal microscopy. Scale bars represent 20 µm. * indicates statistically significant differences.

Various calcium stores are present in the cell, which could explain the selective staining of vesicles in **Figure 2.6**. It is well established that the main intracellular calcium store is the endoplasmic reticulum (ER), together with the Golgi apparatus and mitochondria. However, there are other small-volume stores, such as acidocalcisomes, endosomes or lysosomes, dispersed throughout the cell that are considered as secondary Ca^{2+} stores [45,46]. Despite the classification in main and secondary Ca stores, the concentration of calcium can reach comparable values between the lysosome lumen and the lumen of the ER [47]. As previously mentioned, Fluo-4 in all the serum-containing samples, as well as in the control FBS- exhibited homogeneous staining of the cytosol, proving that the fluorophore was not able to enter the ER, Golgi apparatus or mitochondria, as expected. Thus, it seems feasible that the small green-stained vesicles ranging from 0.3 to 0.6 µm in size observed could be attributed to intracellular Ca^{2+} localised in individual vesicular stores (*e.g.* lysosomes, endosomes, etc.) enriched by the presence of dissolved HA NPs.

We expect these vesicles to have a compromised membrane to allow the entrance of the Fluo-4 molecule. It has to be noted that the fluorescence intensity for the serum-free samples loaded with NPs had to be decreased during the analysis to avoid the saturation of the vesicles. This adjustment reduced the overall fluorescence and masked the contribution of cytosolic calcium, which could be observed before this modification. Hence, the selective staining of calcium-rich vesicles does not exclude an increase in cytosolic Ca^{2+}, which would be responsible for the cytotoxicity. Unfortunately, the results reported by other authors on intracellular calcium determination does not discriminate between free cytosolic Ca^{2+} from Ca^{2+} retained in vesicles. This is for instance the case of the studies that rely on the quantification of fluorescence intensity by microplate reader or by FC [17,20].

The observation of such stained vesicles has been sometimes attributed to subcellular compartmentalisation [48]. Even though we demonstrate the absence of these highly fluorescent vesicles in the control samples and in all the serum-supplemented conditions, which clearly discarded this possibility, further analysis has to be done in order to confirm the presence and determine the composition of the vesicles.

2.3.6. Transmission Electron Microscopy and Cryo-Soft X-ray Tomography

Transmission electron microscopy (TEM) and cryo-soft X-ray tomography (cryo-SXT) were performed in selected specimens (*i.e.* serum-free samples) to check the uptake of NPs and to assess the distribution of calcium-rich vesicles inside the cells. TEM, as a high-resolution technique, with a resolution below 5 nm, is typically used to evaluate the internalisation of nanomaterials. In contrast, cryo-SXT is a novel technique that uses X-ray to image frozen pristine samples in the water window region (*i.e.* between the carbon K edge at 284 eV and the oxygen K edge at 543 eV) with a resolution of about 25 to 40 nm. Within this region, X-rays are absorbed an order of magnitude more strongly by carbon and nitrogen-containing organic material than by water, allowing direct visualisation of the cellular structures while water remains nearly transparent [49,50]. Thus, comparing both techniques, while TEM has the advantage of resolution, it requires major processing steps such as fixing, dehydration and slicing to observe the samples. All along these steps, electrolytes and low molecular weight organic compounds can potentially be washed out from the cells and any information concerning the presence of ionic soluble content will be missed [45]. In addition, artefacts can be easily introduced during sample processing. Instead, cryo-SXT has a lower resolution than TEM but enables mesoscale imaging of the whole cellular ultrastructure without any processing other than vitrification [51,52]. Thus, the possibility to image cells under near-native conditions is a strong asset of this technique. Moreover, cryo-SXT offers the possibility to quantify the results and distinguish cellular structures based on linear absorption coefficients, following the Beer-Lambert law [49,53].

With respect to the TEM results, illustrated in **Figure 2.7**, samples of cells supplemented with HA and MgHA NPs in serum-free conditions were examined, together with a control without NPs. The results not only confirmed the uptake of nanoparticles in both supplemented samples, but they also denoted the absence of electrodense vesicles comparable in size to the ones observed by confocal fluorescence microscopy. Instead, other vesicles (either empty or with residual content) were seen, which was consistent with the idea that electrolytes such as Ca^{2+} and P_i were lost during sample processing.

However, it was impossible to know the original composition of these organelles using this technique.

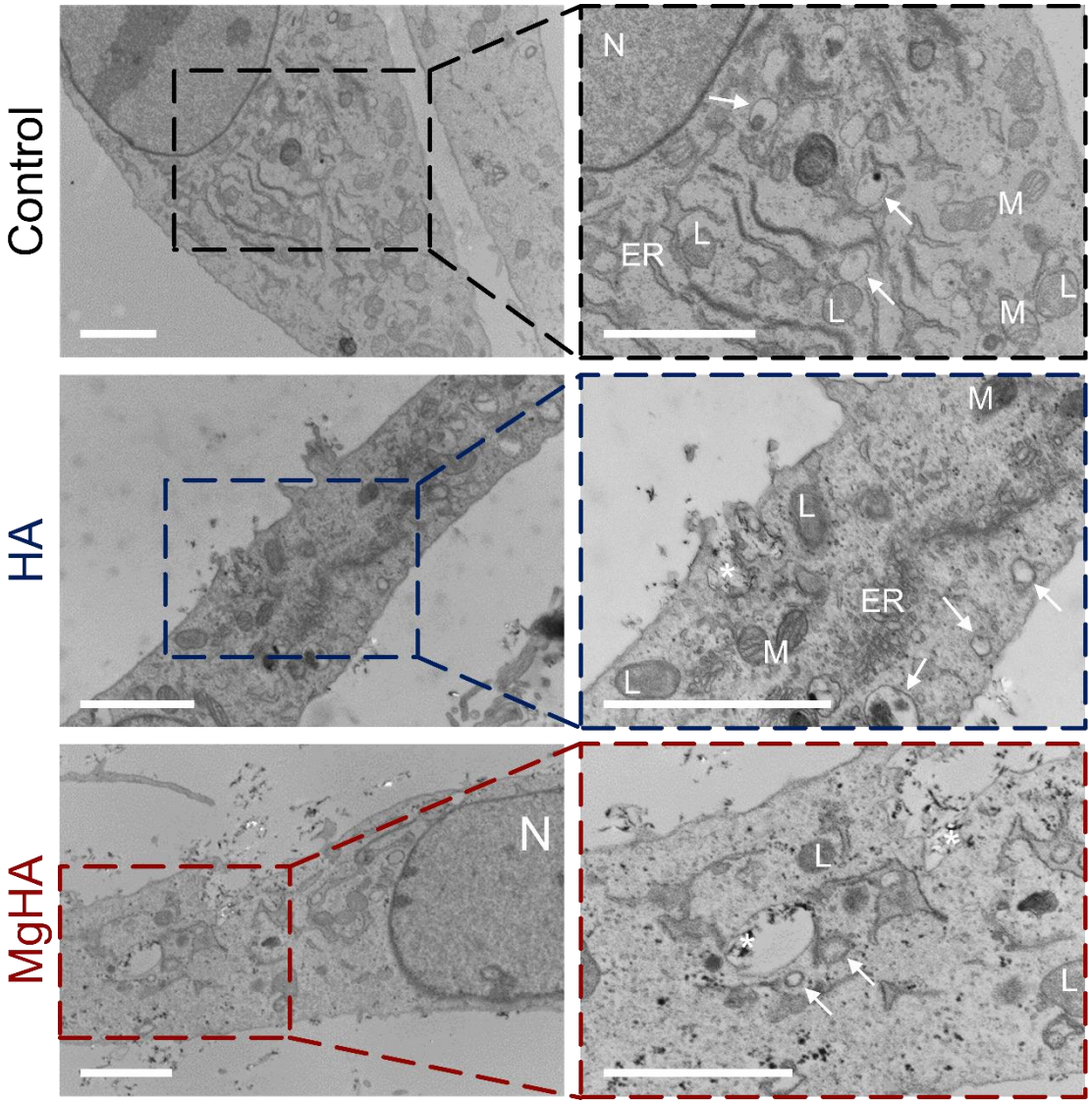

Figure 2.7. TEM images of cells without the addition of nanomaterials (control) and after the supplementation of HA and MgHA NPs in serum-free conditions. * indicates NPs. ER, L and M stand for endoplasmic reticulum, lysosomes and mitochondria, respectively. White arrows point vesicles (either empty or with residual content). Scale bars denote 2 µm.

In contrast, cryo-SXT revealed interesting differences compared to TEM. **Figure 2.8** shows the X-ray projection images that provide an overview of the cell of interest (**i** and **iv**), together with relevant tomographic sections taken from the tilt series (**ii** and **v**) and their segmentation (**iii** and **vi**). Videos of the whole aligned tilt series can be found in the Supplementary Information. In the selected sections, small highly absorbing vesicles of around 0.3 to 0.6 µm and reaching up to 1 µm were readily visible. Similar-looking vesicles have been ascribed by other authors as lipid droplets (LDs), due to their small size and their high carbon content that highly absorbs at 520 eV [54]. However, LDs are usually described as fully dense dark vesicles by cryo-SXT or, in some cases, as vesicles containing one lighter vesicle within [49]. Furthermore, three different components of the

endocytic pathway can be distinguished. First, early endosomes that can be considered as sorting vesicles and are agreed to appear as membrane-bound organelles with a relatively uniform interior by cryo-SXT. Multivesicular bodies (MVBs), formed from early endosomes by the invagination of the membrane into their own lumen, which, imaged by cryo-SXT, should clearly contain one or more internal lighter vesicles. And lysosomes, the last organelle of the endocytic pathway that break down biomolecules into simple compounds thanks to many hydrolytic enzymes, and typically show an electrodense lumen with internal granular structures [49,54,55]. In this regard, **Figure 2.8 v** shows that most electrodense vesicles contained more than 2 low-absorbing vesicles, which suggested the presence of endocytic vesicles rather than LDs and, more specifically, of MVBs. Actually, MVBs are organelles formed by the maturation of early endosomes. They are also known as late endosomes and are always identified in the degradation pathway of any endocytic process [56]. In the case of **Figure 2.8 ii**, a lower density of MVB vesicles was observed along with larger grainy structures compatible with lysosomes or endolysosomes, as well as a large vesicle containing pristine HA NPs. In general, the large number of the darker MVBs would match with the green-stained vesicles observed by fluorescence confocal microscopy (**Figure 2.6B).** However, distinguishing LDs from MVBs is not so straightforward.

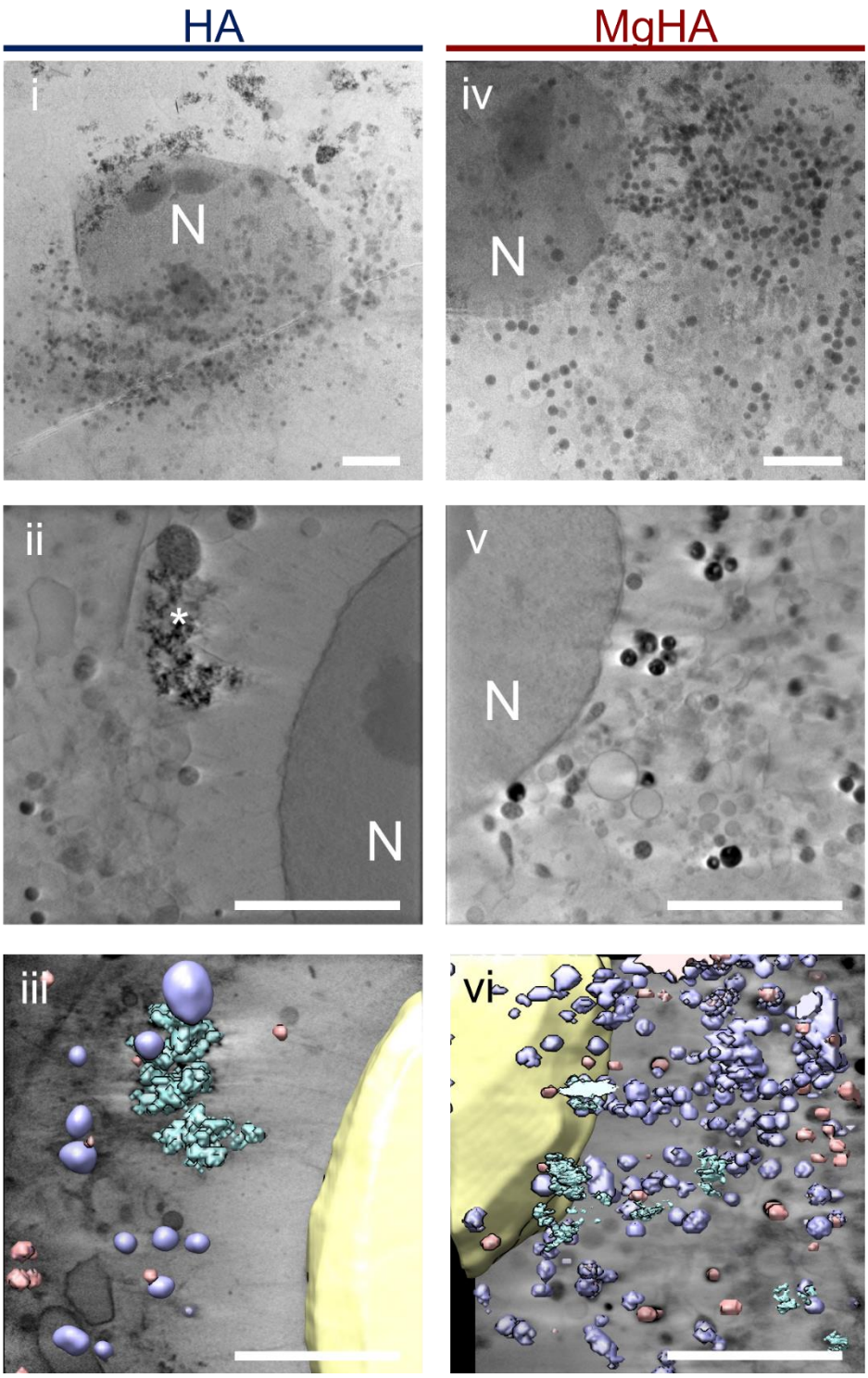

Figure 2.8. Cryo-SXT of cells after 3 h of exposure to HA and MgHA NPs. **i** and **iv** showing mosaic projections, **ii** and **v** display relevant tomographic sections, and **iii** and **vi** reveal the segmentation of the same stacked tomograms. N denotes nuclei and * stands for internalised NPs. Nuclei are segmented in yellow, lipid droplets in pink, nanoparticles in blue and multivesicular bodies in purple. Scale bar represents 5 µm.

Apart from discrimination of the different organelles by visual inspection, cryo-SXT allows quantitative determination of the linear absorption coefficient (LAC) for each

cellular component [50,57]. Therefore, in order to better elucidate the nature of these small vesicles, the selected tilt series were segmented and their LACs quantified (**Table 2.2**). Nuclei (segmented in yellow) resulted in a LAC of 0.29 ± 0.02 μm^3, while internalised NPs presented a high LAC value of 1.94 ± 0.02 μm^3. In addition, two different vesicles were identified: LDs with a LAC of 1.42 ± 0.03 μm^3, and MVBs with a LAC value of 1.09 ± 0.05 μm^3. It is worth noting that the standard deviation obtained for these values is very low, this indicates the high similarity of LACs between both sample conditions. The differences in LAC values between LD and MVB proved compositional differences between both types of vesicles. Thus, based on LAC values we could unambiguously map MVBs and LDs from the analysed cells (**Figure 2.8 iii** and **vi**). It is known that LD is typically the structure with the highest LAC value due to its increased carbon content compared to the other organelles, which agrees with the results obtained (LAC of LDs was 1.42 μm^3 vs. LAC of nuclei 0.29 μm^3). The fact that cells with internalised NPs contained MVBs with LAC values close to the LDs ones, implies that these vesicles should contain highly absorbing elements. In combination with the very high LAC value of the solid NPs, it indicates that the electrodense vesicles may contain degraded NPs. Accordingly, these results suggest that the Ca^{2+}-rich vesicles identified by confocal microscopy, should not be considered as artefacts and they likely correspond to MVBs.

Table 2.2. Linear absorption coefficient (LAC) of the different cellular components

	Nucleus (μm^3)	**Nanoparticles (μm^3)**	**Lipid Droplets (μm^3)**	**Multivesicular Bodies (μm^3)**
	Yellow	Blue	Pink	Purple
HA	0.29 ± 0.02	1.94 ± 0.02	1.42 ± 0.03	1.11 ± 0.03
MgHA				1.07 ± 0.04

Moreover, although both samples had Ca-rich vesicles with similar LACs (*i.e.* 1.11 ± 0.03 μm^3 and 1.07 ± 0.04 μm^3 for HA and MgHA, respectively), the segmentation revealed different size and distribution of these vesicles. Specifically, HA presented a lower amount of vesicles but of larger dimensions, whilst the vesicles in MgHA were smaller but present in higher amounts. Analysis of the tomograms obtained for the cell exposed to HA NPs showed the capture of a less advanced degradation state of the NPs, which together with the tomogram of the cell exposed to MgHA allows seeing the evolution of the degradation of these materials.

An additional aspect to explore in the future from cryo-SXT is cryospectroscopic imaging by changing the imaging energy from 520 eV. In a recent work by Gal *et al.* the authors set the energy to 353 eV, which is the absorbing energy for Ca, to investigate the distribution of calcium-containing organelles in calcifying and non-calcifying species in algae [58]. A very distinct Ca^{2+} map was shown, proving to be a powerful tool to trace calcium stores in pristine conditions. This technique applied to our samples would allow gaining further insights into the quantification and distribution of intracellular calcium.

The study of intracellular calcium is of major relevance when trying to elucidate the fate of internalised NPs, as changes in the cytosolic calcium of the cells help to understand

the cytotoxicity caused by HA NPs. Through the combination of different techniques, both conventional and advanced, we have been able to detect the presence of multiple MVB which potentially carry degraded NPs. However, discrimination of these Ca-rich stores from cytosolic calcium would be needed to better assess toxicity. We have demonstrated the limitations of various techniques in this regard, but also the great potential of intracellular calcium probes combined with cryo-SXT.

2.4. Conclusions

The main goal of this work was to understand and to prove the cytotoxic mechanism of hydroxyapatite NPs using the common techniques in the field together with cryo-SXT imaging at the ALBA synchrotron. The studies revealed the internalisation of the HA NPs as the main toxicity mechanism, with minor contribution coming from the material interaction with the outer cell surface. It was noticed that the results from FC when applied to investigate the uptake of NPs need to be carefully analysed, as the contribution of the HA NPs attached to the cell membrane can induce wrong conclusions. The use of intracellular calcium probes revealed increased levels in the calcium content of the samples supplemented with NPs. The major contribution to the intracellular calcium was from the staining of a high number of small calcium-rich vesicles. The results from cryo-SXT proved that these vesicles were MVBs and not a staining artefact. Despite the high resolution of TEM, dehydration of the sample impeded the study of these vesicles due to their liquid content. Overall, the combination of calcium-fluorescent probes together with cryo-SXT provided the best tools to investigate intracellular calcium of cells with internalised HA NPs.

2.5. References

[1] T.N. Tram Do, W.-H. Lee, C.-Y. Loo, A. V Zavgorodniy, R. Rohanizadeh, Hydroxyapatite nanoparticles as vectors for gene delivery, Ther. Deliv. 3 (2012) 623–632. https://doi.org/10.4155/tde.12.39.

[2] Z.-S. Liu, S.-L. Tang, Z.-L. Ai, Effects of hydroxyapatite nanoparticles on proliferation and apoptosis of human hepatoma BEL-7402 cells., World J. Gastroenterol. 9 (2003) 1968–71. https://doi.org/10.3748/wjg.v9.i9.1968.

[3] J. Hu, Z.-S. Liu, S.-L. Tang, Y.-M. He, Effect of hydroxyapatite nanoparticles on the growth and p53/c-Myc protein expression of implanted hepatic VX 2 tumor in rabbits by intravenous injection, World J. Gastroenterol. 13 (2007) 2798–2082. https://doi.org/10.3748/wjg.v13.i20.2798.

[4] S.-H. Chu, D.-F. Feng, Y.-B. Ma, Z.-Q. Li, Hydroxyapatite nanoparticles inhibit the growth of human glioma cells in vitro and in vivo, Int. J. Nanomedicine. 7 (2012) 3659–3666. https://doi.org/10.2147/IJN.S33584.

[5] F. Qing, Z. Wang, Y. Hong, M. Liu, B. Guo, H. Luo, X. Zhang, Selective effects of hydroxyapatite nanoparticles on osteosarcoma cells and osteoblasts, J. Mater. Sci. Mater. Med. 23 (2012) 2245–2251. https://doi.org/10.1007/s10856-012-4703-6.

[6] S. Dey, M. Das, V.K. Balla, Effect of hydroxyapatite particle size, morphology and crystallinity on proliferation of colon cancer HCT116 cells, Mater. Sci. Eng.

C. 39 (2014) 336–339. https://doi.org/10.1016/j.msec.2014.03.022.

[7] Z. Zhao, M. Espanol, J. Guillem-Marti, D. Kempf, A. Diez-Escudero, M.-P. Ginebra, Ion-doping as a strategy to modulate hydroxyapatite nanoparticle internalization, Nanoscale. 8 (2015) 1595–1607. https://doi.org/10.1039/C5NR05262A.

[8] A. Guilbert, M. Gautier, I. Dhennin-Duthille, N. Haren, H. Sevestre, H. Ouadid-Ahidouch, Evidence that TRPM7 is required for breast cancer cell proliferation, Am. J. Physiol. Cell Physiol. 297 (2009) C493–C502. https://doi.org/10.1152/ajpcell.00624.2008.

[9] I. Dhennin-Duthille, M. Gautier, M. Faouzi, A. Guilbert, M. Brevet, D. Vaudry, A. Ahidouch, H. Sevestre, H. Ouadid-Ahidouch, High Expression of Transient Receptor Potential Channels in Human Breast Cancer Epithelial Cells and Tissues: Correlation with Pathological Parameters, Cell. Physiol. Biochem. 28 (2011) 813–822. https://doi.org/10.1159/000335795.

[10] P. Rybarczyk, M. Gautier, F. Hague, I. Dhennin-Duthille, D. Chatelain, J. Kerr-Conte, F. Pattou, J.-M. Regimbeau, H. Sevestre, H. Ouadid-Ahidouch, Transient receptor potential melastatin-related 7 channel is overexpressed in human pancreatic ductal adenocarcinomas and regulates human pancreatic cancer cell migration, Int. J. Cancer. 131 (2012) E851–E861. https://doi.org/10.1002/ijc.27487.

[11] E. Abed, R. Moreau, Importance of melastatin-like transient receptor potential 7 and cations (magnesium, calcium) in human osteoblast-like cell proliferation, Cell Prolif. 40 (2007) 849–865. https://doi.org/10.1111/j.1365-2184.2007.00476.x.

[12] L.Y. He, X.M. Zhang, B. Liu, Y. Tian, W.H. Ma, Effect of magnesium ion on human osteoblast activity, Brazilian J. Med. Biol. Res. 49 (2016) 1–6. https://doi.org/10.1590/1414-431X20165257.

[13] M. Motskin, D.M. Wright, K. Muller, N. Kyle, T.G. Gard, A.E. Porter, J.N. Skepper, Hydroxyapatite nano and microparticles: Correlation of particle properties with cytotoxicity and biostability, Biomaterials. 30 (2009) 3307–3317. https://doi.org/10.1016/j.biomaterials.2009.02.044.

[14] S. Neumann, A. Kovtun, I.D. Dietzel, M. Epple, R. Heumann, The use of size-defined DNA-functionalized calcium phosphate nanoparticles to minimise intracellular calcium disturbance during transfection, Biomaterials. 30 (2009) 6794–6802. https://doi.org/10.1016/j.biomaterials.2009.08.043.

[15] Y. Wang, J. Wang, H. Hao, M. Cai, S. Wang, J. Ma, Y. Li, C. Mao, S. Zhang, In Vitro and in Vivo Mechanism of Bone Tumor Inhibition by Selenium-Doped Bone Mineral Nanoparticles, ACS Nano. 10 (2016) 9927–9937. https://doi.org/10.1021/acsnano.6b03835.

[16] Z. Liu, Y. Xiao, W. Chen, Y. Wang, B. Wang, G. Wang, X. Xu, R. Tang, Calcium phosphate nanoparticles primarily induce cell necrosis through lysosomal rupture: the origination of material cytotoxicity, J. Mater. Chem. B. 2 (2014) 3480. https://doi.org/10.1039/c4tb00056k.

[17] L.-H. Huang, X.-Y. Sun, J.-M. Ouyang, Shape-dependent toxicity and

mineralization of hydroxyapatite nanoparticles in A7R5 aortic smooth muscle cells, Sci. Rep. 9 (2019) 18979. https://doi.org/10.1038/s41598-019-55428-9.

[18] E.C. Cho, J. Xie, P.A. Wurm, Y. Xia, Understanding the Role of Surface Charges in Cellular Adsorption versus Internalization by Selectively Removing Gold Nanoparticles on the Cell Surface with a I2/KI Etchant, Nano Lett. 9 (2009) 1080–1084. https://doi.org/10.1021/nl803487r.

[19] G.B. Braun, T. Friman, H.-B. Pang, A. Pallaoro, T.H. de Mendoza, A.-M.A. Willmore, V.R. Kotamraju, A.P. Mann, Z.-G. She, K.N. Sugahara, N.O. Reich, T. Teesalu, E. Ruoslahti, Etchable plasmonic nanoparticle probes to image and quantify cellular internalization, Nat. Mater. 13 (2014) 904–911. https://doi.org/10.1038/nmat3982.

[20] W. Tang, Y. Yuan, C. Liu, Y. Wu, X. Lu, J. Qian, Differential cytotoxicity and particle action of hydroxyapatite nanoparticles in human cancer cells, Nanomedicine. 9 (2014) 397–412. https://doi.org/10.2217/nnm.12.217.

[21] M. Šupová, T. Suchý, Z. Sucharda, E. Filová, J.N.L.M. Kinderen, M. Steinerová, L. Bačáková, G.S. Martynková, The comprehensive in vitro evaluation of eight different calcium phosphates: Significant parameters for cell behavior, J. Am. Ceram. Soc. 102 (2019) 2882–2904. https://doi.org/10.1111/jace.16110.

[22] M. Epple, Review of potential health risks associated with nanoscopic calcium phosphate, Acta Biomater. 77 (2018) 1–14. https://doi.org/10.1016/j.actbio.2018.07.036.

[23] J. Gustavsson, M.-P. Ginebra, J.A. Planell, E. Engel, Osteoblast-like cellular response to dynamic changes in the ionic extracellular environment produced by calcium-deficient hydroxyapatite, J. Mater. Sci. Mater. Med. 23 (2012) 2509–2520. https://doi.org/10.1007/s10856-012-4705-4.

[24] J.-M. Sadowska, J. Guillem-Marti, E.B. Montufar, M. Espanol, M.-P. Ginebra, Biomimetic Versus Sintered Calcium Phosphates: The In Vitro Behavior of Osteoblasts and Mesenchymal Stem Cells, Tissue Eng. Part A. 23 (2017) 1297–1309. https://doi.org/10.1089/ten.tea.2016.0406.

[25] J.M. Sadowska, J. Guillem-Marti, M. Espanol, C. Stähli, N. Döbelin, M.-P. Ginebra, In vitro response of mesenchymal stem cells to biomimetic hydroxyapatite substrates: A new strategy to assess the effect of ion exchange, Acta Biomater. 76 (2018) 319–332. https://doi.org/10.1016/j.actbio.2018.06.025.

[26] P. Kord Forooshani, B.P. Lee, Recent approaches in designing bioadhesive materials inspired by mussel adhesive protein, J. Polym. Sci. Part A Polym. Chem. 55 (2017) 9–33. https://doi.org/10.1002/pola.28368.

[27] L. Oliver-Cervelló, H. Martin-Gómez, L. Reyes, F. Noureddine, E. Ada Cavalcanti-Adam, M. Ginebra, C. Mas-Moruno, An Engineered Biomimetic Peptide Regulates Cell Behavior by Synergistic Integrin and Growth Factor Signaling, Adv. Healthc. Mater. 10 (2021) 2001757. https://doi.org/10.1002/adhm.202001757.

[28] J. Otón, E. Pereiro, A.J. Pérez-Berná, L. Millach, C.O.S. Sorzano, R. Marabini, J.M. Carazo, Characterization of transfer function, resolution and depth of field of a soft X-ray microscope applied to tomography enhancement by Wiener

deconvolution, Biomed. Opt. Express. 7 (2016) 5092. https://doi.org/10.1364/BOE.7.005092.

[29] J.R. Kremer, D.N. Mastronarde, J.R. McIntosh, Computer Visualization of Three-Dimensional Image Data Using IMOD, J. Struct. Biol. 116 (1996) 71–76. https://doi.org/10.1006/jsbi.1996.0013.

[30] R. Gordon, R. Bender, G.T. Herman, Algebraic Reconstruction Techniques (ART) for three-dimensional electron microscopy and X-ray photography, J. Theor. Biol. 29 (1970) 471–481. https://doi.org/10.1016/0022-5193(70)90109-8.

[31] S. Diallo-Garcia, D. Laurencin, J.-M. Krafft, S. Casale, M.E. Smith, H. Lauron-Pernot, G. Costentin, Influence of Magnesium Substitution on the Basic Properties of Hydroxyapatites, J. Phys. Chem. C. 115 (2011) 24317–24327. https://doi.org/10.1021/jp209316k.

[32] W.M. Chirdon, W.J. O'Brien, R.E. Robertson, Adsorption of catechol and comparative solutes on hydroxyapatite, J. Biomed. Mater. Res. 66B (2003) 532–538. https://doi.org/10.1002/jbm.b.10041.

[33] H.S. Yang, J. Park, W.G. La, H.-K. Jang, M. Lee, B.-S. Kim, 3,4-Dihydroxyphenylalanine-Assisted Hydroxyapatite Nanoparticle Coating on Polymer Scaffolds for Efficient Osteoconduction, Tissue Eng. Part C. 18 (2012) 245–251. https://doi.org/10.1089/ten.tec.2011.0373.

[34] V. Ozhukil Kollath, S. Mullens, J. Luyten, K. Traina, R. Cloots, Effect of DOPA and dopamine coupling on protein loading of hydroxyapatite, Mater. Technol. 31 (2016) 241–245. https://doi.org/10.1179/1753555715Y.0000000048.

[35] C. Corbo, R. Molinaro, A. Parodi, N.E. Toledano Furman, F. Salvatore, E. Tasciotti, The impact of nanoparticle protein corona on cytotoxicity, immunotoxicity and target drug delivery, Nanomedicine. 11 (2016) 81–100. https://doi.org/10.2217/nnm.15.188.

[36] T. Kawasaki, Hydroxyapatite as a liquid chromatographic packing, J. Chromatogr. A. 544 (1991) 147–184. https://doi.org/10.1016/S0021-9673(01)83984-4.

[37] C.D. Walkey, W.C.W. Chan, Understanding and controlling the interaction of nanomaterials with proteins in a physiological environment, Chem. Soc. Rev. 41 (2012) 2780–2799. https://doi.org/10.1039/C1CS15233E.

[38] A. Lesniak, A. Salvati, M.J. Santos-Martinez, M.W. Radomski, K.A. Dawson, C. Åberg, Nanoparticle Adhesion to the Cell Membrane and Its Effect on Nanoparticle Uptake Efficiency, J. Am. Chem. Soc. 135 (2013) 1438–1444. https://doi.org/10.1021/ja309812z.

[39] L. Chen, J.M. Mccrate, J.C.-M. Lee, H. Li, The role of surface charge on the uptake and biocompatibility of hydroxyapatite nanoparticles with osteoblast cells, Nanotechnology. 22 (2011) 105708. https://doi.org/10.1088/0957-4484/22/10/105708.

[40] S. Behzadi, V. Serpooshan, W. Tao, M.A. Hamaly, M.Y. Alkawareek, E.C. Dreaden, D. Brown, A.M. Alkilany, O.C. Farokhzad, M. Mahmoudi, Cellular uptake of nanoparticles: journey inside the cell, Chem. Soc. Rev. 46 (2017)

4218–4244. https://doi.org/10.1039/C6CS00636A.

[41] T.T. Morgan, H.S. Muddana, E.İ. Altinoğlu, S.M. Rouse, A. Tabaković, T. Tabouillot, T.J. Russin, S.S. Shanmugavelandy, P.J. Butler, P.C. Eklund, J.K. Yun, M. Kester, J.H. Adair, Encapsulation of Organic Molecules in Calcium Phosphate Nanocomposite Particles for Intracellular Imaging and Drug Delivery, Nano Lett. 8 (2008) 4108–4115. https://doi.org/10.1021/nl8019888.

[42] M. Kopp, O. Rotan, C. Papadopoulos, N. Schulze, H. Meyer, M. Epple, Delivery of the autofluorescent protein R-phycoerythrin by calcium phosphate nanoparticles into four different eukaryotic cell lines (HeLa, HEK293T, MG-63, MC3T3): Highly efficient, but leading to endolysosomal proteolysis in HeLa and MC3T3 cells., PLoS One. 12 (2017) e0178260. https://doi.org/10.1371/journal.pone.0178260.

[43] V. Sokolova, D. Kozlova, T. Knuschke, J. Buer, A.M. Westendorf, M. Epple, Mechanism of the uptake of cationic and anionic calcium phosphate nanoparticles by cells, Acta Biomater. 9 (2013) 7527–7535. https://doi.org/10.1016/j.actbio.2013.02.034.

[44] J. Guo, Y. Lao, D.C. Chang, Calcium and Apoptosis, in: Handb. Neurochem. Mol. Neurobiol., Springer US, Boston, MA, 2009: pp. 597–622. https://doi.org/10.1007/978-0-387-30370-3_33.

[45] S. Patel, R. Docampo, Acidic calcium stores open for business: expanding the potential for intracellular Ca2+ signaling, Trends Cell Biol. 20 (2010) 277–286. https://doi.org/10.1016/j.tcb.2010.02.003.

[46] J. Yang, Z. Zhao, M. Gu, X. Feng, H. Xu, Release and uptake mechanisms of vesicular Ca2+ stores, Protein Cell. 10 (2019) 8–19. https://doi.org/10.1007/s13238-018-0523-x.

[47] K.A. Christensen, J.T. Myers, J.A. Swanson, pH-dependent regulation of lysosomal calcium in macrophages, J. Cell Sci. 115 (2002) 599–607. http://www.pnas.org/cgi/doi/10.1073/pnas.89.21.10079.

[48] D. Thomas, S.C. Tovey, T.J. Collins, M.D. Bootman, M.J. Berridge, P. Lipp, A comparison of fluorescent Ca2+indicator properties and their use in measuring elementary and global Ca2+signals, Cell Calcium. 28 (2000) 213–223. https://doi.org/10.1054/ceca.2000.0152.

[49] J. Groen, J.J. Conesa, R. Valcárcel, E. Pereiro, The cellular landscape by cryo soft X-ray tomography, Biophys. Rev. 11 (2019) 611–619. https://doi.org/10.1007/s12551-019-00567-6.

[50] J. Guo, C.A. Larabell, Soft X-ray tomography: virtual sculptures from cell cultures, Curr. Opin. Struct. Biol. 58 (2019) 324–332. https://doi.org/10.1016/j.sbi.2019.06.012.

[51] G. Schneider, P. Guttmann, S. Heim, S. Rehbein, F. Mueller, K. Nagashima, J.B. Heymann, W.G. Müller, J.G. McNally, Three-dimensional cellular ultrastructure resolved by X-ray microscopy, Nat. Methods. 7 (2010) 985–987. https://doi.org/10.1038/nmeth.1533.

[52] M. Harkiolaki, M.C. Darrow, M.C. Spink, E. Kosior, K. Dent, E. Duke, Cryo-

soft X-ray tomography: using soft X-rays to explore the ultrastructure of whole cells, Emerg. Top. Life Sci. 2 (2018) 81–92. https://doi.org/10.1042/ETLS20170086.

[53] J.C. Niclis, S. V Murphy, D.Y. Parkinson, A. Zedan, A.H. Sathananthan, D.S. Cram, P. Heraud, Three-dimensional imaging of human stem cells using soft X-ray tomography, J. R. Soc. Interface. 12 (2015) 20150252. https://doi.org/10.1098/rsif.2015.0252.

[54] B. Kepsutlu, V. Wycisk, K. Achazi, S. Kapishnikov, A.J. Pérez-Berná, P. Guttmann, A. Cossmer, E. Pereiro, H. Ewers, M. Ballauff, G. Schneider, J.G. McNally, Cells Undergo Major Changes in the Quantity of Cytoplasmic Organelles after Uptake of Gold Nanoparticles with Biologically Relevant Surface Coatings, ACS Nano. 14 (2020) 2248–2264. https://doi.org/10.1021/acsnano.9b09264.

[55] M. Chiappi, J.J. Conesa, E. Pereiro, C.O.S. Sorzano, M.J. Rodríguez, K. Henzler, G. Schneider, F.J. Chichón, J.L. Carrascosa, Cryo-soft X-ray tomography as a quantitative three-dimensional tool to model nanoparticle:cell interaction, J. Nanobiotechnology. 14 (2016) 15. https://doi.org/10.1186/s12951-016-0170-4.

[56] J. Gruenberg, The endocytic pathway: a mosaic of domains, Nat. Rev. Mol. Cell Biol. 2 (2001) 721–730. https://doi.org/10.1038/35096054.

[57] G. McDermott, M.A. Le Gros, C.G. Knoechel, M. Uchida, C.A. Larabell, Soft X-ray tomography and cryogenic light microscopy: the cool combination in cellular imaging, Trends Cell Biol. 19 (2009) 587–595. https://doi.org/10.1016/j.tcb.2009.08.005.

[58] A. Gal, A. Sorrentino, K. Kahil, E. Pereiro, D. Faivre, A. Scheffel, Native-state imaging of calcifying and noncalcifying microalgae reveals similarities in their calcium storage organelles, Proc. Natl. Acad. Sci. 115 (2018) 11000–11005. https://doi.org/10.1073/pnas.1804139115.

Chapter 3

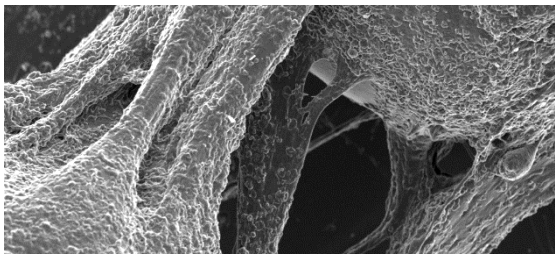

Microspheres with Ion-Doped Hydroxyapatite Nanoparticles for Enhanced Bone Regeneration

MICROSPHERES WITH ION-DOPED HYDROXYAPATITE NANOPARTICLES FOR ENHANCED BONE REGENERATION

Scope

Chapter 3 aims to explore the incorporation of ion-doped hydroxyapatite nanoparticles in gelatine microspheres as a system to release therapeutic ions for bone tissue engineering. Magnesium, zinc and strontium will be studied as doping ions due to their presence in natural bone and their crucial function in the bone regeneration process. The present chapter focuses on the development and the physicochemical characterisation of gelatine-(doped) hydroxyapatite composite microspheres. Their capacity to deliver the therapeutic ions to the cell culture media will be investigated.

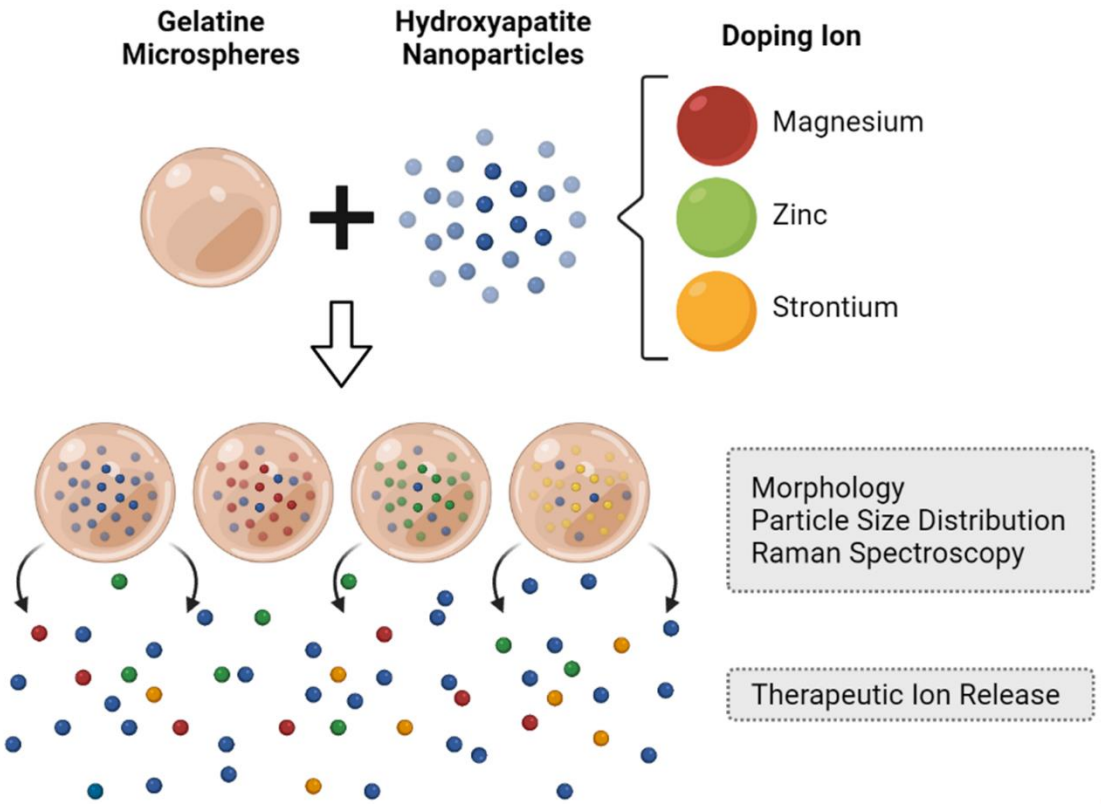

3.1. Introduction

Microspheres (MS) of different compositions have been extensively studied for bone regeneration applications. Due to the high sphericity, MS offer improved injectability and packing conditions, as well as reduced *in vivo* inflammatory response, compared to irregular particles [1]. An advantageous characteristic of MS is their large surface area which favours cell adhesion and expansion [2]. Considering the aforementioned benefits, an interesting and underexplored application of the MS is in the formulation of bioinks, providing a stable surface for cell attachment while avoiding the need of modifying the hydrogel composition and stiffness [3]. Moreover, MS have been investigated as delivery systems, as they can provide a controlled release of drugs, growth factors and other therapeutic agents [4–6].

The use of such molecules is widely spread, but they present important limitations. For example, the need for high doses in the case of BMP-2 growth factor leads to ectopic bone formation, inflammation or even bone cancer [7,8]. Other molecules such as chemotherapeutic drugs lack sensitivity and present common side effects like bone marrow suppression, drug resistance and relapse [9]. Instead, the application of ions arises as a promising alternative. Ions are natural elements found in the human body that are involved in many biological processes, including bone formation. For instance, magnesium has been reported to be vital in bone metabolism, stimulating osteoblast proliferation during the early stages of osteogenesis [10,11]. The depletion of this ion has been associated with bone fragility [12]. Zinc inhibits osteoclast differentiation whilst promoting osteoblastic activity and collagen production and, thus, stimulating bone growth and mineralisation [13–15]. On the other hand, strontium ions have been found to enhance pre-osteoblast replication and differentiation, promoting the *in vivo* bone formation [16]. Additionally, it is known that Sr^{2+} inhibits bone resorption and induces osteoclast apoptosis [17]. Strontium ranelate has been used in the treatment of osteoporosis showing a low incidence of fractures [18].

All these ions are found in the natural hydroxyapatite (HA), which is the main inorganic component of bones. Indeed, the most notable difference between synthetic and biological hydroxyapatite is the presence of multiple foreign ions in natural HA. The main ionic incorporation is CO_3^{2-} in the site of PO_4^{3-} or OH^-. Besides, different monovalent and bivalent cations (such as Na^+, Mg^{2+} and Sr^{2+}) can substitute Ca^{2+} ions. Hence, the chemical formula for biological HA is usually described as $Ca_{10-x}M_x(PO_4)_{6-y}(HPO_4, CO_3)_y(OH)_{2-z}N_z$, where M and N represent cationic and anionic ions, respectively, and x, y and z stand for the molar number of the foreign ions [19]. Regardless of the small amounts of some of these ions in bone (*e.g.* Mg^{2+} accounts for 0.6-1.5 wt% of the bone, Sr^{2+} for 0.05 wt% and Zn^{2+} represents <0.1 wt% [20]), these trace elements are crucial in the bone remodelling process, as stated previously. Therefore, ionic substitutions in synthetic HA have been extensively studied as a way to improve the performance of these materials in bone tissue engineering [21,22]. The type of ions determines the mechanism of incorporation in the HA structure (either substituting another ion in its crystalline lattice or being incorporated in the hydrated layer of the surface), and the doping concentration [23,24]. For instance, Mg ions can progressively substitute Ca in the apatite structure, but the incorporation is limited [25]. On the contrary, Sr can replace Ca in the whole range of composition [26,27]. Regarding the maximum incorporation of Zn^{2+} in the crystal lattice of HA, discrepant results have been published. Some authors reported a substitution limit of ≈10 wt%, while others succeed at adding up to ≈20 wt% [28,29]. Mg-substituted HA has been reported to improve adhesion, proliferation and metabolic

activation of bone-related cells compared to non-doped HA [30]; Zn-substituted HA presented enhanced bioactivity as well as antibacterial properties [13]; and Sr-substituted HA has been found to stimulate osteoblast differentiation [31]. Nonetheless, the incorporation of ions modifies the physicochemical properties of HA, affecting the crystal structure, the crystallinity percentage, the surface charge, and the crystal solubility along with the release capacity of the introduced ions [32].

Hydroxyapatite crystals found in bone present dimensions that usually range between 20 and 50 nm in length, 15 nm in width and 2-5 nm in thickness [33]. It is relatively simple to obtain synthetic HA NPs with close resemblance to the one in the human body, and they have been widely used in the bone regeneration field. For instance, their addition in the composition of different gels and cell-laden ink is a way to enhance the osteogenesis and the osteoinduction of the cells embedded within [34–38] while improving the mechanical properties of the final hydrogels [39–41]. On the other hand, the possibility of incorporating foreign ions into synthetic HA NPs has been successfully explored in previous studies for different applications ranging from protein delivery systems to cancer therapy [42–44]. The combination of these two approaches may be beneficial for the development of new biomaterials with enhanced bioactive properties. Moreover, apart from the ability to deliver the therapeutic ions from the HA NPs, the use of bigger – micrometric – particles may, at the same time, provide physical cues for the cells to attach, proliferate and differentiate inside the 3D environment of hydrogels. Therefore, the development of microspheres containing ion-doped HA NPs will be of major interest, especially for the generation of reinforced hydrogels with superior biological properties.

The aim of the present work is to develop composite MS made of gelatine and HA NPs for bone regeneration applications, either directly as a bone filler or for their incorporation in different kinds of hydrogels. The incorporation of doping ions related to the bone remodelling process (*i.e.* Mg^{2+}, Zn^{2+} and Sr^{2+}) into the NPs will be explored. Furthermore, the resulting NPs will be introduced into the MS and their physicochemical properties studied. The release of the therapeutic ions from the MS will also be explored.

3.2. Experimental Section

3.2.1. Synthesis of Mg-, Zn- and Sr-Doped Hydroxyapatite Nanoparticles

Magnesium (MgHA), zinc (ZnHA) and strontium-doped (SrHA) hydroxyapatite nanoparticles were obtained by the neutralisation of calcium hydroxide with ortho-phosphoric acid, following the protocol described in the previous chapter. Briefly, 333 mM calcium hydroxide solution ($Ca(OH)_2$, 96 wt% pure, Fluka) was mixed with magnesium chloride ($MgCl_2$, 98 wt% pure, Sigma-Aldrich), zinc chloride ($ZnCl_2$, 98 wt% pure, Sigma-Aldrich) or strontium chloride ($SrCl_2 \cdot 6\ H_2O$, 99 wt% pure, Sigma-Aldrich) for the synthesis of MgHA, ZnHA and SrHA, respectively. The amount of salt added was calculated to achieve 5 wt% and 10 wt% of either Mg^{2+}, Zn^{2+} or Sr^{2+}. Subsequently, 200 mM H_3PO_4 (85 wt% pure, Panreac) was added dropwise into each mixture at a rate of 1 ml min^{-1}. Non-doped hydroxyapatite nanoparticles (HA) were included as a control in the study. The reaction was performed under constant stirring at 40 ^oC, according to the following equation:

$$10\ Ca(OH)_2 + 6\ H_3PO_4 \rightarrow Ca_{10}(PO_4)_6(OH)_2 + 18\ H_2O \qquad \textbf{Equation 3.1}$$

At pH 8, the addition of H_3PO_4 was stopped and the product was stirred for 30 min at 40 ^oC. Afterwards, the solution matured overnight at room temperature before being rinsed

five times with ddH_2O, performing centrifugation cycles of 5 min at 800 g (5430 R, Eppendorf). Finally, the powder was freeze-dried (Cryodos, Telstar).

3.2.2. Synthesis of Nanoparticle-Charged Gelatine Microspheres

Prior to the microspheres synthesis, a suspension of 10 wt% ion-doped NPs and 10 wt% sodium citrate (Sigma-Aldrich) was prepared. The solution was sonicated with a high-frequency ultrasound probe sonicator (450D, Branson Digital) using a 3 mm diameter tip at 40% amplitude for 2 min. Afterwards, the NPs dispersion was mixed 1:1 with 30 wt% gelatine solution (Fluka) at 50 ºC and 40 ml were added dropwise into a beaker containing 400 ml of olive oil at 50 ºC under stirring for the synthesis of the microspheres. After 10 min, the emulsion was cooled down to 4 ºC and stirred for 30 min. Subsequently, 400 ml of cold acetone were added and the mixture was left in stirring for 1 h before being filtered to collect the synthesised microspheres. The final product was rinsed with acetone, dried and further sieved to 40-100 µm. Moreover, a control condition consisting of gelatine MS without the addition of NPs was included in the study. To synthesise these particles, 40 ml of 15 wt% gelatine solution at 50 ºC were added into the initial beaker and the previously described protocol was followed.

100 mM N-(3-dimethylaminopropyl)-N′-ethylcarbodiimide hydrochloride (EDC, Sigma-Aldrich) and 150 mM N-hydroxysuccinimide (NHS, Sigma-Aldrich) solutions were prepared in water/cold acetone (20:80 v/v). They were mixed 1:1 and used to immerse the sieved MS for 1.5 h. Afterwards, the powder was thoroughly rinsed with ddH_2O and dried.

3.2.3. Physicochemical Characterisation of the Nanoparticles

Characterisation of the NPs comprised analysis of the phase composition by X-ray diffraction (XRD, D8 Advance, Bruker) using Cu Kα radiation at 40 kV and 40 mA. Data were collected with a step size of 0.02º over the 2θ range from 20 to 60º with a counting time of 2 s per step. Phase identification was accomplished by comparing the results with the standard patterns of HA (ICDD PDF 09-0432). The crystallite size (D) of the NPs was determined following Scherrer's equation:

$$D = \frac{K \cdot \lambda}{\beta \cdot \cos\theta} \qquad \textbf{Equation 3.2}$$

Where K is a constant varying with crystal habit and here is set to 0.9, λ corresponds to the wavelength of the X-ray beam (*i.e.* 0.15406 nm for Cu Kα radiation), β is the full width at half maximum for the (002) diffraction peak, and θ is the diffraction angle.

In addition, Raman spectroscopy (inVia Qontor, Renishaw) was conducted with a 723 nm laser at 100% power. The frequency range analysed was 726-1812 cm^{-1} with 1 s exposition and 40 accumulations per sample.

3.2.4. Physicochemical Characterisation of the Microspheres

The morphological evaluation of the different MS was performed by optical microscopy (AE2000, Motic). Moreover, the particle size distribution was assessed through image analysis (FIJI, ImageJ software, [45]) of the obtained acquisitions. MS composition was examined through Raman spectroscopy, using the previously described parameters.

3.2.5. Study of the Ion Release in Cell Culture Media

In order to study the ionic release of the microspheres in cell culture medium, 10 mg of each MS were put in contact with 1 ml of Dulbecco's modified eagle medium (DMEM) supplemented with 10% foetal bovine serum (FBS), 20 mM 4-(2-hydroxyethyl)-1-piperazineethanesulfonic acid buffer (HEPES), 2 mM L-glutamine, 50 U ml^{-1} penicillin and 50 µg ml^{-1} streptomycin (all from Gibco), for four days at 37 ºC. The medium was changed daily and the supernatants were collected and diluted 20-fold in 2 wt% HNO_3 (69 wt% for trace metal analysis, PanReac AppliChem). Ca^{2+}, P_i and Mg^{2+} concentrations were determined by inductively coupled plasma optical emission spectrometry (ICP-OES, 5100, Agilent Technologies), whereas inductively coupled plasma mass spectrometry (ICP-MS, 7800, Agilent Technologies) was used to study Sr^{2+} and Zn^{2+} levels in cell culture medium. ^{44}Ca, ^{31}P, ^{24}Mg, ^{66}Zn and ^{88}Sr signals were calibrated against a multi-element standard solution (Inorganic Ventures). This experiment was done in triplicate (n=3) for each MS type.

In addition, the MS after the ion release experiments were rinsed in water followed by ethanol and, upon drying, were analysed by Raman spectroscopy using a laser power set to 10%, 2 s of exposition and 100 accumulations.

3.2.6. Statistical Analysis

All data were reported as mean values ± standard deviation. A normality test was performed to determine if data were modelled by a normal distribution. Statistically significant differences between groups were analysed by one-way ANOVA test followed by Tukey's post-hoc pairwise comparison. Statistical analysis was performed using Minitab Statistical Software.

3.3. Results and Discussion

The aim of this work was to develop microspheres for bone regeneration applications with enhanced bioactivity and the capacity to deliver therapeutic ions. To this end, composite MS made of gelatine and HA NPs doped with either Mg^{2+}, Zn^{2+} or Sr^{2+} were synthesised by a simple water in oil emulsion method. The main consequences of this doping strategy were investigated by studying the ion incorporation to the crystal lattice of HA NPs, the morphological implications in the final MS and their ion release behaviour, which would determine the availability of the therapeutic ions in the surrounding media. This strategy permitted the sustained release of trace metals critical in the bone remodelling process while supplying attaching moieties to the cells.

3.3.1. Physicochemical Characterisation of the Doped Hydroxyapatite Nanoparticles

Hydroxyapatite nanoparticles were successfully synthesised using a wet precipitation method, obtaining non-doped hydroxyapatite (HA), magnesium-doped (MgHA), zinc-doped (ZnHA) and strontium-doped (SrHA) NPs. **Figure 3.1A** shows the XRD patterns of each synthesis. All peaks matched those corresponding to HA (ICCD PDF 09-0432), demonstrating the precipitation of phase pure HA with no secondary crystalline phases

obtained, except for the Zn10 specimen, where a small peak between the (102) and (201) diffraction peaks revealed the formation of a new phase consisting on $Zn_3(PO_4)_2$. In addition, broader peaks were observed for the two ZnHA samples, indicating a reduction in the crystallite size and/or an increase in the crystal strain with the incorporation of Zn^{2+}, as also reported by other authors [46].

It has been extensively reported that ionic substitutions in the crystal lattice of HA can create distortion of the crystal structure due to discrepancies between the radius of the substituting ion and the substituted one. This mismatch usually causes the contraction or expansion of the lattice, resulting in peak shifting in the XRD spectra. Therefore, in the present work, the peak shift of the (002) diffraction peak was investigated because it does not overlap with other reflections and has a sharp shape [47]. As expected, the detailed examination of the (002) diffraction peak revealed slight shifts when introducing the doping ions. The incorporation of Mg^{2+} and Zn^{2+} produced a slight shift towards higher 2θ angles, whereas a deviation to lower angles was found for SrHA NPs. Moreover, these shifts were accentuated as more doping ions were incorporated during the synthesis. This phenomenon is caused by the substitution of Ca^{2+} ions by the different doping ions into the HA crystalline structure. It has been previously reported that the smaller size of the Mg (0.065 nm) and Zn (0.075 nm) radius compared to the Ca ionic radius (0.099 nm) reduces the cell parameters of HA, which explains the (002) peak shift towards higher angles. In contrast, Sr^{2+} presents a larger ionic radius (0.120 nm) than Ca, and its incorporation on the lattice is reported to cause an expansion of the parameters, producing the peak shift to lower angles [20,48].

An estimation of the crystallite size was calculated using Scherrer's equation in the (002) reflection, and the results are displayed in **Figure 3.1C**. The value does not have a standard deviation because it was calculated only in one X-ray diffractogram. A crystallite size of 27.85 nm was found for the non-doped HA NPs and was maintained at 27.97 nm for the Mg5 sample. This parameter decreased to 24.00 nm in the case of Mg10, to 25.73 and 24.68 nm for the Zn5 and Zn10 samples, respectively, and to 26.91 nm for the Sr5. In contrast, a crystallite size of 31.52 nm was obtained for the Sr10 sample. This follows the expected trend, as in general, the incorporation of ions in the crystal lattice should entail a reduction in crystallite size regardless of the type of ion, as has been repeatedly reported in the literature [23,25,46,49]. The low incorporation of Mg^{2+} in the Mg5 condition may explain the maintenance of the HA crystallite size. On the other hand, the increase of this parameter for the Sr10 sample was unexpected since the literature reported a reduction of crystal size for strontium substitutions of up to 50 at% [50].

The results of Raman spectroscopy are summarised in **Figure 3.1B**. They revealed the presence of the characteristic vibration bands of HA in all the samples. The band at ≈960 cm^{-1} corresponds to the v_1 symmetric stretching vibration of the P-O bond and the vibration bands in the region between ≈1030-1070 cm^{-1} to the phosphate v_3 antisymmetric stretching vibrations [51]. Additionally, the 960 cm^{-1} band presented a marked shift to the left in both SrHA samples, which has been reported by other authors to result from the crystal lattice expansion induced by the incorporation of Sr^{2+} ions [52]. Furthermore, the same band was wider in the Mg10 sample, a phenomenon that has also been reported in the literature. Indeed, the broadening of the 960 cm^{-1} band is associated with the deformation of PO_4^{3-} structure by surrounding magnesium ions, which demonstrates the Mg^{2+} substitution in the crystal lattice of HA that causes the formation of a new vibration band at 950 cm^{-1} [48,53].

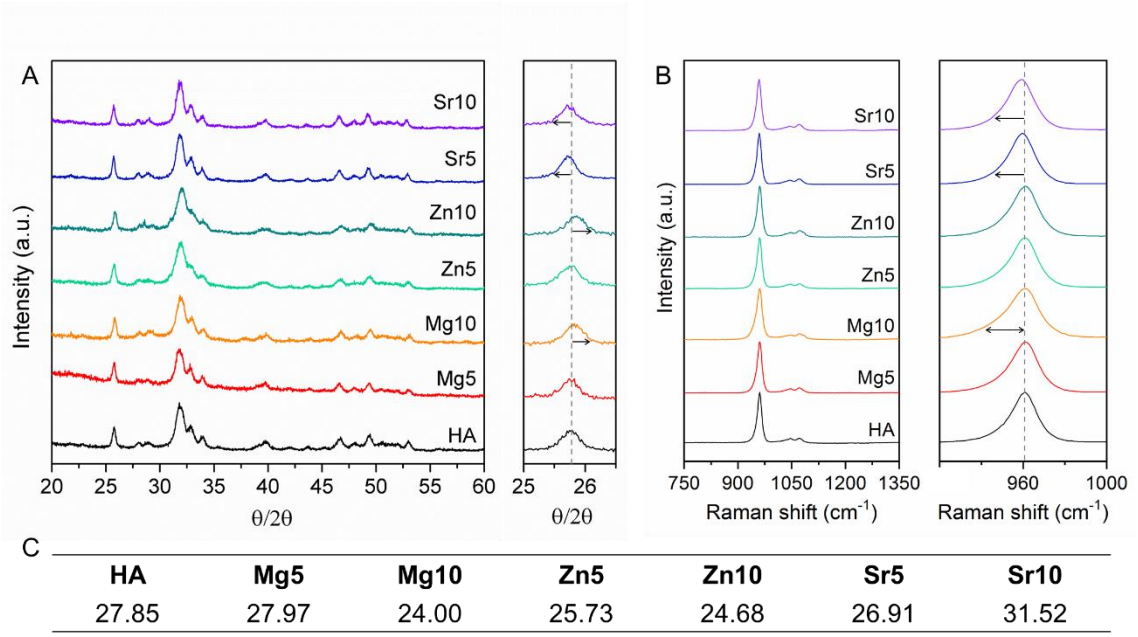

C

HA	Mg5	Mg10	Zn5	Zn10	Sr5	Sr10
27.85	27.97	24.00	25.73	24.68	26.91	31.52

Figure 3.1 Characterisation of the synthesised ion-doped hydroxyapatite nanoparticles. **A** X-ray diffractograms and magnified region (25-26.5º) of the (002) peak. **B** Raman spectra and amplification of the 960 cm^{-1} band. Arrows indicate small changes in the spectrum. **C** Crystallite size (in nm) of the different NPs, calculated in the (002) reflection with Scherrer's equation.

Previous characterisation studies by ICP performed in our group using the same synthesis protocol further confirmed the substitution of Mg^{2+}, Zn^{2+} and Sr^{2+} ions for Ca^{2+} ions in the HA structure, with a decrease of the Ca/P ratios in a dose-dependent manner for all the substituted NPs, while maintaining the (Ca + doping ion)/P ratios at ≈1.7 [43]. The ion doping concentration in the synthesised NPs were 1.23 wt% and 2.17 wt% for the Mg5 and Mg10 samples, 3.98 wt% and 8.04 wt% for the Zn5 and Zn10 NPs, and 3.54 wt% and 5.70 wt% for the Sr5 and Sr10 specimens. The ionic incorporation of Mg was close to the limit reported in the literature (*i.e.* 2.5 wt% [25]) for the higher concentration sample, while the strontium addition was far away from the expected [26]. Furthermore, the Zn incorporated was more than 80%, indicating a high addition efficiency.

3.3.2. Physicochemical Characterisation of the Microspheres

The morphology of the synthesised microspheres both in a dry and wet state was analysed by optical microscopy after sieving (**Figure 3.2**). The incorporation of NPs reduced the transparency of the gelatine MS, regardless of the type of NPs. The sphericity of the gelatine MS was maintained when introducing HA, 5 wt% of ZnHA, and SrHA NPs at both 5 and 10 wt%. However, the MS tended to lose their shape with the magnesium doping. It was hypothesised that in these syntheses, the gelification of the MS was shielded by the interaction between the NPs and the gelatine chains. This was supported by the work of Xing *et al.*, where they purified a gelatine solution from divalent metal ions and the subsequent chemical cross-linking with EDC formed a stronger gelatine network thanks to the removal of the interactions between divalent cations and the carboxylic groups of the gelatine chains [54]. Thus, we believe that the leaching of certain ions from the NPs interferes with the cross-linking process. Moreover, the swelling

observed for the wet MS despite the cross-linking process was due to the hydration of the gelatine chains.

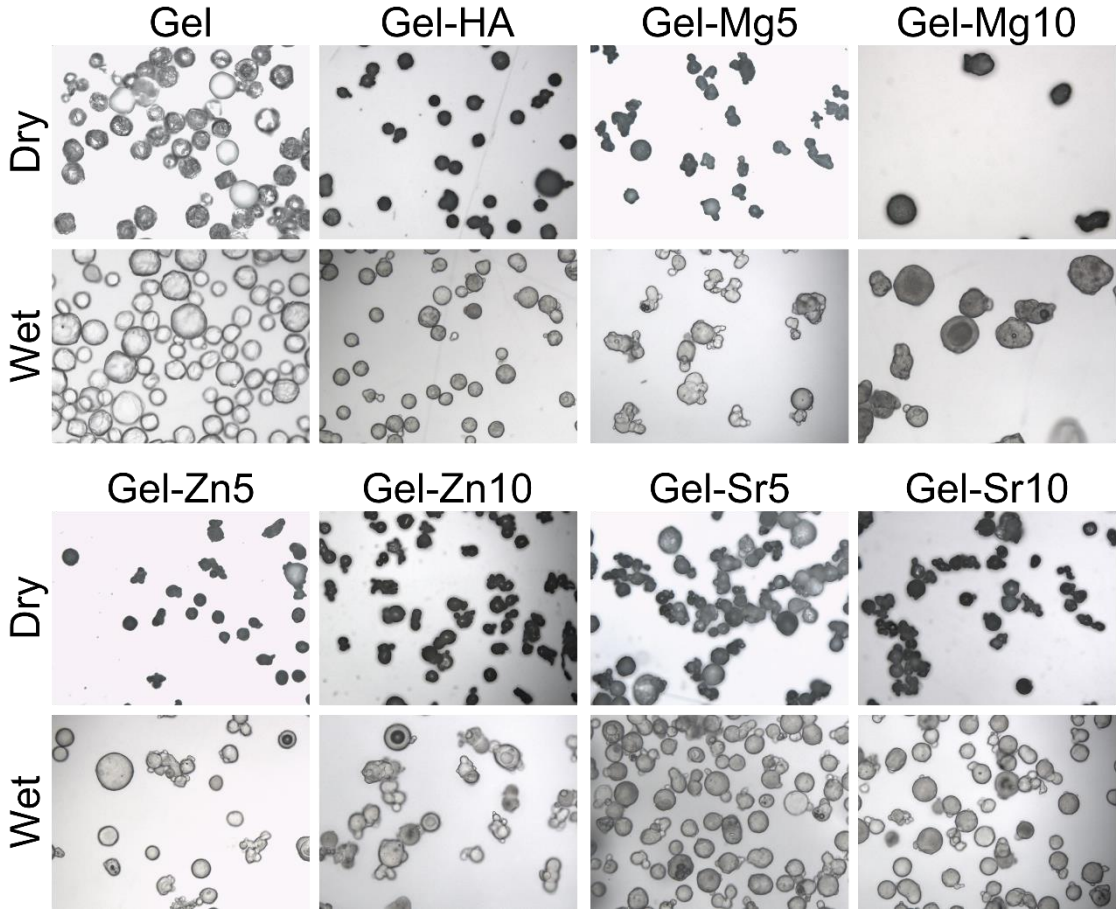

Figure 3.2 Morphology of the different microspheres after the incorporation of Mg^{2+}-, Zn^{2+}- and Sr^{2+}-doped HA nanoparticles, either in a dry state or in water suspension. Microspheres without nanoparticles (Gel) and with non-doped nanoparticles (Gel-HA) were included as controls.

Image analysis of the optical acquisitions was performed to determine the size distribution of the different syntheses. **Figure 3.3** contains the data of each type of MS once sieved, cross-linked and dried. All the conditions presented a monomodal normal particle size distribution (**Figure 3.3A**), with an average diameter size of 62 ± 13 µm. The control – gelatine – MS showed a mean size of 72 ± 15 µm, while the addition of HA NPs led to a marked decrease in the diameter size. Precisely, the incorporation of non-doped HA NPs reduced the mean size down to 59 ± 13 µm, whereas the zinc and strontium doping diminished it in a dose-dependent manner. The diameter sizes were 48 ± 14 µm and 55 ± 14 µm for the MS with higher doping levels (*i.e.* Gel-Zn10 and Gel-Sr10, respectively). In contrast, the addition of magnesium-doped NPs in the MS presented a completely different pattern: whilst Gel-Mg5 exhibited similar results compared to the Gel-HA samples, the MS with the higher Mg^{2+} content (*i.e.* Gel-Mg10) showed a marked increase in the mean diameter up to 91 ± 16 µm. This may be attributed to changes in the viscosity of the initial gelatine-NPs solution. As explained above, the leaching of certain divalent cations from the NPs can potentially interact with the carboxylic groups of the gelatine chains, creating hydrogen bonds between them. This has been shown to increase the

hydrogel viscosity and to impair the subsequent covalent cross-linking through EDC chemistry [54].

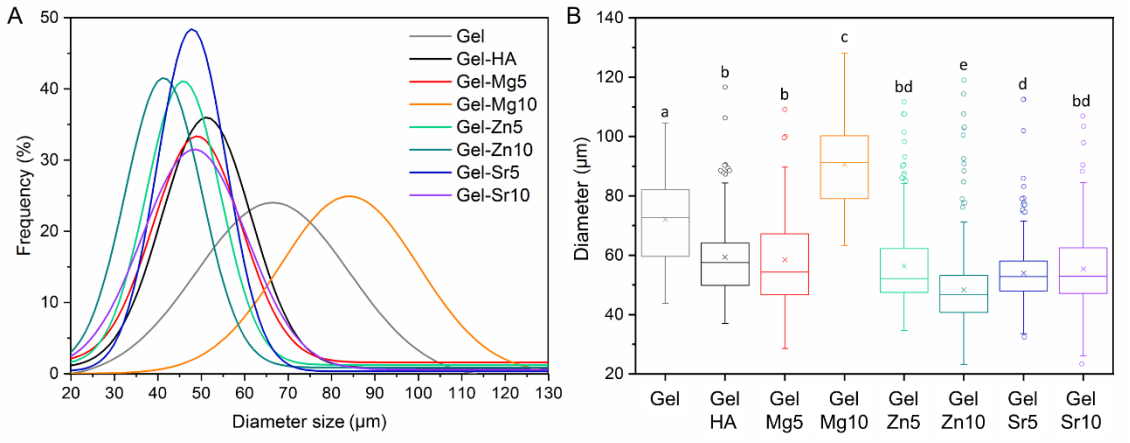

Figure 3.3 Particle size distribution of the microspheres. **A** Distribution plot representing the frequency of microsphere diameter observations, and **B** Boxplot indicating mean (x), quartiles, max, min and outliers (o). Each outlier corresponds to a single microsphere. Different letters indicate statistically significant differences between conditions.

Furthermore, Raman spectroscopy was conducted to identify the chemical composition of the synthesised MS. Several characteristic bands were studied, the major one of HA and four corresponding to gelatine, as displayed in **Figure 3.4A**. The presence of HA NPs was demonstrated with the ≈960 cm^{-1} band, which corresponds to the symmetric stretching mode v_1 vibration of the PO_4^{3-} groups [56]. Regarding the gelatine, four different group of bands were identified in the Raman spectra. The first one, from ≈800 to 1040 cm^{-1}, corresponds to the stretching mode vibrations of different C – C bonds, mainly assigned to amino acids such as proline, hydroxyproline, tyrosine and tryptophan [56]. The amide III band of the gelatine was observed from ≈1240 to 1300 cm^{-1}, and is related to C – N stretching vibrations and N – H bending vibrations. The third band (≈1450 cm^{-1}) corresponds to CH_2 in-plane bending vibration mode of the gelatine, while the last region (≈1650 to 1700 cm^{-1}) is the amide I band that correlate to C = O stretching bond vibrations [55,57].

The cross-linking of the gelatine of the MS did not result in major changes in the spectra when compared to the non-cross-linked MS. The four characteristic group of bands of the gelatine were observed for all the MS after cross-linking them (**Figure 3.4B**), which demonstrated that the reticulation of the gelatine was not altering the composition of the final MS. In addition, the band corresponding to the HA was found in all the samples containing HA NPs, which accounts for the proper incorporation of the particles in the MS, without losing them after the cross-linking and subsequent rinsing processes. It was observed that the cross-linking process resulted in a slight increment in the intensity of the amide vibration bands, which was more pronounced in the amide I band. This observation is in agreement with previous works [58,59], which attributed this phenomenon to the formation of new amide groups by the EDC cross-linking between carboxylic acids and primary amines.

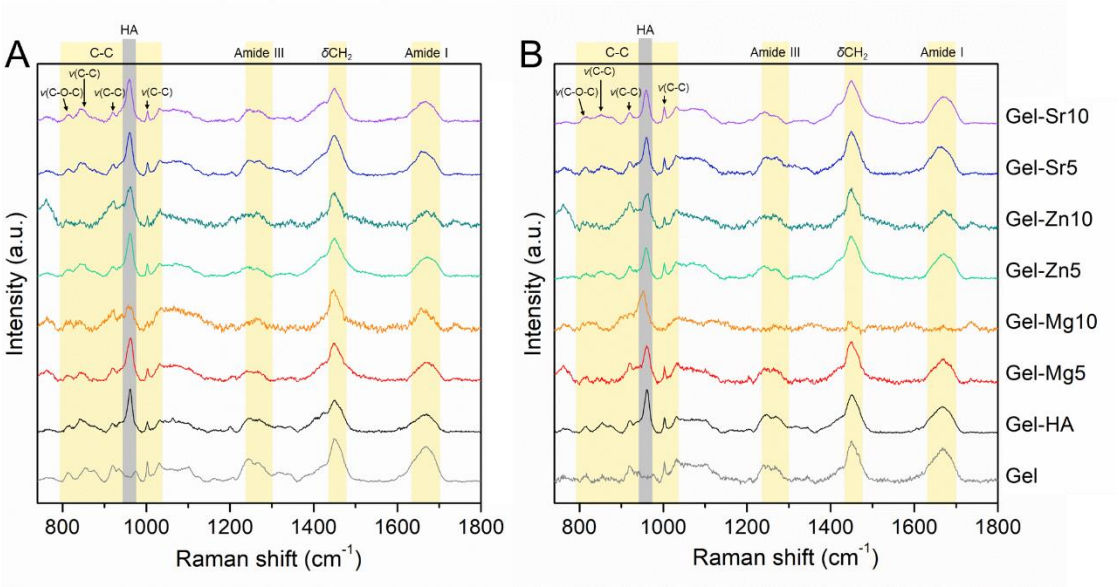

Figure 3.4 Raman spectroscopy of the MS (**A**) before and (**B**) after the cross-linking process. The grey band at 960 cm^{-1} is characteristic of HA, while the yellow regions are distinctive of gelatine: carbon bonds (C-C) region, assigned to *v*(C-O-C) of proline, hydroxyproline and tyrosine at 813 cm^{-1}, *v*(C-C) of proline, hydroxyproline, tyrosine and tryptophan at 853-873 cm^{-1}, *v*(C-C) of proline at 919 cm^{-1}, and *v*(C-C) of phenylalanine at 1002 cm^{-1}; amide III band at 1240-1300 cm^{-1}; vibrations of CH_2 bonds at 1450 cm^{-1}; and amide I band at 1650-1700 cm^{-1} [56].

3.3.3. Ion Release in Cell Culture Media

HA NPs are reactive when placed in solution, exchanging ions with the environment. This has been precisely the main attraction of these NPs as they can potentially deliver key ions introduced within their structure. The main concern is to have an appropriate dose released, within the therapeutic range.

The release behaviour of the ions from the MS into the cell culture media along time was checked by ICP analysis. The major ions (*i.e.* Ca^{2+}, P_i and Mg^{2+}) were quantified by ICP-OES, while the minor ions (*i.e.* Zn^{2+} and Sr^{2+}) were analysed by ICP-MS. These results are represented in **Figures 3.5**, **3.6** and **3.7**.

Figure 3.5 summarises the concentration of major ions in the cell culture medium (DMEM). It can be observed that the concentration of these elements remained stable in DMEM during the course of the study: 2.03 mM Ca^{2+}, 1.30 mM P_i and 0.85 mM Mg^{2+} (**Figure 3.5A**), in agreement with the levels reported by the manufacturer. Although the control (Gel) MS slightly lowered the concentrations of these ions in the medium since the first moment, the decrease was small and the levels remained quite stable throughout the culture (*i.e.* ≈1.77 mM, ≈1.14 mM and ≈0.75 mM for Ca, P and Mg ions, respectively, **Figure 3.5B**). The ion uptake by the Gel MS could be attributed to either the electrostatic attraction of free cations by the carboxylate groups of the gelatine or to the precipitation of solid calcium phosphate [54]. On the contrary, when DMEM was put in contact with MS containing any type of NPs, a clear decrease in the concentrations of Ca and P ions from day 1 onwards was found, indicating a depletion of these ions. At 6 h there was a higher content of Ca^{2+} in the medium for some of the MS (Gel-Mg10 (2.31 mM, **Figure 3.5E**), Gel-Zn5 (2.19 mM, **Figure 3.5F**) and Gel-Sr10 (2.88 mM, **Figure 3.5I**), as well as a higher content of P_i in the case of Mg-containing MS (1.55 mM in both Gel-Mg5 and

Gel-Mg10, **Figure 3.5D** and **E**). Nonetheless, the concentrations of calcium decreased down to 1.10 - 1.40 mM on day 4 and the phosphorus concentration was around 0.70 and 0.90 mM on the same day for all the NPs-containing samples.

Figure 3.6 shows the ICP-MS quantification for trace metal ions in the cell culture medium, namely zinc and strontium. Their ionic levels in the control DMEM were stable during the study at around 18 µM and 2.8 µM, respectively, **Figure 3.6A**. Very similar concentrations were obtained when incubating Gel MS, indicating no interaction between these ions and the gelatine chains. However, a slight decrease in the zinc content was observed on the 4th day of culture (13.9 µM, **Figure 3.6B**). This reduction is attributed to the electrostatic attraction of the cation for the carboxylic groups of the gelatine chains, as suggested previously for Ca and Mg ions. Contrastingly, an increase in the initial Zn and Sr concentrations was observed in the NPs-containing MS. As expected, this phenomenon was especially pronounced in Zn- and Sr-doped MS for Zn^{2+} and Sr^{2+} ions, respectively (**Figure 3.6F-I**). Indeed, the concentrations increased notoriously for the samples containing higher amounts of doping ion (*i.e.* >1000 µM Zn^{2+} for Gel-Zn10 and >500 µM Sr^{2+} for Gel-Sr10). Furthermore, in the conditions with Zn and Sr doping, it was observed that the levels of these ions were always above those found in the cell culture medium, demonstrating a continuous release from the MS. Notwithstanding, this release was progressively waning with time, following an asymptotic trend. In another vein, one striking result was the release of Zn^{2+} and Sr^{2+} in the Gel-HA and Gel-Mg10 MS (**Figure 3.6C** and **E**). The presence of such ions in these samples may be explained by impurities in the reagents used in the NPs synthesis. For example, the presence of ionic impurities in the $Ca(OH)_2$ is common and can easily show up when measuring ionic concentrations at the micromolar level [60].

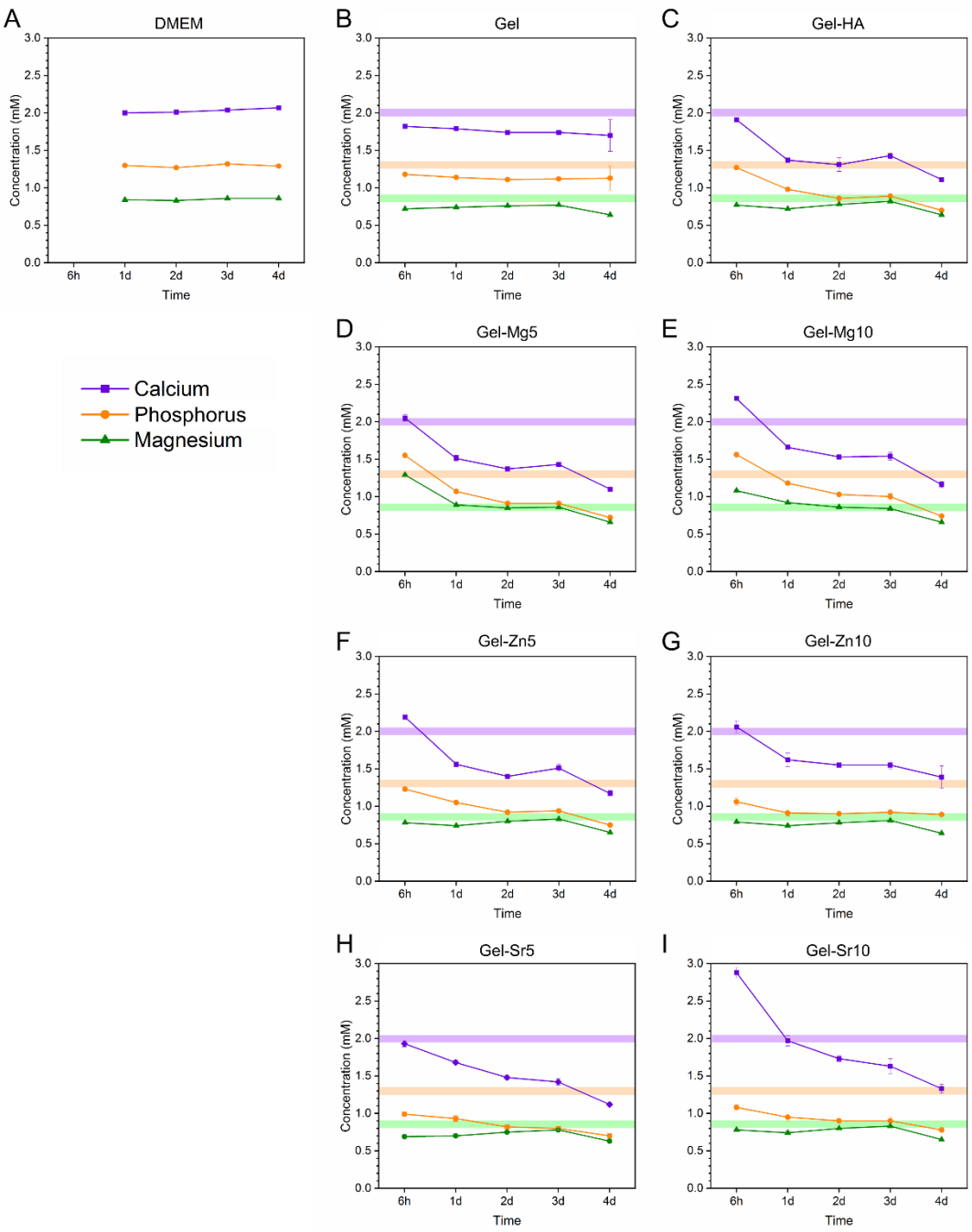

Figure 3.5 Calcium, phosphorus and magnesium ionic concentrations in the cell culture medium after the incubation of the different MS at different times. Results obtained by ICP-OES.

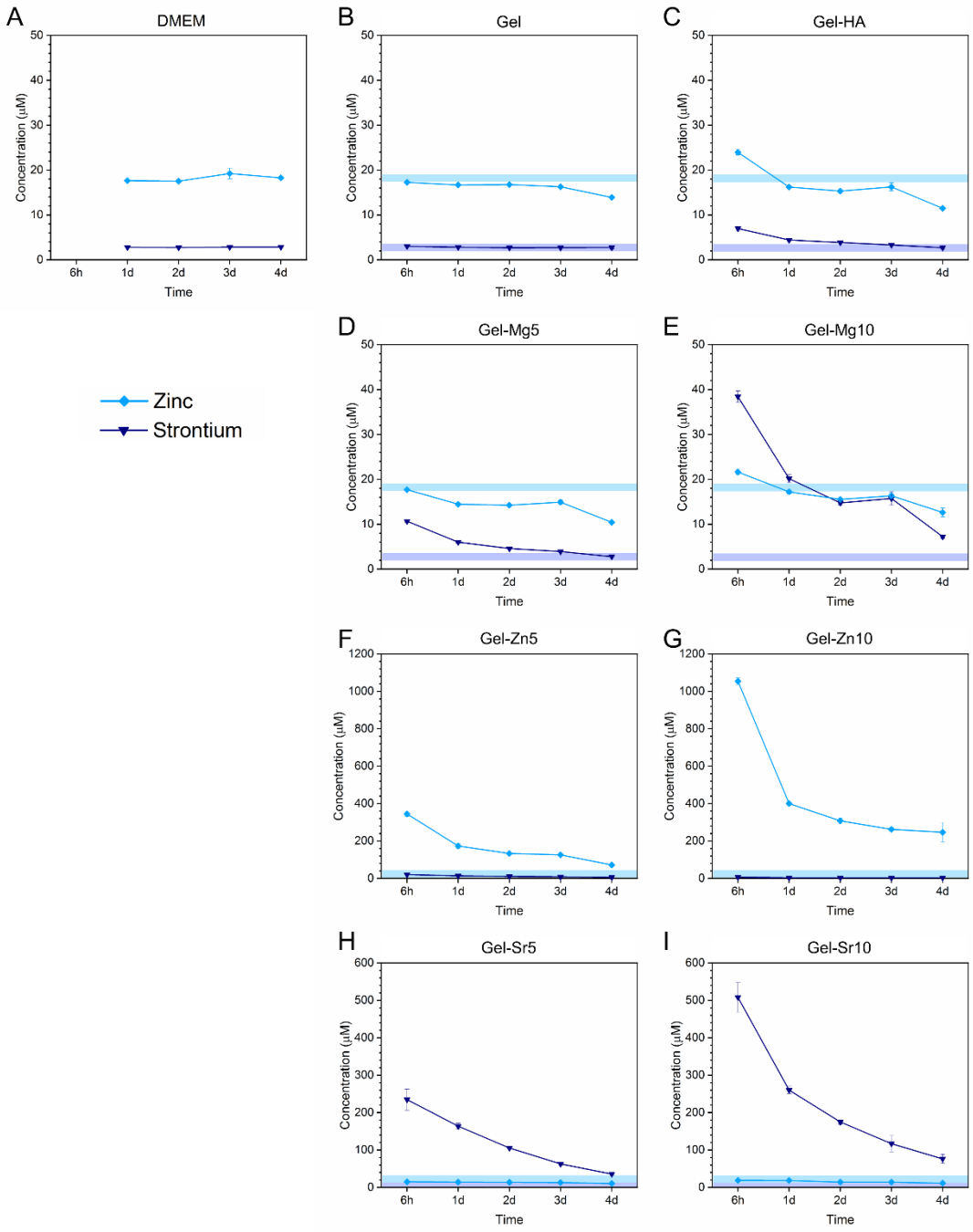

Figure 3.6 Zinc and strontium ionic concentrations in the cell culture medium after the incubation of the different MS at different times. Results obtained by ICP-MS.

Additionally, the cumulative release from or uptake by the material was calculated and represented in **Figure 3.7A** and **B**. Rather than a release, a sustained uptake of Ca and P ions from the medium was noted for all the conditions. Such behaviour could be explained by the precipitation of CaP fostered by an initial ion release originated by the dissolution of the HA NPs. This phenomenon has been previously reported in the literature [61–63]. On the other hand, the ionic exchange of magnesium ions (**Figure 3.7C**) was less accentuated than the uptake observed for Ca and P. This indicates the limited implication of Mg in the precipitation of CaP, which can be explained by its marked inhibitory effect on HA nucleation and growth [64,65]. Altogether, the early release of ions in the medium

is attributed to an initial partial dissolution of the NPs, whilst the subsequent ionic uptake is associated with the precipitation of calcium phosphate salts. It is worth noting that the observed NPs dissolution is compatible with the potential precipitation of CaP in the cell culture medium. This process would lead to a new CaP phase with lower solubility than the pristine HA NPs [66]. Furthermore, it can be noticed that the precipitated phase was not uptaking all the ions released in the medium. Hence, the therapeutic effect of the free ions remained plausible.

For the release of therapeutic ions, the fundamental key point is the use of materials that naturally dissolve. In the context of doped-HA NPs, both the elevated intrinsic surface area of the NPs and the effect of the doping ion distorting the crystal lattice is what triggers their dissolution. In this sense, previous works reported an increased dissolution rate of synthetic HA doped with Mg^{2+} [25] and Sr^{2+} [23,49,67] compared to non-doped materials. However, the dissolution of these NPs will increase the Ca^{2+} and P_i concentrations in the medium, leading to the supersaturation of the solution. This saturation causes the precipitation of a more thermodynamically stable phase, such as HA with lower doping ion content (the lower the doping, the less reactive HA becomes). This is in agreement with the work of Lee *et al.*, where they also showed precipitation of HA in DMEM on an apatitic substrate [68].

In order to know if the developed MS may promote the desirables biological effects, the levels of ions released need to be compared with the therapeutic range reported in the literature. On the one hand, several *in vitro* studies showed a positive effect on osteoblast proliferation and MSC osteogenic differentiation with Mg levels between 83 µM and 4.2 mM [69,70]. Although in the present study, Gel-Mg5 and Gel-Mg10 released 0.4 mM and 0.2 mM Mg^{2+} at the first time point (**Figure 3.7C**), the lack of sustained release in the media suggested that this system was not successful enough for its use in the bone regeneration field. Regarding Zn^{2+}, *in vitro* studies with different bone-related cells revealed that doses from 1 µM to 50 µM stimulate osteoblast proliferation and ALP expression, as well as extracellular matrix calcification and overexpression of RUNX2 protein [71–75]. However, high doses of zinc (600 – 900 µM) were found to be cytotoxic [76]. The initial Zn^{2+} release from Gel-Zn5 and Gel-Zn10 was 325 µM and 1035 µM, respectively (**Figure 3.7D**). None of the concentrations are within the reported therapeutic range of this ion, and the latter value can be considered cytotoxic. Nevertheless, the ion release ratio decreases with time and the levels released from day 1 onwards were significantly lower (**Figure 3.6F** and **G**). Therefore, the preincubation of these MS prior to their contact with cells might be beneficial, and the further ionic release can potentially be in the therapeutic levels of Zn^{2+}. Finally, previous works reported that concentrations of Sr^{2+} up to 1 mM stimulate proliferation osteoinduction [27,77,78]. Other works showed that 8 mg Sr^{2+} g^{-1} per day were beneficial for cell proliferation and osteogenic differentiation [79]. Regarding the therapeutic oral doses of Sr^{2+} in *in vivo* studies, 23 µM to 210 µM are proposed to be sufficient to restore the normal function in osteopenic animals [80,81]. In the current study, Gel-Sr5 and Gel-Sr10 presented an initial Sr^{2+} release of 232 and 505 µM, respectively (**Figure 3.7E**). Moreover, the cumulative release after 4 days in culture was 588 and 1122 µM for the same samples. These results revealed that the behaviour of these MS can be considered favourable for the induction of osteogenesis, both *in vitro* and *in vivo*. Nonetheless, in order to determine the therapeutic potential of this system, further studies would be required.

Therefore, we can conclude that when MS containing NPs are in contact with the cell culture medium a dissolution of the NPs and subsequent precipitation takes place, caused

by the low solubility of the HA. Although the nature of the precipitating CaP was not determined, it was expected to obtain an apatitic phase due to the pH conditions.

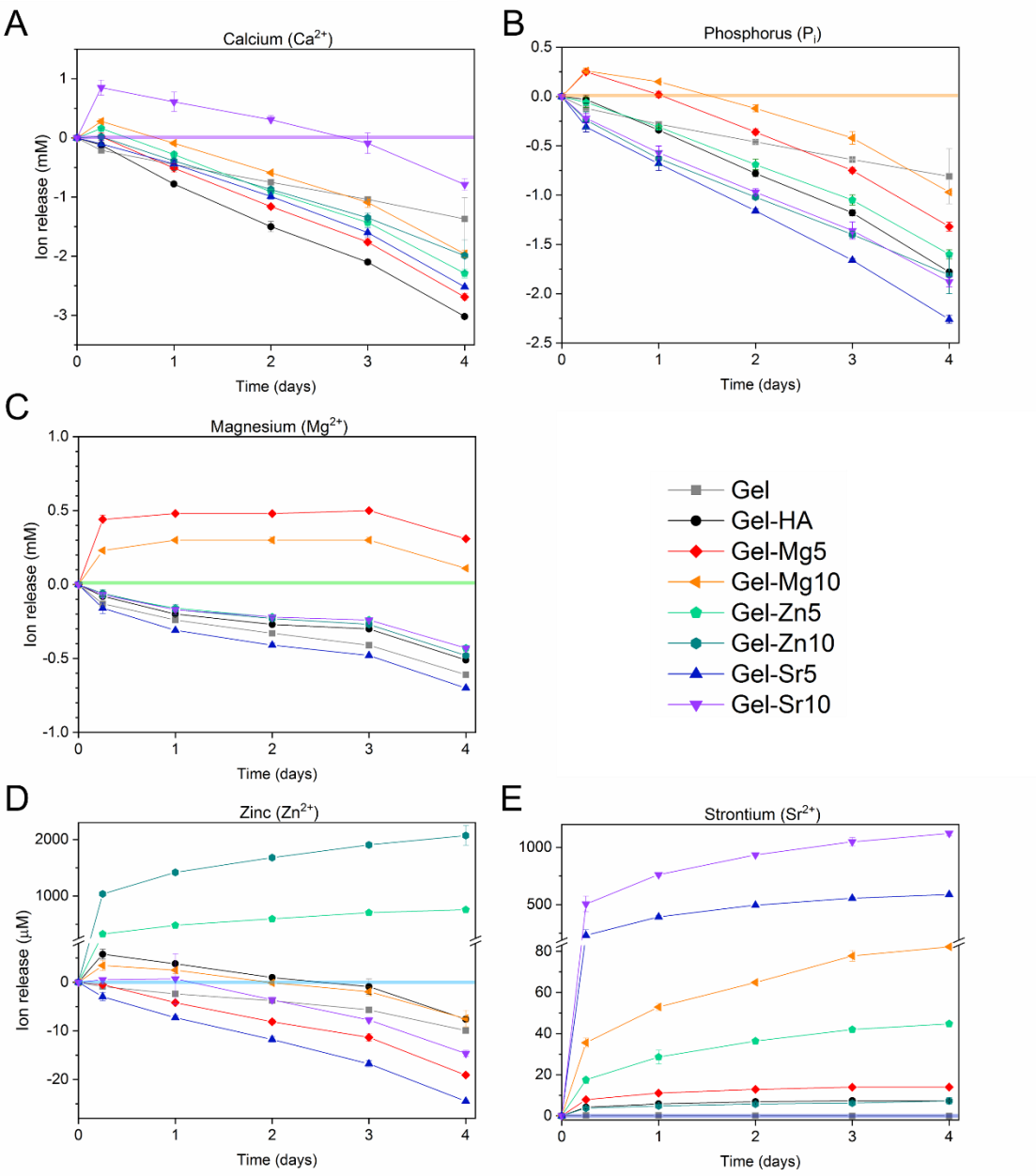

Figure 3.7 Cumulative release or uptake of Ca^{2+}, P_i, Mg^{2+}, Zn^{2+} and Sr^{2+} ions by the material during the incubation of all the developed MS.

In order to confirm the partial dissolution of the NPs, the MS were analysed by Raman spectroscopy after being incubated in the cell culture medium. From the results, an important reduction in the HA 960 cm^{-1} band was recognised (**Figure 3.8B**), in comparison to the as-prepared MS shown in **Figure 3.8A**. These data are in agreement with the ICP results and corroborate the NPs gradual dissolution for all the conditions.

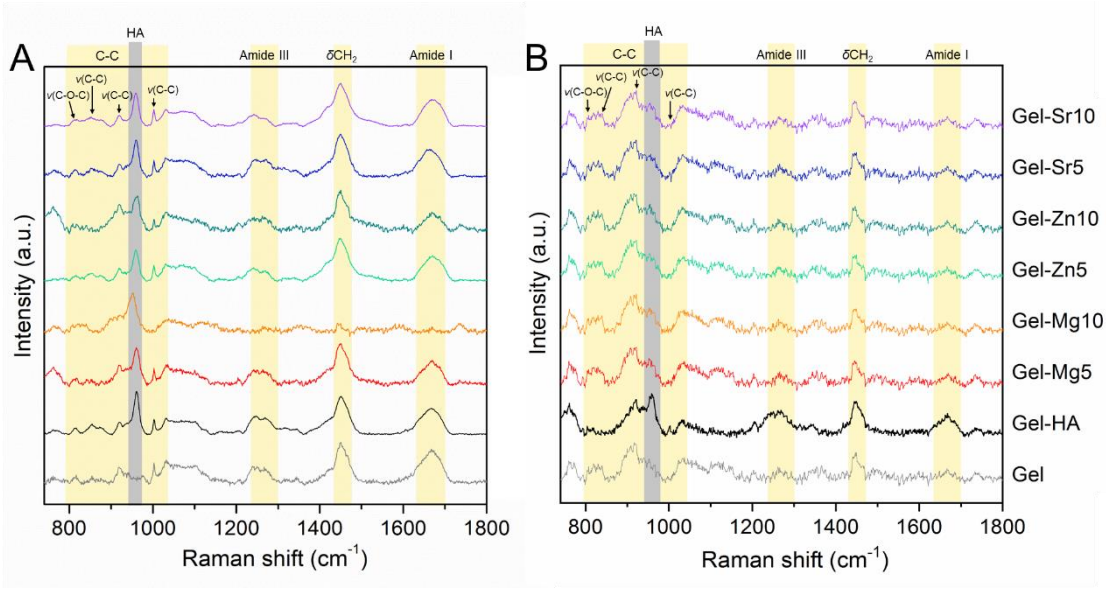

Figure 3.8 Raman spectroscopy of all the MS before (**A)** and after (**B**) being incubated for 4 days in cell culture medium. The grey band at 960 cm^{-1} is characteristic of HA, while the yellow regions are distinctive of gelatine: carbon bonds (C-C) region, assigned to *ν*(C-O-C) of proline, hydroxyproline and tyrosine at 813 cm^{-1}, *ν*(C-C) of proline, hydroxyproline, tyrosine and tryptophan at 853-873 cm^{-1}, *ν*(C-C) of proline at 919 cm^{-1}, and *ν*(C-C) of phenylalanine at 1002 cm^{-1}; amide III band at 1240-1300 cm^{-1}; vibrations of CH_2 bonds at 1450 cm^{-1}; and amide I band at 1650-1700 cm^{-1} [56].

In this chapter, Mg^{2+}, Zn^{2+} and Sr^{2+} doped-hydroxyapatite nanoparticles were successfully synthesised and incorporated into gelatine microspheres. These ions have been proved to be incorporated in the crystalline core of the hydroxyapatite, and are released in the cell culture medium showing different behaviours. On the one hand, the Mg concentrations reached with the Mg-doped MS seemed to be insufficient for a therapeutic application. Zn-doped MS would need a previous preincubation as their initial Zn^{2+} release could be lethal for the cells. Finally, Sr-doped samples showed a promising release performance for their further use in bone regeneration applications. This approach has countless possibilities, as the combination of MS with different doping ions or the incorporation of various doped-NPs in the same MS can be explored and used as a way to improve bone regeneration. Although further investigation needs to be done, several authors suggested that the strategy of delivering metal ions is a promising and beneficial alternative to the common use of growth factors [82,83].

3.4. Conclusion

In conclusion, the use of hydroxyapatite-gelatine composite microspheres for the delivery of therapeutic ions has been found to be promising for its easy and effective ionic incorporation in the HA crystal lattice and further synthesis of NPs-containing MS. Phase pure ion-doped HA NPs (*i.e.* Mg^{2+}, Zn^{2+} and Sr^{2+}) were successfully obtained, presenting morphological differences among the conditions in terms of sphericity and size distribution. Despite the dissolution/precipitation events observed during the release kinetics study, the doping ions were found to be able to be released from the MS to different extents. Although further *in vitro* and *in vivo* investigations are needed to

determine whether the released levels of Mg^{2+}, Zn^{2+} and Sr^{2+} are appropriate to induce changes in the cell performance, the ICP study suggested that MgHA MS would not reach the therapeutic Mg^{2+} levels and the ZnHA MS might be cytotoxic. Finally, SrHA samples exhibited a promising release performance for their further use in bone regeneration applications.

3.5. References

[1] K.M.Z. Hossain, U. Patel, I. Ahmed, Development of microspheres for biomedical applications: a review, Prog. Biomater. 4 (2015) 1–19. doi:10.1007/s40204-014-0033-8.

[2] J. Malda, C.G. Frondoza, Microcarriers in the engineering of cartilage and bone, Trends Biotechnol. 24 (2006) 299–304. doi:10.1016/j.tibtech.2006.04.009.

[3] R. Levato, J. Visser, J.A. Planell, E. Engel, J. Malda, M.A. Mateos-Timoneda, Biofabrication of tissue constructs by 3D bioprinting of cell-laden microcarriers, Biofabrication. 6 (2014) 035020. doi:10.1088/1758-5082/6/3/035020.

[4] W. Yuan, Y. Cai, Y. Chen, X. Hong, Z. Liu, Porous microsphere and its applications, Int. J. Nanomedicine. 8 (2013) 1111. doi:10.2147/IJN.S41271.

[5] R.A. Perez, A. El-Fiqi, J.-H. Park, T.-H. Kim, J.-H. Kim, H.-W. Kim, Therapeutic bioactive microcarriers: Co-delivery of growth factors and stem cells for bone tissue engineering, Acta Biomater. 10 (2014) 520–530. doi:10.1016/j.actbio.2013.09.042.

[6] M. Dang, L. Saunders, X. Niu, Y. Fan, P.X. Ma, Biomimetic delivery of signals for bone tissue engineering, Bone Res. 6 (2018) 25. doi:10.1038/s41413-018-0025-8.

[7] M.M. Martino, P.S. Briquez, K. Maruyama, J.A. Hubbell, Extracellular matrix-inspired growth factor delivery systems for bone regeneration, Adv. Drug Deliv. Rev. 94 (2015) 41–52. doi:10.1016/j.addr.2015.04.007.

[8] M.J. Dalby, A.J. García, M. Salmeron-Sanchez, Receptor control in mesenchymal stem cell engineering, Nat. Rev. Mater. 3 (2018) 17091. doi:10.1038/natrevmats.2017.91.

[9] M.S. Isakoff, S.S. Bielack, P. Meltzer, R. Gorlick, Osteosarcoma: Current Treatment and a Collaborative Pathway to Success, J. Clin. Oncol. 33 (2015) 3029–3035. doi:10.1200/JCO.2014.59.4895.

[10] F. Witte, The history of biodegradable magnesium implants: A review☆, Acta Biomater. 6 (2010) 1680–1692. doi:10.1016/j.actbio.2010.02.028.

[11] A. Bigi, E. Foresti, R. Gregorini, A. Ripamonti, N. Roveri, J.S. Shah, The role of magnesium on the structure of biological apatites, Calcif. Tissue Int. 50 (1992) 439–444. doi:10.1007/BF00296775.

[12] R.K. Rude, H.E. Gruber, Magnesium deficiency and osteoporosis: animal and human observations, J. Nutr. Biochem. 15 (2004) 710–716. doi:10.1016/j.jnutbio.2004.08.001.

[13] E.S. Thian, T. Konishi, Y. Kawanobe, P.N. Lim, C. Choong, B. Ho, M. Aizawa, Zinc-substituted hydroxyapatite: a biomaterial with enhanced bioactivity and

antibacterial properties, J. Mater. Sci. Mater. Med. 24 (2013) 437–445. doi:10.1007/s10856-012-4817-x.

[14] T. Huang, G. Yan, M. Guan, Zinc Homeostasis in Bone: Zinc Transporters and Bone Diseases, Int. J. Mol. Sci. 21 (2020) 1236. doi:10.3390/ijms21041236.

[15] C.O. Molokwu, Y. V Li, Zinc Homeostasis and Bone Mineral Density, Ohio Res. Clin. Rev. 15 (2006).

[16] S. Pors Nielsen, The biological role of strontium, Bone. 35 (2004) 583–588. doi:10.1016/j.bone.2004.04.026.

[17] E. Boanini, P. Torricelli, M. Fini, A. Bigi, Osteopenic bone cell response to strontium-substituted hydroxyapatite, J. Mater. Sci. Mater. Med. 22 (2011) 2079–2088. doi:10.1007/s10856-011-4379-3.

[18] P.J. Marie, Strontium as therapy for osteoporosis, Curr. Opin. Pharmacol. 5 (2005) 633–636. doi:10.1016/j.coph.2005.05.005.

[19] R. Zapanta LeGeros, Apatites in biological systems, Prog. Cryst. Growth Charact. 4 (1981) 1–45. doi:10.1016/0146-3535(81)90046-0.

[20] E. Boanini, M. Gazzano, A. Bigi, Ionic substitutions in calcium phosphates synthesized at low temperature, Acta Biomater. 6 (2010) 1882–1894. doi:10.1016/j.actbio.2009.12.041.

[21] S.C. Cox, P. Jamshidi, L.M. Grover, K.K. Mallick, Preparation and characterisation of nanophase Sr, Mg, and Zn substituted hydroxyapatite by aqueous precipitation, Mater. Sci. Eng. C. 35 (2014) 106–114. doi:10.1016/j.msec.2013.10.015.

[22] T. Tite, A.-C. Popa, L.M. Balescu, I.M. Bogdan, I. Pasuk, J.M.F. Ferreira, G.E. Stan, Cationic Substitutions in Hydroxyapatite: Current Status of the Derived Biofunctional Effects and Their In Vitro Interrogation Methods, Materials (Basel). 11 (2018) 2081. doi:10.3390/ma11112081.

[23] C. Rey, C. Combes, C. Drouet, H. Sfihi, Chemical Diversity of Apatites, Adv. Sci. Technol. 49 (2006) 27–36. doi:10.4028/www.scientific.net/AST.49.27.

[24] C. Rey, C. Combes, C. Drouet, H. Sfihi, A. Barroug, Physico-chemical properties of nanocrystalline apatites: Implications for biominerals and biomaterials, Mater. Sci. Eng. C. 27 (2007) 198–205. doi:10.1016/j.msec.2006.05.015.

[25] A. Bigi, G. Falini, E. Foresti, M. Gazzano, A. Ripmonti, N. Roveri, Rietveld structure refinements of calcium hydroxylapatite containing magnesium, Acta Crystallogr. Sect. B Struct. Sci. 52 (1996) 87–92. doi:10.1107/S0108768195008615.

[26] C. Capuccini, P. Torricelli, E. Boanini, M. Gazzano, R. Giardino, A. Bigi, Interaction of Sr-doped hydroxyapatite nanocrystals with osteoclast and osteoblast-like cells, J. Biomed. Mater. Res. Part A. 89A (2009) 594–600. doi:10.1002/jbm.a.31975.

[27] M. Schumacher, A. Henß, M. Rohnke, M. Gelinsky, A novel and easy-to-prepare strontium(II) modified calcium phosphate bone cement with enhanced mechanical properties, Acta Biomater. 9 (2013) 7536–7544. doi:10.1016/j.actbio.2013.03.014.

[28] F. Miyaji, Y. Kono, Y. Suyama, Formation and structure of zinc-substituted

calcium hydroxyapatite, Mater. Res. Bull. 40 (2005) 209–220. doi:10.1016/j.materresbull.2004.10.020.

[29] F. Ren, R. Xin, X. Ge, Y. Leng, Characterization and structural analysis of zinc-substituted hydroxyapatites, Acta Biomater. 5 (2009) 3141–3149. doi:10.1016/j.actbio.2009.04.014.

[30] D. Laurencin, N. Almora-Barrios, N.H. de Leeuw, C. Gervais, C. Bonhomme, F. Mauri, W. Chrzanowski, J.C. Knowles, R.J. Newport, A. Wong, Z. Gan, M.E. Smith, Magnesium incorporation into hydroxyapatite, Biomaterials. 32 (2011) 1826–1837. doi:10.1016/j.biomaterials.2010.11.017.

[31] V. Aina, L. Bergandi, G. Lusvardi, G. Malavasi, F.E. Imrie, I.R. Gibson, G. Cerrato, D. Ghigo, Sr-containing hydroxyapatite: morphologies of HA crystals and bioactivity on osteoblast cells, Mater. Sci. Eng. C. 33 (2013) 1132–1142. doi:10.1016/j.msec.2012.12.005.

[32] M. Šupová, M. Supová, Substituted hydroxyapatites for biomedical applications: A review, Ceram. Int. 41 (2015) 9203–9231. doi:10.1016/j.ceramint.2015.03.316.

[33] J.D. Pasteris, B. Wopenka, E. Valsami-Jones, Bone and Tooth Mineralization: Why Apatite?, Elements. 4 (2008) 97–104. doi:10.2113/GSELEMENTS.4.2.97.

[34] A. Thorpe, S. Creasey, C. Sammon, C. Le Maitre, Hydroxyapatite nanoparticle injectable hydrogel scaffold to support osteogenic differentiation of human mesenchymal stem cells, Eur. Cells Mater. 32 (2016) 1–23. doi:10.22203/eCM.v032a01.

[35] T.T. Demirtaş, G. Irmak, M. Gümüşderelioğlu, A bioprintable form of chitosan hydrogel for bone tissue engineering, Biofabrication. 9 (2017) 035003. doi:10.1088/1758-5090/aa7b1d.

[36] A. Wenz, K. Borchers, G.E.M. Tovar, P.J. Kluger, Bone matrix production in hydroxyapatite-modified hydrogels suitable for bone bioprinting, Biofabrication. 9 (2017) 044103. doi:10.1088/1758-5090/aa91ec.

[37] M. Carles-Carner, L.S. Saleh, S.J. Bryant, The effects of hydroxyapatite nanoparticles embedded in a MMP-sensitive photoclickable PEG hydrogel on encapsulated MC3T3-E1 pre-osteoblasts, Biomed. Mater. 13 (2018) 045009. doi:10.1088/1748-605X/aabb31.

[38] S. Suvarnapathaki, X. Wu, D. Lantigua, M.A. Nguyen, G. Camci-Unal, Hydroxyapatite-Incorporated Composite Gels Improve Mechanical Properties and Bioactivity of Bone Scaffolds, Macromol. Biosci. 20 (2020) 2000176. doi:10.1002/mabi.202000176.

[39] H.-R. Lin, Y.-J. Yeh, Porous alginate/hydroxyapatite composite scaffolds for bone tissue engineering: Preparation, characterization, and in vitro studies, J. Biomed. Mater. Res. 71B (2004) 52–65. doi:10.1002/jbm.b.30065.

[40] A.K. Gaharwar, S.A. Dammu, J.M. Canter, C.-J. Wu, G. Schmidt, Highly Extensible, Tough, and Elastomeric Nanocomposite Hydrogels from Poly(ethylene glycol) and Hydroxyapatite Nanoparticles, Biomacromolecules. 12 (2011) 1641–1650. doi:10.1021/bm200027z.

[41] Z. Emami, M. Ehsani, M. Zandi, H. Daemi, M.-H. Ghanian, R. Foudazi, Modified hydroxyapatite nanoparticles reinforced nanocomposite hydrogels based on gelatin/oxidized alginate via Schiff base reaction, Carbohydr. Polym.

Technol. Appl. 2 (2021) 100056. doi:10.1016/j.carpta.2021.100056.

[42] S. Dasgupta, S.S. Banerjee, A. Bandyopadhyay, S. Bose, Zn- and Mg-Doped Hydroxyapatite Nanoparticles for Controlled Release of Protein, Langmuir. 26 (2010) 4958–4964. doi:10.1021/la903617e.

[43] Z. Zhao, Effect of doping ions and organic molecules on the precipitation and biological interactions of nanostructured calcium phosphates, Universitat Politècnica de Catalunya, 2015.

[44] A. Barbanente, B. Palazzo, L.D. Esposti, A. Adamiano, M. Iafisco, N. Ditaranto, D. Migoni, F. Gervaso, R. Nadar, P. Ivanchenko, S. Leeuwenburgh, N. Margiotta, Selenium-doped hydroxyapatite nanoparticles for potential application in bone tumor therapy, J. Inorg. Biochem. 215 (2021) 111334. doi:10.1016/J.JINORGBIO.2020.111334.

[45] J. Schindelin, I. Arganda-Carreras, E. Frise, V. Kaynig, M. Longair, T. Pietzsch, S. Preibisch, C. Rueden, S. Saalfeld, B. Schmid, J.-Y. Tinevez, D.J. White, V. Hartenstein, K. Eliceiri, P. Tomancak, A. Cardona, Fiji: an open-source platform for biological-image analysis, Nat. Methods. 9 (2012) 676–682. doi:10.1038/nmeth.2019.

[46] A. Bigi, E. Foresti, M. Gandolfi, M. Gazzano, N. Roveri, Inhibiting effect of zinc on hydroxylapatite crystallization, J. Inorg. Biochem. 58 (1995) 49–58. doi:10.1016/0162-0134(94)00036-A.

[47] I. Gutowska, Z. Machoy, B. Machaliński, The role of bivalent metals in hydroxyapatite structures as revealed by molecular modeling with the HyperChem software, J. Biomed. Mater. Res. Part A. 75A (2005) 788–793. doi:10.1002/jbm.a.30511.

[48] S. Diallo-Garcia, D. Laurencin, J.-M. Krafft, S. Casale, M.E. Smith, H. Lauron-Pernot, G. Costentin, Influence of Magnesium Substitution on the Basic Properties of Hydroxyapatites, J. Phys. Chem. C. 115 (2011) 24317–24327. doi:10.1021/jp209316k.

[49] Z.Y. Li, W.M. Lam, C. Yang, B. Xu, G.X. Ni, S.A. Abbah, K.M.C. Cheung, K.D.K. Luk, W.W. Lu, Chemical composition, crystal size and lattice structural changes after incorporation of strontium into biomimetic apatite, Biomaterials. 28 (2007) 1452–1460. doi:10.1016/j.biomaterials.2006.11.001.

[50] A. Bigi, E. Boanini, C. Capuccini, M. Gazzano, Strontium-substituted hydroxyapatite nanocrystals, Inorganica Chim. Acta. 360 (2007) 1009–1016. doi:10.1016/j.ica.2006.07.074.

[51] C. Rey, O. Marsan, C. Combes, C. Drouet, D. Grossin, S. Sarda, Characterization of Calcium Phosphates Using Vibrational Spectroscopies, in: Adv. Calcium Phosphate Biomater., Springer, Berlin, Heidelberg, 2014: pp. 229–266. doi:10.1007/978-3-642-53980-0_8.

[52] V. Aina, G. Lusvardi, B. Annaz, I.R. Gibson, F.E. Imrie, G. Malavasi, L. Menabue, G. Cerrato, G. Martra, Magnesium- and strontium-co-substituted hydroxyapatite: the effects of doped-ions on the structure and chemico-physical properties, J. Mater. Sci. Mater. Med. 23 (2012) 2867–2879. doi:10.1007/s10856-012-4767-3.

[53] S. Batool, U. Liaqat, Z. Hussain, M. Sohail, Synthesis, Characterization and

Process Optimization of Bone Whitlockite, Nanomaterials. 10 (2020) 1856. doi:10.3390/nano10091856.

[54] Q. Xing, K. Yates, C. Vogt, Z. Qian, M.C. Frost, F. Zhao, Increasing Mechanical Strength of Gelatin Hydrogels by Divalent Metal Ion Removal, Sci. Rep. 4 (2014) 4706. doi:10.1038/srep04706.

[55] G.S. Mandair, M.D. Morris, Contributions of Raman spectroscopy to the understanding of bone strength, Bonekey Rep. 4 (2015) 620. doi:10.1038/bonekey.2014.115.

[56] H. Ye, Rahul, U. Kruger, T. Wang, S. Shi, J. Norfleet, S. De, Burn-related Collagen Conformational Changes in ex vivo Porcine Skin using Raman Spectroscopy, Sci. Rep. 9 (2019) 19138. doi:10.1038/s41598-019-55012-1.

[57] B.G. Frushour, J.L. Koenig, Raman scattering of collagen, gelatin, and elastin, Biopolymers. 14 (1975) 379–391. doi:10.1002/bip.1975.360140211.

[58] G. Kulkarni, P. Guha Ray, P.K. Byram, M. Kaushal, S. Dhara, S. Das, Tailorable hydrogel of gelatin with silk fibroin and its activation/crosslinking for enhanced proliferation of fibroblast cells, Int. J. Biol. Macromol. 164 (2020) 4073–4083. doi:10.1016/j.ijbiomac.2020.09.016.

[59] G. Kulkarni, P. Guha Ray, S. Das, S. Biswas, S. Dhara, S. Das, Raman spectroscopy assisted biochemical evaluation of L929 fibroblast cells on differentially crosslinked gelatin hydrogels, Spectrochim. Acta Part A Mol. Biomol. Spectrosc. 257 (2021) 119760. doi:10.1016/j.saa.2021.119760.

[60] S. Sprio, A. Tampieri, E. Landi, M. Sandri, S. Martorana, G. Celotti, G. Logroscino, Physico-chemical properties and solubility behaviour of multi-substituted hydroxyapatite powders containing silicon, Mater. Sci. Eng. C. 28 (2008) 179–187. doi:10.1016/j.msec.2006.11.009.

[61] J.-M. Sadowska, J. Guillem-Marti, E.B. Montufar, M. Espanol, M.-P. Ginebra, Biomimetic Versus Sintered Calcium Phosphates: The In Vitro Behavior of Osteoblasts and Mesenchymal Stem Cells, Tissue Eng. Part A. 23 (2017) 1297–1309. doi:10.1089/ten.tea.2016.0406.

[62] G. Daculsi, Biphasic calcium phosphate concept applied to artificial bone, implant coating and injectable bone substitute, Biomaterials. 19 (1998) 1473–1478.

[63] S. Cazalbou, D. Eichert, X. Ranz, C. Drouet, C. Combes, M.F. Harmand, C. Rey, Ion exchanges in apatites for biomedical applications, J. Mater. Sci. Mater. Med. 16 (2005) 405–409.

[64] L. Wang, G.H. Nancollas, Calcium Orthophosphates: Crystallization and Dissolution, Chem. Rev. 108 (2008) 4628–4669. doi:10.1021/cr0782574.

[65] P.N. Kumta, C. Sfeir, D.-H. Lee, D. Olton, D. Choi, Nanostructured calcium phosphates for biomedical applications: novel synthesis and characterization, Acta Biomater. 1 (2005) 65–83. doi:10.1016/j.actbio.2004.09.008.

[66] A. Ruffini, S. Sprio, L. Preti, A. Tampieri, Synthesis of Nanostructured Hydroxyapatite via Controlled Hydrothermal Route, in: Biomater. Tissue Reconstr. or Regen., IntechOpen, 2019. doi:10.5772/intechopen.85091.

[67] H.B. Pan, Z.Y. Li, W.M. Lam, J.C. Wong, B.W. Darvell, K.D.K. Luk, W.W. Lu,

Solubility of strontium-substituted apatite by solid titration, Acta Biomater. 5 (2009) 1678–1685. doi:10.1016/j.actbio.2008.11.032.

[68] J.T.Y. Lee, Y. Leng, K.L. Chow, F. Ren, X. Ge, K. Wang, X. Lu, Cell culture medium as an alternative to conventional simulated body fluid, Acta Biomater. 7 (2011) 2615–2622. doi:10.1016/j.actbio.2011.02.034.

[69] W.-C. Lu, E. Pringa, L. Chou, Effect of magnesium on the osteogenesis of normal human osteoblasts, Magnes. Res. 30 (2017) 42–52. doi:10.1684/mrh.2017.0422.

[70] J.-W. Park, T. Hanawa, J.-H. Chung, The relative effects of Ca and Mg ions on MSC osteogenesis in the surface modification of microrough Ti implants, Int. J. Nanomedicine. Volume 14 (2019) 5697–5711. doi:10.2147/IJN.S214363.

[71] J.P. O'Connor, D. Kanjilal, M. Teitelbaum, S.S. Lin, J.A. Cottrell, Zinc as a Therapeutic Agent in Bone Regeneration, Materials (Basel). 13 (2020) 2211. doi:10.3390/ma13102211.

[72] S. Horiuchi, M. Hiasa, A. Yasue, K. Sekine, K. Hamada, K. Asaoka, E. Tanaka, Fabrications of zinc-releasing biocement combining zinc calcium phosphate to calcium phosphate cement, J. Mech. Behav. Biomed. Mater. 29 (2014) 151–160. doi:10.1016/j.jmbbm.2013.09.005.

[73] A. Togari, S. Arakawa, M. Arai, S. Matsumoto, Alteration of in vitro bone metabolism and tooth formation by zinc, Gen. Pharmacol. Vasc. Syst. 24 (1993) 1133–1140. doi:10.1016/0306-3623(93)90360-A.

[74] A. Ito, H. Kawamura, M. Otsuka, M. Ikeuchi, H. Ohgushi, K. Ishikawa, K. Onuma, N. Kanzaki, Y. Sogo, N. Ichinose, Zinc-releasing calcium phosphate for stimulating bone formation, Mater. Sci. Eng. C. 22 (2002) 21–25. www.elsevier.com/locate/msec (accessed October 10, 2021).

[75] A. Cerovic, I. Miletic, S. Sobajic, D. Blagojevic, M. Radusinovic, A. El-Sohemy, Effects of Zinc on the Mineralization of Bone Nodules from Human Osteoblast-like Cells, Biol. Trace Elem. Res. 116 (2007) 61–71.

[76] S. Srivastava, N. Kumar, R.S. Thakur, P. Roy, Role of Vanadium (V) in the Differentiation of C3H10t1/2 Cells Towards Osteoblast Lineage: A Comparative Analysis with Other Trace Elements, Biol. Trace Elem. Res. 152 (2013) 135–142. doi:10.1007/s12011-013-9602-2.

[77] J. Braux, F. Velard, C. Guillaume, S. Bouthors, E. Jallot, J.-M. Nedelec, D. Laurent-Maquin, P. Laquerrière, A new insight into the dissociating effect of strontium on bone resorption and formation, Acta Biomater. 7 (2011) 2593–2603. doi:10.1016/j.actbio.2011.02.013.

[78] M. Montesi, S. Panseri, M. Dapporto, A. Tampieri, S. Sprio, Sr-substituted bone cements direct mesenchymal stem cells, osteoblasts and osteoclasts fate, PLoS One. 12 (2017) 1–13. doi:10.1371/journal.pone.0172100.

[79] S. Tadier, R. Bareille, R. Siadous, O. Marsan, C. Charvillat, S. Cazalbou, J. Amédée, C. Rey, C. Combes, Strontium-loaded mineral bone cements as sustained release systems: Compositions, release properties, and effects on human osteoprogenitor cells, J. Biomed. Mater. Res. Part B Appl. Biomater. 100B (2012) 378–390. doi:10.1002/jbm.b.31959.

[80] P.J. Marie, P. Ammann, G. Boivin, C. Rey, Mechanisms of Action and

Therapeutic Potential of Strontium in Bone, Calcif. Tissue Int. 69 (2001) 121–129. doi:10.1007/s002230010055.

[81] S.G. Dahl, P. Allain, P.J. Marie, Y. Mauras, G. Boivin, P. Ammann, Y. Tsouderos, P.D. Delmas, C. Christiansen, Incorporation and Distribution of Strontium in Bone, Bone. 28 (2001) 446–453.

[82] K. Glenske, P. Donkiewicz, A. Köwitsch, N. Milosevic-Oljaca, P. Rider, S. Rofall, J. Franke, O. Jung, R. Smeets, R. Schnettler, S. Wenisch, M. Barbeck, Applications of Metals for Bone Regeneration, Int. J. Mol. Sci. 19 (2018) 826. doi:10.3390/ijms19030826.

[83] E. Bosch-Rué, L. Diez-Tercero, B. Giordano-Kelhoffer, L.M. Delgado, B.M. Bosch, M. Hoyos-Nogués, M.A. Mateos-Timoneda, P.A. Tran, F.J. Gil, R.A. Perez, Biological Roles and Delivery Strategies for Ions to Promote Osteogenic Induction, Front. Cell Dev. Biol. 8 (2021) 1809. doi:10.3389/fcell.2020.614545.

Chapter 4

Microsphere Incorporation as a Strategy to Tune the Biological Performance of Bioinks

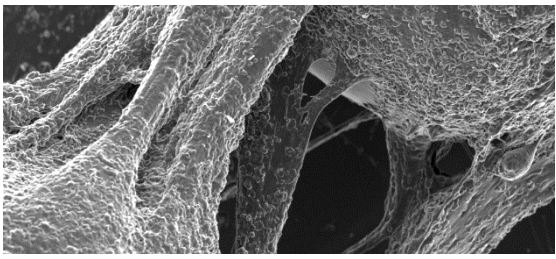

MICROSPHERE INCORPORATION AS A STRATEGY TO TUNE THE BIOLOGICAL PERFORMANCE OF BIOINKS

Scope

The modulation of the hydrogel properties is required in the development of bioinks in order to achieve a self-supporting ink that is extrudable and maintains its stability after printing while assuring the viability of the cells embedded within. One underexplored strategy is the incorporation of microspheres to alginate-based formulations as a way to provide cell-adhesion moieties while improving the mechanical properties of the final cell-laden inks. Therefore, in **Chapter 4**, the gelatine and gelatine-hydroxyapatite microspheres developed in the previous chapter, together with calcium-deficient hydroxyapatite microspheres, will be added in the formulation of bioinks, and their rheological and biological implications will be assessed. Will their surface serve as an anchorage point for the osseous cells? Will the mineral charge be sufficient for the stimulation of osteogenic differentiation of the cells embedded?

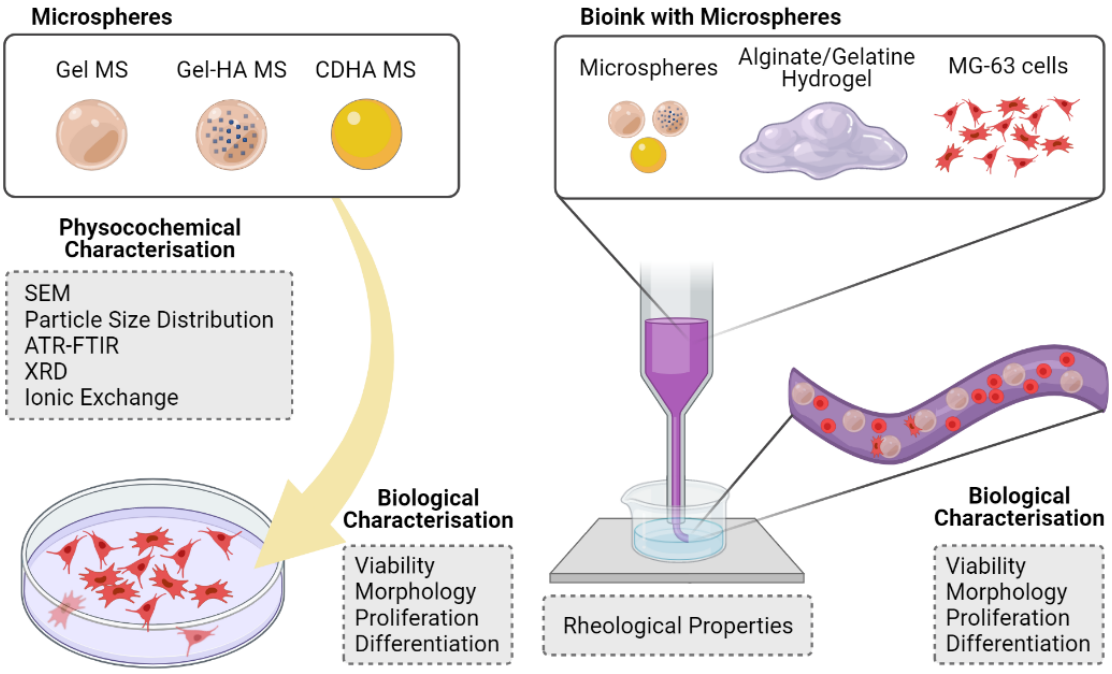

4.1. Introduction

In recent years, the tissue engineering field has progressed from two-dimensional (2D) cell culture to 3D models. Indeed, 3D systems are biologically more relevant, as they can reproduce better the physiological environment of the tissues [1,2]. This evolution has been possible thanks to the expansion of additive manufacturing technologies, that permit to develop complex structures using layer by layer deposition. Moreover, they allow to control and tune different features, such as the scaffold architecture or the size and shape of the porosity for the specific application and cell type [3].

The initial approach concerning 3D models was to generate biocompatible scaffolds that could be further seeded with cells. More recently, 3D bioprinting has advanced these techniques by the loading of cells directly in the ink, creating a promising approach to enhance the regenerative process. Although a lot of advances have been done in the development of extrusion-based bioinks, the optimal mechanical and biological requirements are usually antagonistic, which makes the perfect bioink difficult to obtain [4]. Indeed, low polymer content bioinks, which would be desirable for cell survival and cell migration, may compromise the shape fidelity of the printed struts. In this sense, the ideal cell-laden ink must be mechanically stable and provide high resolution when printed. Regarding the cellular needs, it must be highly biocompatible and allow the proliferation and differentiation of the cells [5–8].

Hydrogels are the most used materials for the formulation of bioinks, mainly due to their ability to sustain living cells and their adjustable mechanical properties. In particular, alginate is currently one of the most attractive candidates, considering its easy cross-linking capability, which takes place through divalent cation gelation, high availability, low cost and safety not only for the human body but also for the embedded cells [9]. Nevertheless, its main drawback is the lack of bioactivity, which has led to the implementation of additional processing strategies. One of them is the incorporation of bioactive polymers, such as gelatine, collagen, hyaluronic acid and chitosan among others, to encourage cell adhesion and proliferation in a tissue-specific manner [10,11]. However, due to the complexity of these proteins, it becomes difficult to control the specific signals presented to the cells. The functionalisation of the initial polymer with short cell-adhesive peptides, mainly RGD-based sequences, has been proposed as an alternative way to mimic the extracellular matrix (ECM) and to improve the cell attachment and spreading within the bioinks [12–14]. The main drawback of this approach is the requirement of an additional cross-linking step to bind the bioactive molecule to the alginate [15,16], which not only lengthens the process but may adversely affect the rheological properties of the final bioink and, in turn, their manipulation and *in vitro* performance.

As an alternative strategy, the combination of alginate with different inorganic materials has been explored, which is especially attractive in the field of bone regeneration as it may allow endowing the ink with additional osteogenic cues. The incorporation of bioglass nanoparticles (NPs) capable of delivering biologically active ions such as calcium and silicon in the bioinks has been studied, reporting increased ALP levels and enhanced osteodifferentiation [17,18]. In the same line, the use of hydroxyapatite (HA) particles in gels and bioinks has been proved to increase osteogenic differentiation [19–21].

Besides the incorporation of nanomaterials, the addition of microspheres (MS) in the formulation of bioinks may be of major interest as they can solve the cell-adhering issues

by providing the cells with a surface to attach and improve the mechanical properties of the final constructs. Some studies explored this strategy, using polymeric MS [22–24]. Levato *et al.* added PLA MS into GelMA-based bioinks reporting increased compressive modulus, as well as enhanced cell adhesion and osteogenic differentiation for the condition with preseeded MS [22]. Likewise, in the work of Tan *et al.* the compressive properties of agarose-collagen hydrogels were improved by the incorporation of PLGA MS. Moreover, they demonstrated the viability and proliferation of different cell types preseeded on the MS [23]. Abu Awwad *et al.* explored the delivery of bone therapeutic agents from PLGA MS in a bioprinted system, showing the promotion of osteogenic differentiation of MSC [24]. In spite of the interesting findings, in these works, the authors only explored the incorporation of PLA/PLGA MS to the bioinks. In the present work, we intend to assess the performance of MS with different compositions, including polymeric, hybrid and ceramic MS, exploring their role not only as a support for cell adhesion but also as a way to tune cell behaviour.

We hypothesise that the design of simple, robust and tuneable alginate-based bioinks through the incorporation of microspheres with improved affinity for bone, would be a strong asset to the field of bone bioprinting. MS of three different compositions are analysed, including: i) gelatine, ii) hydroxyapatite nanoparticle (HA NPs)- containing gelatine; and iii) calcium-deficient hydroxyapatite. The performance of the different MS is tested by direct cell seeding on the MS and also after bioink extrusion of a formulation combining an alginate/gelatine hydrogel with MS and cells. The ability of the cells to colonise the MS in the bioink formulation is further tested using two different degrees of hydrogel cross-linking.

4.2. Experimental Section

4.2.1. Synthesis of Gelatine Microspheres

Gelatine microspheres (Gel MS) were prepared by a water in oil emulsion. Specifically, gelatine (Fluka) solution 15 wt% in bi-distilled water (ddH_2O) was preheated to 50 ^oC. Subsequently, the solution was added dropwise into 50 ^oC preheated 400 ml olive oil with mechanical stirring at 900 rpm to form an emulsion. After 10 min, the mixture was put in an ice bath and stirred for 30 min, prior to the incorporation of cold acetone. The emulsion was left stirring for 1 h before being filtered to collect the synthesised MS. The final powder was rinsed with acetone and left to dry before sieving to the desired particle size (*i.e.* 40-100 µm). The MS were further cross-linked following a protocol slightly different from the one applied in **Chapter 3**. The MS were immersed in a cold aqueous solution of 50 mM N-(3-dimethylaminopropyl)-N′-ethylcarbodiimide hydrochloride (EDC, Sigma-Aldrich) and 75 mM N-hydroxysuccinimide (NHS, Sigma-Aldrich) for 1.5 h and thoroughly rinsed with distilled water.

4.2.2. Synthesis of Hydroxyapatite-Containing Gelatine Microspheres

For the synthesis of the hydroxyapatite-containing gelatine microspheres (Gel-HA MS), hydroxyapatite nanoparticles (HA NPs) were incorporated into the initial gelatine solution before following the previous protocol. Therefore, HA NPs were produced by a wet precipitation method, as described elsewhere [25]. Briefly, 200 mM H_3PO_4 (85 wt% pure, PanReac AppliChem) was added dropwise into a solution of 333 mM $Ca(OH)_2$ (96 wt% pure, Fluka) under constant stirring at 40 ^oC at a rate of 1 ml min^{-1}, according to the

Equation 4.1. The supplementation of phosphoric acid was stopped when the pH reached 8 and the product was left stirring for 30 min. Afterwards, stirring was stopped and the suspension was left to mature overnight at room temperature before being rinsed three times with ddH_2O after centrifugation (5430 R, Eppendorf). The final powder was freeze-dried (Cryodos, Telstar).

$$10\ Ca(OH)_2 + 6\ H_3PO_4 \rightarrow Ca_{10}(PO_4)_6(OH)_2 + 18\ H_2O \qquad \textbf{Equation 4.1}$$

A suspension of 10 wt% HA NPs and 10 wt% sodium citrate (Sigma-Aldrich) was prepared and subsequently sonicated in a high-frequency ultrasound probe sonicator (450D, Branson Digital) using a 3 mm diameter tip at 40% amplitude for 2 min. The dispersion was mixed 1:1 with a 30 wt% gelatine solution and added in the oil as previously described. This resulted in microspheres loaded with 25 wt% of HA (dry weight), which were additionally sieved and cross-linked following the same cross-linking procedure as for the Gel MS.

4.2.3. Synthesis of Calcium-Deficient Hydroxyapatite Microspheres

A previously established protocol [26] was adapted for the synthesis of the calcium-deficient HA (CDHA) MS. The powder phase of the calcium phosphate cement consisted of α-tricalcium phosphate (α-TCP), obtained by sintering a mixture of calcium hydrogen phosphate ($CaHPO_4$, Sigma-Aldrich) and calcium carbonate ($CaCO_3$, Sigma-Aldrich) to a Ca/P ratio of 1.5 in an oven (CRN-58, Hobersal) at 1400 ºC for 15 h and subsequent quenching in air. The resulting α-TCP was milled in a planetary mill (Pulverisette 6, Fritsch GmbB) to obtain a mean powder-particle size of 2.8 μm [27], and 2 wt% of precipitated HA (Merck) was added as a seed. In order to obtain the calcium phosphate cement slurry, the seeded α-TCP powder and 1 wt% of sodium citrate were mixed with a 5 wt% gelatine solution in phosphate-buffered saline (PBS, Gibco) in a liquid-to-powder ratio of 1.2. This resulted in microspheres with 94 wt% load of mineral content (dry weight).

To synthesise the MS, 3 ml of the ceramic slurry were added drop by drop into 300 ml of olive oil previously heated to 60 ºC. The emulsion was mechanically stirred (BDC 2002, Heidolph) for 2 h. Afterwards, the MS were separated from the emulsion by the addition of 0.01% Triton X-100 (Sigma-Aldrich) in Ringer's solution (0.9% sodium chloride, PanReac AppliChem). The MS were further washed with acetone and the remaining gelatine cross-linked with EDC/NHS following the previously described protocol. Finally, the powder was immersed in Ringer's solution for a week, to allow the hydrolysis of α-TCP to CDHA, according to **Equation 4.2**. Once the setting was done, the MS were dried and sieved from 40 to 100 μm.

$$3\ Ca_3(PO_4)_2 + H_2O \rightarrow Ca_9(PO_4)_5(HPO_4)(OH) \qquad \textbf{Equation 4.2}$$

4.2.4. Physicochemical Characterisation of the Microspheres

The morphological evaluation of the different MS was performed by field emission scanning electron microscopy (FESEM, JSM-7001F, JEOL) with a previous carbon coating. The size distribution of the MS was assessed through image analysis (FIJI, ImageJ software [28]) of optic microscopy (AE2000, Motic) acquisitions.

Fourier-transform infrared spectroscopy (FTIR, Nicolet 6700, Thermo Scientific) in the attenuated total reflectance (ATR) mode was used to check the presence of the functional groups of apatite and gelatine in the different MS. Data were obtained with a spectral resolution of 4 cm^{-1} and averaging of 64 scans, in the 700 to 2000 cm^{-1} range. Moreover, phase composition of both Gel-HA MS and CDHA MS was determined by X-ray powder diffraction (XRD, D8 Advance, Bruker) using Cu Kα radiation at 40 kV and 40 mA, collecting the data with a step size of 0.02º. The counting time was 2 s per step and the acquisition was done from 20 to 40º 2θ range. The diffractograms were compared to the standard pattern of HA (ICDD PDF 09-0432) for the indexing of the peaks.

In addition, calcium and phosphorus ionic exchanges in cell culture media were measured. 10 mg of MS were put in contact with 1 ml of Dulbecco's modified eagle medium (DMEM) supplemented with 10% foetal bovine serum (FBS), 20 mM 4-(2-hydroxyethyl)-1-piperazineethanesulfonic acid buffer (HEPES), 2 mM L-glutamine, 50 U ml^{-1} penicillin and 50 µg ml^{-1} streptomycin (all from Gibco), for four days. The medium was changed daily and the supernatants were collected, diluted 20-fold in 2 wt% HNO_3 (69 wt% pure, PanReac AppliChem) and analysed by inductively coupled plasma optical emission spectrometry (ICP-OES, 5100, Agilent Technologies). ^{44}Ca and ^{31}P signals were calibrated against a multi-element standard solution (Inorganic Ventures).

4.2.5. Preparation of the Bioinks

MG-63 pre-osteoblast cells (ATCC) were cultured in supplemented DMEM in a 95% humidified atmosphere containing 5% CO_2 at 37 ºC. Previous to cell incorporation in the bioinks, the materials and the powders were sterilised with 70% ethanol or by low-pressure plasma treatment, respectively.

Three formulations were studied, depending on which type of MS was used: Gel, Gel-HA or CDHA. Moreover, a bioink without the addition of MS was used as a control. Additionally, two different cross-linkings were tested, resulting in a total of eight different bioinks. In all the cases, sieved MS (40 to 100 µm) were used.

Sodium alginate (PanReac AppliChem) and gelatine were dissolved in DMEM at concentrations of 6 and 8 w/v %, respectively, and mixed in a 1:1 ratio. Cells ($2 \cdot 10^6$ cells ml^{-1}) and MS (60 mg ml^{-1}) were incorporated in the inks. The components were thoroughly mixed and homogenised by hand. The mixture was immediately extruded at 30 mm s^{-1} through a 22 Ga nozzle directly to a 150 mM $CaCl_2$ (Sigma-Aldrich) bath, by means of a customised 3D printer (Fundació CIM). Afterwards, the bioinks were rinsed three times with supplemented DMEM and maintained at 37 ºC and 5% CO_2 atmosphere.

As previously mentioned, two different cross-linking protocols were investigated: (1) a strong cross-linking (sCL) consisting of immersion for 15 min in the $CaCl_2$ bath, followed by maintenance in supplemented DMEM enriched with $CaCl_2$ up to 5 mM and (2) a weak cross-linking (wCL) consisting of immersion for 10 min in the initial $CaCl_2$ bath followed with maintenance in the original supplemented DMEM.

Moreover, discs were prepared for rheological studies. The samples were prepared by extruding 1 ml of bioink without cells into a ø= 20 mm mould and cross-linking them using either wCL or sCL protocols.

4.2.6. Rheological Study

The rheological properties of the four bioinks formulations without cells were analysed. The measurements were carried out on a rotational rheometer (Discovery HR-2, TA Instrument), using a rough parallel plate geometry (ø= 20 mm) with a gap of 1 mm (10 times the size of the MS). First, an oscillatory amplitude (OA) sweep was performed from 10% to 1000% at a constant frequency of 1 Hz to analyse the viscoelasticity. The second test was a 3-interval thixotropy test (3-ITT) to study the thixotropy and the shape-retention ability of the bioinks. Precisely, it consisted of three consecutive oscillatory intervals, all of them at a constant frequency of 1 Hz: (1) a low strain within the linear viscoelastic region (LVR) of the previous amplitude sweeps (*i.e.* 10%) for 1 min to simulate the rest condition of the bioink before being extruded, (2) a high strain, above the fluid point of the amplitude sweep (*i.e.* when G' = G", 700%) for 30 s to mimic the extrusion process and (3) the conditions of the first interval to simulate the rest condition of the bioink just immediately after being extruded. The data of the third interval was acquired using a fast sampling mode, in contrast to the normal acquisition mode used in the other intervals.

Additionally, the two CL used in the present work were compared using discs. The rheological analysis was performed at the same rotational rheometer using a rough parallel plate geometry (ø= 20 mm) with a gap of 3 mm. Specifically, the test consisted of a short oscillatory step with a strain of 10% (within the LVR of the bioinks) and a constant frequency of 1 Hz for 2 min to mimic the rest conditions of the bioinks just immediately after extrusion. Each sample was analysed at 0, 7 and 14 days.

4.2.7. Direct Cell Culture on the Microspheres

The behaviour of MG-63 cells in direct contact with the different MS was examined and compared to the biological results of the bioink. To do so, 48-well plates were treated with 1 wt% albumin in PBS to prevent cell adhesion. 10 mg of MS were added to each well and MG-63 cells were seeded on top at a concentration of 50000 cells ml^{-1}. A control sample with no MS was also included in the study. The biological performance was examined in terms of cell viability, cell proliferation, cell morphology and gene expression, using the following protocols.

4.2.8. Cell Viability Analysis

The migration and the viability of the MG-63 either cultured directly on the MS or inside the bioinks were assessed by live/dead (L/D) staining at different time points (*i.e.* 0, 3, 7, 14 and 21 days). Specifically, 3 µM calcein AM (Santa Cruz Biotechnology) and 1.5 µM propidium iodide (PI, Sigma-Aldrich) were supplemented to the cells into fresh media as indicators of live and dead cells, respectively. The stained cells were imaged under a laser confocal scanning microscope (LSM 800, Zeiss). In addition, the images of the bioinks obtained at day 0 were used to quantify the cell viability after the extrusion using ImageJ software.

4.2.9. Cell Proliferation and Cell Morphology Evaluation

Cell proliferation either on the MS or inside the hydrogels was evaluated at 0, 3, 7, 14 and 21 days with Presto Blue (Invitrogen) assay, following the manufacturer's instructions and measuring the fluorescence in a microplate reader (540 nm excitation/590 nm emission wavelengths). Afterwards, the samples were rinsed with PBS to remove the staining and fresh cell culture media was added.

The evaluation of the cell morphology and the cell adhesion to the MS was done at days 3, 7 and 14 for the cells cultured with the MS and after 21 and 14 days in culture for sCL and wCL bioinks, respectively. The specimens were rinsed with PBS and subsequently fixed with 4 wt% paraformaldehyde solution (PFA, EMS) for 20 min at room temperature. The cells were permeabilised through incubation with 0.05% Triton X-100 in PBS for 15 min before staining them with Alexa Fluor 546 phalloidin (1:400, Invitrogen) in 0.05% Triton X-100 for 1 h. For nuclei staining, the samples were put in contact with 4′,6-diamidino-2-phenylindole (DAPI, 1:1000, Sigma-Aldrich) for 2 min. All steps were followed by rinsing with 0.15% glycine solution (Sigma-Aldrich) in PBS. Finally, the samples were visualised with confocal LSM.

In addition, the cell adhesion and spreading were checked by SEM (Phenom XL, PhenomWorld) in the wCL Gel MS-containing bioink. The samples cultured for 14 days were fixed with 2.5% glutaraldehyde solution, dehydrated in an increasing series of ethanol solutions and sputtered with a thin layer of carbon to allow observation.

4.2.10. Gene Expression Assessment

The cell differentiation to osteoblastic phenotype was assessed by measuring the gene expression of osteogenic markers through reverse transcription quantitative polymerase chain reaction (RT-qPCR). Prior to the RNA extraction with RNeasy Mini Kit (Qiagen), the bioinks were incubated with alginate-dissolving buffer (55 mM sodium citrate, 30 mM EDTA, 150 mM NaCl, pH= 6.8) for 10 min at 37 ºC, and the, alginate was eliminated by centrifuging 10 min at 300 g. The RNA obtained was quantified spectrophotometrically with Take3 micro-volume plate (BioTek Instruments) and reverse transcription was performed using QuantiTect Reverse Transcription Kit (Qiagen). cDNA was amplified with the QuantiFast SYBR Green RT-PCR Kit (Qiagen) in a Mic qPCR Cycler (Biomolecular Systems), using specific primers listed in **Table 4.1**. In all runs, melt curve analysis was done to ensure the specificity of the primers. Moreover, a negative control was run in parallel to verify the absence of contamination. Relative gene expression levels were evaluated using the $2^{-\Delta\Delta Ct}$ method and GAPDH was used as the housekeeping gene. Data were normalised to the control at days 3 and 7 for the culture onto the MS and in the bioinks, respectively.

Table 4.1. Primers' sequences used for RT-qPCR

Gene	Primers' sequences (Fw= forward; Rv= reverse)
Glyceraldehyde 3-phosphate dehydrogenase (GAPDH)	Fw: 5'-TTGCCATCAATGACCCCTTCA-3' Rv: 5'-CGCCCCACTTGATTTTGGA-3'
Alkaline phosphatase (ALP)	Fw: 5'-ATCTTTGGTCTGGCTCCCATG-3' Rv: 5'-TTTCCCGTTCACCGTCCAC-3'
Collagen type I (Col. I)	Fw: 5'-AGGTCCCCCTGGAAAGAA-3' Rv: 5'-AATCCTCGAGCACCCTGA-3'
Runt-related transcription factor 2 (RUNX2)	Fw: 5'-AAATGCCTCCGCTGTTATGAA-3' Rv: 5'-GCTCCGGCCCACAAATCT-3'
Osterix (OSX)	Fw: 5'-TGCTTGAGGAGGAAGTTCAC-3' Rv: 5'-AGGTCACTGCCCACAGAGTA-3'
Osteopontin (OPN)	Fw: 5'-AGCTGGATGACCAGAGTGCT-3' Rv: 5'-TGAAATTCATGGCTGTGGAA-3'
Osteocalcin (OCN)	Fw: 5'-ATGAGAGCCCTCACACTCCT-3' Rv: 5'-CTTGGACACAAAGGCTGCAC-3'

4.2.11. Statistical Analysis

All data are presented as mean ± standard deviation, except for the viability and proliferation outcomes, where mean ± standard error of the mean is reported. The distribution of the data was checked with Shapiro-Wilk test. Significant differences between samples were determined using ANOVA followed by Tukey's posthoc test or Kruskal-Wallis test for normally and non-normally distributed data, respectively. Significance level was set for $p<0.05$. Statistical analysis was performed using SPSS software.

4.3. Results

4.3.1. Physicochemical Characterisation of the Microspheres

The morphology and microstructure of the different MS observed by SEM are depicted in **Figure 4.1A**. All the conditions, *i.e.* Gel MS, Gel-HA MS and CDHA MS, showed a high degree of sphericity and the diameter size was shown to be in the range of 40 to 100 µm, as expected from the sieving step. Moreover, needle-shaped HA NPs were observed, embedded in a gelatine matrix, in the Gel-HA MS when the backscattering detector was used. The microstructure of the CDHA MS consisted of an entangled network of nanometric plate-like crystals resulting from the setting reaction of α-TCP to CDHA.

Image analysis was performed to determine the size distribution of the MS. As observed in **Figure 4.1B**, all of them presented a monomodal normal particle size distribution. The average size diameter of the three types of MS was similar in dry conditions, being Gel MS the ones with the largest size, with a mean value of 82 ± 16 µm. On the other hand, Gel-HA MS and CDHA MS showed a mean size of 73 ± 17 and 66 ± 15 µm, respectively. Although gelatine was chemically cross-linked, the MS increased their volume in contact with an aqueous solution due to swelling. Thus, the particle size increased to 106 ± 30 µm for Gel MS and 123 ± 32 µm for the Gel-HA MS. An almost negligible volume gain

was observed for the wet CDHA microspheres, reaching an average diameter of 71 ± 17 µm, which was consistent with their mostly inorganic nature.

Figure 4.1C compiles experimental ATR−FTIR patterns of both gelatine and HA NPs, together with the spectra obtained for the different synthesised MS. The gelatine spectrum presented the amide I band corresponding to the C=O stretching at ≈1650 cm^{-1}, the amide II bands at ≈1550 cm^{-1} and ≈1450 cm^{-1} of NH and CH_2 bending, respectively, and the amide III band in the range 1250–650 cm^{-1}, with the NH bending shown at ≈1240 cm^{-1} [29]. On the other hand, the HA NPs spectrum exhibited the typical PO_4^{3-} absorption bands at 960 and 1030-1100 cm^{-1}, corresponding to the symmetric stretching (ν_1) and asymmetric stretching (ν_3) vibrational modes of the P-O bond, respectively [30,31]. Moreover, the presence of additional bands was detected at 870, 1414 and 1470 cm^{-1}, representative of the out-of-plane bend vibration (ν_2) and asymmetric stretch vibration (ν_3) of CO_3^{2-} [32,33]. These findings suggested B-type carbonation of apatite, probably caused by the dissolution of CO_2 during the synthesis of the HA NPs [25]. All MS spectra matched with these patterns and the relative intensity of the characteristic bands of gelatine and HA found in each condition was consistent with their composition (*i.e.* Gel MS only contained gelatine, Gel-HA MS were composed of 75 wt% gelatine and 25 wt% HA, and CDHA MS were made of 6 wt% gelatine and 94 wt% CDHA). No other unidentified bands were detected, which indicates the absence of unreacted compounds within the limits of detection of the technique (*i.e.* EDC, NHS and sodium citrate).

The XRD analysis (**Figure 4.1D**) revealed that the inorganic phase in both Gel-HA MS and CDHA MS were phase pure with no other peaks than those corresponding to the apatite phase. In addition, in both cases, broad peaks were observed, which accounts for the low-crystallinity of the resulting apatitic product, compatible with its nanometric nature. In the case of CDHA MS, it was demonstrated that the end-product of the hydrolysis of α-TCP was CDHA and that the presence of gelatine did not hinder the reaction.

ICP-OES results depicted in **Figure 4.1E** revealed that Ca^{2+} and P_i concentrations in the DMEM medium were 2.01 ± 0.05 and 1.30 ± 0.02 mM, respectively, and remained stable during the whole experiment. A small alteration of both ion levels was observed when Gel MS were immersed in DMEM, with around 13% lower values throughout the study. In contrast, a more pronounced decrease of Ca^{2+} and Pi concentration was found when Gel-HA MS and CDHA MS were immersed in the culture medium. Both uptook Ca^{2+} ions from the medium, reaching concentrations of 1.11 mM and 1.28 mM after 4 days in culture, respectively. Following the same trend, P_i levels in Gel-HA MS and CDHA MS were considerably reduced all along the study. Indeed, P_i levels in Gel-HA MS were the lowest at all the time points, reaching a reduction of up to 50% at day 4.

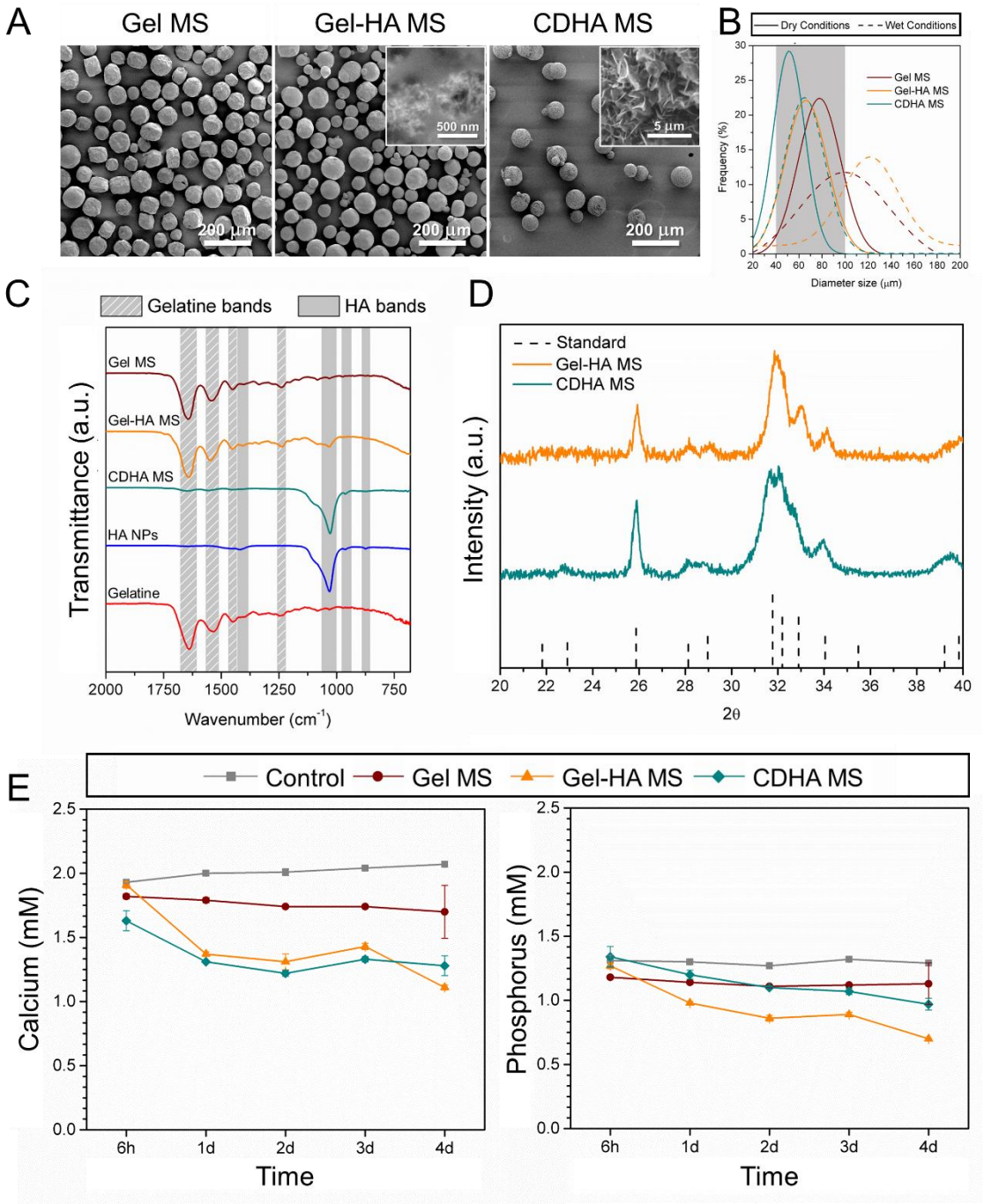

Figure 4.1. Physicochemical characterisation of Gel MS, Gel-HA MS and CDHA MS. **A** SEM images of the MS and high-magnification in the insets showing their surface. **B** Size distribution of the different MS, in both dry and wet conditions. The MS were sieved from 40 to 100 µm before the measurement, the grey area representing the sieving applied. **C** ATR-FTIR spectra of the synthesised MS, along with the spectra of the commercial gelatine and the synthesised HA NPs. Stripped and shaded regions correspond to the characteristic bands of gelatine and HA NPs, respectively. **D** X-ray diffraction patterns of Gel-HA MS and CDHA MS. **E** Calcium and phosphorus concentration of the cell culture media in contact with the various MS for 4 days, determined by ICP-OES.

4.3.2. Rheology and Shape Fidelity of the Bioinks

Rheological studies of the four different bioink formulations were performed without the addition of cells. The bioink formulation consisted of an alginate-gelatine hydrogel mixed with the different MS (Gel MS, Gel-HA MS and CDHA MS). A hydrogel without MS was included as a control.

The outcome of the oscillatory amplitude sweep (**Figure 4.2A**) showed a viscoelastic behaviour of the four bioinks, as evidenced by a LVR of solid-like behaviour (G'>G'' and constant moduli) at low and medium strains, followed by a transition to liquid behaviour at high strains, where G'' became higher than G'. The damping factor (G''/G' at rest conditions) was calculated and compiled in **Table 4.2**. Interestingly, the damping factor obtained for Gel MS and CDHA MS bioinks was similar to the control. In contrast, Gel-HA MS bioink presented a larger distance between both moduli, with a damping factor of 0.33, indicating a higher elastic behaviour than the other conditions. Furthermore, the addition of Gel MS increased the equivalent elastic modulus (G'_{eq}, storage modulus at rest conditions) of the bioink from 268 ± 40 Pa to 598 ± 197 Pa, whereas with the incorporation of Gel-HA MS, this effect was significantly higher, reaching a G'_{eq} of 2937 ± 645 Pa. In contrast, the addition of CDHA MS resulted in a small G'_{eq} increase of up to 332 ± 71 Pa. As a consequence, the yield stress (the end of the LVR, when the G' starts to decrease) was much higher in the Gel-HA MS (917 ± 80 Pa) than in the other bioinks, which presented similar values: 281 ± 30 Pa, 310 ± 4 Pa and 314 ± 10 Pa for control, Gel MS and CDHA MS, respectively. Finally, the flow stress, *i.e.*, the beginning of the flow region (when G' = G''), was affected in an analogous way to the G'_{eq}, but with smaller increments. In particular, the control condition presented flow stress of 989 ± 53 Pa, Gel MS of 1409 ± 200 Pa, Gel-HA MS of 2926 ± 166 Pa and CDHA MS of 1025 ± 128 Pa.

The 3-ITT test evidenced a G' recovery of 91% for the control, 84% for Gel MS, 73% for Gel-HA MS and 88% for CDHA MS just 5 s after being sheared at a high strain (**Figure 4.2B**). Moreover, the recovery after 30 s was almost complete for the control bioink (97%), Gel MS (92%) and CDHA MS (96%). On the other hand, Gel-HA MS bioink recovered 81% of its initial G'.

To compare the wCL and sCL, discs were prepared for each condition and cross-linked for 10 and 15 min, respectively. As seen in **Figure 4.2C**, the cross-linking process was crucial for achieving self-supporting bioinks, as the storage modulus increased up to 10000 Pa. Moreover, the final G' was found to be similar in all the cases, irrespective of the initial G'_{eq} differences among them. On the other hand, the progressive degradation of the cross-linked hydrogels during the culture was evident in all the conditions, as shown in **Figure 4.2D**. The wCL discs containing MS lost around 70% of their G' after 7 days of culture, while the loss in the control disc was slightly lower, at around 50%. This cross-linking reduction along the time lead to a final decrease of G' of 80% for the MS-containing discs and 65% for the control discs after 14 days of incubation. In the case of sCL samples, the G' loss was around 40-50% in all the conditions at day 7, increasing an additional 5% loss at day 14 for all the samples. These findings demonstrated that the Ca^{2+} supplementation in the cell culture media was key for the preservation of the cross-linking of the hydrogels.

Table 4.2. Data obtained from the oscillatory amplitude sweep assay

	G'$_{eq}$ (Pa)	G''$_{eq}$ (Pa)	Damping factor	Yield stress (Pa)	Flow stress (Pa)
Control	268 ± 40	151 ± 13	0.5634	281 ± 30	989 ± 53
Gel MS	598 ± 197	308 ± 59	0.5150	310 ± 04	1409 ± 200
Gel-HA MS	2937 ± 645	958 ± 115	0.3261	917 ± 80	2926 ± 166
CDHA MS	332 ± 71	185 ± 21	0.5572	314 ± 10	1025 ± 128

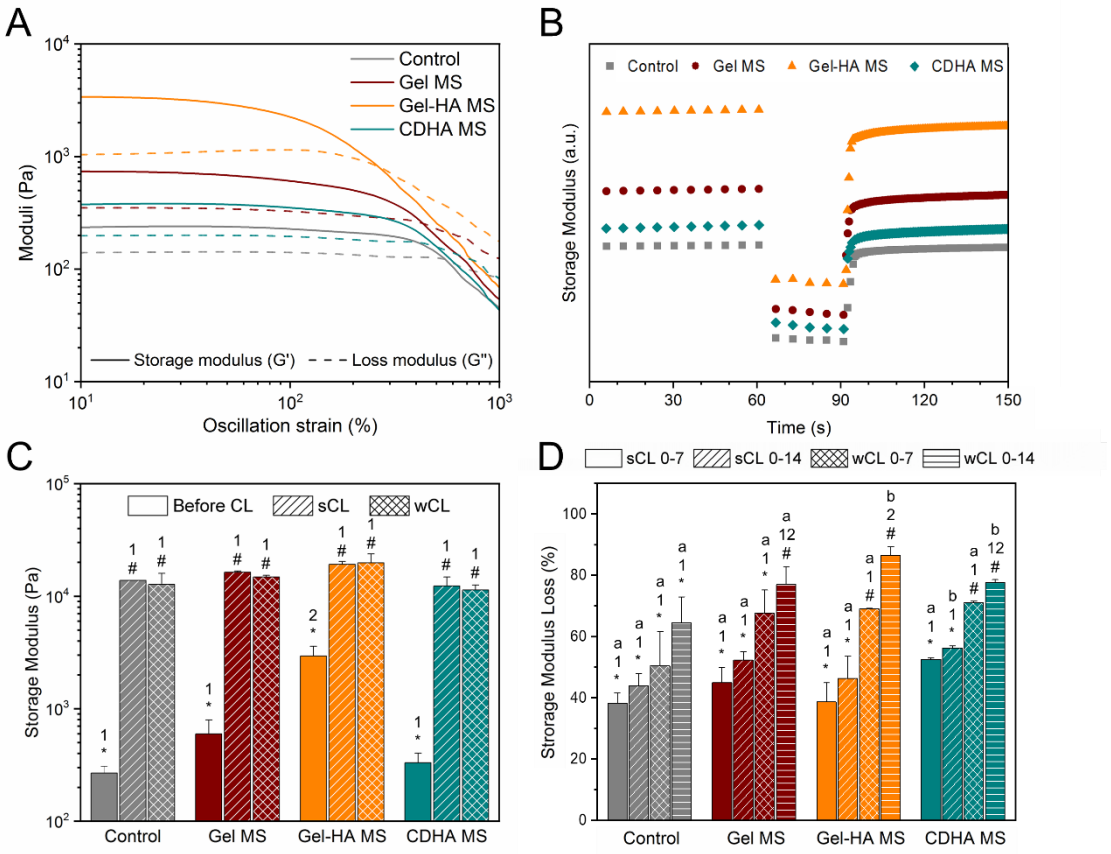

Figure 4.2. Rheological properties of the synthesised bioinks. **A** Oscillatory amplitude sweep results showing the G' and G'' evolution over strain. **B** G' recovery of the bioinks after being put under a high strain to mimic the extrusion process. **C** G' of each condition after being cross-linked for 15 or 10 min corresponding to the sCL and wCL protocols, compared to the non-cross-linked samples. **D** G' loss of the two cross-linkings studied after 7 and 14 days in culture. Different letters indicate statistically significant differences between time points in the same condition, different numbers indicate statistically significant differences between conditions, and different symbols indicate statistically significant differences between cross-linkings.

4.3.3. Cell Cultures on the Microspheres

Cell behaviour on the MS was examined in terms of viability, proliferation, morphology and gene expression. The results after 1 day of cell culture showed that the initial cell

adhesion to all MS types was similar, as observed in **Figure 4.3A** and quantified in **4.3C**. After 3 days of cell culture, cell proliferation was promoted especially on Gel MS and Gel-HA MS. Nevertheless, cell counts were comparable between conditions at day 14 (≈3-fold of the initially seeded cells), confirming a proper cell growth in all the samples throughout the study, with a similar proliferation rate over the study for all the MS. Regarding the distribution of the cells on the MS, L/D images revealed that cells adhered to all three types of MS and had the ability to proliferate and fully colonise them. However, a non-negligible number of dead cells were detected in CDHA MS samples on days 7 and 14.

The actin fibres and nuclei stainings in **Figure 4.3B** helped to certify the cell adhesion on the MS of all natures, as well as their organisation on the samples. Indeed, in all the conditions cells tended to attach, spread and multiply on the surface and in-between the MS. Furthermore, the expression of osteogenic genes was examined and is summarised in **Figure 4.3D**. In general, CDHA MS presented the most osteoinductive properties among the different MS. When compared to the control, cells on CDHA MS exhibited a 4.5-fold expression of ALP at day 3, a 2 or 2.5-fold expression of Col. I at all the time points, a 4-fold expression of OPN at day 7, and a general 2-fold expression of OCN. Moreover, Gel-HA MS also upregulated the expression of Col. I at days 3 and 14, of OPN at day 14 and of OCN at day 7 of culture, all of them with a 1.5-fold relative to the control. The contribution of the HA NPs was observed comparing the results of Gel-HA MS and Gel MS in terms of ALP expression at day 3 and the expression of OPN and OCN at 14 and 7 days, respectively, although not all the differences were statistically significant. Interestingly, RUNX2 had an important overexpression of 4-fold and 5-fold at day 14 for Gel-HA MS and CDHA MS, respectively, yet the expression in Gel MS was the highest with a 7-fold change to the control.

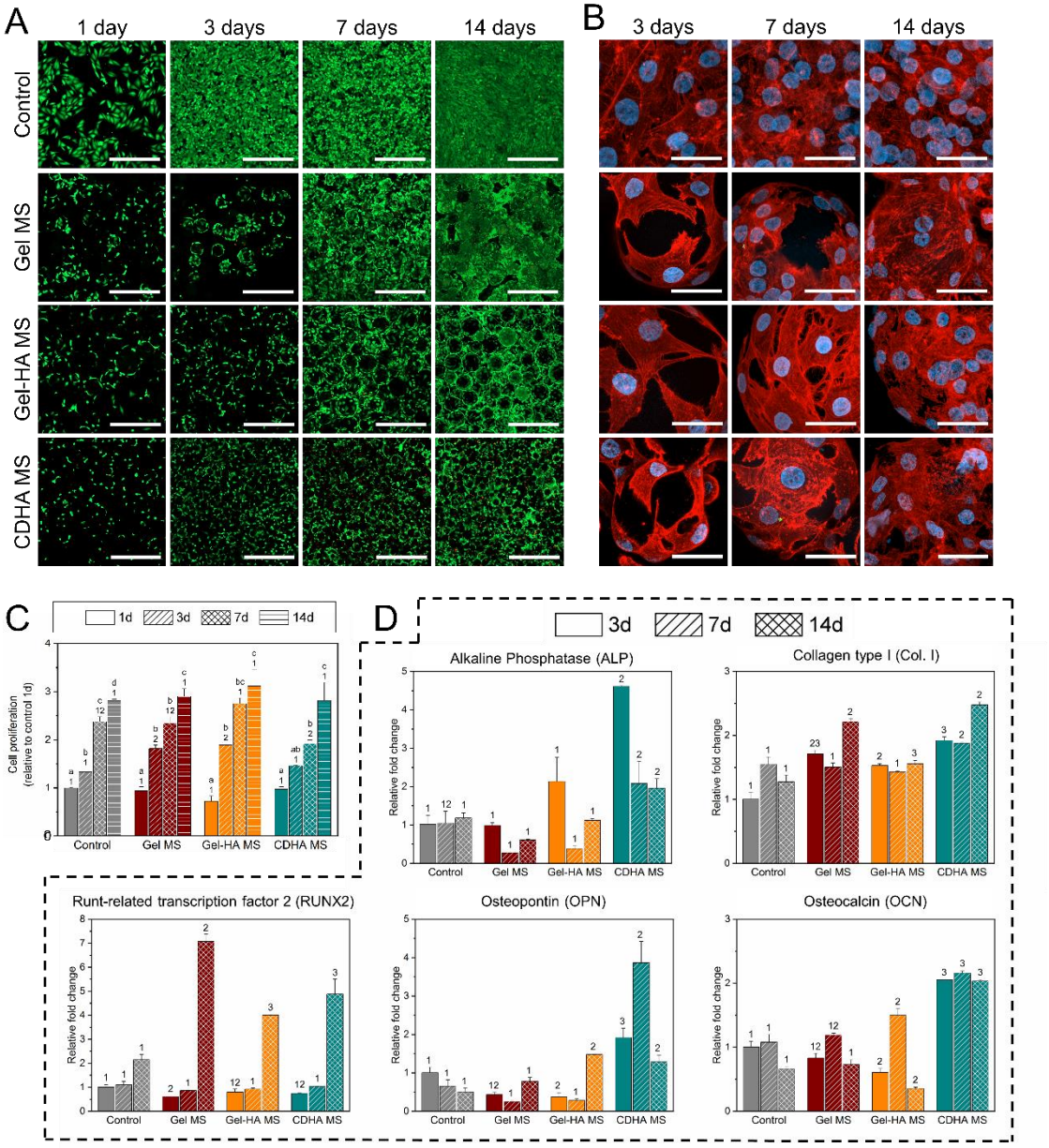

Figure 4.3. Behaviour of MG-63 cells cultured on the different MS. **A** Live/dead staining images at days 1, 3, 7 and 14. Live cells stained in green and dead cells in red. Scalebar represents 500 µm. **B** Cell morphology pictures at 3, 7 and 14 days of culture. Cell nuclei in blue and actin fibres in red. Scalebar represents 40 µm. **C** Cell proliferation measured through resazurin-based method. **D** Gene expression of osteogenic markers for the cells seeded in the MS at days 3, 7 and 14. Control samples at day 3 were used as a reference to determine the fold changes. Different letters indicate statistically significant differences between time points in the same condition and different numbers indicate statistically significant differences between conditions at each time point.

4.3.4. Cell Viability and Cell Migration in the Bioinks

In order to study the performance of the cells in the bioinks, four different formulations were prepared by mixing the alginate, the gelatine and each type of MS with the cells. A control bioink without the incorporation of MS was also included. The extrusion was

done through a 22 Ga nozzle directly into a $CaCl_2$ bath, as described in the experimental section. In addition, two different cross-linking protocols were investigated (*i.e.*, wCL and sCL). The sCL allowed to study the final constructs up to 21 days of cell culture, while the wCL bioinks lost stability after 14 days in culture.

The visualisation of the cells embedded in the bioinks was done by confocal microscopy. Representative live/dead (L/D) images in **Figure 4.4A** and **B** proved that ≥90% of the cells were viable (green fluorescent cells) and only a small number of dead cells (red fluorescent ones) were observed at 3, 7, 14 and 21 days of culture for all the conditions. In contrast, the L/D ratios immediately after the extrusion (*i.e.* at day 0) were slightly lower, especially for the bioinks containing Gel-HA MS and CDHA MS, independently of the cross-linking protocol applied. Therefore, the viability at day 0 was quantified for the two initial cross-linking times and compared among the four bioinks. **Figure 4.4C** shows that in general, the differences between the cross-linkings were minimal, demonstrating that their effects on cells at the initial time point were similar. Moreover, it was observed that the control condition presented the highest cell viability (93.0% ± 0.4), followed by the Gel MS bioink with 90.8% ± 0.9 of the cells alive. A significant decrease in the viability of the cells was found in the other two conditions, indicating that the incorporation of apatite-containing MS reduced the cell survival rate at earlier time points. Indeed, Gel-HA MS exhibited cell mortality of 21.3% ± 1.5, similar to that of CDHA MS bioinks with 18.4% ± 1.2 of dead cells. In spite of this, the initial viability rates for all the bioinks were sufficient for the cells to survive and proliferate, indicating a suitable performance for all the conditions.

With regards to the evolution of the cells in the bioinks, it was observed that initially, MG-63 cells were embedded in the alginate matrix. After several days of culture, the cells close to the MS started migrating and attaching to the Gel MS and Gel-HA MS, as can be appreciated in the insets of **Figure 4.4A** and **B**. The time needed for this process highly depended on the cross-linking applied: in the bioinks with sCL the migration started at day 7 (**Figure 4.4A**), while the bioinks with wCL exhibited cell migration and attachment to the MS earlier, at day 3 (**Figure 4.4B**). Although to a lesser extent, the confocal images also proved that these phenomena occurred in the CDHA MS bioinks.

It is worth noting that at the latest time points evaluated (*i.e.* 14 days for wCL and 21 days for sCL), the cells that remained unattached to the MS increased their size in some of the conditions (marked with arrows), especially in the control and Gel MS bioinks in the case of the wCL bioink (**Figure 4.4B**). This observation suggested the formation of small cell spheroids as a consequence of cell growth, which will be further analysed in the next section.

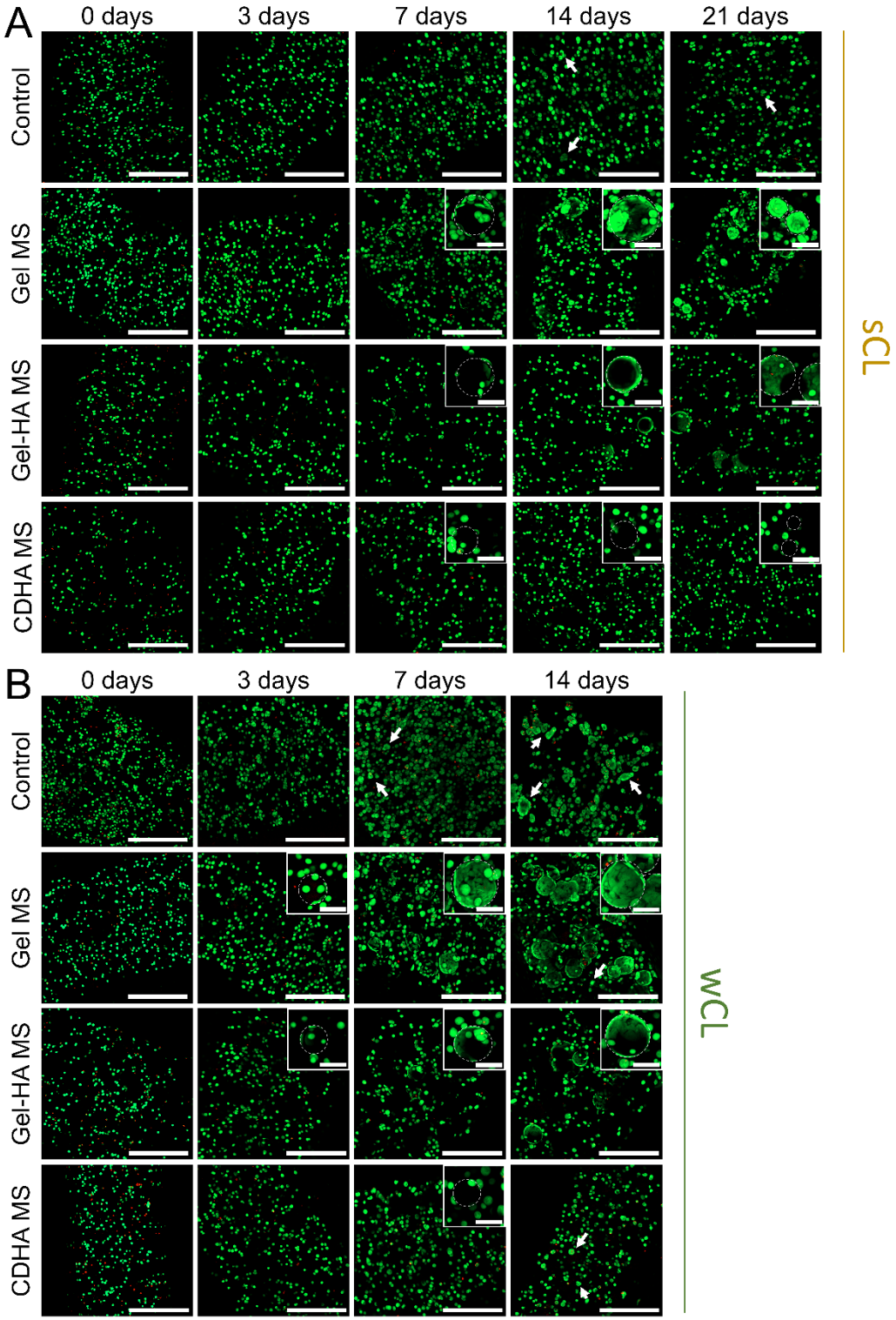

C

	Control	Gel MS	Gel-HA MS	CDHA MS
Strong CL	93.54±0.63 % (1,*)	92.10±1.83 % (1,*)	77.96±4.19 % (2,*)	80.65±0.99 % (2,*)
Weak CL	92.53±0.05 % (1,*)	89.32±0.22 % (1,*)	79.19±1.15 % (2,*)	82.21±2.52 % (2,*)

Figure 4.4. Evolution of MG-63 cell viability in the different bioinks. Live/dead images of the bioinks with sCL (**A**) and wCL (**B**) at 0, 3, 7, 14 and 21 days of culture. Live cells stained in green and dead cells in red. Insets show magnification of cells attached to the different MS. Dashed circles indicate MS, and arrows cell clusters forming spheroids. Scale bars represent 500 µm for the full images and 100 µm for the insets. **C** Quantification of the cell viability at day 0, immediately after the bioinks extrusion. Different numbers indicate statistically significant differences between conditions for each CL and different symbols indicate statistically significant differences between cross-linkings within the same condition.

4.3.5. Cell Proliferation and Cell Morphology in the Bioinks

Cell proliferation in the bioinks was evaluated through Presto Blue assay at 0, 3, 7, 14 and 21 days (**Figure 4.5A** and **B**). The results confirmed the proliferation of MG-63 in all conditions. In the case of sCL bioinks, the cell number in all the MS-containing bioinks remained unaltered for the first week and registered a 3-fold increase from day 7 to day 14, reaching a plateau that lasted until day 21. In contrast, the cell number in the control bioink exhibited a constant growth throughout the cell culture, up to 5-fold increase at day 21. Regarding the wCL bioinks, similar proliferation rates were found also for all the conditions at each time point. Cell number rose sharply from day 0 to day 3 and in all the bioinks, and afterwards cell growth essentially stopped at a 4-fold cell number for MS-containing bioinks and 3.5-fold value for the control samples. In general, the results showed that all MS-loaded bioinks supported cell proliferation, reaching a plateau of cell population earlier or later depending on the degree of cross-linking. The stronger the cross-linking the longer it took for the cells to start proliferating and to reach the final plateau.

Figure 4.5C and **D** display the morphology of the cells inside the different bioinks at the last incubation time point, investigated using phalloidin and DAPI to stain the actin filaments and the nuclei, respectively. Overall, proper attachment and spreading were observed for the cells adhered to the MS in the Gel MS and Gel-HA MS samples (top rows of **Figure 4.5C** and **D**). In contrast, CDHA MS bioink was not able to promote cell migration and attachment to the MS. In general, the cells that did not adhere to the MS presented rounded morphologies, typical of alginate-based bioinks. It was noticeable their ability to cluster and form cell spheroids for all the conditions, as evidenced in the bottom rows of **Figure 4.5C** and **D**. Bigger spheroids were found in the pristine bioink, compared to the MS-containing formulations. Moreover, although cell morphology was comparable in the two CL conditions, it was observed that the wCL allowed the formation of larger cell colonies, as evidenced by the number of nuclei in each spheroid (bottom row of **Figure 4.5C** vs. bottom row of **Figure 4.5D**), especially noticeable in the control specimens. All these findings are in agreement with the L/D results of the previous section.

Additionally, SEM images were taken for the wCL Gel MS bioink (**Figure 4.5E**). The prior dehydration of the sample resulted in the exposure of the embedded MS through the alginate network, showing the cells well attached and spread on the MS, in agreement with the confocal microscopy results.

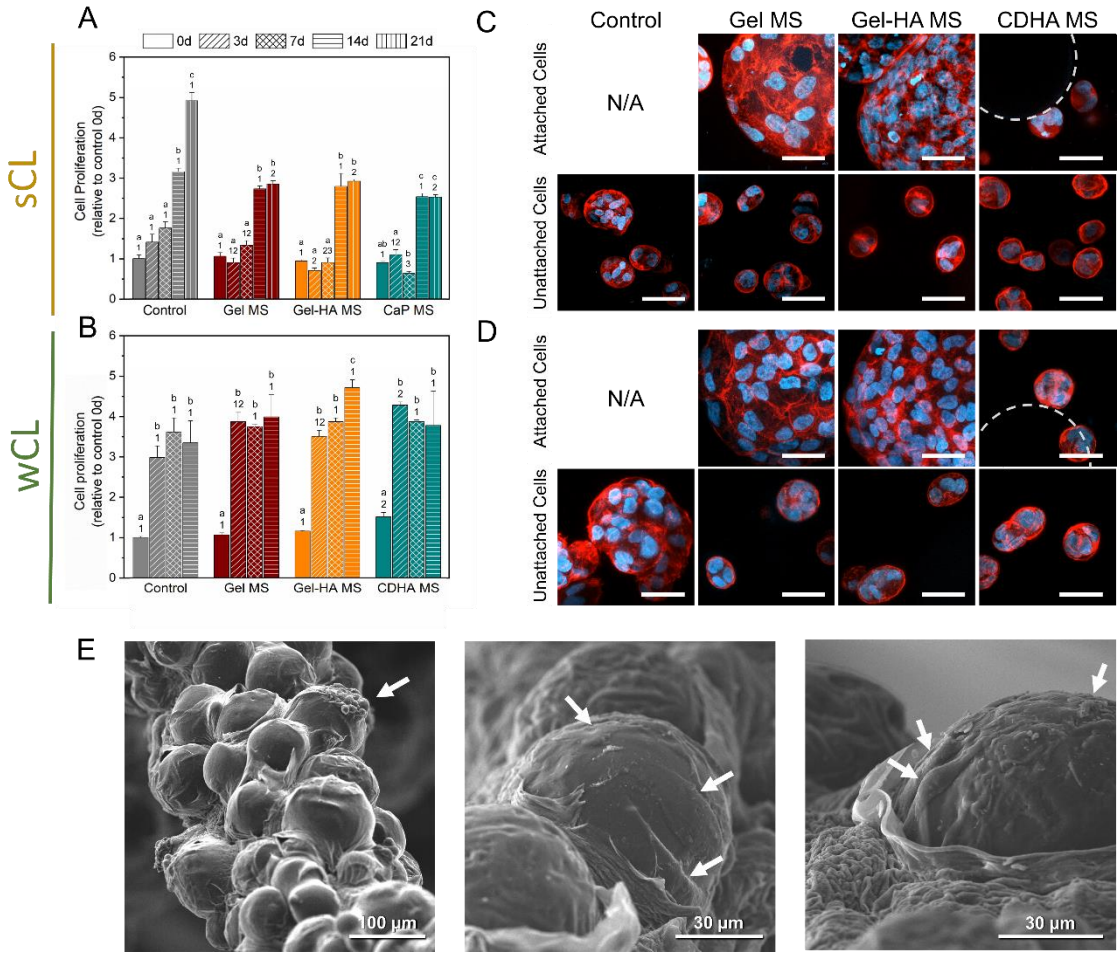

Figure 4.5. Cell behaviour in the developed bioinks. **A** Cell proliferation results of the sCL samples and **B** of the wCL condition along the study. Different letters indicate statistically significant differences between time points in the same condition and different numbers indicate statistically significant differences between conditions at each time point. **C** Cell morphology in the sCL bioinks at day 21 and **D** in the wCL bioinks at day 14, observed by fluorescence confocal microscopy. Top rows show cells attached to the MS inside the bioinks, bottom rows exhibit unattached cells suspended within the cell-laden ink. Nuclei in blue and actin fibres in red. Dashed circles indicate CDHA MS. Scale bars denote 50 µm. **E** SEM images of the wCL Gel MS bioink. Arrows indicate cells attached and spread on the MS.

4.3.6. Gene Expression of the Cells in the Bioinks

Since the wCL bioinks promoted a faster cell response compared to the sCL condition, wCL specimens were chosen for the gene expression analysis of osteogenic markers. Overall, the MS-containing bioinks presented an overexpression of all the osteogenic genes compared to the control sample, irrespective of their nature. Analysing the results in more detail, they indicated that Gel MS significantly upregulated the expression of ALP, RUNX2, OSX and OPN at day 7 but most notably at 14 days of culture, as shown in **Figure 4.6**. In the case of Gel-HA MS and CDHA MS samples at 14 days, ALP, OSX and OPN were also overexpressed compared to the control. However, not all the differences were statistically significant. Moreover, Col. I and OCN genes presented the highest expression in the Gel-HA MS bioink for the two studied time points, with a ≈4-

fold (at day 7) and ≈6-fold (at day 14) increase of Col. I gene with respect to the control, with statistically significant differences. In contrast, CDHA MS showed low expression of these genes.

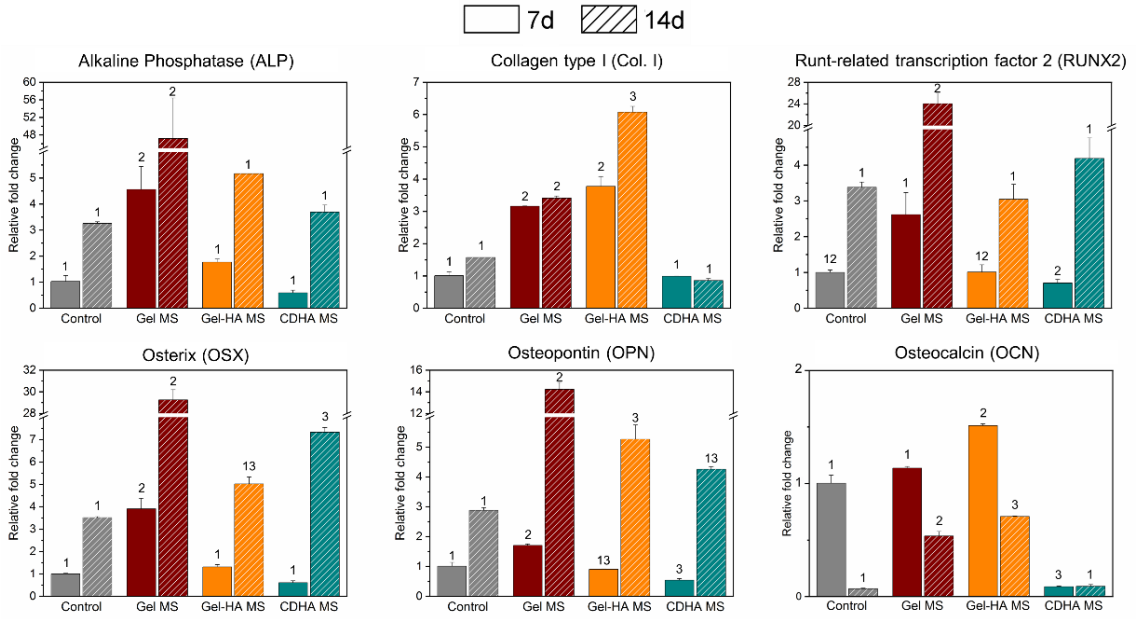

Figure 4.6. Gene expression of osteogenic markers for the cells in wCL bioinks at day 7 and 14 of culture. Control bioink at day 7 was used as a reference to determine the fold changes. Different numbers indicate statistically significant differences between conditions at each time point.

4.4. Discussion

The development of bioinks requires a compromise between the improvement of their biological performance and their mechanical properties. Alginate-based bioinks are typically chemically modified to provide cell adhesive moieties to improve the behaviour of the embedded cells. However, their rheological properties can be detrimentally altered by these modifications. In the search for the optimal bioink, we propose the incorporation of microspheres with different bone-related functionalities to an alginate-based bioink, in order to enhance both cell attachment and differentiation while improving their mechanical performance. The initial hydrogel composition consisted of a mixture of alginate (6 wt%) and gelatine (8 wt%). On the one hand, the alginate supported cell viability, glued the MS due to its ability to gellify in the presence of Ca^{2+} ions and provided mechanical stability to the construct. On the other hand, the gelatine was incorporated in the formulation in views of enhancing the rheological properties and to provide also a protective environment for the cells during the extrusion and in the initial hours of culture. Subsequently, it was expected to gradually diffuse from the inks during cell culture, since no gelatine cross-linking treatment was applied.

In this study, microspheres of three different compositions were successfully synthesised. Gelatine MS (Gel MS) were chosen for its biocompatibility [34], while calcium phosphate containing-MS were selected as a possible strategy to enhance the osteogenic or osteoinductive properties of the bioinks [35,36]. Their microstructure and chemical composition was verified by SEM, FTIR and XRD (**Figure 4.1A**, **C** and **D**). The size of the cross-linked gelatine-containing MS (*i.e.* Gel MS and Gel-HA MS) sieved from 40 to

100 µm experienced substantial swelling in cell culture medium due to hydration of their gelatine phase (**Figure 4.1B**). The results presented small variations compared to the findings of **Chapter 3** due to the different cross-linking protocols applied. Gel-HA MS presented the most pronounced swelling, which can be explained by the partial screening between Ca^{2+} from the NPs and the carboxylic groups involved in the cross-linking of the gelatine chains. This partial screening could partly block the cross-linking between the hydrogel chains causing their swelling [37]. Importantly, the bioactive nature of the apatite containing-MS (*i.e.* Gel-HA MS and CDHA MS), explained by the inherent reactivity of the apatitic nanocrystals [38], was indirectly proved by the substantial changes in the calcium and phosphorus concentrations in the cell culture media when the microspheres were directly exposed to it (**Figure 4.1E**).

Understanding the rheological properties of the bioinks is fundamental to predict their printability. In this sense, all the bioinks developed in the present work presented a viscoelastic behaviour, as observed in **Figure 4.2A**, which is required in direct ink writing techniques, since the material must be extrudable at high shear rates while assuring a perfect deposition and shape fidelity [39]. Moreover, it was found that the incorporation of microspheres increased both the G'_{eq} and the yield stress that are directly related to the extrudability and shape fidelity of the bioinks. Indeed, the incorporation of fillers in hydrogels is a common strategy to improve their mechanical properties, where the resulting composite partially exhibits the mechanical features of their individual components. When a load is applied to these materials, it will be transferred from the polymer to the stiffer filler (in our case the cross-linked Gel MS and the mineral-containing MS), which will bear part of the load, increasing the global mechanical properties [40]. We observed that the extent of these changes depended highly on the nature of each MS. Precisely, Gel MS doubled the G'_{eq} compared to the control, Gel-HA MS presented a >10-fold increase, while for CDHA MS only a limited gain was observed. Regarding the yield stress, in Gel MS and CDHA MS remained similar to the control, while in Gel-HA MS it was 3 times higher (**Table 4.2**). These differences can be attributed to the marked volume gain of the Gel-HA MS in aqueous media compared to the other types of MS (**Figure 4.1B**), that generated a higher MS/alginate ratio for the same initial volume. Moreover, the apatite-containing MS might present higher rigidity than the Gel MS, which may contribute to the final rheological properties of the hydrogels. Although one could hypothesise that, since these MS contain Ca^{2+}, this could be released and contribute to the cross-linking of the alginate, we consider this as highly improbable for two reasons. First, as shown in the ICP-OES results (**Figure 4.1E**), no Ca^{2+} release was recorded in DMEM, which is the medium where the alginate was dissolved to prepare the inks. Secondly, no effect was found in this direction with the CDHA MS, that also contain Ca^{2+}.

Regarding the 3-ITT results, a fast and almost complete elastic recovery was registered for all the conditions. This is generally linked to the shape fidelity of the filaments and is fundamental in the future development of 3D-printed structures, together with a proper self-supporting capacity [39].

Apart from controlling the shape fidelity during the extrusion, it was fundamental to ensure sufficient mechanical stability of the bioprinted ink when immersed in the cell culture medium. This was explored investigating two different cross-linking protocols for the alginate hydrogel, which consisted in varying the initial $CaCl_2$ bath time and the supplementation or not of the cell culture media throughout the study (*i.e.* wCL consisting of 10 min CL in 150 mM $CaCl_2$, and sCL consisting of 15 min CL with 150 mM $CaCl_2$

and additional supplementation of up to 5 mM $CaCl_2$ in the cell culture medium during the culture). Increasing the CL from 10 to 15 min did not have any substantial effect. The initial G' value for both CL conditions was ≈10000 Pa, comparable to the results of cross-linked hydrogels previously reported in the literature [41–43]. This parameter, which accounts for the stiffness of the bioink and is related to the self-supporting capacity of the extruded and cross-linked filaments, did not change between the two CL (**Figure 4.2C**). In contrast, the Ca^{2+} supplementation in the culture media was crucial for the bioink stability during the subsequent days of incubation. Indeed, rheology results displayed important differences in the loss of G' between the two CL conditions at both day 7 and 14, with variations of up to 40% in the Gel-HA MS samples at day 14 (**Figure 4.2D**). The loss of stiffness is associated with the hydrogel degradation, which can be explained by the exchange of divalent by monovalent cations that revert the gelation of alginate, destabilising the hydrogel network and solubilising the polymer [44,45]. For this reason, the addition of $CaCl_2$ to the culture media permitted better stability in sCL bioinks compared to wCL ones, allowing to study the cell performance up to 21 days of culture instead of the 14 days of the wCL conditions.

In order to investigate the performance of the synthesised MS, cell viability, proliferation and morphology studies with MG-63 cells seeded directly onto the MS were carried out. In addition, the expression of several osteoblastic differentiation genes was explored. For the cell culture studies MG-63 cells were used, which present an immature preosteoblastic phenotype. Being an immortalised cell line, they are an unlimited cell source and present a more reliable reproducibility than primary cells [46]. The large number of conditions that were tested *in vitro*, together with the high cell concentration these studies required, urged us to work with reliable and fast-growing cells. The results summarised in **Figure 4.3** demonstrated that MG-63 cells were able to attach and grow on the MS, showing a good proliferation rate in all the tested conditions. They presented a similar morphology among conditions. Regarding gene expression, CDHA MS showed, overall, higher levels of all osteogenic genes at all time points. Hence, it can be stated that CDHA MS had better osteoinductive properties than the other MS. The high capacity of certain calcium phosphate materials to induce osteogenic differentiation of stem cells has been largely described [27,36], mostly related to the triggered ion exchange and specific morphological features such as their porosity, geometry and SSA. Despite Gel-HA MS also upregulated certain genes compared to the control sample, no major differences were observed between Gel MS and Gel-HA MS.

A step forward in this investigation was to assess the behaviour of MG-63 cells embedded in bioinks containing the synthesised MS. Prior to the cell culture, two cross-linkings were performed, a weak and a strong cross-link to assess not only the mechanical stability of the constructs but also the capacity of the cells to migrate to the MS and proliferate. The first aspect explored was the effect of shear stress during the extrusion on cell viability. The results showed that the dispensation through the nozzle was one of the most critical steps for the cells in 3D-bioprinted inks. In fact, during extrusion-based bioprinting cells are exposed to different mechanical forces, where shear stress is the main cause of cell death [47]. Gel-HA MS and CDHA MS bioinks presented a statistically significant reduction of 20% in the cell survival rate (**Figure 4.4C**), revealing that the incorporation of ceramic-based MS was unfavourable for the cells at the extrusion step. Notwithstanding, it was the rheology of Gel-HA MS bioink which clearly differed from the other conditions, presenting flow stress of ≈3000 Pa compared to the other formulations where it was near 1000 Pa (**Table 4.2**). Since in the Gel MS condition the survival rate of the cells was high, it indicates that the shear forces applied cannot be the

reason for the cell death in the bioinks with mineral-loaded MS. In fact, similar shear stress values have been reported to present high cell survival [48]. From this point of view, it is not clear the cause of the initial cell death and further investigation would be required. Despite the slight reduction in cell viability for some of the conditions during extrusion, the subsequent cell culture up to 21 days showed similar proliferation behaviour regardless of the MS type.

Notwithstanding, the results revealed that the rigidity of the alginate hydrogel extremely influenced cell behaviour. First, the L/D images exhibited substantial differences in cell migration between the two CL conditions, as MG-63 started attaching to the MS mainly at day 3 in the wCL bioinks while for sCL samples cell attachment to the MS was delayed starting at day 7 (**Figure 4.4A**). Moreover, proliferation data in **Figure 4.5A** also supported the impact of bioink stiffness on the cells: in the wCL MS-containing bioinks cells were able to proliferate to a great extent at day 3, whereas in the sCL this phenomenon did not happen until day 14. Therefore, the results demonstrated the need for viscosity relaxation for the cells to migrate, attach and proliferate inside the bioinks. These findings are in agreement with previous literature, where several works proved that the stiffness of the bioink directly affects the cell performance at different extents. For instance, it has been reported that softer matrices seem to promote hMSC spreading [49], proliferation [43] and their differentiation to a neurogenic lineage, while stiffer hydrogels tend to induce osteogenesis [50]. In conclusion, the cross-linking conditions of hydrogels is a fundamental issue in bioink development and must be optimised to have the desirable cell behaviour without compromising the mechanical stability of the construct.

Cells embedded in the different bioinks presented spherical morphologies, and only when attached to the MS were able to spread (**Figure 4.4A**). In addition, MG-63 presented a highly proliferative profile in all the samples, rising up to 4-fold the initial cell number in wCL bioinks (**Figure 4.5B**). Nonetheless, the system forced the cells to proliferate on themselves forming cell clusters, where the cells remained spherical. Cell proliferation in alginate hydrogels has been extensively studied in the literature, and controversial results have been published. Indeed, several studies report that cells are not able to proliferate due to the lack of cell adhesive sites in the alginate molecule, which usually leads to hydrogel modification by the incorporation of high amounts of RGD peptides [51,52]. In contrast, other studies showed that alginate by itself supports cell proliferation, although exhibiting rounded-shaped cells [45]. The same phenomenon has been observed in hydrogels with cell-adhesive moieties, where it is thought that their highly hydrophilic microenvironment force the cells to spherical shapes [53]. The capacity of the cells to easily spread is a crucial point, as some 3D microenvironments can prevent osteogenic differentiation by restricting cell growth and cell spreading [54]. Therefore, the presence of particles that served as cell attaching points is one of the strengths of the present approach, as it allows the normal phenotype and function of the cells.

Regarding the gene expression of the cells embedded in the bioinks, RT-qPCR results indicated that the highest expression of certain osteogenic genes such as ALP, RUNX2, OSX and OPN occurred in Gel MS bioinks, with significant differences compared to the other types of MS (**Figure 4.6**). These findings differ from the results obtained in the cells seeded directly onto the MS, where CDHA MS were found to be the ones that better promote the osteogenic differentiation (**Figure 4.3D**). It is important to highlight that in the case of the cell-laden inks, not only the contribution of the cells attached to the MS was analysed, but also the gene expression of the cells forming spheroids within the alginate. Therefore, the most feasible explanation is that the marked cell differentiation

in Gel MS bioink compared to the other conditions was due to the direct contact of the cells with the MS, which was shown to be substantially higher in this condition than in the other specimens. In fact, apart from the physicochemical properties of the material, cell-material interaction has been reported to have a significant influence on cell differentiation [55,56]. In view of the differences in terms of osteogenic markers' expression between the bioinks and the direct cell seeding onto the MS, it was demonstrated that changes in the system and, thus, in the cell environment largely influenced cell behaviour. The ability of the cells to move inside the hydrogel and migrate to reach the MS proved that preseeding of the cells in the MS prior to their incorporation into the bioink was not needed. However, the attachment to the CDHA MS was not shown to be effective, which hinder their osteogenic properties, and a preseeding would be a strategy to boost it. Therefore, preseeded MS can be used to assure cell attachment and incorporated into the bioink after 1 to 3 days in culture, depending on the MS nature and the cell type studied.

The present strategy, based on the incorporation of microspheres in cell-laden inks, offers promising perspectives. First, the versatility of the approach enables its extrapolation to fields other than bone regeneration. For instance, using MS of other natures and even as drug-release or ion release agents, as shown in **Chapter 3**, may allow transferring this solution into other applications such as chondral regeneration, soft tissue or ocular tissue engineering. Moreover, the system provides a versatile soft matrix for more complex biofabrication approaches. For example, it can be combined with core/shell strategies localising the MS either in the shell or the core of the strands to confer them specific functionalities [57]. Finally, as the proposed solution is simple and robust, it would open the path to become a product more accessible than other more sophisticated cell therapies found in the literature.

4.5. Conclusions

The introduction of microspheres of different natures (*i.e.* gelatine, gelatine containing hydroxyapatite nanoparticles, and CDHA) into an alginate-based bioink allowed not only to tune its rheological properties but also to modulate the cell performance. The MS provided a substrate where bone cells were able to attach, proliferate and differentiate, which was found to be highly dependent on the migration capacity of the cells. Overall, the potential that this approach offers is valuable for its simplicity and ease of properties' tuning.

4.6. References

[1] A. Abbott, Biology's new dimension, Nature. 424 (2003) 870–872. doi:10.1038/424870a.

[2] T. Andersen, P. Auk-Emblem, M. Dornish, 3D Cell Culture in Alginate Hydrogels, Microarrays. 4 (2015) 133–161. doi:10.3390/microarrays4020133.

[3] A.-V. Do, B. Khorsand, S.M. Geary, A.K. Salem, 3D Printing of Scaffolds for Tissue Regeneration Applications, Adv. Healthc. Mater. 4 (2015) 1742–1762. doi:10.1002/adhm.201500168.

[4] R. Levato, T. Jungst, R.G. Scheuring, T. Blunk, J. Groll, J. Malda, From Shape to

Function: The Next Step in Bioprinting, Adv. Mater. 32 (2020) 1906423. doi:10.1002/adma.201906423.

[5] J. Malda, J. Visser, F.P. Melchels, T. Jüngst, W.E. Hennink, W.J.A. Dhert, J. Groll, D.W. Hutmacher, 25th Anniversary Article: Engineering Hydrogels for Biofabrication, Adv. Mater. 25 (2013) 5011–5028. doi:10.1002/adma.201302042.

[6] S. V. Murphy, A. Atala, 3D bioprinting of tissues and organs, Nat. Biotechnol. 32 (2014) 773–785. doi:10.1038/nbt.2958.

[7] P.S. Gungor-Ozkerim, I. Inci, Y.S. Zhang, A. Khademhosseini, M.R. Dokmeci, Bioinks for 3D bioprinting: an overview, Biomater. Sci. 6 (2018) 915–946. doi:10.1039/C7BM00765E.

[8] I. Matai, G. Kaur, A. Seyedsalehi, A. McClinton, C.T. Laurencin, Progress in 3D bioprinting technology for tissue/organ regenerative engineering, Biomaterials. 226 (2020) 119536. doi:10.1016/j.biomaterials.2019.119536.

[9] A.C. Hernández-González, L. Téllez-Jurado, L.M. Rodríguez-Lorenzo, Alginate hydrogels for bone tissue engineering, from injectables to bioprinting: A Review, Carbohydr. Polym. (2019) 115514. doi:10.1016/j.carbpol.2019.115514.

[10] C.C. Piras, D.K. Smith, Multicomponent polysaccharide alginate-based bioinks, J. Mater. Chem. B. 8 (2020) 8171–8188. doi:10.1039/D0TB01005G.

[11] Z. Li, S. Huang, Y. Liu, B. Yao, T. Hu, H. Shi, J. Xie, X. Fu, Tuning Alginate-Gelatin Bioink Properties by Varying Solvent and Their Impact on Stem Cell Behavior, Sci. Rep. 8 (2018) 1–8. doi:10.1038/s41598-018-26407-3.

[12] J. Jia, D.J. Richards, S. Pollard, Y. Tan, J. Rodriguez, R.P. Visconti, T.C. Trusk, M.J. Yost, H. Yao, R.R. Markwald, Y. Mei, Engineering alginate as bioink for bioprinting, Acta Biomater. 10 (2014) 4323–4331. doi:10.1016/j.actbio.2014.06.034.

[13] M.D. Sarker, S. Naghieh, A.D. McInnes, L. Ning, D.J. Schreyer, X. Chen, Bio-fabrication of peptide-modified alginate scaffolds: Printability, mechanical stability and neurite outgrowth assessments, Bioprinting. 14 (2019) e00045. doi:10.1016/j.bprint.2019.e00045.

[14] L. Ning, N. Zhu, F. Mohabatpour, M.D. Sarker, D.J. Schreyer, X. Chen, Bioprinting Schwann cell-laden scaffolds from low-viscosity hydrogel compositions, J. Mater. Chem. B. 7 (2019) 4538–4551. doi:10.1039/C9TB00669A.

[15] N.O. Dhoot, C.A. Tobias, I. Fischer, M.A. Wheatley, Peptide-modified alginate surfaces as a growth permissive substrate for neurite outgrowth, J. Biomed. Mater. Res. 71A (2004) 191–200. doi:10.1002/jbm.a.30103.

[16] J.A. Rowley, G. Madlambayan, D.J. Mooney, Alginate hydrogels as synthetic extracellular matrix materials, Biomaterials. 20 (1999) 45–53. doi:10.1016/S0142-9612(98)00107-0.

[17] M. Ojansivu, A. Rashad, A. Ahlinder, J. Massera, A. Mishra, K. Syverud, A. Finne-Wistrand, S. Miettinen, K. Mustafa, Wood-based nanocellulose and bioactive glass modified gelatin–alginate bioinks for 3D bioprinting of bone

cells, Biofabrication. 11 (2019) 035010. doi:10.1088/1758-5090/ab0692.

[18] J. Olmos Buitrago, R.A. Perez, A. El-Fiqi, R.K. Singh, J.-H. Kim, H.-W. Kim, Core–shell fibrous stem cell carriers incorporating osteogenic nanoparticulate cues for bone tissue engineering, Acta Biomater. 28 (2015) 183–192. doi:10.1016/j.actbio.2015.09.021.

[19] T.T. Demirtaş, G. Irmak, M. Gümüşderelioğlu, A bioprintable form of chitosan hydrogel for bone tissue engineering, Biofabrication. 9 (2017) 035003. doi:10.1088/1758-5090/aa7b1d.

[20] H.-R. Lin, Y.-J. Yeh, Porous alginate/hydroxyapatite composite scaffolds for bone tissue engineering: Preparation, characterization, and in vitro studies, J. Biomed. Mater. Res. 71B (2004) 52–65. doi:10.1002/jbm.b.30065.

[21] Y. Luo, A. Lode, C. Wu, J. Chang, M. Gelinsky, Alginate/Nanohydroxyapatite Scaffolds with Designed Core/Shell Structures Fabricated by 3D Plotting and in Situ Mineralization for Bone Tissue Engineering, ACS Appl. Mater. Interfaces. 7 (2015) 6541–6549. doi:10.1021/am508469h.

[22] R. Levato, J. Visser, J.A. Planell, E. Engel, J. Malda, M.A. Mateos-Timoneda, Biofabrication of tissue constructs by 3D bioprinting of cell-laden microcarriers, Biofabrication. 6 (2014) 035020. doi:10.1088/1758-5082/6/3/035020.

[23] Y.J. Tan, X. Tan, W.Y. Yeong, S.B. Tor, Hybrid microscaffold-based 3D bioprinting of multi-cellular constructs with high compressive strength: A new biofabrication strategy, Sci. Rep. 6 (2016) 39140. doi:10.1038/srep39140.

[24] H.A.-D.M. Abu Awwad, L. Thiagarajan, J.M. Kanczler, M.H. Amer, G. Bruce, S. Lanham, R.M.H. Rumney, R.O.C. Oreffo, J.E. Dixon, Genetically-programmed, mesenchymal stromal cell-laden & mechanically strong 3D bioprinted scaffolds for bone repair, J. Control. Release. 325 (2020) 335–346. doi:10.1016/j.jconrel.2020.06.035.

[25] Z. Zhao, M. Espanol, J. Guillem-Marti, D. Kempf, A. Diez-Escudero, M.-P. Ginebra, Ion-doping as a strategy to modulate hydroxyapatite nanoparticle internalization, Nanoscale. 8 (2015) 1595–1607. doi:10.1039/C5NR05262A.

[26] R.A. Perez, S. Del Valle, G. Altankov, M.-P. Ginebra, Porous hydroxyapatite and gelatin/hydroxyapatite microspheres obtained by calcium phosphate cement emulsion, J. Biomed. Mater. Res. B Appl. Biomater. 97B (2011) 156–166. https://onlinelibrary-wiley-com.recursos.biblioteca.upc.edu/doi/pdf/10.1002/jbm.b.31798 (accessed September 23, 2019).

[27] A. Barba, A. Diez-Escudero, Y. Maazouz, K. Rappe, M. Espanol, E.B. Montufar, M. Bonany, J.M. Sadowska, J. Guillem-Marti, C. Öhman-Mägi, C. Persson, M.-C. Manzanares, J. Franch, M.-P. Ginebra, Osteoinduction by Foamed and 3D-Printed Calcium Phosphate Scaffolds: Effect of Nanostructure and Pore Architecture, ACS Appl. Mater. Interfaces. 9 (2017) 41722–41736. doi:10.1021/acsami.7b14175.

[28] J. Schindelin, I. Arganda-Carreras, E. Frise, V. Kaynig, M. Longair, T. Pietzsch, S. Preibisch, C. Rueden, S. Saalfeld, B. Schmid, J.-Y. Tinevez, D.J. White, V. Hartenstein, K. Eliceiri, P. Tomancak, A. Cardona, Fiji: an open-source platform

for biological-image analysis, Nat. Methods. 9 (2012) 676–682. doi:10.1038/nmeth.2019.

[29] J.. Muyonga, C.G.. Cole, K.. Duodu, Fourier transform infrared (FTIR) spectroscopic study of acid soluble collagen and gelatin from skins and bones of young and adult Nile perch (Lates niloticus), Food Chem. 86 (2004) 325–332. doi:10.1016/j.foodchem.2003.09.038.

[30] L. Berzina-Cimdina, N. Borodajenko, Research of Calcium Phosphates Using Fourier Transform Infrared Spectroscopy, in: Infrared Spectrosc. - Mater. Sci. Eng. Technol., InTech, 2012. doi:10.5772/36942.

[31] S. Koutsopoulos, Synthesis and characterization of hydroxyapatite crystals: A review study on the analytical methods, J. Biomed. Mater. Res. 62 (2002) 600–612. doi:10.1002/jbm.10280.

[32] A. Diez-Escudero, M. Espanol, S. Beats, M.-P. Ginebra, In vitro degradation of calcium phosphates: Effect of multiscale porosity, textural properties and composition, Acta Biomater. 60 (2017) 81–92. doi:10.1016/j.actbio.2017.07.033.

[33] M.E. Fleet, The carbonate ion in hydroxyapatite: Recent X-ray and infrared results, Front. Biosci. 5 (2013) 643–652.

[34] X. Wang, Q. Ao, X. Tian, J. Fan, H. Tong, W. Hou, S. Bai, Gelatin-Based Hydrogels for Organ 3D Bioprinting, Polymers (Basel). 9 (2017) 401. doi:10.3390/polym9090401.

[35] S. V Dorozhkin, Nanosized and nanocrystalline calcium orthophosphates, Acta Biomater. 6 (2010) 715–734. doi:10.1016/j.actbio.2009.10.031.

[36] A. Barradas, H. Yuan, C. van Blitterswijk, P. Habibovic, Osteoinductive biomaterials: current knowledge of properties, experimental models and biological mechanisms, Eur. Cells Mater. 21 (2011) 407–429. doi:10.22203/eCM.v021a31.

[37] Q. Xing, K. Yates, C. Vogt, Z. Qian, M.C. Frost, F. Zhao, Increasing Mechanical Strength of Gelatin Hydrogels by Divalent Metal Ion Removal, Sci. Rep. 4 (2014) 4706. doi:10.1038/srep04706.

[38] J. Gustavsson, M. Ginebra, E. Engel, J. Planell, Ion reactivity of calcium-deficient hydroxyapatite in standard cell culture media, Acta Biomater. 7 (2011) 4242–4252. doi:10.1016/j.actbio.2011.07.016.

[39] A. Schwab, R. Levato, M. D'Este, S. Piluso, D. Eglin, J. Malda, Printability and Shape Fidelity of Bioinks in 3D Bioprinting, Chem. Rev. 120 (2020) 11028–11055. doi:10.1021/acs.chemrev.0c00084.

[40] D. Ji, J. Kim, Recent Strategies for Strengthening and Stiffening Tough Hydrogels, Adv. NanoBiomed Res. 1 (2021) 2100026. doi:10.1002/anbr.202100026.

[41] A. Lueckgen, D.S. Garske, A. Ellinghaus, D.J. Mooney, G.N. Duda, A. Cipitria, Enzymatically-degradable alginate hydrogels promote cell spreading and in vivo tissue infiltration, Biomaterials. 217 (2019) 1–11. doi:10.1016/j.biomaterials.2019.119294.

[42] A. Lueckgen, D.S. Garske, A. Ellinghaus, R.M. Desai, A.G. Stafford, D.J. Mooney, G.N. Duda, A. Cipitria, Hydrolytically-degradable click-crosslinked alginate hydrogels, Biomaterials. 181 (2018) 189–198. doi:10.1016/j.biomaterials.2018.07.031.

[43] Q. Wei, J. Young, A. Holle, J. Li, K. Bieback, G. Inman, J.P. Spatz, E.A. Cavalcanti-Adam, Soft Hydrogels for Balancing Cell Proliferation and Differentiation, ACS Biomater. Sci. Eng. 6 (2020) 4687–4701. doi:10.1021/acsbiomaterials.0c00854.

[44] S.K. Bajpai, S. Sharma, Investigation of swelling/degradation behaviour of alginate beads crosslinked with Ca2+ and Ba2+ ions, React. Funct. Polym. 59 (2004) 129–140. doi:10.1016/j.reactfunctpolym.2004.01.002.

[45] A. Grigore, B. Sarker, B. Fabry, A.R. Boccaccini, R. Detsch, Behavior of Encapsulated MG-63 Cells in RGD and Gelatine-Modified Alginate Hydrogels, Tissue Eng. Part A. 20 (2014) 2140–2150. doi:10.1089/ten.tea.2013.0416.

[46] E. Czekanska, M. Stoddart, R. Richards, J. Hayes, In search of an osteoblast cell model for in vitro research, Eur. Cells Mater. 24 (2012) 1–17. doi:10.22203/eCM.v024a01.

[47] S. Boularaoui, G. Al Hussein, K.A. Khan, N. Christoforou, C. Stefanini, An overview of extrusion-based bioprinting with a focus on induced shear stress and its effect on cell viability, Bioprinting. 20 (2020) e00093. doi:10.1016/j.bprint.2020.e00093.

[48] K. Nair, M. Gandhi, S. Khalil, K.C. Yan, M. Marcolongo, K. Barbee, W. Sun, Characterization of cell viability during bioprinting processes, Biotechnol. J. 4 (2009) 1168–1177. doi:10.1002/biot.200900004.

[49] D.F. Duarte Campos, A. Blaeser, K. Buellesbach, K.S. Sen, W. Xun, W. Tillmann, H. Fischer, Bioprinting Organotypic Hydrogels with Improved Mesenchymal Stem Cell Remodeling and Mineralization Properties for Bone Tissue Engineering, Adv. Healthc. Mater. 5 (2016) 1336–1345. doi:10.1002/adhm.201501033.

[50] A.J. Engler, S. Sen, H.L. Sweeney, D.E. Discher, Matrix Elasticity Directs Stem Cell Lineage Specification, Cell. 126 (2006) 677–689. doi:10.1016/j.cell.2006.06.044.

[51] S. Hafeez, H.W. Ooi, F.L. Morgan, C. Mota, M. Dettin, C. van Blitterswijk, L. Moroni, M.B. Baker, Viscoelastic Oxidized Alginates with Reversible Imine Type Crosslinks: Self-Healing, Injectable, and Bioprintable Hydrogels, Gels. 4 (2018) 85. doi:10.3390/gels4040085.

[52] K.B. Fonseca, S.J. Bidarra, M.J. Oliveira, P.L. Granja, C.C. Barrias, Molecularly designed alginate hydrogels susceptible to local proteolysis as three-dimensional cellular microenvironments, Acta Biomater. 7 (2011) 1674–1682. doi:10.1016/j.actbio.2010.12.029.

[53] C. Wang, Y. Gong, Y. Zhong, Y. Yao, K. Su, D.-A. Wang, The control of anchorage-dependent cell behavior within a hydrogel/microcarrier system in an osteogenic model, Biomaterials. 30 (2009) 2259–2269. doi:10.1016/j.biomaterials.2008.12.072.

[54] L.G. Major, A.W. Holle, J.L. Young, M.S. Hepburn, K. Jeong, I.L. Chin, R.W. Sanderson, J.H. Jeong, Z.M. Aman, B.F. Kennedy, Y. Hwang, D.-W. Han, H.W. Park, K.-L. Guan, J.P. Spatz, Y.S. Choi, Volume Adaptation Controls Stem Cell Mechanotransduction, ACS Appl. Mater. Interfaces. 11 (2019) 45520–45530. doi:10.1021/acsami.9b19770.

[55] J. Rychly, B.J. Nebe, Cell-material interaction, BioNanoMaterials. 14 (2013) 153–160. doi:10.1515/bnm-2013-0019.

[56] S. Hanson, R.N. D'Souza, P. Hematti, Biomaterial–Mesenchymal Stem Cell Constructs for Immunomodulation in Composite Tissue Engineering, Tissue Eng. Part A. 20 (2014) 2162–2168. doi:10.1089/ten.tea.2013.0359.

[57] A.R. Akkineni, T. Ahlfeld, A. Lode, M. Gelinsky, A versatile method for combining different biopolymers in a core/shell fashion by 3D plotting to achieve mechanically robust constructs, Biofabrication. 8 (2016) 045001. doi:10.1088/1758-5090/8/4/045001.

Chapter 5

Bioink Functionalisation with Integrin-Selective Peptidomimetics

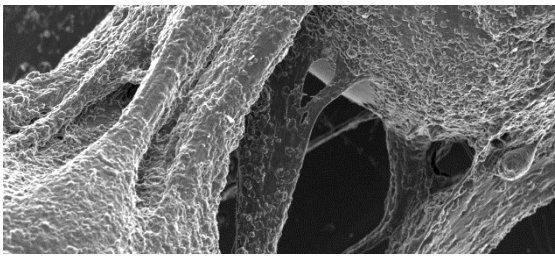

BIOINK FUNCTIONALISATION WITH INTEGRIN-SELECTIVE PEPTIDOMIMETICS

Scope

Looking for alternative ways to provide bioactivity to alginate bioinks, the following chapter focuses on the functionalisation of the polymer with selective peptidomimetics. Carbodiimide chemistry is a widely used approach for the coupling of small RGD peptides to alginate, achieving an improvement of its biological properties. Moreover, the design of peptidomimetics with selective activity towards one specific receptor has been explored in the literature as a strategy to enhance the cellular response of natural peptides. $\alpha_5\beta_1$ and $\alpha_v\beta_3$ integrins have been found to be crucial in the osteogenic process, and synthetic ligands have been developed to tackle them. In **Chapter 5** the functionalisation of alginate with bone-related integrin selective peptidomimetics will be investigated. Furthermore, these functionalised alginates will be used for the synthesis of new cell-laden inks.

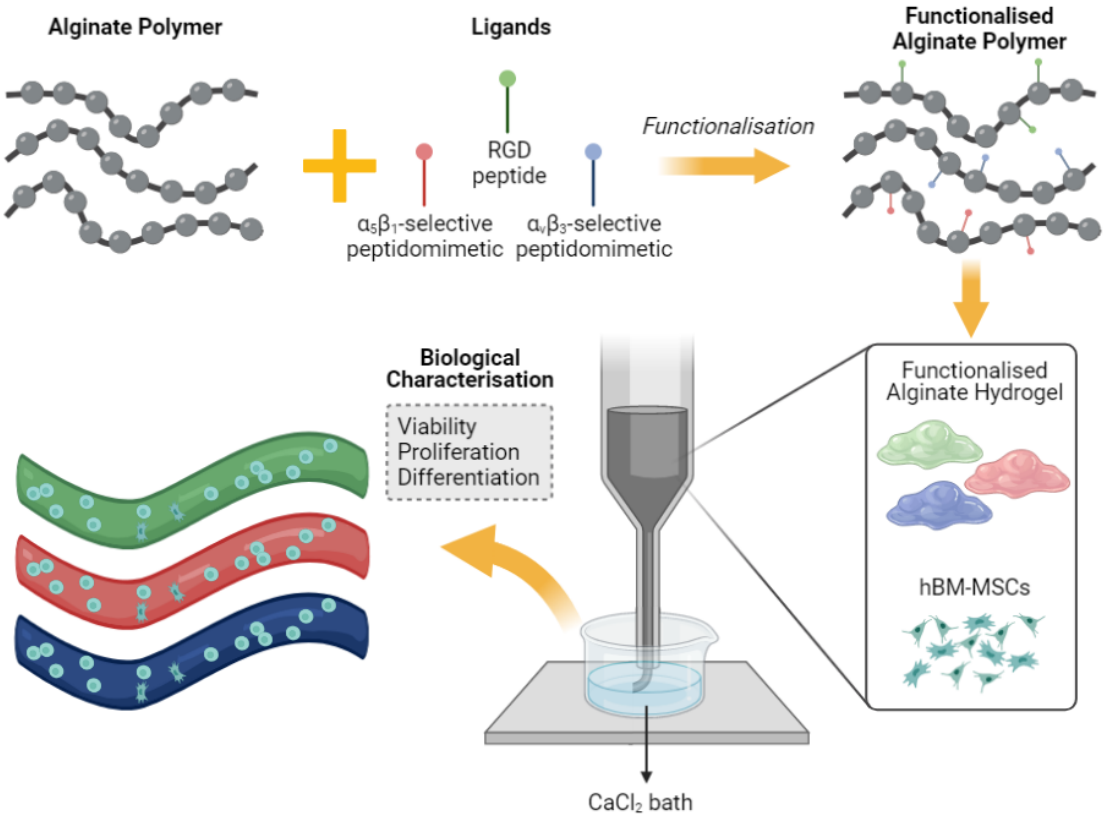

5.1. Introduction

Three-dimensional (3D) systems allow the creation of environments closer to the *in vivo* situation than traditional 2D cell cultures. In this context, 3D bioprinting has emerged as a promising technology in the bone regeneration field, offering the capacity to design 3D constructs with precise control of the spatial distribution of biomaterials, cells and bioactive molecules [1]. The majority bioprinting techniques are based on the use of cell-laden inks, and their development still needs significant research to optimise both printability and cell function.

Alginate is one of the most used hydrogels for the embedding of cells, due to its gentle gelation capacity, high versatility and applicability to different fabrication methods and bioprinting technologies, and the ease in the control/tuning of its mechanical and biological properties [2]. Despite its biocompatibility, however, alginate is not bioactive as it lacks cell adhesive moieties, which are crucial for the correct function of adhering cells [3]. In this regard, the coupling of the cell adhesive sequence arginine-glycine-aspartic acid (RGD) by covalent attachment is a well-established approach to improve cell adhesion on alginate hydrogels and other materials [4–6]. RGD is described as the minimal cell-binding motif in fibronectin and many other proteins of the extracellular matrix (ECM), and it is recognised by different integrin subtypes that are involved in multiple biological pathways [7]. Therefore, in addition to cell-adhesive events, integrin targeting may also foster other biological processes, including cell survival and proliferation, migration and differentiation [8]. More specifically, in the bone tissue engineering field several works coupling RGD peptides to alginate hydrogels reported not only increased levels of cell adhesion and proliferation [6,9,10] but also enhanced values of differentiation of mesenchymal stem cells (MSCs) towards osteoblastic lineage [11]. These results highlight the potential of such ECM-inspired approach for the development of alginate-based cell-laden inks, as reported in a few recent studies [12,13].

Nonetheless, the use of linear RGD peptides entails a number of constraints, such as poor to moderate specificity and affinity for integrins, as well as low stability against enzymatic degradation [14,15]. To overcome these limitations, the use of synthetic peptidomimetics based on the RGD sequence has drawn increasing attention over the last few years. These molecules are designed to bind with high affinity specific integrin subtypes by mimicking the pharmacophore of their natural ligands and optimizing ligand-receptor interactions [8]. Moreover, they present high stability in serum and do not elicit immune reactions [16]. Of the whole subset of RGD-binding integrins, $\alpha_5\beta_1$ (known as the fibronectin receptor) and $\alpha_v\beta_3$ (known as the vitronectin receptor) stand out as prominent receptors for bone tissue regeneration. The β_1 integrin subfamily is the most widely expressed in osteoblasts and MSCs [17,18], while $\alpha_v\beta_3$ is the most abundant integrin in osteosarcoma cells [19]. Moreover, the activation of $\alpha_5\beta_1$ is associated with the overexpression of osteogenic markers, the osseointegration of implants and ectopic bone formation [20–24]. In contrast, the lack of this integrin subtype is related to bone loss [25]. On the other hand, the functions of $\alpha_v\beta_3$ integrin remain controversial, but some studies attribute to this receptor a significant role in matrix mineralisation and in the osteodifferentiation of MSCs through BMP-2 induction [26,27]. Likewise, both integrins have also been associated with mechanotransduction processes [28–30], which have the potential to further regulate cellular behaviour in terms of adhesion or differentiation by providing mechanical cues to the cells.

The capacity to discriminate $\alpha_5\beta_1$ and $\alpha_v\beta_3$ integrin subtypes in vitro and promote integrin-specific cell adhesion with peptidomimetics has been demonstrated [31,32]. In

subsequent studies, we further showed that functionalization of titanium with these ligands improved osteoblast behaviour [33], the adhesion and osteodifferentiation of MSCs [34,35] and bone formation in vivo [34].

However, these integrin-selective peptidomimetics have been mostly tested as surface modification strategies, commonly in 2D configurations, but their effects in 3D environments within a hydrogel matrix are unknown. 3D models better reproduce the physiological conditions of the tissues, and are thus biologically more relevant [36,37].

Based on these premises, we propose for the first time the covalent immobilisation of $\alpha_5\beta_1$ and $\alpha_v\beta_3$ integrin-selective peptidomimetics on alginate hydrogels. The main goal of this strategy is to develop new cell-laden inks for 3D bioprinting with improved cell performance compared to standard RGD-alginate conjugated bioinks, as a first step towards the development of advanced 3D-printed bone tissue constructs.

5.2. Experimental Section

5.2.1. Alginate Functionalisation and Characterisation

The custom-made $\alpha_5\beta_1$- and $\alpha v\beta_3$-selective peptidomimetics were synthesised by a combination of solution and solid-phase peptide synthesis (SPPS), as previously described in the literature [31,38]. Their design was based on the RGD sequence and their structures were optimised through docking studies into the crystal structure of the receptors, as well as competitive solid-phase integrin binding assays. Moreover, a linear RGD peptide (H-GGGGRGDSP-OH, Genscript) was also included in the study as a control. The chemical structure of the three compounds is summarised in **Figure 5.1A**.

The two peptidomimetics and the RGD peptide were covalently attached to alginate by standard carbodiimide chemistry, as described elsewhere [4,9]. Briefly, 1% (v/v) sodium alginate (PanReac AppliChem) was dissolved in MES buffer, consisting of 0.1 M 2-(N-morpholino)ethanesulfonic acid (MES) and 0.3 M NaCl (both from Sigma-Aldrich) adjusted at pH 6.5. Subsequently, N-(3-dimethylaminopropyl)-N′-ethylcarbodiimide hydrochloride (EDC, Sigma-Aldrich) and N-hydroxysuccinimide (NHS, Sigma-Aldrich) were added to the solution to activate the carboxylic acid groups (50 mg EDC and 15 mg NHS per g of alginate). The mixture was stirred for 15 min and followed by the incorporation of either one of the peptidomimetics or the RGD peptide (4 mg per g of alginate). The reaction was allowed to proceed for 24 h at room temperature. The alginate was then dialysed for 4 days using dialysis tubing with MWCO of 3500 Da (Spectra/Por). The purified alginate was freeze-dried and stored at -20 ºC.

The immobilisation of the peptidomimetics and the RGD peptide to the alginate was corroborated by proton nuclear magnetic resonance (^{1}H NMR) spectroscopy. To this end, 5 mg of each functionalised alginate were dissolved in 700 µl D_2O (99.9%) and analysed on a 400 MHz Bruker spectrometer at 298 K (Bruker Ascend 400). Deuterated dimethylformamide was used as an internal standard

5.2.2. Cell Culture

Human bone marrow-derived mesenchymal stem cells (hBM-MSC, ATCC) were cultured in advanced Dulbecco's modified eagle medium (adv. DMEM, Gibco) supplemented with 10% foetal bovine serum (FBS), 20 mM 4-(2-hydroxyethyl)-1-piperazineethanesulfonic acid buffer (HEPES), 50 U ml^{-1} penicillin, 50 µg ml^{-1}

streptomycin and 2 mM L-glutamine, all from Gibco. Cells were maintained at 37 ºC, in a 95% humidified atmosphere with 5% CO_2 and the culture medium was changed twice a week. Cells at passages 3 to 4 were used to carry out the experiments.

5.2.3. Bioink Synthesis

Three bioinks were tested, based on alginate functionalised with (1) RGD peptide; (2) $\alpha_5\beta_1$-selective peptidomimetic; and (3) $\alpha_v\beta_3$-selective peptidomimetic. Pristine alginate was used as control bioink.

Prior to the synthesis of the bioinks, all the materials and the alginates were sterilised with ethanol and low-pressure plasma, respectively. The conjugated alginates were dissolved in adv. DMEM at 3 wt% and manually mixed with 10^6 hBM-MSC. The mixtures were extruded by means of an extrusion-based 3D printer (Pastecaster BCN 3D+, Fundació CIM) at 30 mm s^{-1} through a 22 Ga nozzle directly to a 150 mM $CaCl_2$ (Sigma-Aldrich) bath. After 10 min, the cell-laden inks were rinsed with adv. DMEM and left in culture for 21 days.

5.2.4. Cell Viability and Proliferation

Cell viability in the hydrogels was investigated by staining the cells at different time points (*i.e.* 0, 3, 7, 14 and 21 days) using 3 µM calcein-AM (Santa Cruz Biotechnology) as live indicator in green fluorescence and 1.5 µM propidium iodide (PI, Sigma-Aldrich) as dead indicator in red fluorescence. The stained cells were imaged under a fluorescence confocal laser scanning microscope (LSM 800, Zeiss). In addition, cell viability was further quantified from the images obtained at each time point, with the help of ImageJ software [39], calculating the ratio between live cells over the total number of cells.

Cell proliferation in the bioinks was assessed using a resazurin-based viability reagent (Presto Blue, Invitrogen), following the manufacturer's instructions and measuring the fluorescence at 540/590 nm in a microplate reader (Synergy HTX, BioTek Instruments). Data are presented as fold change to the control at day 0. The bioinks were rinsed with phosphate-buffered saline (PBS) to remove the staining and fresh adv. DMEM was added.

5.2.5. Osteogenic Differentiation

Differentiation of hBM-MSC was assessed by measuring alkaline phosphatase (ALP) activity of the cells embedded in the alginate hydrogels. On days 7, 14 and 21, the cell culture medium was removed and the bioinks were immediately frozen at -80 ºC. To extract proteins from the samples, hydrogels were thawed and mammalian protein extraction reagent (M-PER, Thermo Fisher) was added and incubated for 30 min at room temperature. Afterwards, the bioink was removed and the supernatant was used for the next steps. ALP activity was quantified using SensoLyte pNPP Alkaline Phosphatase Assay Kit (Anaspec), following the manufacturer's instructions. Briefly, the M-PER supernatants were incubated at 37 ºC with the reagents of the kit. After 1 h, the reaction was stopped and the absorbance was measured at 405 nm in a microplate reader (Synergy HTX, BioTek Instruments). For each sample, ALP levels were normalised to cell number. To do so, the release of lactate dehydrogenase (LDH) from the lysates was quantified using the Cytotoxicity Detection Kit^{PLUS} (Roche). The solution was incubated for 10 min with the reagents of the kit, the reaction stopped and the absorbance read at 492 nm in a microplate reader (Synergy HTX, BioTek Instruments).

In addition, cell differentiation to the osteoblastic lineage was determined by measuring gene expression of different osteogenic markers by means of reverse transcription quantitative polymerase chain reaction (RT-qPCR). Total RNA was extracted using TRIzol reagent (Invitrogen) following the manufacturer's protocol. Briefly, bioinks were collected in Eppendorf tubes and incubated for 20 min at room temperature with 1 ml TRIzol. RNA isolation was performed by chloroform/isopropanol method. Afterwards, centrifugation at 12000 g at 4 ^{o}C for 15 min was done to precipitate the RNA. For complete isolation, RNA samples were purified using RNeasy Mini Kit columns (Qiagen). The RNA obtained was quantified spectrophotometrically with Take3 micro-volume plate (BioTek Instruments) followed by cDNA synthesis using QuantiTect Reverse Transcription Kit (Qiagen). The gene expression was assessed with QuantiFast SYBR Green RT-PCR Kit (Qiagen) in a Mic qPCR Cycler (Biomolecular systems) using the primer sequences specified in **Table 5.1**. Negative controls were included to check the absence of contamination. Moreover, in order to ensure the specificity of the reaction, melt curve analysis was done in all runs. Relative gene expression levels were calculated using the $2^{-\Delta\Delta Ct}$ method. GAPDH was used as the housekeeping gene and the data were normalised to the control bioink at day 3.

Table 5.1. Primers' sequences used for RT-qPCR

Gene	**Primers' sequences (Fw= forward; Rv= reverse)**
Glyceraldehyde 3-phosphate dehydrogenase (GAPDH)	Fw: 5'-TTGCCATCAATGACCCCTTCA-3'
	Rv: 5'-CGCCCCACTTGATTTTGGA-3'
Collagen type I (Col. I)	Fw: 5'-AGGTCCCCCTGGAAAGAA-3'
	Rv: 5'-AATCCTCGAGCACCCTGA-3'
Runt-related transcription factor 2 (RUNX2)	Fw: 5'-AAATGCCTCCGCTGTTATGAA-3'
	Rv: 5'-GCTCCGGCCCACAAATCT-3'
Osteopontin (OPN)	Fw: 5'-AGCTGGATGACCAGAGTGCT-3'
	Rv: 5'-TGAAATTCATGGCTGTGGAA-3'
Osteocalcin (OCN)	Fw: 5'-ATGAGAGCCCTCACACTCCT-3'
	Rv: 5'-CTTGGACACAAAGGCTGCAC-3'

5.2.6. Statistical Analysis

All data are reported as means ± standard error of the mean. Data distribution was checked with Shapiro-Wilk test and significant differences between samples were determined using one-way ANOVA with Tukey's post hoc test. p-values <0.05 were considered statistically significant. Statistical analysis was performed using Minitab 19 software.

5.3. Results and Discussion

Alginate-based bioinks represent a promising solution for tissue regeneration applications due to their biocompatibility and tuneable properties. As alginate is not able to support cell adhesion, functionalisation strategies with the cell adhesive sequence RGD have been widely studied to enhance its bioactivity. However, RGD is not integrin-selective and its biological potential is moderate. Thus, the present work aims to immobilise $\alpha_5\beta_1$ and $\alpha_v\beta_3$ integrin-selective peptidomimetics to alginate, in order to improve the biological performance of the polymer. In detail, the purpose of this strategy is to endow the hydrogels with highly specific integrin-binding cues to achieve improved cell adhesion through interaction with integrins, and, eventually, obtain bioinks with enhanced osteogenic potential.

5.3.1. Alginate Bioink Characterisation

Sodium alginate was functionalised either with one of the non-peptidic molecules or with the linear RGD peptide via carbodiimide chemistry. ^{1}H NMR analysis was performed to verify the appropriate coupling of the molecules to the polymer. **Figure 5.1B** displays the spectra obtained of the original and the modified alginates. The signals corresponding to the typical alginate polymer chains consisting of mannuronate and guluronate blocks were detected in the four spectra (3.5 to 5 ppm). It was also possible to observe signals corresponding to coupling by-products (*i.e.* EDC) at 1.2, 2 and 2.8 ppm for the modified samples [40]. However, no additional signals were obtained for the anchored peptidomimetics and RGD peptide. Although NMR has been used to characterise different alginate modifications, such as the introduction of norbornene groups [6], PEG molecules [41] and certain peptides [42], the results highly depend on the sensitivity of the equipment. Therefore, the detection of small molecules such as peptide sequences can be hindered due to the large differences in concentration between alginate and the immobilised molecules. Indeed, the peptide/alginate ratio used in the present study was almost half of the one used in previous studies that were able to detect its presence by NMR [42].

The functionalised alginates were mixed with hBM-MSC and extruded through a nozzle directly to a $CaCl_2$ bath, as depicted in **Figure 5.1C**. Although ionic gelation of hydrogels is associated with poor mechanical stability [43], the final cell-laden inks (**Figure 5.1D**) were stable and maintained their integrity over 21 days of culture. In fact, physical cross-linking is preferable for the *in vivo* application of bioinks because it is a reversible process that allows the progressive exchange of divalent by monovalent cations that revert the gelation of the hydrogel while eventually releasing the differentiated cells, together with their surrounding matrix [44,45]. As the loss of integrity was not evidently shown during the cell culture of the present work, this phenomenon is expected to occur in a longer term.

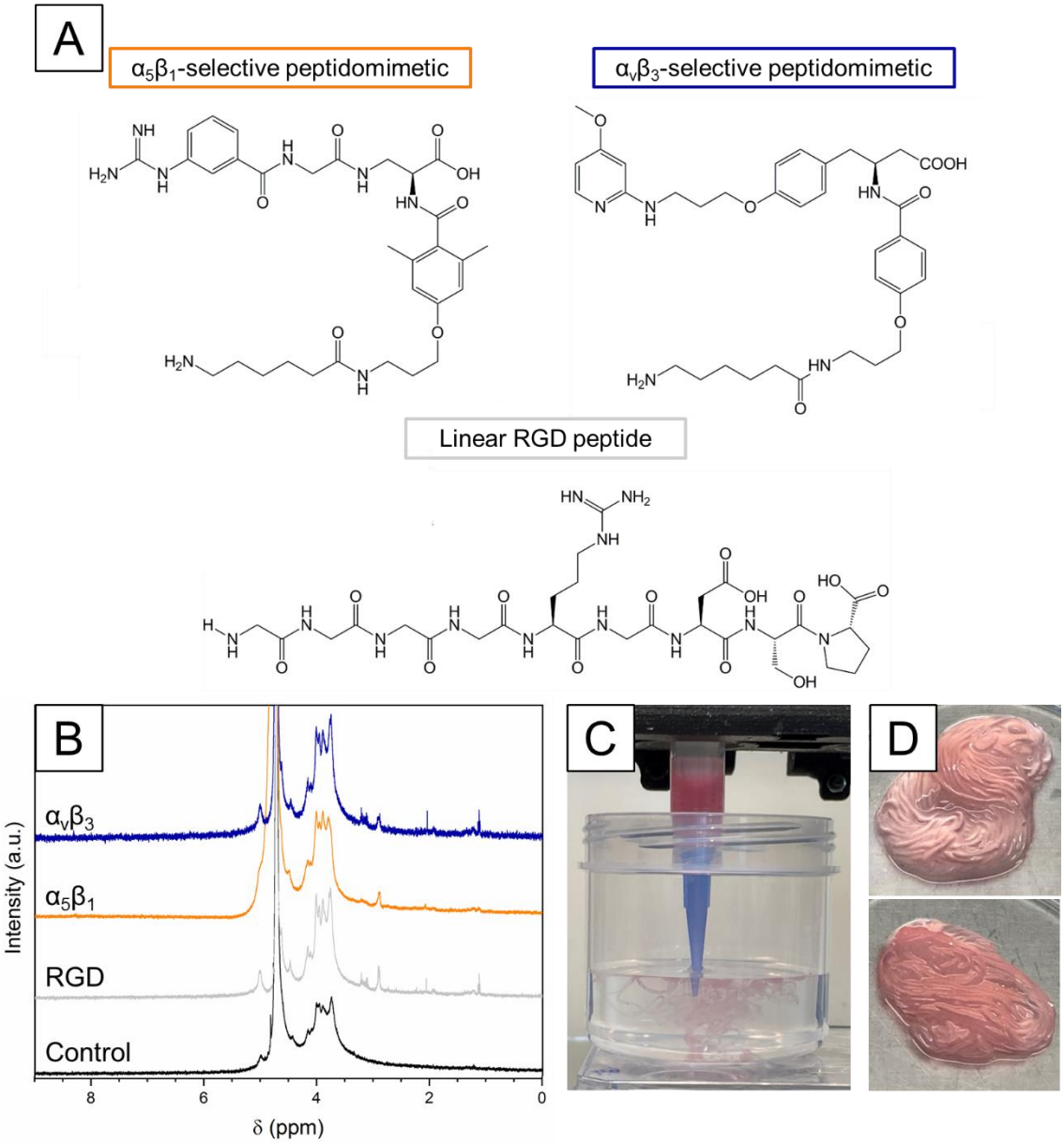

Figure 5.1. **A** Chemical structure of the three compounds used to functionalise alginate: $\alpha_5\beta_1$-selective and $\alpha_v\beta_3$-selective peptidomimetics, and the RGD peptide. **B** ^{1}H NMR spectra of the different alginates. **C** Images of the printing process of the alginate bioinks. **D** Pictures of the resulting alginate bioinks.

5.3.2. Cell Viability and Morphology

hBM-MSC were encapsulated within the alginates to form four different bioinks, *i.e.* a negative control with non-modified alginate, a positive control with alginate functionalised with the linear RGD peptide, and two alginate hydrogels functionalised with either the $\alpha_5\beta_1$- or $\alpha_v\beta_3$-selective non-peptidic mimetics. Cell compatibility is an essential requirement in cell-laden inks [46]. In our case, to study the cytotoxicity, cells were imaged with live/dead staining using a fluorescence confocal microscope at 0, 3, 7, 14 and 21 days. As shown in **Figure 5.2A**, most cells were found to be alive (in green) in all cell-laden inks at all the time points tested, which highlights the proper biocompatibility of all the hydrogels. Overall, the highest cell death (cells in red) was

observed at the shortest time points (*i.e.* days 0 and 3) in all the conditions, which indicates that the extrusion through the nozzle is a critical step for cell viability, as previously stated in the literature [47,48]. To better quantify the differences observed in the images, cell viability percentages were analysed and graphed in **Figure 5.2B**. It was observed that at day 0 all the bioinks presented ≈70% of living cells. The viability increased throughout the study, especially for the cells in the three modified-alginate samples, which reached ≥90% viability at day 7 of culture. In contrast, the percentage of living cells in the control bioink remained stable at ≈70% for 7 days and afterwards it achieved the levels of the other bioinks, close to 95%, at days 14 and 21. Furthermore, live/dead staining showed that cells were homogeneously distributed in all cell-laden inks, exhibiting spherical morphologies and comparable sizes within all hydrogel condition and time points (**Figure 5.2A**). Although functionalisation with integrin binding ligands is generally associated with enhanced cell spreading and focal adhesion formation on 2D metallic and polymeric substrates [49–51], the complexity of the 3D system did not allow to visualise an enhancement in cell adhesion, neither using the two peptidomimetics, nor the linear RGD peptide.

In this regard, it should be noted that, unlike 2D environments, 3D hydrogels limit cell spreading due to the dense matrix network and the fact that integrin activation is not restricted to the ventral side of the cells. Hereof, several works highlight the importance of ECM stiffness and stress relaxation as a fundamental property to understand and modify the cell-ECM interactions. Thus, the modification of the degradability and stiffness of the alginate matrix has been studied aiming at improving cell spreading. These strategies may imply the use of cleavable peptides by matrix metalloproteases [52,53] or tuning the stress relaxation of alginate by different oxidising methodologies and cross-linking protocols [52,54,55]. In general, higher cell spreading and extensive filopodia formation have been observed in alginate hydrogels with faster relaxation properties. Although our system did not consider such modifications, it is noteworthy that cell viability remained excellent at all the studied time points and that the inks supported osteodifferentiation, as discussed below.

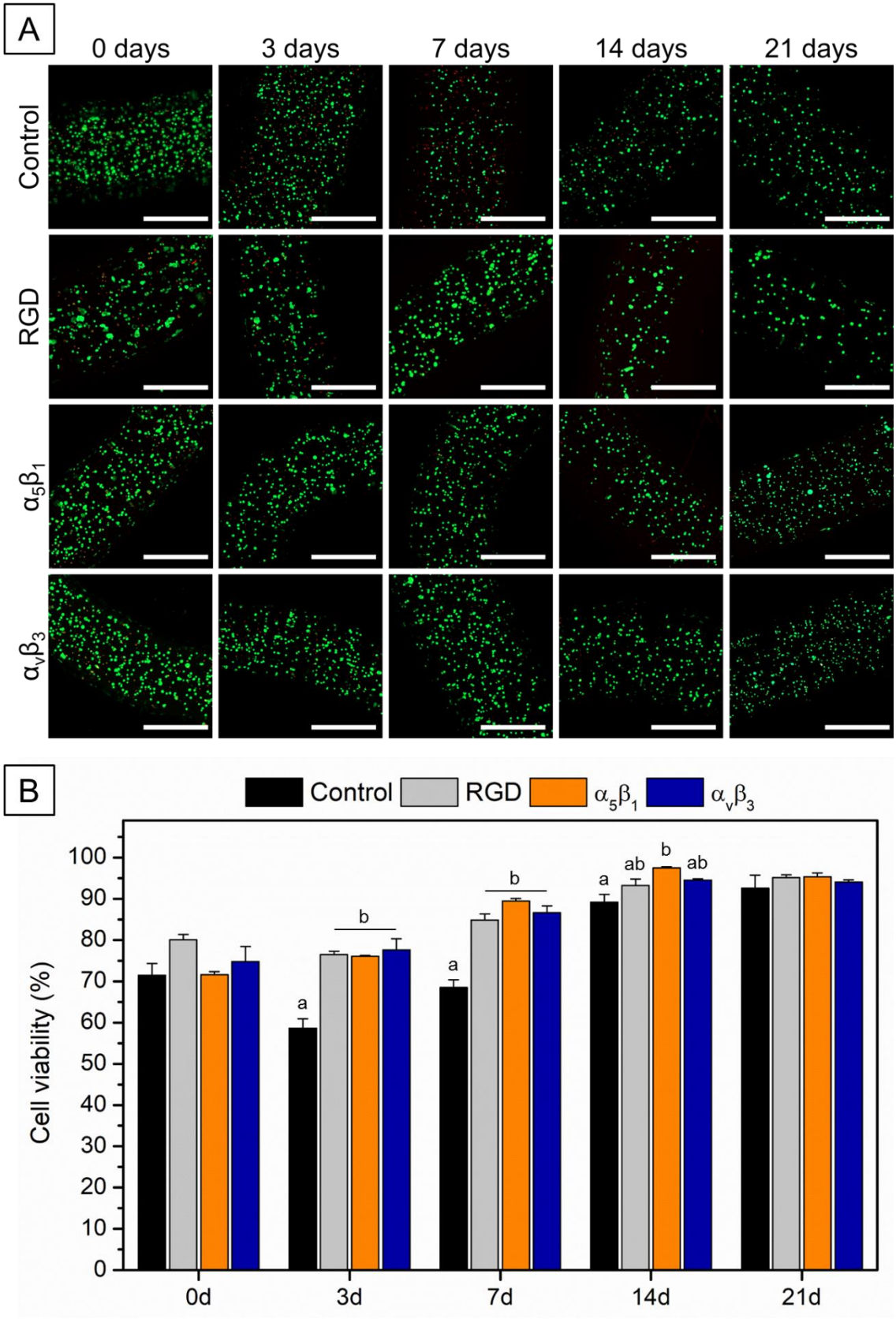

Figure 5.2. Cell viability within the four bioinks throughout the study. **A** Representative images of live/dead staining at each time point. Green and red fluorescence represent living and dead cells, respectively. Scale bar denotes 500 μm. **B** Cell viability

quantification from the images acquired. Different letters indicate statistically significant differences among conditions at each time point.

5.3.3. Cell Proliferation

Proliferation of hBM-MSC on the synthesised bioinks was quantified at 0, 3, 7, 14 and 21 days of culture by means of a resazurin-based assay. The results in **Figure 5.3** indicate a statistically comparable cell number after the extrusion for all the cell-laden inks. Subsequently, the control, RGD and $\alpha_v\beta_3$ samples presented a slow and progressive cell growth throughout the time in culture, reaching up to ≈1.5-1.75-fold increased values at the longer time points. On the contrary, the cell number in the alginate functionalised with the $\alpha_5\beta_1$-selective peptidomimetic remained constant throughout the entire study, suggesting the lack of cell proliferation for this condition. Whereas the increased proliferative rates for RGD and $\alpha v\beta_3$-selective hydrogels correlate well with their integrin binding activity, the non-proliferative cell behaviour of the $\alpha_5\beta_1$-selective sample is unexpected and differs from previous studies in 2D, where the stimulation of $\alpha_5\beta_1$ by the non-peptidic ligand was reported to significantly increase the proliferation of both SaOS-2 cells and hMSC [33,34].

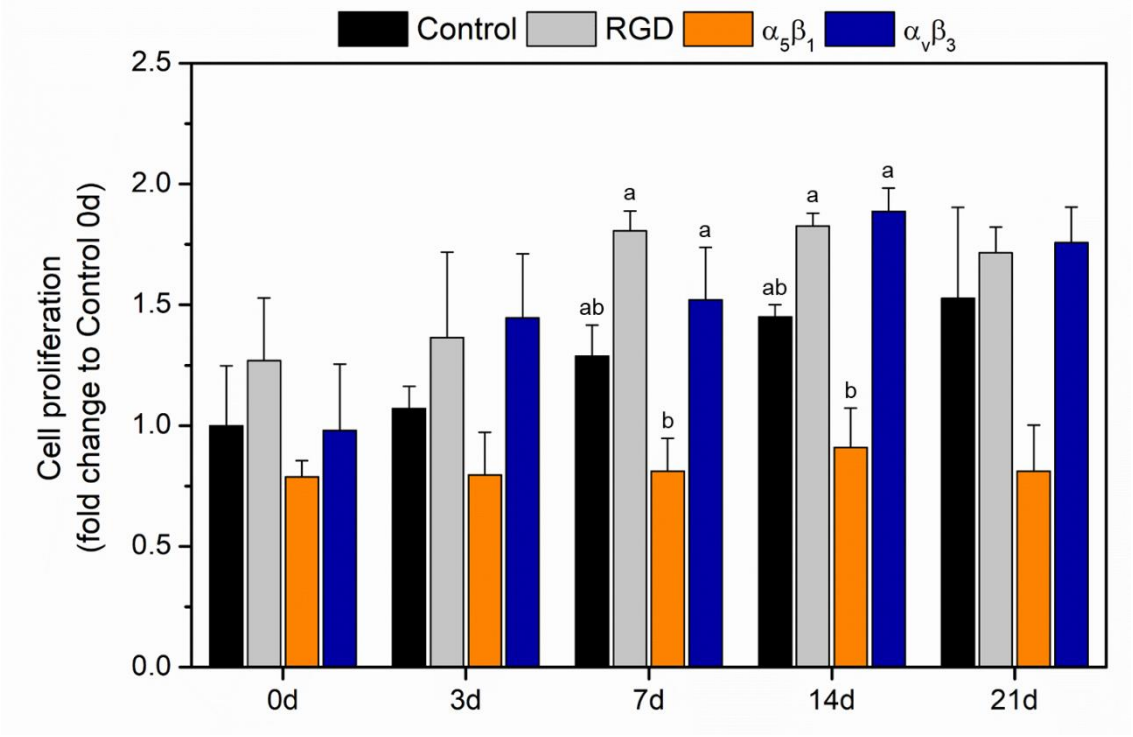

Figure 5.3. Cell proliferation of the hBM-MSC embedded in the different bioinks at each time point, measured through resazurin-based viability assay. Different letters indicate statistically significant differences among conditions at each time point, $p<0.05$, n= 3.

5.3.4. Osteogenic Differentiation

The osteoinductive potential of the two peptidomimetics was evaluated in terms of hBM-MSC differentiation to the osteoblastic lineage and compared to non-functionalised and RGD-functionalised control hydrogels.

On the one hand, ALP activity at 7, 14 and 21 days was studied for the four different alginate bioinks, as summarised in **Figure 5.4**. Overall, that the cells encapsulated in the bioinks functionalised with either of the non-peptidic integrin-selective ligands presented significantly higher ALP activity at 14 and 21 days than the cells embedded in the samples with RGD peptide, with additional significant differences at 7 days between the cell-laden inks with $\alpha_5\beta_1$ non-peptidic mimetic and the RGD-coupled samples. These findings are well in agreement with the reported higher integrin-binding activity of the synthetic ligands for $\alpha_5\beta_1$ and $\alpha_v\beta_3$ integrins, compared to the RGD peptide [56]. As specified before, these two integrin subtypes play a major role in the osteogenic commitment of undifferentiated cells. Moreover, the statistically significant differences between the $\alpha_5\beta_1$ samples and the $\alpha_v\beta_3$ bioinks at days 7 and 21 suggested a higher differentiation potential for the $\alpha_5\beta_1$ mimetic than for the $\alpha_v\beta_3$-selective ligand. Considering the previously observed trends in cell proliferation (**Figure 5.3**), $\alpha_5\beta_1$-selective peptidomimetic seems to promote hBM-MSC differentiation to osteoblastic lineage rather than cell growth, which is an expected behaviour for non-differentiated cells, as both processes present an antagonistic relationship.

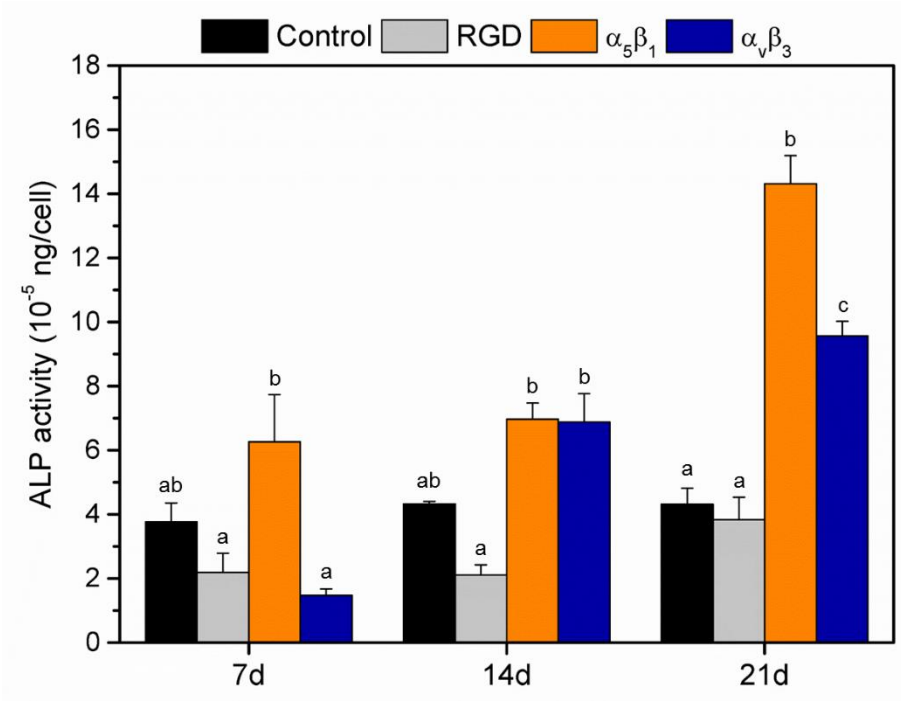

Figure 5.4. Alkaline phosphatase (ALP) activity of the cells in the different alginate bioinks, quantified at 7, 14 and 21 days of culture. Different letters indicate statistically significant differences among conditions at each time point.

On the other hand, the commitment of hBM-MSC to the osteoblastic lineage was further investigated by RT-qPCR, evaluating the gene expression of different osteogenic markers (**Figure 5.5**). Two early-expression markers were studied, namely Col. I and RUNX2. Regarding the Col. I gene, it was found to be significantly overexpressed in presence of RGD and $\alpha_v\beta_3$ peptidomimetic at both short (3 and 7 days) and long (14 days) time points. The analysis of RUNX2 expression revealed similar trends but to a much lower extent, reaching only significant increased expression for $\alpha_v\beta_3$ at 7 days and for RGD at 14 days, compared to the other conditions. In contrast, the presence of the $\alpha_5\beta_1$ peptidomimetic resulted in a lower expression of these early genes.

Moreover, OPN and OCN were also analysed as late osteogenic markers. In regards to the first one, its expression in the peptidomimetic samples remained similar – or even lower – to the control bioink for the first three time points (*i.e.* 3, 7 and 14 days). However, overexpression of ≈15-fold in this gene was observed at day 21 for the cells in the $\alpha_5\beta_1$-alginate bioink, with significant differences to the other samples. Concerning the results of OCN expression, no significant differences between the bioinks were found on days 3 and 7. In contrast, on day 14 OCN was 4-time overexpressed in $\alpha_5\beta_1$ bioink. The same trend was maintained at day 21, where $\alpha_5\beta_1$ mimetics increased the expression of this gene in the embedded cells. In addition, the expression of OCN was also increased in the cells of the $\alpha_v\beta_3$ bioink, to a similar extent to the sample with the other synthetic ligand.

In general, the results of ALP activity and PCR exhibited higher osteoinduction properties for the two non-peptidic mimetics, showing improved osteogenic results than the popular, and less active, RGD peptide, which is usually applied for cell adhesion purposes. In this sense, the positive effect of stimulating the $\alpha_v\beta_3$ integrin subtype on the osteodifferentiation of MSCs has been previously reported [57], and the use of a peptidomimetic selective for this integrin subtype has previously been associated with the overexpression of osteogenic differentiation markers [34,35]. In addition, the results indicated that the $\alpha_5\beta_1$-selective ligand also promotes MSC's osteogenic differentiation, which is in agreement with previous works [22,23,34,58]. In the present study, our results suggest that the role of $\alpha_v\beta_3$ in differentiating MSC to the osteoblastic lineage is focused on the first steps of osteogenesis, while $\alpha_5\beta_1$ seems to have an important effect in the later stages.

Interestingly, the expression in the cells of the control sample showed increasing tendencies with time for the two late-expression genes (*i.e.* OPN and OCN). As no differentiation cues were introduced to this cell-laden ink, this overexpression can be attributed to the mechanical stimuli that the alginate hydrogel induced to the embedded hBM-MSC. Indeed, several works have demonstrated that mechanical signals can mediate stem cell performance [59] and, precisely, its osteogenic differentiation [60–62]. In this regard, Huebsch *et al.* found that MSC osteogenic commitment was promoted by alginate hydrogels with elastic moduli ranging from 11 to 30 kPa [60], while Wei *et al.* showed that hydrogels of ≈3 kPa presented a higher osteogenic differentiation of the embedded cells than softer hydrogels (≈1.5 kPa) [61]. Although the rheological properties of the developed bioinks should be fully characterised, the storage moduli of these new bioinks are expected to be comparable to the ones obtained in **Chapter 4**. All the formulations tested in the previous chapter presented a G' of ≈10 kPa after being cross-linked, which is in the range of hydrogels that induce cell osteodifferentiation. Overall, the overexpression of OPN and OCN in the control sample suggested that the mechanical stimuli of alginate hydrogels contribute to the differentiation of the hBM-MSC.

In another vein, regarding cell shape, whether rounded cells maintain their normal proliferation and differentiation potential is a controversial topic in the literature. Some works showed that round-shaped cells embedded in hydrogels lost their intrinsic proliferation capacity as well as their osteogenic differentiation [63], probably explained by the high hydrophilic environment inside such hydrogels [64]. In contrast, other authors reported that spherical shapes may not prevent the proliferation and differentiation of alginate-embedded cells [45]. This last work is in agreement with the present study, where proliferation and differentiation results exhibited changes among conditions. This may imply that the usual cell function was not prevented by the rounded shapes of the cells, as they were able to grow and differentiate regardless of the lack of spreading.

Indeed, functionalization with integrin-selective peptidomimetics proved useful to efficiently promote the expression of both early and late markers of osteodifferentiation, thus endowing alginate with osteogenic activity and outperforming the potential of the classical RGD sequence, the current gold standard employed in alginate modification.

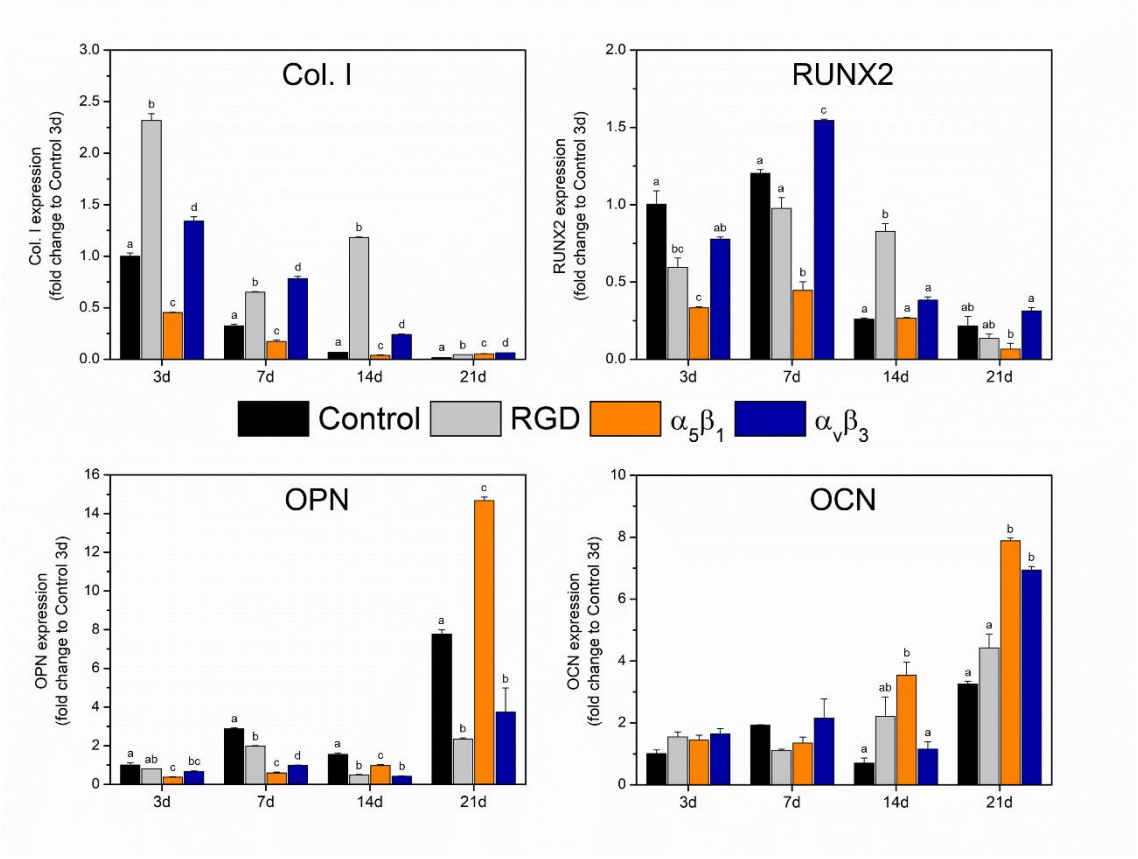

Figure 5.5. Osteogenic markers expression of the hBM-MSC in the bioinks with functionalised alginate quantified by RT-qPCR at 3, 7, 14 and 21 days of culture. Control bioink at day 3 was used as reference to determine the fold changes. Different letters indicate statistically significant differences among conditions at each time point.

5.4. Conclusions

The present work reported the development of new alginate cell-laden inks, taking advantage of a peptide immobilisation strategy through carbodiimide chemistry. For the first time, non-peptidic molecules with $\alpha_5\beta_1$ and $\alpha_v\beta_3$ integrin-selective properties are used for this purpose and applied in the bone regeneration field. Although the presence of these small molecules in the alginates was not detected by ^{1}H NMR, the response of the cells presented significant differences among bioinks. In particular, the two non-peptidic ligands significantly promoted the osteogenic differentiation of hBM-MSC compared not only to the pristine alginate but also to the RGD-functionalised cell-laden ink.

5.5. References

[1] N. Ashammakhi, A. Hasan, O. Kaarela, B. Byambaa, A. Sheikhi, A.K. Gaharwar, A. Khademhosseini, Advancing Frontiers in Bone Bioprinting, Adv. Healthc. Mater. 8 (2019) 1–24. doi:10.1002/adhm.201801048.

[2] A.C. Hernández-González, L. Téllez-Jurado, L.M. Rodríguez-Lorenzo, Alginate hydrogels for bone tissue engineering, from injectables to bioprinting: A Review, Carbohydr. Polym. (2019) 115514. doi:10.1016/j.carbpol.2019.115514.

[3] V. Grigoriou, I.M. Shapiro, E.A. Cavalcanti-Adam, R.J. Composto, P. Ducheyne, C.S. Adams, Apoptosis and Survival of Osteoblast-like Cells Are Regulated by Surface Attachment, J. Biol. Chem. 280 (2005) 1733–1739. doi:10.1074/jbc.M402550200.

[4] J.A. Rowley, G. Madlambayan, D.J. Mooney, Alginate hydrogels as synthetic extracellular matrix materials, Biomaterials. 20 (1999) 45–53. doi:10.1016/S0142-9612(98)00107-0.

[5] R. Lozano, L. Stevens, B.C. Thompson, K.J. Gilmore, R. Gorkin, E.M. Stewart, M. in het Panhuis, M. Romero-Ortega, G.G. Wallace, 3D printing of layered brain-like structures using peptide modified gellan gum substrates, Biomaterials. 67 (2015) 264–273. doi:10.1016/j.biomaterials.2015.07.022.

[6] A. Lueckgen, D.S. Garske, A. Ellinghaus, D.J. Mooney, G.N. Duda, A. Cipitria, Enzymatically-degradable alginate hydrogels promote cell spreading and in vivo tissue infiltration, Biomaterials. 217 (2019) 1–11. doi:10.1016/j.biomaterials.2019.119294.

[7] T.G. Kapp, F. Rechenmacher, S. Neubauer, O. V Maltsev, E.A. Cavalcanti-Adam, R. Zarka, U. Reuning, J. Notni, H.-J. Wester, C. Mas-Moruno, J. Spatz, B. Geiger, H. Kessler, A Comprehensive Evaluation of the Activity and Selectivity Profile of Ligands for RGD-binding Integrins, Sci. Rep. 7 (2017) 39805. doi:10.1038/srep39805.

[8] C. Mas-Moruno, R. Fraioli, F. Rechenmacher, S. Neubauer, T.G. Kapp, H. Kessler, αvβ3- or α5β1-Integrin-Selective Peptidomimetics for Surface Coating, Angew. Chemie Int. Ed. 55 (2016) 7048–7067. doi:10.1002/anie.201509782.

[9] N.O. Dhoot, C.A. Tobias, I. Fischer, M.A. Wheatley, Peptide-modified alginate surfaces as a growth permissive substrate for neurite outgrowth, J. Biomed. Mater. Res. 71A (2004) 191–200. doi:10.1002/jbm.a.30103.

[10] M. Shachar, O. Tsur-Gang, T. Dvir, J. Leor, S. Cohen, The effect of immobilized RGD peptide in alginate scaffolds on cardiac tissue engineering, Acta Biomater. 7 (2011) 152–162. doi:10.1016/j.actbio.2010.07.034.

[11] S.J. Bidarra, C.C. Barrias, M.A. Barbosa, R. Soares, P.L. Granja, Immobilization of Human Mesenchymal Stem Cells within RGD-Grafted Alginate Microspheres and Assessment of Their Angiogenic Potential, Biomacromolecules. 11 (2010) 1956–1964. doi:10.1021/bm100264a.

[12] M.D. Sarker, S. Naghieh, A.D. McInnes, L. Ning, D.J. Schreyer, X. Chen, Bio-fabrication of peptide-modified alginate scaffolds: Printability, mechanical stability and neurite outgrowth assessments, Bioprinting. 14 (2019) e00045. doi:10.1016/j.bprint.2019.e00045.

[13] J. Jia, D.J. Richards, S. Pollard, Y. Tan, J. Rodriguez, R.P. Visconti, T.C. Trusk, M.J. Yost, H. Yao, R.R. Markwald, Y. Mei, Engineering alginate as bioink for bioprinting, Acta Biomater. 10 (2014) 4323–4331. doi:10.1016/j.actbio.2014.06.034.

[14] J.H. Collier, T. Segura, Evolving the use of peptides as components of

biomaterials, Biomaterials. 32 (2011) 4198–4204. doi:10.1016/j.biomaterials.2011.02.030.

[15] C. Mas-Moruno, Surface functionalization of biomaterials for bone tissue regeneration and repair, in: Pept. Proteins as Biomater. Tissue Regen. Repair, Elsevier, 2018: pp. 73–100. doi:10.1016/B978-0-08-100803-4.00003-6.

[16] L. Pollaro, C. Heinis, Strategies to prolong the plasma residence time of peptide drugs, Medchemcomm. 1 (2010) 319–324. doi:10.1039/C0MD00111B.

[17] S. Gronthos, K. Stewart, S.E. Graves, S. Hay, P.J. Simmons, Integrin Expression and Function on Human Osteoblast-like Cells, J. Bone Miner. Res. 12 (1997) 1189–1197. doi:10.1359/jbmr.1997.12.8.1189.

[18] S. Gronthos, P.J. Simmons, S.E. Graves, P.G. Robey, Integrin-mediated Interactions Between Human Bone Marrow Stromal Precursor Cells and the Extracellular Matrix, Bone. 28 (2001) 174–181.

[19] L. Postiglione, G. Di Domenico, L. Ramaglia, S. Montagnani, S. Salzano, F. Di Meglio, L. Sbordone, M. Vitale, G. Rossi, Behavior of SaOS-2 Cells Cultured on Different Titanium Surfaces, J. Dent. Res. 82 (2003) 692–696. doi:10.1177/154405910308200907.

[20] O. Fromigué, J. Brun, C. Marty, S. Da Nascimento, P. Sonnet, P.J. Marie, Peptide-based activation of alpha5 integrin for promoting osteogenesis, J. Cell. Biochem. 113 (2012) 3029–3038. doi:10.1002/jcb.24181.

[21] M.M. Martino, M. Mochizuki, D.A. Rothenfluh, S.A. Rempel, J.A. Hubbell, T.H. Barker, Controlling integrin specificity and stem cell differentiation in 2D and 3D environments through regulation of fibronectin domain stability, Biomaterials. 30 (2009) 1089–1097. doi:10.1016/j.biomaterials.2008.10.047.

[22] Z. Hamidouche, O. Fromigue, J. Ringe, T. Haupl, P. Vaudin, J.-C. Pages, S. Srouji, E. Livne, P.J. Marie, Priming integrin 5 promotes human mesenchymal stromal cell osteoblast differentiation and osteogenesis, Proc. Natl. Acad. Sci. 106 (2009) 18587–18591. doi:10.1073/pnas.0812334106.

[23] T.A. Petrie, J.E. Raynor, C.D. Reyes, K.L. Burns, D.M. Collard, A.J. García, The effect of integrin-specific bioactive coatings on tissue healing and implant osseointegration, BiomaterialsBiomaterials. 29 (2008) 2849–2857. doi:10.1016/j.biomaterials.2008.03.036.

[24] T.A. Petrie, C.D. Reyes, K.L. Burns, A.J. García, Simple application of fibronectin–mimetic coating enhances osseointegration of titanium implants, J. Cell. Mol. Med. 13 (2009) 2602–2612. doi:10.1111/j.1582-4934.2008.00476.x.

[25] C. Dufour, X. Holy, P.J. Marie, Transforming growth factor-β prevents osteoblast apoptosis induced by skeletal unloading via PI3K/Akt, Bcl-2, and phospho-Bad signaling, Am. J. Physiol. Metab. 294 (2008) E794–E801. doi:10.1152/ajpendo.00791.2007.

[26] C.-F. Lai, S.-L. Cheng, αvβ Integrins Play an Essential Role in BMP-2 Induction of Osteoblast Differentiation, J. Bone Miner. Res. 20 (2005) 330–340. doi:10.1359/JBMR.041013.

[27] G.B. Schneider, R. Zaharias, C. Stanford, Osteoblast Integrin Adhesion and Signaling Regulate Mineralization, J. Dent. Res. 80 (2001) 1540–1544. doi:10.1177/00220345010800061201.

[28] M.G. Haugh, T.J. Vaughan, L.M. McNamara, The role of integrin αVβ3 in osteocyte mechanotransduction, J. Mech. Behav. Biomed. Mater. 42 (2015) 67–75. doi:10.1016/j.jmbbm.2014.11.001.

[29] S. Rahmouni, A. Lindner, F. Rechenmacher, S. Neubauer, T.R.A. Sobahi, H. Kessler, E.A. Cavalcanti-Adam, J.P. Spatz, Hydrogel Micropillars with Integrin Selective Peptidomimetic Functionalized Nanopatterned Tops: A New Tool for the Measurement of Cell Traction Forces Transmitted through α v β 3 - or α 5 β 1 -Integrins, Adv. Mater. 25 (2013) 5869–5874. doi:10.1002/adma.201301338.

[30] P. Roca-Cusachs, N.C. Gauthier, A. del Rio, M.P. Sheetz, Clustering of a5b1 integrins determines adhesion strength whereas avb3 and talin enable mechanotransduction, Proc. Natl. Acad. Sci. 106 (2009) 16245–16250. doi:10.1073/pnas.0902818106.

[31] F. Rechenmacher, S. Neubauer, J. Polleux, C. Mas-Moruno, M. De Simone, E.A. Cavalcanti-Adam, J.P. Spatz, R. Fässler, H. Kessler, Functionalizing αvβ3- or α5β1-Selective Integrin Antagonists for Surface Coating: A Method To Discriminate Integrin Subtypes In Vitro, Angew. Chemie Int. Ed. 52 (2013) 1572–1575. doi:10.1002/anie.201206370.

[32] F. Rechenmacher, S. Neubauer, C. Mas-Moruno, P.M. Dorfner, J. Polleux, J. Guasch, B. Conings, H.-G. Boyen, A. Bochen, T.R. Sobahi, R. Burgkart, J.P. Spatz, R. Fässler, H. Kessler, A Molecular Toolkit for the Functionalization of Titanium-Based Biomaterials That Selectively Control Integrin-Mediated Cell Adhesion, Chem. - A Eur. J. 19 (2013) 9218–9223. doi:10.1002/chem.201301478.

[33] R. Fraioli, F. Rechenmacher, S. Neubauer, J.M. Manero, J. Gil, H. Kessler, C. Mas-Moruno, Mimicking bone extracellular matrix: Integrin-binding peptidomimetics enhance osteoblast-like cells adhesion, proliferation, and differentiation on titanium, Colloids Surfaces B Biointerfaces. 128 (2015) 191–200. doi:10.1016/j.colsurfb.2014.12.057.

[34] R. Fraioli, S. Neubauer, F. Rechenmacher, B.M. Bosch, K. Dashnyam, J.-H. Kim, R.A. Perez, H.-W. Kim, F.J. Gil, M.P. Ginebra, J.M. Manero, H. Kessler, C. Mas-Moruno, Control of stem cell response and bone growth on biomaterials by fully non-peptidic integrin selective ligands, Biomater. Sci. 7 (2019) 1281–1285. doi:10.1039/C8BM01466C.

[35] R. Fraioli, P.M. Tsimbouri, L.E. Fisher, A.H. Nobbs, B. Su, S. Neubauer, F. Rechenmacher, H. Kessler, M.-P. Ginebra, M.J. Dalby, J.M. Manero, C. Mas-Moruno, Towards the cell-instructive bactericidal substrate: exploring the combination of nanotopographical features and integrin selective synthetic ligands, Sci. Rep. 7 (2017) 16363. doi:10.1038/s41598-017-16385-3.

[36] A. Abbott, Biology's new dimension, Nature. 424 (2003) 870–872. doi:10.1038/424870a.

[37] T. Andersen, P. Auk-Emblem, M. Dornish, 3D Cell Culture in Alginate Hydrogels, Microarrays. 4 (2015) 133–161. doi:10.3390/microarrays4020133.

[38] S. Neubauer, F. Rechenmacher, R. Brimioulle, F.S. Di Leva, A. Bochen, T.R. Sobahi, M. Schottelius, E. Novellino, C. Mas-Moruno, L. Marinelli, H. Kessler, Pharmacophoric Modifications Lead to Superpotent αvβ3 Integrin Ligands with Suppressed α5β1 Activity, J. Med. Chem. 57 (2014) 3410–3417.

doi:10.1021/jm500092w.

[39] J. Schindelin, I. Arganda-Carreras, E. Frise, V. Kaynig, M. Longair, T. Pietzsch, S. Preibisch, C. Rueden, S. Saalfeld, B. Schmid, J.-Y. Tinevez, D.J. White, V. Hartenstein, K. Eliceiri, P. Tomancak, A. Cardona, Fiji: an open-source platform for biological-image analysis, Nat. Methods. 9 (2012) 676–682. doi:10.1038/nmeth.2019.

[40] A. Schulz, M.M. Gepp, F. Stracke, H. von Briesen, J.C. Neubauer, H. Zimmermann, Tyramine-conjugated alginate hydrogels as a platform for bioactive scaffolds, J. Biomed. Mater. Res. Part A. 107 (2019) 114–121. doi:10.1002/jbm.a.36538.

[41] O. Chaudhuri, L. Gu, D. Klumpers, M. Darnell, S.A. Bencherif, J.C. Weaver, N. Huebsch, H.-P. Lee, E. Lippens, G.N. Duda, D.J. Mooney, Hydrogels with tunable stress relaxation regulate stem cell fate and activity, Nat. Mater. 15 (2016) 326–334. doi:10.1038/nmat4489.

[42] H.W. Ooi, C. Mota, A. Tessa Ten Cate, A. Calore, L. Moroni, M.B. Baker, Thiol−Ene Alginate Hydrogels as Versatile Bioinks for Bioprinting, Biomacromolecules. 19 (2018) 3390–3400. doi:10.1021/acs.biomac.8b00696.

[43] K. Hölzl, S. Lin, L. Tytgat, S. Van Vlierberghe, L. Gu, A. Ovsianikov, Bioink properties before, during and after 3D bioprinting, Biofabrication. 8 (2016) 032002. doi:10.1088/1758-5090/8/3/032002.

[44] S.K. Bajpai, S. Sharma, Investigation of swelling/degradation behaviour of alginate beads crosslinked with Ca2+ and Ba2+ ions, React. Funct. Polym. 59 (2004) 129–140. doi:10.1016/j.reactfunctpolym.2004.01.002.

[45] A. Grigore, B. Sarker, B. Fabry, A.R. Boccaccini, R. Detsch, Behavior of Encapsulated MG-63 Cells in RGD and Gelatine-Modified Alginate Hydrogels, Tissue Eng. Part A. 20 (2014) 2140–2150. doi:10.1089/ten.tea.2013.0416.

[46] I. Matai, G. Kaur, A. Seyedsalehi, A. McClinton, C.T. Laurencin, Progress in 3D bioprinting technology for tissue/organ regenerative engineering, Biomaterials. 226 (2020) 119536. doi:10.1016/j.biomaterials.2019.119536.

[47] A. Blaeser, D.F. Duarte Campos, U. Puster, W. Richtering, M.M. Stevens, H. Fischer, Controlling Shear Stress in 3D Bioprinting is a Key Factor to Balance Printing Resolution and Stem Cell Integrity, Adv. Healthc. Mater. 5 (2016) 326–333. doi:10.1002/adhm.201500677.

[48] S. Boularaoui, G. Al Hussein, K.A. Khan, N. Christoforou, C. Stefanini, An overview of extrusion-based bioprinting with a focus on induced shear stress and its effect on cell viability, Bioprinting. 20 (2020) e00093. doi:10.1016/j.bprint.2020.e00093.

[49] R. Fraioli, K. Dashnyam, J.-H. Kim, R.A. Perez, H.-W. Kim, J. Gil, M.-P. Ginebra, J.M. Manero, C. Mas-Moruno, Surface guidance of stem cell behavior: Chemically tailored co-presentation of integrin-binding peptides stimulates osteogenic differentiation in vitro and bone formation in vivo, Acta Biomater. 43 (2016) 269–281. doi:10.1016/j.actbio.2016.07.049.

[50] C. Mas-Moruno, R. Fraioli, F. Albericio, J.M. Manero, F.J. Gil, Novel Peptide-Based Platform for the Dual Presentation of Biologically Active Peptide Motifs on Biomaterials, ACS Appl. Mater. Interfaces. 6 (2014) 6525–6536.

doi:10.1021/am5001213.

[51] U. Hersel, C. Dahmen, H. Kessler, RGD modified polymers: biomaterials for stimulated cell adhesion and beyond, Biomaterials. 24 (2003) 4385–4415. doi:10.1016/S0142-9612(03)00343-0.

[52] A. Lueckgen, D.S. Garske, A. Ellinghaus, D.J. Mooney, G.N. Duda, A. Cipitria, Enzymatically-degradable alginate hydrogels promote cell spreading and in vivo tissue infiltration, Biomaterials. 217 (2019) 119294. doi:10.1016/j.biomaterials.2019.119294.

[53] K.B. Fonseca, S.J. Bidarra, M.J. Oliveira, P.L. Granja, C.C. Barrias, Molecularly designed alginate hydrogels susceptible to local proteolysis as three-dimensional cellular microenvironments, Acta Biomater. 7 (2011) 1674–1682. doi:10.1016/j.actbio.2010.12.029.

[54] S. Hafeez, H.W. Ooi, F.L. Morgan, C. Mota, M. Dettin, C. van Blitterswijk, L. Moroni, M.B. Baker, Viscoelastic Oxidized Alginates with Reversible Imine Type Crosslinks: Self-Healing, Injectable, and Bioprintable Hydrogels, Gels. 4 (2018) 85. doi:10.3390/gels4040085.

[55] O. Chaudhuri, L. Gu, M. Darnell, D. Klumpers, S.A. Bencherif, J.C. Weaver, N. Huebsch, D.J. Mooney, Substrate stress relaxation regulates cell spreading, Nat. Commun. 6 (2015) 1–7. doi:10.1038/ncomms7365.

[56] T.G. Kapp, F. Rechenmacher, S. Neubauer, O. V. Maltsev, E.A. Cavalcanti-Adam, R. Zarka, U. Reuning, J. Notni, H.-J. Wester, C. Mas-Moruno, J. Spatz, B. Geiger, H. Kessler, A Comprehensive Evaluation of the Activity and Selectivity Profile of Ligands for RGD-binding Integrins, Sci. Rep. 7 (2017) 39805. doi:10.1038/srep39805.

[57] J.-L. Su, J. Chiou, C.-H. Tang, M. Zhao, C.-H. Tsai, P.-S. Chen, Y.-W. Chang, M.-H. Chien, C.-Y. Peng, M. Hsiao, M.-L. Kuo, M.-L. Yen, CYR61 regulates BMP-2-dependent osteoblast differentiation through the {alpha}v{beta}3 integrin/integrin-linked kinase/ERK pathway, J. Biol. Chem. 285 (2010) 31325–31336. doi:10.1074/JBC.M109.087122.

[58] R. Agarwal, C. González-García, B. Torstrick, R.E. Guldberg, M. Salmerón-Sánchez, A.J. García, Simple Coating with Fibronectin Fragment Enhances Stainless Steel Screw Osseointegration in Healthy and Osteoporotic Rats, Biomaterials. 63 (2015) 137–145. doi:10.1016/j.biomaterials.2015.06.025.

[59] D.E. Discher, D.J. Mooney, P.W. Zandstra, Growth Factors, Matrices, and Forces Combine and Control Stem Cells, Science (80-.). 324 (2009) 1673–1677. doi:10.1126/science.1171643.

[60] N. Huebsch, P.R. Arany, A.S. Mao, D. Shvartsman, O.A. Ali, S.A. Bencherif, J. Rivera-Feliciano, D.J. Mooney, Harnessing traction-mediated manipulation of the cell/matrix interface to control stem-cell fate., Nat. Mater. 9 (2010) 518–26. doi:10.1038/nmat2732.

[61] Q. Wei, J. Young, A. Holle, J. Li, K. Bieback, G. Inman, J.P. Spatz, E.A. Cavalcanti-Adam, Soft Hydrogels for Balancing Cell Proliferation and Differentiation, ACS Biomater. Sci. Eng. 6 (2020) 4687–4701. doi:10.1021/acsbiomaterials.0c00854.

[62] T.H. Kim, D.B. An, S.H. Oh, M.K. Kang, H.H. Song, J.H. Lee, Creating stiffness

gradient polyvinyl alcohol hydrogel using a simple gradual freezing–thawing method to investigate stem cell differentiation behaviors, Biomaterials. 40 (2015) 51–60. doi:10.1016/j.biomaterials.2014.11.017.

[63] L.G. Major, A.W. Holle, J.L. Young, M.S. Hepburn, K. Jeong, I.L. Chin, R.W. Sanderson, J.H. Jeong, Z.M. Aman, B.F. Kennedy, Y. Hwang, D.-W. Han, H.W. Park, K.-L. Guan, J.P. Spatz, Y.S. Choi, Volume Adaptation Controls Stem Cell Mechanotransduction, ACS Appl. Mater. Interfaces. 11 (2019) 45520–45530. doi:10.1021/acsami.9b19770.

[64] C. Wang, Y. Gong, Y. Zhong, Y. Yao, K. Su, D.-A. Wang, The control of anchorage-dependent cell behavior within a hydrogel/microcarrier system in an osteogenic model, Biomaterials. 30 (2009) 2259–2269. doi:10.1016/j.biomaterials.2008.12.072.

General Conclusions

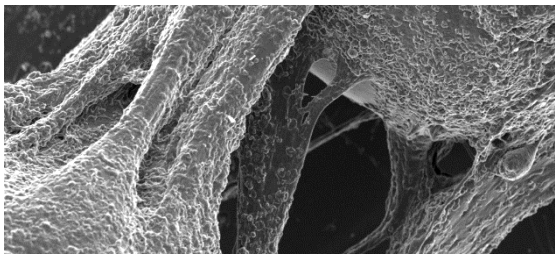

GENERAL CONCLUSIONS

The present PhD thesis was devoted to investigate the cytotoxic mechanism of hydroxyapatite nanoparticles in bone cancer therapy, and to develop new strategies to improve bone regeneration in critical-sized defects. The following conclusions were reached:

- Regarding the use of hydroxyapatite (HA) nanoparticles (NPs) for cancer treatment purposes, the results demonstrated that their main mechanism of toxicity comes from their internalisation into cells, with a minor contribution coming from the interaction of the material with the cell surface. Moreover, as it is necessary to evaluate NPs internalisation and subsequent degradation in the tumour cells, the use of conventional characterisation techniques was explored. It was demonstrated that flow cytometry and transmission electron microscopy, which are frequently used to evaluate the presence of solid NPs, present important drawbacks when working with these particles, such as the overestimation of the internalised NPs due to membrane bounding, and the lack of information about the NPs degradation, respectively. Contrastingly, the use of an intracellular calcium probe revealed the presence of small vesicles filled with soluble calcium, which were further studied through cryo-soft X-ray tomography. They resulted to be multivesicular bodies generated by the degradation of the internalised HA NPs. The combination of all these techniques allows a more detailed analysis of the toxicity of internalised NPs. (**Chapter 2**)

- Apart from the interest of HA NPs as anticancer drugs, doping of these NPs with therapeutic ions is drawing great attention in the bone regeneration field as they can help activate specific cellular cascades. Therefore, composite microspheres (MS) consisting of gelatine and ion-doped HA NPs were successfully synthesised for future use in the formulation of novel bioinks. The introduction of therapeutic ions such as Mg^{2+}, Zn^{2+} or Sr^{2+} entailed morphological changes in terms of sphericity and size distribution of the MS. Importantly, despite the complex dissolution/precipitation reactions of the MS in the cell culture medium, progressive liberation of the incorporated ions was found in all the conditions. Moreover, it was demonstrated that the extent of delivery could be easily controlled by tuning the doping concentration in the NPs. (**Chapter 3**)

- With regards to the biological performance of the mineral loaded MS, various types of MS with different HA loadings (*i.e.* gelatine, gelatine containing HA NPs, and calcium-deficient HA) were seeded with MG-63 cells on them. The results proved that cells were able to attach and proliferate in all the materials. In addition, CDHA MS were found to better promote osteogenic differentiation than the other conditions. The subsequent introduction of the MS into alginate-based bioinks was studied as an approach to overcome the lack of bioactivity of this polymer. This strategy allowed tuning the rheological properties of the final constructs and provided adhesion sites to the embedded cells. Furthermore, supplementation of Ca^{2+} in the media proved to have a pronounced effect on the maintenance of the bioink matrix stiffness, which influenced, as well, the behaviour of the embedded cells. Although all the formulations showed perfect biocompatibility, the stiffness relaxation permitted earlier cell migration to the MS and their proliferation. Gene expression results of the cell-laden inks revealed enhanced osteogenic differentiation in the constructs where it was easier for the cells to migrate on the MS, demonstrating a high influence of direct interaction of the cells with the MS. (**Chapter 4**)

- Apart from the use of NPs, functionalisation of alginate bioinks with $\alpha_5\beta_1$ and $\alpha_v\beta_3$ integrin-selective peptidomimetics was studied as an alternative approach to introduce bioactivity. This system proved to be a good strategy to endow alginate with osteogenic activity, outperforming the potential of the classical RGD sequence, the current gold standard employed in alginate modification. The results demonstrate that the two non-peptidic molecules significantly promoted the expression of both early and late osteodifferentiation markers, by MSC embedded in the constructs and did not compromise the stability and biocompatibility of the ink throughout the study. (**Chapter 5**)

Publications and Conferences

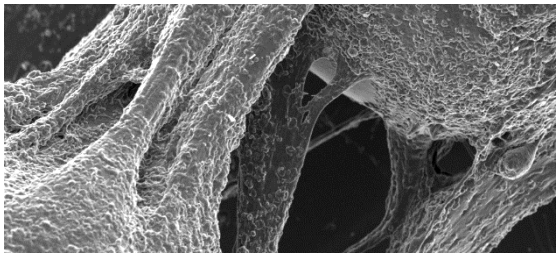

PUBLICATIONS AND CONFERENCES

Publications

Y. Raymond, **M. Bonany**, C. Lehmann, E. Thorel, R. Benítez, J. Franch, M. Espanol, X. Solé-Martí, M-C. Manzanares, C. Canal, M-P. Ginebra. *Hydrothermal processing of 3D-printed calcium phosphate scaffolds enhances bone formation in vivo: a comparison with biomimetic treatment*. Acta Biomater, (2021). https://doi.org/10.1016/j.actbio.2021.09.001

A. Barba, A. Diez-Escudero, M. Espanol, **M. Bonany**, J-M. Sadowska, J. Guillem-Marti, C. Öhman-Mägi, C. Persson, M-C. Manzanares, J. Franch, M-P. Ginebra. *The impact of biomimicry in the design of osteoinductive bone substitutes: nanoscale matters.* ACS Appl. Mater. Interfaces, 11 (9), 8818-30 (2019). https://doi.org/10.1021/acsami.8b20749

A. Diez-Escudero, M. Espanol, **M. Bonany**, X. Lu, C. Persson, M-P. Ginebra. *Heparinization of Beta Tricalcium Phosphate: Osteo-immunomodulatory Effects.* Adv. Healthc. Mater., 7 (5), 1700867 (2017). https://doi.org/10.1002/adhm.201700867

A. Barba, A. Diez-Escudero, Y. Maazouz, K. Rappe, M. Espanol, E-B. Montufar, **M. Bonany**, J-M. Sadowska, J. Guillem-Marti, C. Öhman-Mägi, C. Persson, M-C. Manzanares, J. Franch, M-P. Ginebra. *Osteoinduction by Foamed and 3D-Printed Calcium Phosphate Scaffolds: Effect of Nanostructure and Pore Architecture.* ACS Appl. Mater. Interfaces, 9 (48), 41722-36 (2017). https://doi.org/10.1021/acsami.7b14175

M. Bonany, M. Espanol, C. Mas-Moruno, M-P. Ginebra. *Bioink Functionalisation with Integrin-Selective Peptidomimetics.* (under preparation)

M. Bonany, M. Espanol, M-P. Ginebra. *Microspheres with Ion-Doped Hydroxyapatite Nanoparticles for Enhanced Bone Regeneration.* (under preparation)

M. Bonany, M. Espanol, L. Del Mazo, M-P. Ginebra. *Microspheres Incorporation as a Powerful Strategy to Tune the Biological Performance of Bioinks.* (under preparation)

M. Bonany, A. J. Pérez-Berná, T. Dučić, E. Pereiro, H. Martin-Gómez, C. Mas-Moruno, S. van Rijt, M. Espanol, M-P. Ginebra. *Hydroxyapatite Nanoparticles-Cell Interaction: the Fate of Membrane-Bound and Internalised Nanoparticles.* (under preparation)

Conference Participation

M. Bonany, M. Espanol, M-P. Ginebra. *Microspheres: a powerful strategy to tune the biological performance of bioinks*. 6th World Congress of the Tissue Engineering and Regenerative Medicine International Society (TERMIS). November 2021, virtual conference. **Oral communication**

A. Barba, A. Diez-Escudero, M. Espanol, M. Bonany, J-M. Sadowska, J. Guillem-Marti, C. Öhman-Mägi, C. Persson, M-C. Manzanares, J. Franch, M-P. Ginebra. *Nanoscale relevance in the osteoinductive properties of biomimetic bone substitutes*. IADR/AADR/CADR General Session & Exhibition. March 2020, Washington D.C. (EUA). **Poster communication**

M. Bonany, M. Espanol, Z. Zhao, M-P. Ginebra. *Understanding the cytotoxicity of doped hydroxyapatite nanoparticles on osteosarcoma cells.* 30th Annual Conference of the European Society for Biomaterials (ESB). September 2019, Desden (Germany). **Oral communication**

M. Espanol, M. Bonany, M. Alcaina, Z. Zhao, M-P. Ginebra. *Understanding the cytotoxicity of hydroxyapatite doped nanoparticles on osteosarcoma cells*. V Congreso Hispano-Luso de Cerámica y Vidrio. October 2018, Barcelona (Spain). **Oral communication**

M. Bonany, M. Espanol, M-P. Ginebra. *Understanding the interaction of hydroxyapatite nanoparticles with cells*. 9th International Workshop on Interfaces: New Frontiers in Biomaterials. April 2018, Santiago de Compostela (Spain). **Poster and flash communication**

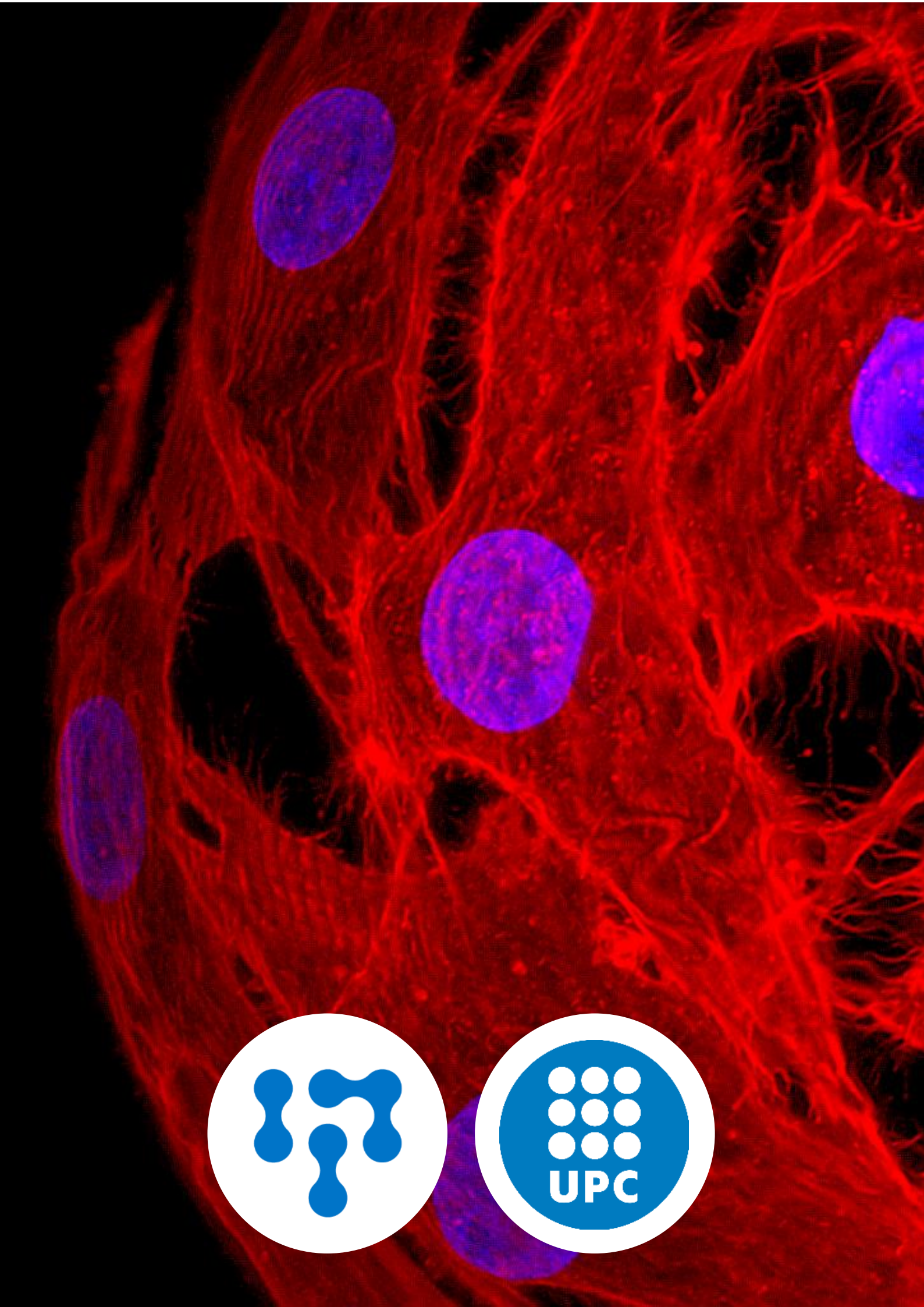
UPC